APPLICATION OF POLARIZED RAMAN SPECTROSCOPY FOR ANALYSIS OF PHASE TRANSITIONS AND ANISOTROPIC BEHAVIOR OF SOFT CONDENSED MATTER

A Dissertation
Presented to
The Academic Faculty

by

Min Sang Park

In Partial Fulfillment
of the Requirements for the Degree
Doctor of Philosophy in the
School of Materials Science and Engineering

Georgia Institute of Technology
May 2012

APPLICATION OF POLARIZED RAMAN SPECTROSCOPY FOR ANALYSIS OF PHASE TRANSITIONS AND ANISOTROPIC BEHAVIOR OF SOFT CONDENSED MATTER

Approved by:

Dr. Mohan Srinivasarao, Advisor
School of Materials Science & Engineering
Georgia Institute of Technology

Dr. Mostafa A. El-sayed
Chemistry & Biochemistry
Georgia Institute of Technology

Dr. Anselm Griffin
School of Materials Science & Engineering
Georgia Institute of Technology

Dr. Laren M. Tolbert
Chemistry & Biochemistry
Georgia Institute of Technology

Dr. Jung Ok Park
School of Materials Science & Engineering
Georgia Institute of Technology

Dr. Elsa Reichmanis
School of Chemical & Biomolecular Engineering
Georgia Institute of Technology

Dr. Alberto Fernandez-Nieves
School of Physics
Georgia Institute of Technology

Dr. Alejandro Rey
Department of Chemical Engineering
McGill University

Date Approved: Jan. 9. 2012

ACKNOWLEDGEMENTS

First and foremost, I wish to express my gratitude to Professor Mohan Srinivasarao for all his help as my thesis advisor. His ideas, guidance, and support have been invaluable to me in my work. The joy and enthusiasm he has for the scientific research was contagious and motivational for me. I appreciate Dr. Jung O. Park for her encouragement and advice throughout my graduate training. Also, the many helpful discussions and criticisms, and valuable suggestions from my thesis committee, Prof. Elsa Reichmanis, Prof. Laren M. Tolbert, Prof. Mostafa A. El-sayed, Prof. Anselm Griffin, Prof. Alberto Fernandez-Nieves, Prof. Alejandro Rey (McGill Univ.), have been of great assistance.

I would like to acknowledge my collaborators, Prof. Elsa Reichmanis & Avishek Aiyar at Georgia Tech (chapter 7, 8, 9), Prof. Satyendra Kumar & Dr. Seung. Y. Jung at Kent State University (chapter 4), Prof. Subbu. S. Venkatraman & Dr. Yee. S. Wong at Nanyang Technological University (chapter 6). My group member, Beom-Jin Yoon, has contributed significantly to derive equations for the calculation of orientation degree. Without his help, I must have struggled to accomplish the quantification of orientation degree.

My fellow graduate students have helped to provide a stimulating, comfortable, and friendly atmosphere in which to work. Although I could not list all of these people, I cannot fail to mention a few. Previous and current group members, Dr. Vivek Sharma & Dr. Matija Crne, Dr. Xuxia Yao, Beom-Jin, Minsu, Karthik have helped adapting myself and becoming skillful with facilities in our lab. My best friends, Seokwon, Eunkyung, Dr.

Han G. Chae, Dr. Iltae Kim, Dr. Seung G. Lee, Dr. Sehoon Chang, Dr. Michelle Schlea, Dr. Katie Campbell, Junghaw and Avi, have spent lots of time during my graduate. The time we shared together has been always happy and a great comfort to my studying abroad.

My thesis work could never have been accomplished without the help and devotion of my with Deuk Kil. For all her love and understanding, there is no paper expression of thanks. The existence and devotion of my family, my daughter Su-Ahn (also, second daughter about-to-be-born), my mother, grandmother, brothers Min Kyu & Seung Hun, and sister/brother in-laws has been my meaning of life. Thus, I willingly dedicate my dissertation to my lovely family. I love them forever.

TABLE OF CONTENTS

3 DETERMINATION OF ORIENTATIONAL ORDER PARAMTERS IN A UNIAXIAL NEMATIC LIQUID CRYSTALLINE PHASE 39

LIST OF TABLES

Page

LIST OF FIGURES

Page

LIST OF SYMBOLS

k_B	Boltzmann constant
T	temperature
eV	electronvolt
N_u	uniaxial nematic phase
N_b	biaxial nematic phase
SmC	smectic C phase
E_o	amplitude of incident electric field
v	frequency of radiation
λ	wavelength of light
H_z	hertz
c	velocity of light
$\tilde{\nu}$	wavenumber of vibration
h	Planck constant
μ	dipole moment
α	molecular polarizability
α_0	polarizability at equilibrium position
ν_m	frequency of molecular vibration
q_k^o	amplitude of the displacement of kth-atom
q_k	displacement of kth-atom in the molecule from its equilibrium
$\left(\partial\alpha / \partial q_k \right)_{q_k=0}$	the rate of polarizability change with respect to the displacement of kth-atom from the equilibrium position

v^i	initial vibrational state
N_{v^i}	the number of molecules in the initial state
Q_v	vibration partition function
I_s	intensity of Raman scattering
$\frac{\partial\sigma}{\partial\Omega}$	Raman scattering cross-section
E_i	directional cosine of the incident electric polarization vector
E_j	directional cosine of the scattered electric polarization vector
I_{ij}	intensity of Raman scattering for any combination of polarization vectors of incident and scattered light
I_{ll}	intensity resolved by the analyzer with the polarization direction parallel to the polarization direction of incident light
$I_{\perp}$	intensity resolved by the analyzer with the polarization direction perpendicular to the polarization direction of incident light
R	depolarization ratio, $R = I_{\perp} / I_{ll}$
R_{iso}	depolarization ratio in isotropic phase
$\Omega(\alpha,\beta,\gamma)$	Euler's angle
$f(\alpha,\beta,\gamma)$	orientational distribution function (ODF)
$f_{mp}(\alpha,\beta)$	most probable orientational distribution function
$\langle P_{lmn} \rangle$	orientational order parameter
T_{NI}	isotropic-nematic phase transition temperature
T_g	glass transition temperature
T_m	melting temperature
T/T_{NI}	reduced temperature

T_{N-SmA}	nematic-smectic A phase transition temperature
$\boldsymbol{n}$	preferred direction of molecular orientation, called director
$r = \dfrac{\partial \alpha'_{zz}}{\partial \alpha'_{yy}}$	Raman tensor ratio
ω_i	Lagrange multipliers
k	experimental factor
ς	Leslie angle
$\alpha_1,\ \alpha_2,\ \alpha_3$	Leslie viscosities
p	aspect ratio of molecular shape
ξ	Tumbling parameter
ε	stretch ratio, $\varepsilon = {}^{l}\!/_{L}$, l: the final length, L: the initial length
Ψ	angle between the symmetry axis of Raman tensor and the helix axis
χ_c	degree of crystallinity
Δn	refractive index difference
b.p.	boiling point
M_w	molecular weight
δ	disclination line
$I_{C=C}$	Raman intensity associated to C=C stretching in thiophene ring

LIST OF ABBREVIATIONS

LCs:	liquid crystals
DSC:	differential scanning calorimetry
SEM/TEM:	scanning/transmission electron microscopy
AFM:	atomic force microscopy
STM:	scanning tunneling microscopy
NMR:	nuclear magnetic resonance
IR:	infrared
WAXRD:	wide angle x-ray diffraction
S/N:	signal-to-noise
N. A.:	numerical aperture
PLLA:	poly($_{L}$-lactic acid)
rr-P3HT:	regio-regular poly (3-hexylthiophenes)
P3AT:	poly(3-alkylthiophene)
P3EHT:	poly(3-(2'-ethyl)hexylthiophene)
$CHCl_3$:	chloroform
DNA:	deoxyribonucleic acid
ODF:	orientational distribution function
5CB:	4'-pentyl-4-cyanobiphenyl
8CB:	4'-octyl-4-cyanobiphenyl
PAA:	4,4'-dimethoxyazoxybenzene
MBBA:	N-(*p*'-methoxybenzylidene)-*p*-n butylaniline)
E2:	5CB-host-LC mixture
A131:	4-((4-dodecylphenyl)diazenyl)phenyl 2-methyl-3-(4-(4-octylbenzoyloxy) benzyledeneamino)benzoate

E7:	eutectic mixture of 4 kinds of cyanobiphenyl nematogens
CCD:	charge-coupled device
LCD:	liquid crystal display
DFT:	density functional theory
POM:	polarized optical microscope
FWHM:	full width at half-maximum
TCB	trichlorobenzene
P	polarizer
A	analyzer
kD	kilodalton. Dalton is the unit of weight, one-twelfth the weight of an atom of ^{12}C. Thus, the molecular weight of water is 18 daltons.

SUMMARY

The importance of research in soft matter, as a major class of materials including liquid crystals, polymers, colloids, emulsions, and forms, is attributed to the behavior resemblances in each branch of soft matter responding to the external perturbations. Hence, one of the most required inquiries in soft matter physics is understanding how the structures with characteristic length scales evolve in response to external perturbations, and concomitant phase transitions. We have focused on adopting polarized Raman spectroscopy to probe phase transitions in soft materials consisting of anisometric components and the evolution of molecular orientational ordering as a complementary tool to other methodologies, but distinct in some respects. The primary task is quantifying the degree of molecular orientation, i.e., obtaining orientational order parameters, in liquid crystal (LCs) system. Thermal evolution of orientation degree in a hitherto elusive biaxial nematic (N_b) phase as well as a commonly known uniaxial nematic (N_u) phase were interrogated from the measurements of anisotropy in polarized Raman intensities. We demonstrated reliable and applicable method to quantify the orientation degree for systems possessing anisotropic ordering.

We also addressed a strong potential of Raman spectroscopy that the changes of vibrational energy reflect the variations of intermolecular interactions and structural changes on the molecular level induced by phase transitions. As a subfield of soft matter, we characterized phase transitions and anisotropic ordering observed in an evaporating conjugated polymer solution and elucidated the mechanism of the entities undergoing phase transitions using mainly polarized Raman spectroscopy. In addition, we have

shown that tracking Raman spectral changes can provide valuable information for understanding structure-property relations when the measurements of the evolution in physical properties are carried out simultaneously.

CHAPTER 1

INTRODUCTION

1.1 What is "Soft Matter"?

A simple dichotomy of the physical states of materials from mechanical point of view lets one classify "*hard*" matter and "*soft*" matter. Judging by the degree of freedom in motion of atoms and its spatial ordering, however, it is not simple to define "*soft*" and "*hard*" in materials science. The answer to "*what is soft matter?*" is not so simple since it covers a variety of physical states observed from a great number of material systems. In materials science, soft matter is a subfield of condensed matter comprising a variety of states that are easily deformable by external stresses, electric or magnetic fields, or by thermal fluctuations. The research areas of colloids, amphiphiles, liquid crystals (LCs), polymers, and biological tissues which may seem to be distinct subjects individually, are indeed classes of soft matter [1-5] as P. G. deGennes, "*founding father of soft matter*", referred in his Nobel lecture in 1991 [6].

What makes soft matter intriguing is that the comprising species exhibit structures with characteristic length scales that are much larger than atomic or molecular length scale, but much smaller than a macroscopic, classical body; hence there is an intermediate, *mesoscopic* regime [1, 2, 7, 8]. The relationship between the size/shape of components and the physical length scales exhibit some universality for a diverse set of material systems [2, 9]. First universality, "s*oftness*", is associated with the physical structure at mesoscopic length scale formed by the secondary bonds, which can be perturbed by weak external field. For soft matter, the energy required to perturb the physical structure is on the order of thermal energy ($k_BT \approx 1/40\ eV$), which implies that many of interactions in these systems are entropic in origin, whereas the energy scales to perturb of covalent bond in molecular crystal is a lot higher at room temperature (>10 *eV*) [1].

Another common feature lies in phase behavior among the different classes of materials. Mesoscopic units organize into ordered phases without external stimuli, i.e., *self-assemble into ordered phases*, which is the consequence of the effective interactions being repulsive at short distance and attractive at long distance that balance each other [1, 4, 5, 10]. Combined with the capability of being tunable with weak external fields, their rich structural diversity via self-assembly have been areas of intensive research activity [11-14]. From great technological interests, numbers of research groups have focused on diverse architectures via self-assembly of components of soft materials for cutting-edge applications: 3-dimensional periodicity of colloidal particles for suitable photonic band-gap material [15-17], self-assembly of block copolymers into a variety of ordered phases as a template for the use in lithography [18-20], the self-assembly of peptide amphiphiles into cylindrical nano-fibers [21, 22], nano-segregated liquid crystals into a variety of mesophases for the nanoscale ion-pathways [23, 24] among others. Understanding the way these ordered structures arise leads to many questions concerning the microstructure, phase transitions, structural kinetics of complex materials in bulk, at interface as well as in confined geometry. Accordingly, soft matter activities embrace site-selective chemistry and tailoring of supramolecular complexes, physical mechanisms governing the final structure of the condensed system.

One of the most fundamental understandings in soft matter physics is phase transitions and structural evolutions under the external perturbations. Phase transitions almost always accompany a change in the molecular order and the system undergoing phase transitions adopts new structures. In most soft matter, the degree of molecular order lies between the perfect long-range positional and translational order as well as orientational order, as a single crystal possesses, and the complete disorder in isotropic liquids. Among the ordered structures in soft matter, we are focusing on two different types of the intermediate order: an *equilibrium liquid crystalline state* and *non-equilibrium state with partial crystallinity* [3]. Components in liquid crystalline phases are arranged with a long-range orientational order and, in some specific cases, with a quasi-long range translational order in one and two dimensions [10]. The structures in liquid crystalline phase are usually formed via self-organizations of the components with high anisotropy in the molecular shape, of polymers composed of rigid-rod like mesogen attached by the flexible side chains, of anisometric aggregates/colloidal particles, or rod-like polymers in a concentrated solution. Systems with a partial crystallinity are, on the other hand, prevented from reaching their equilibrium state due to slow dynamics of mesoscopic scale components, in which microscopic regions with crystalline order coexist with disordered regions. Semi-crystalline polymer is one of the soft matter systems with a partial crystallinity, which comprises small crystals in a matrix of much less ordered chains.

For the study of phase transitions in soft matter, therefore, the primary tasks are to address: *i) How to define a parameter that characterizes the state of molecular order, so-called "order parameter", and how to quantify it?* and *ii) what is the mechanism of the entities undergoing phase transitions?* In order to answer these questions, a variety of methods to characterize the phase behaviors have been used [25, 26].

1.2 Characterization of Soft Matter

Along with the traditional method of differential scanning calorimetry (DSC) that helps identifying phase transitions in a thermotropic system, but gives little information about systems in which enthalpies of transitions are very small [27, 28], various characterization techniques have been adopted to explore the phase transitions and distinct phase behaviors of components in soft matter [25]. Scattering methods with different radiation sources (light, neutron, and x-rays) provide structural information based on the concept of interference and its relation to the structure. In addition, properties such as the translational diffusion coefficient, hydrodynamic radius and its size distribution, as well as rotational and internal motions are measured in dynamic scattering based on local intensity fluctuations of scattered light [29]. A primary tool in featuring the character of many of these phases has been microscopy. While limited spatial resolution in optical microscopy (a Rayleigh limit of $\lambda/2$) and elaborate sample preparations for electron microscopy (SEM/TEM) impose restrictions on the use of conventional microscopy, they have still succeeded in imaging the ordered structure according to length scale of interest [30-32]. The characterizations of the surface of the soft matter systems are performed using surface probe microscopy techniques such as atomic force microscopy (AFM) and scanning tunneling microscopy (STM) with nano-scale resolution [33, 34]. Spectroscopic techniques such as nuclear magnetic resonance (NMR) [35, 36], ultraviolet (UV)-visible light [37], fluorescence [38], infrared (IR) spectroscopy [39] are some of the most powerful characterization tools for elucidating the ambiguity of structure in soft matter based on the symmetry considerations. Different regions of the light spectrum provide different kinds of information as results of many interactions of the given electromagnetic radiation with matter, which yield information about certain characteristic features rather than providing a three-dimensional picture of structure [40].

Each of these has particular advantages and disadvantages for characterizing soft matter and detailed remarks are not enumerated in this thesis. There are many fine texts of general descriptions about characterization in soft materials [41-43]. Suffice it to say that no single technique will provide all the desirable information, and they can be understood even better by making the full use of many characterization techniques. Therefore, finding unexplored ways to characterize soft matter physics using the conventional techniques is as much important as the advance in the characterization by aid of cutting-edge technologies. *The key driver of the researches in this thesis is the* *contribution of polarized Raman spectroscopy to probe phase transitions in soft matter system consisting of anisometric components and the evolution of molecular ordering under external perturbations as a complementary tool to other methodologies, but distinctive in some respects*.

Among a variety of spectroscopic methods, vibrational spectroscopy (Raman / infrared spectroscopy) has been widely used not only for providing basic phase identification, but also for studying the structural chemistry based on spectral alterations [44-46]. Many of the studies have been performed to determine the chemical composition by observing Raman bands at frequencies characteristic of specific chemical bonds and symmetry of molecules [47, 48]. Apart from the role of fingerprint for chemical analysis, a strong potential of Raman spectroscopy lies in the fact that the changes of vibrational energies reflect the extent of intermolecular interactions and structural changes induced by phase transitions [49, 50]. When the material systems are subject to external fields, therefore, valuable information about the extent of molecular order and phase behaviors can be obtainable by Raman spectroscopy. In the condensed state, neighboring components of the same or different species interact with one another and influence their vibrational energies by coupling of vibrations in adjacent species, resulting in relative intensity changes of Raman bands, bands shift in frequency, or evolution of band shape. In addition to the qualitative information, the use of polarized Raman spectroscopy provides us with quantitative information about the intermediate ordering, *the degree of orientation*, which is described in detail in chapter 2.

Finally, several advantages in using Raman spectroscopy as a characterization tool need to be described. It is a nondestructive and non-contact method, thus specific sample and specimen preparations are not required. The two-fold advantages of Raman over IR spectroscopy should be noted: *(i)* samples can be confined or sealed in a transparent glass since a glass dose not absorb the light source for conventional Raman spectroscopy (the visible and near-IR regions (λ: 300 ~1050 *nm*). Thus, it is proper for the analysis of reactive or environment sensitive compounds. *(ii)* Since vibrations of atoms in H_2O is weakly Raman active and does not generally interfere the Raman signal of other species, it is suitable to examine biological compounds in aqueous solution, in contrast to IR spectroscopy that is restricted by very strong absorption of water. In addition, equipped with a high-magnification microscope objective, known as *micro-Raman spectroscope* [51], it requires a sample as small as tens of μm across. Thanks to high photon flux through microscope focus and improved signal-to-noise (S/N) ratio using high N.A objectives, a short data collection time (normally a few seconds) is sufficient, which enables one to monitor the evolution of chemical/physical phenomena induced by external perturbations in real-time.

While several advanced techniques applied to Raman spectroscopy, a direct 3D imaging or chemical imaging of complex structures using confocal [52, 53], and near-field optical microscopy combined with Raman spectrometer [54], an optical trapping of species of interest [55], or a more effective and sensitive tool for biological imaging using coherent anti-stoke scattering [56, 57], are drawing attention, *we focus our attention on the use of conventional polarized micro-Raman spectroscopy to elucidate phase transitions and associated molecular order in the system with complementary data obtained by x-ray diffraction, optical microscopy and AFM.*

1.3 Thesis Outline

This thesis focuses on the contribution of polarized Raman spectroscopy to the characterization of phase transitions and the molecular order in soft matter systems consisting of anisotropic shape species. Chapter 2 provides necessary background of Raman spectroscopy that includes the quantification of the orientation degree using the anisotropy in polarized Raman intensity. The remaining chapters comprise studies about specific materials systems: Chapter 3 introduces the approach of quantifying the orientational order in liquid crystalline phase consisting of low molecular weight compounds. Rather than reproducing the conventional method [58] to obtain orientational order parameters using polarized micro-Raman spectroscopy, we introduce and verify the modified way to obtain the orientational order with more accuracy in LC system. In chapter 4, one of the ambiguous phases in liquid crystals, biaxial nematic (N_b) phase in a thermotropic system, is studied and the degree of biaxial orientation and thermal evolution of order parameters, which is critical to understanding the physical property of this intriguing phase, is addressed. In chapter 5, we predict flow-aligning property of liquid crystals studied in chapter 3 and 4 using experimentally obtained orientational order parameters. Chapter 6 describes the way to characterize the behaviors of polymer chain that exhibits a semi-crystalline phase corresponding to mechanical force in detail, in which chain alignments in stretched poly($_L$-lactic acid) (PLLA) samples are elucidated using polarized Raman spectroscopy.

In the other chapters (chapter 7-9), we make efforts to study phase transitions and film formation mechanism in an evaporating polymer solution using one of the most widely used conjugated polymers, poly (3-hexylthiophenes) (P3HT). We propose the existence of a lyotropic liquid crystalline (LC) phase upon solvent evaporation induced film formation in chapter 7, which has not been reported before. In chapter 8, we discuss periodic undulating patterns that appear at the periphery of drop-cast P3HT film using polarized optical microscopy (POM) and atomic force microscopy (AFM). The results in chapter 8 may support the conclusion of chapter 7, that is, the existence of a lyotropic LC phase while solvent evaporates in a P3HT sessile drop. Finally, the correlation between the morphology development of drop-casting P3HT and electrical property is described in chapter 9 by simultaneously tracking the Raman spectral changes and drain current *in-situ*.

1.4 References

[1] I. W. Hamley, *Introduction to Soft Matter (Polymers, Colloids, Amphiphiles and Liquid Crystals)*. Chichester: John Wiley & Sons, Ltd., 2000.

[2] Daoud, M.; Williams, C. E., Williams, Eds., *Soft Matter Physics*. Berlin: Springer, pp. 289-314, 1999.

[3] R. A. L. Jones, *Soft Condensed Matter*. Oxford: Oxford University Press, 2004.

[4] T. A. Witten, "Insights from soft condensed matter," *Reviews of Modern Physics*, **71**, S367-S373 (1999).

[5] Witten, T. A.; Pincus, P. A. Pincus, *Structured Fluids (Polymers, Colloids, Surfactants)*. Oxford: Oxford University Press, 2004.

[6] P. G. De Gennes, "Soft Matter," *Nobel Lecture*, 1991.

[7] C. N. Likos, “Effective interactions in soft condensed matter physics” *Physics Reports-Review Section of Physics Letters*, **348**, 267-439 (2001).

[8] Arora, A. K.; Tata, B. V. R. “Interactions, structural ordering and phase transitions in colloidal dispersions” *Advances in Colloid and Interface Science,* **78**, 49-97 (1998).

[9] P. G. De Gennes, *Scaling Concepts in Polymer Physics*. Ithaca, NJ: Cornell University Press, 1979.

[10] Chaikin, P. M.; Lubensky, T. C. *Principles of Condensed Matter Physics*. New York: Cambridge University Press, pp. 17-25 and pp. 58-71, 1995.

[11] Whitesides, G. M.; Mathias, J. P.; Seto, C. T. “Molecular self-assembly and nanochemistry - A chemical strategy for the synthesis of nanostructures” *Science*, vol. 254, pp. 1312-1319, (1991).

[12] Mirkin, C. A.; Letsinger, R. L.; Mucic, R. C.; Storhoff, J. J. “A DNA-based method for rationally assembling nanoparticles into macroscopic materials” *Nature,* **382**, pp. 607-609 (1996).

[13] Brinker, C. J.; Lu, Y. F.; Sellinger, A.; Fan, H. Y. “Evaporation-induced self-assembly: Nanostructures made easy” *Advanced Materials,* **11**, 579-585 (1999).

[14] Ikkala, O.; ten Brinke, G. “Hierarchical self-assembly in polymeric complexes: Towards functional materials” *Chemical Communications,* 2131-2137 (2004).

[15] Vos, W. L.; Sprik, R.; vanBlaaderen, A.; Imhof, A.; Lagendijk, A.; Wegdam, G. H. “Strong effects of photonic band structures on the diffraction of colloidal crystals” *Physical Review B,* **53**, 16231-16235 (1996).

[16] Pan, G. S.; Kesavamoorthy, R.; Asher, S. A. “Optically nonlinear Bragg diffracting nanosecond optical switches” *Physical Review Letters,* **78**, 3860-3863 (1997).

[17] vanBlaaderen, A.; Ruel, R.; Wiltzius, P. “Template-directed colloidal crystallization” *Nature,* **385**, 321-324 (1997).

[18] Park, M.; Harrison, C.; Chaikin, P. M.; Register, R. A.; Adamson, D. H. “Block copolymer lithography: Periodic arrays of similar to 10(11) holes in 1 square centimeter” *Science,* **276**, 1401-1404 (1997).

[19] Park, C.; Yoon, J.; Thomas, E. L. “Enabling nanotechnology with self assembled block copolymer patterns” *Polymer,* **44**, 6725-6760 (2003).

[20] Cheng, J. Y.; Mayes, A. M.; Ross, C. A. “Nanostructure engineering by templated self-assembly of block copolymers” *Nature Materials,* **3**, 823-828 (2004).

[21] Hartgerink, J. D.; Beniash, E.; Stupp, S. I. “Self-assembly and mineralization of peptide-amphiphile nanofibers” *Science,* **294**, 1684-1688 (2001).

[22] Hartgerink, J. D.; Beniash, E.; Stupp, S. I. “Peptide-amphiphile nanofibers: A versatile scaffold for the preparation of self-assembling materials” *Proceedings of the National Academy of Sciences of the United States of America,* **99**, 5133-5138 (2002).

[23] Yoshio, M.; Mukai, T.; Ohno, H.; Kato, T. “One-dimensional ion transport in self-organized columnar ionic liquids” *Journal of the American Chemical Society,* **126**, 994-995 (2004).

[24] Kerr, R. L.; Miller, S. A.; Shoemaker, R. K.; Elliott, B. J.; Gin, D. L. “New type of Li ion conductor with 3D interconnected nanopores via polymerization of a liquid organic electrolyte-filled lyotropic liquid-crystal assembly” *Journal of the American Chemical Society,* **131**, 15972-5973 (2009).

[25] Borsali, R.; Pecora, R., Eds., *Soft Matter Characterization*. Dordercht: Springer, pp. 1-38 and references therein, 2007.

[26] M. S. Amer, *Raman sepctroscopy for soft matter applications*. New Jersey: John Wiley & Sons. Inc., 2009.

[27] Roos, Y. H.; Karel, M. “Differntial scanning calorimetry study of phase-transitions affecting the quality of dehydrated materials” *Biotechnology Progress,* **6**, 159-163 (1990).

[28] S. Kumar, Ed., *Liquid Crystals in the Nineties and Beyond* (Thermal Investigations of Phase Transitions in Thermotropic Liquid Crystals. Singapore: World Scientific Publishing Co. Pte. Ltd, pp. 19-80, 1995.

[29] Borsali, R.; Pecora, R., Eds., *Soft Matter Characterization*. Dordercht: Springer, pp.637-673, 2007.

[30] Smalyukh, II; Lavrentovich, O. D.; Kuzmin, A. N.; Kachynski, A. V.; Prasad, P. N. “Elasticity-mediated self-organization and colloidal interactions of solid spheres with tangential anchoring in a nematic liquid crystal” *Physical Review Letters,* **95**, 157801 (2005).

[31] Friedrich, H.; Frederik, P. M.; de With, G.; Sommerdijk, N. “Imaging of self-assembled structures: Interpretation of TEM and cryo-TEM images” *Angewandte Chemie-International Edition,* **49**, 7850-7858 (2010).

[32] Thiberge, S.; Nechushtan, A.; Sprinzak, D.; Gileadi, O.; Behar, V.; Zik, O.; Chowers, Y.; Michaeli, S.; Schlessinger, J.; Moses, E. “Scanning electron microscopy of cells and tissues under fully hydrated conditions” *Proceedings of the National Academy of Sciences of the United States of America,* **101**, 3346-3351 (2004).

[33] Samori, P.; Cicoira, F. *STM and AFM studies on (bio)molecular systems: unravelling the nanoworld*. Berlin: Springer, 2008 and references therein.

[34] Yang, C. W.; Hwang, I. S.; Chen, Y. F.; Chang, C. S.; Tsai, D. P. "Imaging of soft matter with tapping-mode atomic force microscopy and non-contact-mode atomic force microscopy" *Nanotechnology,* **18**, 084009 (2007).

[35] Toledano, P.; Neto, A. M. F., Eds., *Phase Transitions in Complex Fluids* (NMR Studies of Lyotropic Liquid Crystals. New Jersey: World Scientific, pp.81-106, 1998.

[36] Blumich, B.; Blumler, P.; Eidmann, G.; Guthausen, A.; Haken, R.; Schmitz, U.; Saito, K.; Zimmer, G. "The NMR-mouse: Construction, excitation, and applications" *Magnetic Resonance Imaging,* **16**, 479-484 (1998).

[37] Boudouris, B. W.; Ho, V.; Jimison, L. H.; Toney, M. F.; Salleo, A.; Segalman, R. A. "Real-time observation of poly(3-alkylthiophene) crystallization and correlation with transient optoelectronic properties" *Macromolecules,* **44**, 6653-6658 (2011).

[38] Borsali, R.; Pecora, R., Eds., *Soft Matter Characterization* (Fluorescence Correlation Spectroscopy. New York: Springer, pp. 637-673, 2008

[39] B. H. Stuart, *Infrared Spectroscopy: Fundamentals and Applications*. Chichester: John Wiley & Sons Ltd, 2004.

[40] Harris, D. C.; Bertolucci, M. D., *SYMMETRY AND SPECTROSCOPY: An Introduction to Vibrational and Electronic Spectroscopy* New York: Dover Publications, 1978.

[41] Berne, B. J.; Pecora, R., *Dynamic Light Scattering with Applications to Chemistry, Biology and Physics* vol. Dover Publications. New York, 2000.

[42] Borsali, R.; Pecora, R., Eds., *Soft Matter Characterization*. Dordercht: Springer, 2007.

[43] Mendez-Vilas, A.; Diaz, J., Eds., *Microscopy Book Series: Modern Research and Educational Topics of Microscopy*. 2007 http://www.formatex.org/microscopy3.

[44] Iqbal, Z.; Owens, F. J., *Vibrational Spectroscoy of Phase Transition*. Olrando: Academic Press, Chapter 1 and 2, 1984.

[45] Lyon, L. A.; Keating, C. D.; Fox, A. P.; Baker, B. E.; He, L.; Nicewarner, Sr.; Mulvaney, S. P.; Natan, M. J. “Raman spectroscopy” *Analytical Chemistry,* **70**, 341-361 (1998).

[46] R. J. Meier, “Vibrational spectroscopy: a 'vanishing' discipline?” *Chemical Society Reviews,* **34**, 743-752 (2005).

[47] Koenig, J. L.; Angood, A. C. “Raman spectra of poly(ethylene glycols) in solution” *Journal of Polymer Science Part a-2-Polymer Physics,* **8**, 1787-1796 (1970).

[48] Matsuda, Y.; Ebata, T.; Mikami, N. “Vibrational spectroscopy of 2-pyridone and its clusters in supersonic jets: Structures of the clusters as revealed by characteristic shifts of the NH and C=O bands” *Journal of Chemical Physics,* **110**, 8397-8407 (1999).

[49] Li, T. S.; Quillin, M. L.; Phillips, G. N.; Olson, J. S. “Structural determinations of the stretching frequency of co-bound to myoclobin” *Biochemistry,* **33**, 1433-1446 (1994).

[50] Poliakoff, M.; Howdle, S. M.; Kazarian, S. G. “Vibrational spectroscopy in supercritical fluids – From Analysis and hydrogen-bonding to polymers and synthesis” *Angewandte Chemie-International Edition in English,* **34**, 1275-1295 (1995).

[51] Turrell, G.; Corset, J. *Raman Microscopy: developments and applications*. London: Elsevier Academic Press, pp. 175-196, 1996.

[52] Tabaksblat, R.; Meier, R. J.; Kip, B. J. “Confocal Raman microspectroscopy - Theory and application to thin polymer samples” *Applied Spectroscopy,* **46**, 60-68 (1992).

[53] Caspers, P. J.; Lucassen, G. W.; Carter, E. A.; Bruining, H. A.; Puppels, G. J. “In vivo confocal Raman microspectroscopy of the skin: Noninvasive determination of molecular concentration profiles” *Journal of Investigative Dermatology,* **116**, 434-442, (2001).

[54] Jahncke, C. L.; Paesler, M. A.; Hallen, H. D. “Raman imaging with near-field scanning optical microscopy” *Applied Physics Letters,* **67**, 2483-2485 (1995).

[55] Chan, J. W.; Esposito, A. P.; Talley, C. E.; Hollars, C. W.; Lane, S. M.; Huser, T. “Reagentless identification of single bacterial spores in aqueous solution by confocal laser tweezers Raman spectroscopy” *Analytical Chemistry,* **76**, 599-603 (2004).

[56] Zumbusch, A.; Holtom, G. R.; Xie, X. S. “Three-dimensional vibrational imaging by coherent anti-Stokes Raman scattering” *Physical Review Letters,* **82**, 4142-4145 (1999).

[57] Evans, C. L.; Potma, E. O.; Puoris'haag, M.; Cote, D.; Lin, C. P.; Xie, X. S. “Chemical imaging of tissue in vivo with video-rate coherent anti-Stokes Raman scattering microscopy” *Proceedings of the National Academy of Sciences of the United States of America,* **102**, 16807-16812 (2005).

[58] Priestle.Eb; Pershan, P. S. “Investigation of nematic ordering using Raman-scattering” *Molecular Crystals and Liquid Crystals,* **23**, 369-373 (1973).

CHAPTER 2

THEORY AND BACKGROUNDS

2.1 Origin of Raman Spectra

2.1.1 Energy Units and Molecular Spectra

Light is an electromagnetic radiation that has dual wave/particle nature. From its wave nature, electromagnetic radiation consists of electric and magnetic fields that oscillate at mutually perpendicular direction with temporal and spatial periodicity as illustrated in Figure 2.1. The wave field has no wave component in its propagating direction (*x*-direction in Figure 2.1). While materials can absorb both the magnetic and the electric fields, the interaction of the electric field of light is usually about 10^5 stronger than that of the magnetic field [1]. Thus, the interaction between matter and the electric field vector of light is of importance to all spectroscopic techniques [1]. The oscillation of the electric field is described as a function of propagating time, *t* as [1]

$$E = E_0 \cos 2\pi\nu t \tag{2-1}$$

where E_0 is the amplitude of incident electric field and the ν is the frequency of radiation that represents the number of waves passing a given point in a unit time (usually *second*, $s^{-1} = Hz$). The relation between the wavelength of light, λ, which is the distance between two points of the same phase in successive waves, and frequency, ν is given by [1]

$$\nu = \frac{c}{\lambda} \tag{2-2}$$

where *c* is the velocity of light (3×10^{10} *cm/s*). Due to the inconvenience of large numerical values of frequency, in spectroscopy, a third quantity called *wavenumber*, $\tilde{\nu}$, is generally introduced and is given by the relation [1]

$$\tilde{\nu} = \frac{\nu}{c} = \frac{1}{\lambda}\ (cm^{-1}) \tag{2-3}$$

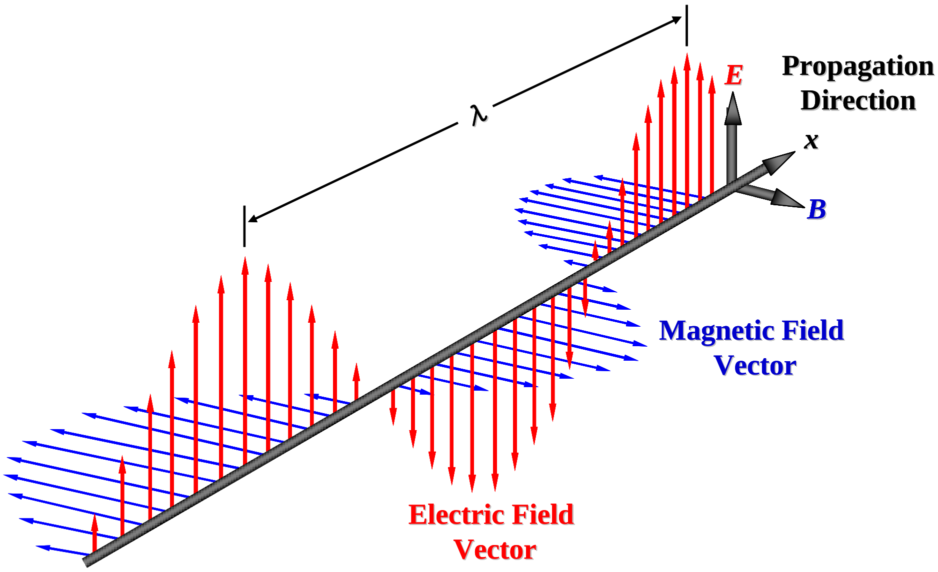

Figure 2.1 Propagation of an electromagnetic wave consisting of electric and magnetic field vectors.

From the nature of particle (photon), a transfer of energy from the radiation to the molecules occur following a condition of

$$E = h\nu = h\frac{c}{\lambda} = hc\tilde{\nu} \tag{2-4}$$

where *h* is Planck's constant (6.6×10^{-34} J·s or 4.14×10^{-15} *eV·s*). Thus, wavenumber is directly proportional to the energy of the transition. For instance, 1*eV* corresponds to λ ~ 1240 *nm*, *v* ~ 2.5×1014 *Hz*, and wavenumber of 8065 cm^{-1}. Inversely we can also approximate the energy from a specific wavelength of light as 1240/ λ (*nm*) ~ energy (*eV*).

Table 2.1 compares the order of energy expressed in terms of λ (*cm*), $\tilde{\nu}$ (cm^{-1}) and *v* (*Hz*) in various spectroscopy methods and spectral regions from the origin of transition [2].

- Translational energy by the motion of the molecule as a whole
- Rotational energy due to the rotation of body along the center of gravity of molecule
- Vibrational energy due to periodic displacement of its atoms from their equilibrium positions

- Electronic energy due to the transition of electrons from one energy level to higher one
- Nuclear energy and energy due to nuclear and electron spins

As shown in Table 2.1, vibrational spectroscopy (Raman & IR) provides information with respect to vibrational transition that appears in the $10^4 \sim 10^2\ cm^{-1}$ region corresponding to energy of $10^{-2} \sim 10^0\ eV$. From "*Heisenberg Uncertainty Principle*" [3, 4], one can approximate the time domain of an energy transition take place by [5]

$$E = h\nu \approx h\frac{1}{Time} \tag{2-5}$$

, which means the time scale associated with the vibrational transition is on the order of 10^{-15}~10^{-13} seconds.

Table 2.1 Energy units for various spectral regions and their energy transition [1].

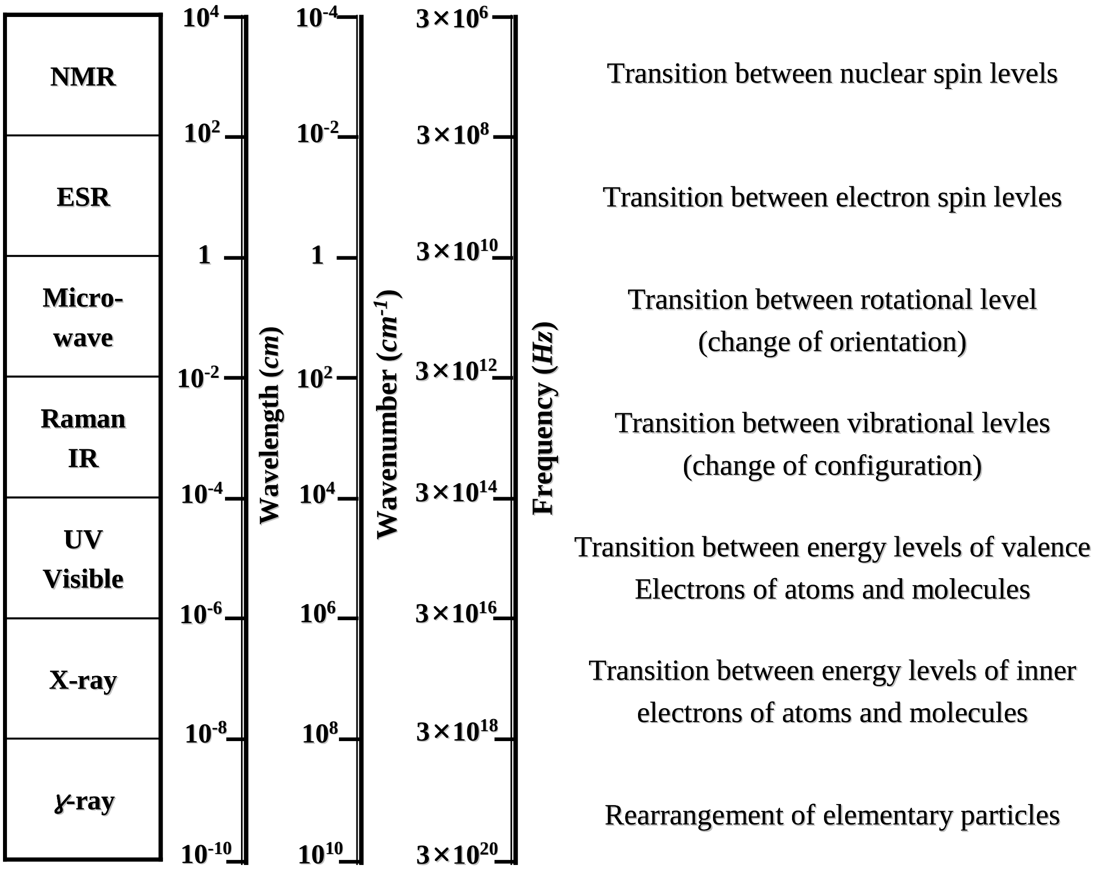

2.1.2 Photo-physical Processes

Although both IR absorption and Raman scattering arise from the vibrational energy transitions of molecules interacting with the incident radiation, the origin of Raman scattering is quite different from that of IR absorption, i.e., they have different selection rules [1, 6]. When a molecule is irradiated by an intense laser beam with electric field, E, it suffers distortions that produce an induced dipole moment, μ, given by the molecular polarizability, α [1]:

$$\mu = \alpha E = \alpha E_0 \cos 2\pi v_0 t \tag{2-6}$$

If a molecule vibrates with a certain frequency, v_m, the displacement of k^{th}-atom in the molecule from its equilibrium position (q_k) is written by [1]

$$q_k = q_k^0 \cos 2\pi v_m t \tag{2-7}$$

where q_k^0 is the amplitude of the displacement. As the extent of polarizability oscillates by the displacement of atom, one can express α in the form of Taylor series as [1]

$$\alpha = \alpha_0 + \left(\frac{\partial \alpha}{\partial q_k}\right)_{q_k=0} q_k + \frac{1}{2}\left(\frac{\partial^2 \alpha}{\partial q_{k'} \partial q_{k''}}\right)_{q_{k'}=q_{k''}=0} q_{k'} q_{k''} + \cdots \tag{2-8}$$

Here α_0 is the polarizability at the equilibrium position ($q_k = 0$), and $\left(\partial \alpha / \partial q_k\right)_{q_k=0}$ is the rate of polarizability change with respect to the displacement of an atom from the equilibrium position. Due to the small amplitude of displacement in the molecular vibration, the higher order terms are insignificant and thus using Eq. (2-8), Eq. (2-6) can be expressed as [1]

$$\begin{aligned}
\mu &= \alpha E = \alpha E_0 \cos(2\pi v_0 t) \\
&= \alpha_0 E_0 \cos 2\pi v_0 t + \frac{1}{2}\left(\frac{\partial \alpha}{\partial q_k}\right)_{q_k=0} q_k^0 E_0 \cos(2\pi v_0 t)\cos(2\pi v_m t) \\
&= \alpha_0 E_0 \cos 2\pi v_0 t + \frac{1}{2}\left(\frac{\partial \alpha}{\partial q_k}\right)_{q_k=0} q_k^0 E_0 \left[\{\cos 2\pi (v_0 - v_m) t\} + \{\cos 2\pi (v_0 + v_m) t\}\right]
\end{aligned} \tag{2-9}$$

In Eq. (2-9), the first term represents an oscillating dipole that is related to the scattered light with the same frequency of incident radiation, ν_0 (Rayleigh scattering), while the second term corresponds to an oscillating dipole that radiates light of frequencies different from that of incident beam: $\nu_0 + \nu_m$ (anti-Stokes) and $\nu_0 - \nu_m$ (Stokes) [1].

For a simple diatomic energy level, a schematic diagram for the photo-physical processes related to IR absorption, normal Raman scattering, resonance Raman scattering, and fluorescence is shown in Figure 2.2 [1, 7]. In IR absorption, the transition of vibrational states ($v = 0 \rightarrow 1$) occurs at the ground electronic state. In normal Raman spectroscopy, vibrational transition is chosen so that its energy state lies in the vibrational energy level ("*virtual state*") that is far below the lowest excited electronic state. The black arrows on the left depict an elastic scattering process (Rayleigh scattering), in which the energy of the irradiation equals that of the scattered light. Normal Raman scattering of which energy differ from that of incident light is displayed with red arrows and corresponding energy difference is $\pm\Delta E$, equal to the energy between $v = 0$ and $v = 1$ at the ground electronic state. From Eq. (2-4), the energy difference (ΔE) is indicated through the difference of wavenumber difference, $\Delta\tilde{\nu}$ so called *Raman Shift* in wavenumber (cm^{-1}), that is constant, independent of wavelength of incident beam [1].

$$\Delta E = h\Delta\nu = hc\Delta\tilde{\nu} = hc\left(\frac{1}{\lambda_{incident}} - \frac{1}{\lambda_{scattered}}\right) \tag{2-10}$$

While the wavenumber is different from frequency as shown in Eq. (2-3), vibrational spectroscopists usually use these two parameters interchangeably. Thus, if a vibrational mode is both Raman and IR active, the Raman shift (cm^{-1}) and the infrared absorption peak frequency are identical. Should Raman scattering occur, the intensity of Raman signal depends on the number of molecules (N_{v^i}) in the initial vibrational state, v^{i}, given by the Boltzmann distribution [7]

$$N_{v^i} \propto N \frac{\exp\left\{ {-E_{v^i}}/{kT} \right\}}{Q_v} \tag{2-11}$$

where Q_v is the vibrational partition function. Therefore, molecules in the initial vibrational state associated to Stoke scattering are even more than that for anti-Stoke scattering. As a result, Stoke scattering is more intense than anti-Stoke scattering unless the temperature is very high in that the population of molecules at lower energy state, v = 0, is much higher than that at v = 1. This is why Stoke scattering is generally adopted in conventional Raman spectroscopy.

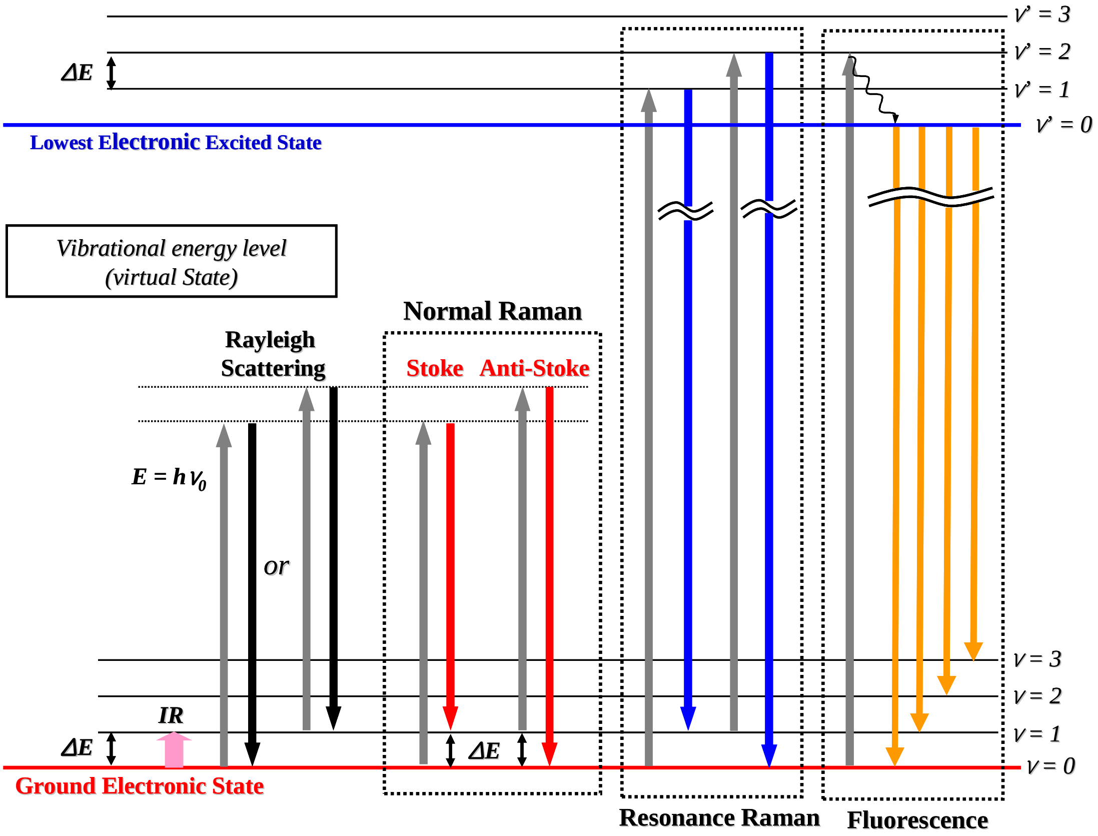

Figure 2.2 Comparison of energy levels for the IR absorption, normal Raman, resonance Raman scattering, and fluorescence.

When the energy of the incoming radiation is adjusted so that it excites molecules to the state corresponding to the energy of electronic transition of particular chromophoric group, the Raman bands originating from these chromophores are selectively enhanced by a factor of 10^3 to 10^5. This is called a resonance Raman scattering. Another critical photo-physical process is fluorescence. Either chromophores in a molecule or impurities may absorb the energy and reemit it as fluorescence. Fluorescence exhibits broad and strong spectrum, which masks the Raman signals resulting in degrading the Raman signal-to-noise ratios (S/N). While both Raman scattering and fluorescence produce photons with the frequencies different from that of the incident photon, there are major differences:

- Raman effects can take place for any frequency of the incident light, whereas fluorescence is anchored at a specific excitation frequency. Actually, Raman shift (cm^{-1}) is independent of the frequency of the incident light, but indicates a separation of frequencies between incident and scattered radiations.
- Fluorescence is a process that the incident light is completely absorbed and the system is transferred to an excited state (e.g. $\nu' = 2$ in Figure 2.2) from which it can return to various energy levels (e.g. $\nu = 0,1,2,3...$ in Figure 2.2). As a result, final energy states of molecules returning after the fluorescence radiation are not fixed, but arbitrary in ground electronic state as shown in Figure 2.2.

2.1.3 Raman Tensor

In an actual molecular system, both μ and E are vectors consisting of three components in the x', y', z' direction and μ can be written in matrix form as:

$$\begin{bmatrix} \mu_{x'} \\ \mu_{y'} \\ \mu_{z'} \end{bmatrix} = \begin{bmatrix} \alpha_{x'x'} & \alpha_{x'y'} & \alpha_{x'z'} \\ \alpha_{y'x'} & \alpha_{y'y'} & \alpha_{y'z'} \\ \alpha_{z'x'} & \alpha_{z'y'} & \alpha_{z'z'} \end{bmatrix} \begin{bmatrix} E_{x'} \\ E_{y'} \\ E_{z'} \end{bmatrix} \tag{2-12}$$

The first matrix on the right-hand side is called the *polarizability tensor* [1, 8]. Raman scattering occurs with a change of energy if one of these components in polarizability tensor changes along the small displacement of atoms, *i.e.*, $\left(\partial\alpha/\partial q_k\right)_{q_k=0} \neq 0$, which means that oscillating polarizability should be neither maximum nor minimum at the equilibrium position ($q_k = 0$). Figure 2.3 illustates a specific example of Raman activity from the vibrations of the CO_2 molecules. Shaded ellipsoids in Figure 2.3 represent the polarizability tensors graphically using a *polarizability ellipsoid* [1, 8]. This is a three-dimensional surface whose distance from the electrical center of the molecule is proportional to $1/\sqrt{\alpha_i}$, where α_i is the polarizability in the *i*-direction from the center of gravity in all directions. Although the size of ellipsoid changes during both the asymmetric (υ_3) and symmetric stretching (υ_1), the slope of the curve near the equilibrium position ($q_k = 0$) is zero for v_3, whereas that for v_1 is non-zero. Thus, symmetric stretching (υ_1) mode in CO_2 is Raman active and asymmetric stretching (υ_3) mode is Raman inactive.

Should the polarizability tensor be symmetric, which is addressed in section 2.2.2, The Raman tensor can be expressed in terms of the directions, *x*, *y* and *z*, along the principal axes. In this case, the direction of dipole moment, μ is collinear with that of incident electric vector, E. In addition, when the principal axes can be coincident with system axes (*X, Y* and *Z*) as shown in Figure 2.4 and then, the polarizability tensor forms as [8];

$$\begin{bmatrix} \alpha_{XX} & 0 & 0 \\ 0 & \alpha_{YY} & 0 \\ 0 & 0 & \alpha_{ZZ} \end{bmatrix} \tag{2-13}$$

Accordingly, the derivative of polarizability, $\partial\alpha/\partial q = \alpha'$ is

$$\begin{bmatrix} \alpha'_{XX} & 0 & 0 \\ 0 & \alpha'_{YY} & 0 \\ 0 & 0 & \alpha'_{ZZ} \end{bmatrix} \tag{2-14}$$

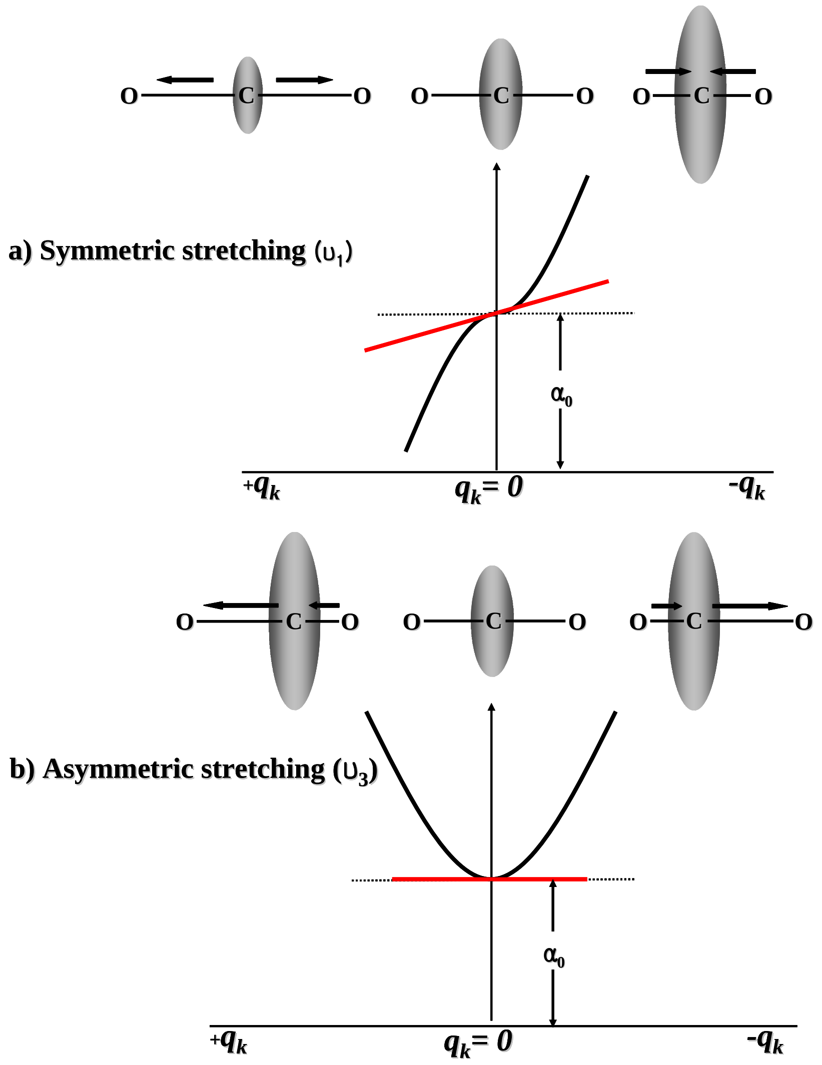

Figure 2.3 Changes in polarizability during (a) symmetric stretching of $C{=}O$ bonds showing non-zero value of $\alpha' = \left({}^{d\alpha}\!/_{dq} \right)$ near the equilibrium position, $\left({}^{d\alpha}\!/_{dq} \right)_{q_k=0} \neq 0$, thus Raman active. (b) Asymmetric stretching mode of CO_2 has α' resulting in Raman inactive [1].

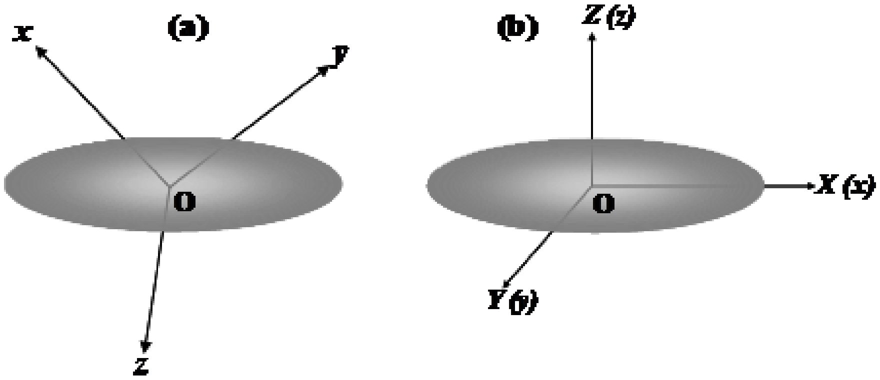

Figure 2.4 Representation of the polarizability ellipsoid from ref. [8]: (a) principal axes not coincident with system axes; (b) principal axes coincident with system axes (*O*-*XYZ*).

2.1.4 Sensitivity of Raman Scattering

The dual sensitivity of Raman scattering is revealed in the equation of dipole moment, Eq. (2-9), where (*i*) the frequency of molecular vibration, ν_m, and (*ii*) the derivative of polarizability, α_{ij}/q_k, appear. The frequency of the molecular vibration, ν_m, is related to mechanical properties such as atomic mass, bond strength or the system geometry (inter-atomic distance, atomic substitutions) and will set the peaks' positions [2]. Advent/disappearance of peaks, therefore, is the basic approach for the identification in analytical chemistry. In addition, some vibrational modes are inherently sensitive to the changes in electronic structure, molecular conformation, and intermolecular interaction and thus, analysis of the variation of peak position can be used to track the structural changes in the sub-fields of soft matter such as polymers and semiconductors. These structure-sensitive vibrations are known for a number of compounds; *e.g.* Raman band attributed to the stretching of –*C*=*C*- in the backbone moiety significantly shift in position toward a lower wavenumber when polydiacethylene single-crystal fiber were deformed in tension [9]. The frequency of the vibration from specific chemical bond is sensitive to its molecular environment (interaction with solvent) [10-12].

The extent of broadness of Raman peaks also provides qualitative information about the order of structure. While the natural broadening of Raman peak arises from the uncertainty in the lower energy state from which transition occurs and the uncertainty in the time for which the energy state is occupied, there are several additional mechanisms to broaden the Raman peak [2]. Broadenings by moving atoms, by collisions of atoms, or by interactions of electrons in neighboring molecules will settle the bandwidth and shape of Raman peaks, which induce a spread of frequency following Lorenzian distribution in character, but there are some broadening mechanisms that produce peaks with Gaussian character [2]. In a molecular system, it is considered that the broadness of Raman peak at a given frequency reflects the regularity of vibrations. In a single crystal, the regularity of vibration is very high due to the very regular structure, so Raman peaks appear quite narrow. In contrast, for materials with less regular structure like amorphous polymers, Raman peaks become broad due to less regularity of vibrations induced.

Parameters related to the vibration-induced charge variations (${}^{\alpha_{ij}}\!/_{q_k}$) will set the intensity of Raman scattering. In the normal Raman scattering process, the proportionality of Raman scattering cross section is defined as the intensity of Raman scattering (I_s) divided by the intensity of incident radiation (I_0) and is expressed by [2]

$$\frac{\partial\sigma}{\partial\Omega} = \frac{I_s}{I_0} \propto \left(\tilde{\nu}_0 - \tilde{\nu}_m\right)^4 \left|\overrightarrow{E_i}\alpha'\overrightarrow{E_s}\right|^2 \tag{2-15}$$

The first term on the right hand side is related to the wavelength of light source for Raman spectroscopy. For conventional Raman spectroscopy, most light sources have the range of wavenumber, $\tilde{\nu}_0$ (from *c.a* 33000 cm^{-1} for UV source (λ ~ 300 *nm*) to c.a. 9700 cm^{-1} for IR source (λ ~ 1050 *nm*)), which is much higher than $\tilde{\nu}_m$ (about 100 to 4000 cm^{-1}) detectable by Raman spectroscopy. Therefore, one can simply assume that Raman intensity varies inversely with the fourth power of the excitation wavelength by the proportionality formula. In the case of *C≡N* stretching mode corresponding to $\tilde{\nu}_m$ =2250

cm^{-1} [13], for example, the cross-section with 488 *nm* laser source (c.a. $\tilde{\nu}_0 = 22000\ cm^{-1}$) would be almost 12 times more than that with 785 *nm* laser source (c.a. $\tilde{\nu}_0 = 12700\ cm^{-1}$).

The second term in the right hand of Eq. (2-15), $\left|\vec{E}\alpha'\vec{E}\right|^2$ reflects the relation between the direction of α' and the directions of incident ($\vec{E_i}$) / scattered ($\vec{E_i}$) electric vectors. If the incident light is not polarized, *i.e.* no preferred direction of wave oscillation, the magnitude of $\left|\vec{E_i}\alpha'\vec{E_j}\right|^2$ is proportional to only the magnitude of α_{ij}/q_k that is influenced by molecular structures and interactions with neighboring molecules. When the incident electric field is linearly polarized and scattered light is resolved using another linear polarizer, the magnitude of $\left|\vec{E}\alpha'\vec{E}\right|^2$ depends on the orientation of principle axes of Raman tensor with respect to the direction of linear polarization of incident beam and the direction of analyzer. Therefore, polarized Raman spectroscopy is a potential tool to obtain orientation information for a system that has an anisotropic ordering, and we will address the use of polarization in Raman spectroscopy in the following section.

2.2 Polarization of Raman Scattering

2.2.1 Directional Information

The distribution of polarized Raman intensities corresponds to the distribution of populations of scattering units interacting with an incident light with a specific polarization direction. Thus, the measurements of polarized Raman intensities enable us to quantify the orientation distribution of the scattering units. Should the main axis of scattering unit be collinear with the long axis of the molecules, it can provide information about the orientation of molecules. It is noteworthy that polarized Raman spectroscopy can in principle yield more information about the orientation distribution of molecules than IR dichroism or birefringence measurement. It is because IR dichroism involves only one beam of polarized radiation and the fraction of the radiation absorbed by molecules depends only on the orientation of the molecules with respect to the polarization vector of the incident beam. By contrast, the intensity of polarized Raman scattering depends on the orientation of the scattering units with respect to two polarization vectors of incident beam and beam scattered. Therefore, if polarized light is incident on the anisotropically oriented molecular system and the scattered radiation is resolved through an analyzer with a specific polarization direction, the intensity of Raman scattering for any combination of polarization vectors of incident and scattered light can be expressed by [14, 15]

$$I_{ij} \propto \left(\sum_{ij} E_i \alpha'_{ij} E_j \right)^2 \tag{2-16}$$

where E_i is the directional cosine of the incident electric polarization vector and E_j is the directional cosine of the scattered electric polarization vector. Eq. (2-16) clearly implies that the intensity of polarized Raman scattering resolved by analyzer includes information about the direction cosine of incident and scattered polarization up to the 4th rank tensorial components. A simple scheme is shown in Figure 2.5, in which the direction of principal component of polarizability, α_{zz}, is in plane of ZY and makes an angle, θ, about the axis Z of the system. Then, the intensities resolved by the analyzer with the polarization direction parallel (I_{ll}) and perpendicular ($I_{\perp}$) to the polarization direction of incident light is given by [16, 17];

$$\begin{aligned} I_{ll} &= I_{ZZ} \propto \left(\alpha'_{zz}\right)^2 \cos^4\theta \\ I_{\perp} &= I_{YZ} \propto \left(\alpha'_{zz}\right) \cos^2\theta \sin^2\theta \end{aligned} \tag{2-17}$$

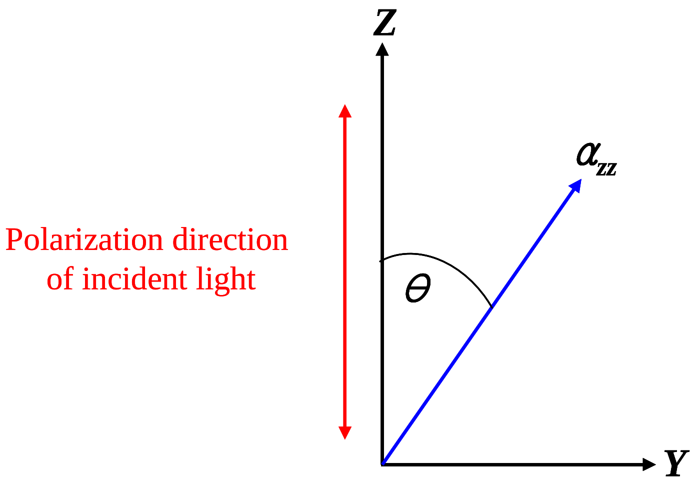

Figure 2.5 Angle between the laboratory axis, *Z*-axis, and principal polarizability component, α_{zz}.

2.2.2 Depolarization Ratio

Depolarization ratio, *R*, provides valuable information about the symmetry of normal mode vibrations that are indispensable in making band assignments for the analysis of chain conformation [18, 19] as well as the secondary structure [20, 21] and molecular orientation [14, 15, 22]. Depolarization ratio is defined as $R = {}^{I_\perp}\!/\!{}_{I_{//}}$, where $I_\perp$ (depolarized intensity) and $I_{//}$ (polarized intensity) represents the Raman scattering intensities when the polarization direction of the analyzer is perpendicular and parallel to that of the incident beam, respectively. Figure 2.6 presents these resolved intensities for backscattering geometry. Information of the symmetry of Raman tensor is usually obtained by the measurements of depolarization ratio in isotropic phase, R_{iso} [1, 22]. In the isotropic phase, polarization arises only because the induced electric dipole has components that spatially vary with respect to the coordinates of the molecule, thus reflects the symmetry of polarizability itself independent of the orientation of molecules. In isotropic phase, depolarized Raman intensity, $I_\perp$, from non-totally symmetric vibration is 3/4 times as strong as polarized intensity, I_{ll}, resulting in $R_{iso} = {}^{3}\!/_{4}$. On the other hand, Raman scattering from totally symmetric vibrations will strongly polarized parallel to the plane of polarization of incident light and thus, $0 < R_{iso} < {}^{3}\!/_{4}$.

Apart from the assignments of Raman bands, the acquisition of the symmetry of vibration Raman tensor is important in order to apply Eq. (2-16) to obtain the orientation information. In order to apply the principle tensor form to Eq. (2.16), we have to use the peak intensities from totally symmetric vibrations [1]; otherwise a quite complex formula to express the intensities with diagonal tensor form may be required [23].

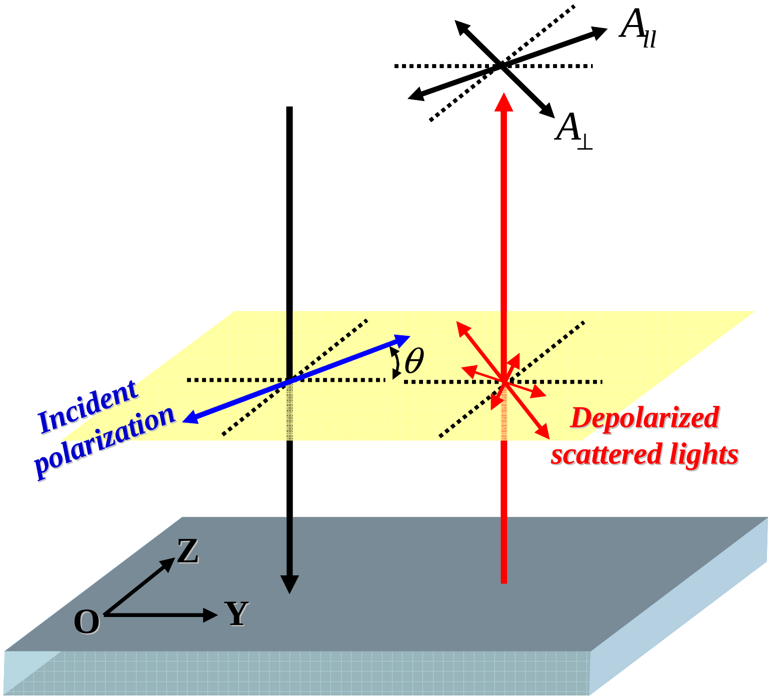

Figure 2.6 Schematic geometry of backscattering (180˚) setup; the polarization direction is kept fixed and depolarized scattered lights are resolved into the analyzer. I_{ll} and $I_{\perp}$ are resolved intensities onto A_{ll} and $A_{\perp}$, respectively. Plane with yellow color is polarization plane of incident light.

2.3 Quantification of Degree of Orientation

2.3.1 Orientational Distribution Function (ODF)

The orientation of a molecular element M is the spatial position of M relative to a right-handed macroscopic laboratory axes, *O-XYZ*. Let us define a set of three mutually perpendicular directions, x, y, z, as the principal axes of Raman tensor and z-axis is the direction of the main tensor component. Then, the transformation of the orientation dependence of physical quantities in the laboratory axes, *O-XYZ* to that in the *O-xyz* axes are expressed in terms of Euler angle, (α,β,γ) [24, 25] (Figure 2.7 (a)). If the *O-xyz* is coordinated with *O-XYZ* system, α is the angle between the *X-axis* and the projection of *z-axis* onto the *XY* plan, β is angle between *z-axis* and *Z-axis*, and γ means rotational degree of M with respect to *z-axis*. The orientation with Euler's angles (α,β,γ) is referred to as $\Omega(\alpha,\beta,\gamma)$ [24, 25].

In a system composed of multi-molecules, however, a distribution of orientations will exist. The orientational distribution function (ODF), denoted by $f(\alpha,\beta,\gamma)$, is used to quantify the probability of an element having an orientation between (α,β,γ) and $(\alpha+d\alpha,\beta+d\beta,\gamma+d\gamma)$. The simple example of $f(\beta+d\beta)$ is shown in Figure 2.7 (b))

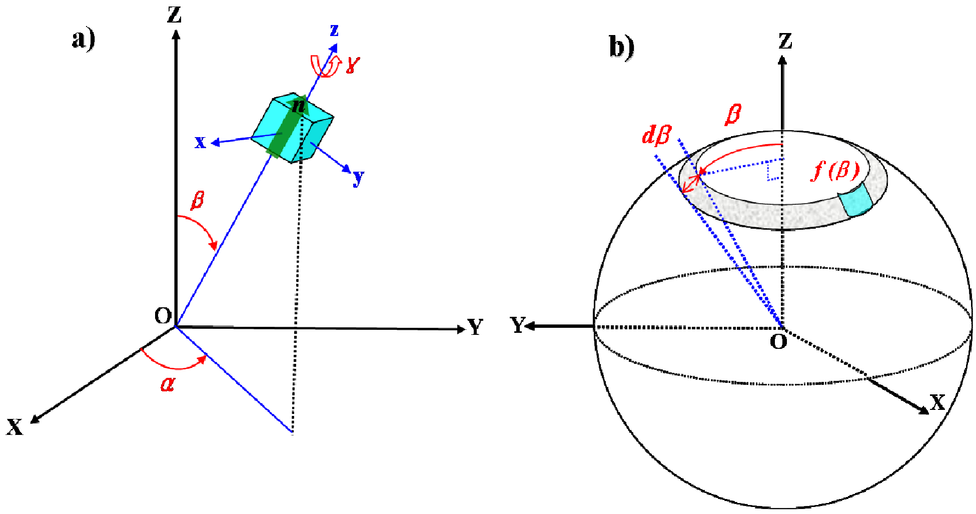

Figure 2.7 a) Representation of the orientation of element, *M*, in terms of Euler angle, $\Omega(\alpha,\beta,\gamma)$, and b) a simple example of ODF dependent of only β angle.

As it is a probability function, it is stipulated that ODF must always positive and normalized [26]:

$$f(\alpha,\beta,\gamma) \geq 0 \text{ for all } \Omega(\alpha,\beta,\gamma) \tag{2-18}$$

$$\int_0^{2\pi}\int_0^{\pi}\int_0^{2\pi} f(\alpha,\beta,\gamma)\sin\beta d\alpha d\beta d\gamma = 1 \tag{2-19}$$

A set of orthogonal functions of the orientation with Euler's angle, $\Omega(\alpha,\beta,\gamma)$, enable us to write the ODF as a series expansion as [27, 28]:

$$f(\alpha,\beta,\gamma) = \sum_{L=0}^{\infty}\sum_{m,n=-L}^{L}\frac{2L+1}{8\pi^2}\left\langle D_{mn}^{L*}\right\rangle D_{mn}^{L}(\alpha,\beta,\gamma) \tag{2-20}$$

$D_{mn}^{L}(\alpha,\beta,\gamma)$ are the Wigner functions and its explicit form is given by [29, 30]

$$D_{mn}^{L}(\alpha,\beta,\gamma) = \exp(-im\alpha)d_{mn}^{L}(\beta)\exp(-in\gamma) \tag{2-21}$$

where the small Wigner function $d_{mn}^{L}(\beta)$ is a function of only β. The moments of the expansion coefficients, $\left\langle D_{mn}^{L}\right\rangle$, known as *order parameters* is the statistical averaged values of D_{mn}^{L} and defined as [28]

$$\left\langle D_{mn}^{L}(\alpha,\beta,\gamma)\right\rangle = \int_{\alpha}\int_{\beta}\int_{\gamma} D_{mn}^{L}(\alpha,\beta,\gamma)\, f(\alpha,\beta,\gamma)\sin\beta d\alpha d\beta d\gamma \tag{2-22}$$

In the isotropic phase, all of coefficients, $\left\langle D_{mn}^{L} \right\rangle$, are zero and some will be nonzero in the ordered phase. The values of the remaining coefficients with nonzero *L* depend on the degree of orientational order. Depending on the values of $L(L \in N)$, the ODF is made up of a set of $(2L+1)^2$ orthogonal functions [28, 29]. The values of indices *m* and *n* lies between *–L* and *+L*. As described in the previous section, polarized Raman spectroscopy can provide directional information up to 4th rank directional information, thus *L=4*.

Further simplification can be made considering the symmetry of the systems and a number of components are left out of consideration [29]. Eq. (2-21) enables one to simplify the expansion coefficients of ODF (Eq. (2-22)) using the symmetries of Raman tensor with respect to *O-xyz* and specimen with respect to *O-XYZ*. Combining Eq. (2-21) with Eq. (2-22) derives [29]

$$\left\langle D_{mn}^{L}(\alpha,\beta,\gamma) \right\rangle = \int_{\alpha}\int_{\beta}\int_{\gamma} \exp(im\alpha) d_{mn}^{L}(\beta) \exp(in\gamma) \times f(\alpha,\beta,\gamma) \sin\beta \, d\alpha \, d\beta \, d\gamma \qquad (2\text{-}23)$$

Herein let us describe 2 symmetries; *i)* Symmetry for which the ODF does not depend on Euler's angle γ since the Raman bands are usually assumed to exhibit cylindrical symmetry, *ii)* Mirror symmetry about *XY* plane for which $\Omega(\alpha,\beta) = \Omega(\alpha,\beta \pm \pi)$ resulting in *L*= even. In this case of cylindrical symmetry of *M*, the rotation about *z-axis* dose not affect the ODF, then the order parameters are to be described as [29]

$$\left\langle D_{mn}^{L}(\alpha,\beta) \right\rangle = \int_{\gamma} \exp(in\gamma) d\gamma \int_{\alpha}\int_{\beta} \exp(im\alpha) d_{m}^{L}(\beta) \times f(\alpha,\beta) \sin\beta \, d\alpha \, d\beta \qquad (2\text{-}24)$$

Since it is given that $\int_{\gamma} \exp(in\gamma) d\gamma = 2\pi\delta_{n0}$ from ref. [29], order parameters have values other than zero when $n = 0$. Combination with the mirror symmetry of specimen in the *YZ* and *XZ* planes of the sample also make order parameters available when *m* is even. In this case, the order parameters are identical to the Legendre polynomials, $\left\langle D_{m0}^{L} \right\rangle = \left\langle P_{Lmo} \right\rangle$. More translations of the symmetry properties into the shape of the ODF are well described in ref [29, 30].

From the specific symmetries of molecule and specimen mentioned above, the ODF is valid for 4th rank directional information (*i.e.* $L=4$) and is expanded with 5 coefficients, $\langle P_{200}\rangle$, $\langle P_{400}\rangle$, $\langle P_{220}\rangle$, $\langle P_{420}\rangle$, and $\langle P_{440}\rangle$ as [28, 31]

$$f(\alpha,\beta)=\sum_{L=0}^{4}\sum_{m=0}^{4}\frac{2L+1}{4\pi^2}\langle P_{Lm0}\rangle P_{Lm0}(\alpha,\beta,\gamma)$$

$$=\frac{1}{8\pi^2}\left\{\begin{array}{l} 1\ +\ \frac{5}{2}\ \langle P_{200}\rangle\left(3\cos^2\beta-1\right)\ +\ 15\ \langle P_{220}\rangle\left(1-\cos^2\beta\right)\cos(2\alpha) \\ +\frac{9}{8}\langle P_{400}\rangle\left(3-30\cos^2\beta+30\cos^4\beta\right) \\ +\frac{135}{2}\langle P_{420}\rangle\left(-1+8\cos^2\beta-7\cos^4\beta\right)\cos(2\alpha) \\ +\frac{315}{4}\langle P_{440}\rangle\left(1-2\cos^2\beta+\cos^4\beta+\right)\cos(4\alpha) \end{array}\right\} \tag{2-25}$$

Orientational order parameters are averaged values, which are suitable to determine the orientation for the system in which molecules are distributed with an anisotropic manner. Each parameter is defined as [32]:

$$\begin{aligned} \langle P_{200}\rangle &= \frac{1}{2}\left\langle 3\cos^2\beta-1\right\rangle \\ \langle P_{220}\rangle &= \frac{1}{4}\left\langle\left(1-\cos^2\beta\right)\cos 2\alpha\right\rangle \\ \langle P_{400}\rangle &= \frac{1}{8}\left\langle 3-30\cos^2\beta+35\cos^4\beta\right\rangle \\ \langle P_{420}\rangle &= \frac{1}{24}\left\langle\left(-1+8\cos^2\beta-7\cos^4\beta\right)\cos 2\alpha\right\rangle \\ \langle P_{440}\rangle &= \frac{1}{16}\left\langle\left(1-2\cos^2\beta+\cos^4\beta\right)\cos 4\alpha\right\rangle \end{aligned} \tag{2-26}$$

2.3.2 Quantification of Order Parameters using Polarized Raman Spectroscopy

In the study of multi-units that are 3-dimensionally distributed in a system, it is necessary to consider the orientation distribution of scattering units on deriving the equation of statistically averaged polarized Raman intensities so that the measured quantity includes information about the distribution of orientation. Then, Eq. (2-16) should be derived with the consideration of the distribution of the scattering units integrated over all possible orientations as [17, 33];

$$I_{ij}\left(\theta\right)=k\int_{\alpha=0}^{2\pi}\int_{\beta=0}^{\pi}f\left(\alpha,\beta\right)\left(E_{ij}(\alpha,\beta,\theta)\right)^{2}\sin d\beta d\alpha d\beta \tag{2-27}$$

The notation I_{ij} denotes the scattering intensity analyzed in *i* direction (in our geometry, *i* ≡ *Z*, *Y*) with incident polarization in *j* direction. *k* is a proportionality constant taking account experimental factors such as incident light intensity, instrumental transmission, light collection efficiency, etc. Based on the backscattering geometry (see Figure 2.6) where the axis of main component, $\alpha_{zz}^{'}$, of Raman tensor lies in the plane of incident polarization, expanding Eq. (2-27) gives two reduced expression of Raman intensities, $I_{ll}\left(\theta\right)=I_{ZZ}\left(\theta\right)$ and $I_{\perp}\left(\theta\right)=I_{YZ}\left(\theta\right)$, accomplished by resolving polarized light intensity onto parallel and perpendicular analyzer orientations. Should the orientation of scattering units be anisotropic, polarized intensity measured will periodically change as a function of angle, θ, between a specific direction in the *YZ* plane with respect to the polarization direction of incident electric vectors. Details about the expansion of Eq. (2-27) are in Appendix I.

Using the full expansions of $I_{ll}\left(\theta\right)$ and $I_{\perp}\left(\theta\right)$ in Appendix A, the simple expression for the depolarization ratio, $R\left(\theta\right)={I_{\perp}\left(\theta\right)}\big/{I_{ll}\left(\theta\right)}$, can be expressed as:

$$\begin{aligned}R\left(\theta\right)&=\frac{I_{\perp}\left(\theta\right)}{I_{ll}\left(\theta\right)}=\frac{I_{YZ}\left(\theta\right)}{I_{ZZ}\left(\theta\right)}\\&=\frac{\left(-1+r\right)^{2}\left\{\begin{array}{l}-40\left\langle P_{200}\right\rangle-240\left\langle P_{220}\right\rangle+\left(105\cos 4\theta-9\right)\left\langle P_{400}\right\rangle\\-2\left[28+90\left(1+7\cos 4\theta\right)\left\langle P_{420}\right\rangle+210\sin^{2}\theta\left\langle P_{440}\right\rangle\right]\end{array}\right\}}{\left\{\begin{array}{l}40\left(4r^{2}-r-3\right)\left[\left(1+3\cos 2\theta\right)\left\langle P_{200}\right\rangle+12\sin^{2}\theta\left\langle P_{220}\right\rangle\right]\\-3(r-1)^{2}\left(9+20\cos 2\theta+35\cos 4\theta\right)\left\langle P_{400}\right\rangle\\-8\left[7\left(3+4r+8r^{2}\right)+30\left(r-1\right)^{2}\sin^{2}\theta\left(3\left(5+7\cos 2\theta\right)\left\langle P_{420}\right\rangle+7\sin^{2}\theta\left\langle P_{440}\right\rangle\right)\right]\end{array}\right\}}\end{aligned} \tag{2-28}$$

Consequently, we are able to obtain 5 different orientational order parameters, $\langle P_{200} \rangle$, $\langle P_{220} \rangle$, $\langle P_{400} \rangle$, $\langle P_{420} \rangle$ and $\langle P_{440} \rangle$, and the ratio of Raman tensor, $r = \alpha'_{yy} / \alpha'_{zz}$ as fitting parameters, by fitting the measured depolarization ratios over the entire range of θ $(0° \sim 360°)$ to Eq. (2-28). The advantage of using depolarization ratios to deduce the order parameters is the fact that experimental factor, k can be eliminated. Also, it is not required to know the exact values of α'_{yy} and α'_{zz}, but the ratio of principle Raman tensor components, $r = \alpha'_{yy} / \alpha'_{zz}$ is needed to obtain order parameters. Specific case studies are described in the following chapters but this method can be a versatile tool to quantify the orientational order in any anisotropic system including low molecular liquid crystals (LCs), polymers, or homogeneous or heterogeneous composites.

2.4 References

[1] Ferraro, J. R.; Nakamoto, K.; Brown, C. W. *Introductory Raman Spectroscopy*, 2nd ed. San Diego: Academic Press, pp. 1-91, 2003.

[2] P. S. Sindhu, *Fundamentals of Molecular Spectroscopy*. Delhi: New Age International Ltd., Publishers, pp. 153-175, 2006.

[3] Born, M. “The statistical interpretation of quantum mechanics” *Nobel Lecture*, 1954.

[4] Wheeler, J. A.; Żurek, W. H. *Quantum theory and measurement*. New York: Princeton University Press, Chapter 2, 1983.

[5] Harris, D. C.; Bertolucci, M. D. *SYMMETRY AND SPECTROSCOPY: An Introduction to Vibrational and Electronic Spectroscopy* New York: Dover Publications, pp. 86-89, 1978.

[6] Harris, D. C.; Bertolucci, M. D. *SYMMETRY AND SPECTROSCOPY: An Introduction to Vibrational and Electronic Spectroscopy* New York: Dover Publications, pp. 151-169, 1978.

[7] Banwell, C. N. *Fundamentals of Molecular Spectroscopy,* 2nd ed. London: McGraw-Hill, 1972.

[8] Long, D. A. *The Raman Effect : A Unified Treatement of the Theory and Raman Scatterign by Molecules*. Chichester: Wiley, pp. 471-495, 2002

[9] Mitra, V. K.; Risen, W. M.; Baughman, R. H. “Laser Raman study of stress dependence of vibrational frequencies of a monocrystalline polydiacetylene” *Journal of Chemical Physics,* **66**, 2731-2736 (1977).

[10] Li, T. S.; Quillin, M. L.; Phillips, G. N.; Olson, J. S. “Structural determinants of the stretching frequency of CO bound to myoglobin” *Biochemistry,* **33**, 1433-1446 (1994).

[11] Poliakoff, M.; Howdle, S. M.; Kazarian, S. G. “Vibrational spectroscopy in supercritical fluids - From analysis and hydrogen-bonding to polymers and

synthesis" *Angewandte Chemie-International Edition in English,* **34**, 1275-1295 (1995).

[12] Zwier, T. S. "The spectroscopy of solvation in hydrogen-bonded aromatic clusters" *Annual Review of Physical Chemistry,* **47**, 205-241 (1996).

[13] Lin-Vien, D.; Colthup, N. B.; Fateley, W. G.; Grasselli, J. G. *The Handbook of Infrared and Raman Characteristic Frequencies of Organic Molecules*. San Diego: Academic Press, pp. 105-113, 1991.

[14] Jen, S.; Clark, N. A.; Pershan, P. S.; Priestley, E. B. "Raman scattering from a nematic liquid crystal: Orientational statistics," *Physical Review Letters,* **31**, 1552-1556 (1973).

[15] Bower, D. I. "Investigation of molecular orientation distributions by polarized Raman scattering and polarized fluorescence" *Journal of Polymer Science Part B-Polymer Physics,* **10**, 2135-2153 (1972).

[16] Long, D. A. *The Raman Effect : A Unified Treatement of the Theory and Raman Scattering by Molecules*. Chichester: Wiley, pp. 98-106, 2002.

[17] Jones, W. J.; Thomas, D. K.; Thomas, D. W.; Williams, G. "On the determination of order parameters for homogeneous and twisted nematic liquid crystals from Raman spectroscopy" *Journal of Molecular Structure,* **708**, 145-163 (2004).

[18] Stokr, J.; Schneider, B.; Doskocilova, D.; Lovy, J.; Sedlacek, P. "Conformational structure of poly(ethylene-terephthalate) - infrared, Raman and NMR-Spectra" *Polymer,* **23**, 714-721 (1982).

[19] Kister, G.; Cassanas, G.; Vert, M. "Effects of morphology, conformation and configuration on the IR and Raman spectra of various poly(lactic acid)s" *Polymer,* **39**, 267-273 (1998).

[20] Lippert, J. L.; Tyminski, D.; Desmeules, P. J. "Determination of secondary structure of proteins by laser Raman spectroscopy" *Journal of the American Chemical Society,* **98**, 7075-7080 (1976).

[21] Pelton, J. T.; McLean, L. R. "Spectroscopic methods for analysis of protein secondary structure" *Analytical Biochemistry,* **277**, 167-176 (2000).

[22] Tanaka, M.; Young, R. J. “Polarised Raman spectroscopy for the study of molecular orientation distributions in polymers” *Journal of Materials Science,* **41**, 963-991 (2006).

[23] Park, M. S.; Wong, Y. S.; Park, J. O.; Venkatraman, S. S.; Srinivasarao, M. “A simple method for obtaining the information of orientation distribution using polarized Raman spectroscopy: Orientation study of structural units in poly(lactic acid)” *Macromolecules,* **44**, 2120-2131 (2011).

[24] Roe, R. J. “Description of crystallite orientation in polycrystalline materials. 3. General solution to pole figure inversion” *Journal of Applied Physics*, **36**, 2024-2031 (1965).

[25] Roe, R. J. “Methods of description of orientation in polymers” *Journal of Polymer Science Part a-2-Polymer Physics,* **8**, 1187-1194 (1970).

[26] Bower, D. I. “Orientation distribution functions for uniaxially oriented polymers” *Journal of Polymer Science Part B-Polymer Physics,* **19**, 93-107 (1981).

[27] Edmonds, A. R. *Angular Momentum in Quantum Mechanics*. Princeton: Princeton University Press, pp. 53-65, 1960.

[28] Luckhurst, G. R.; Veracini, C. A., Eds., *The Molecular Dynamics of Liquid Crystals* (On the Description of Ordering in Liquid Crsytals. Dordrecht: Kluwer Academic Publishers, pp.11-36, 1994.

[29] Vangurp, M. “The use of rotation matrices in the mathematical description of molecular orientations in polymers” *Colloid and Polymer Science,* **273**, 607-625 (1995).

[30] Rose, M. E. *Elementary Theory of Angular Momentum*. New York: Wiley, pp.15-31, 1957.

[31] Southern, C. D.; Gleeson, H. F. “Using the full Raman depolarisation in the determination of the order parameters in liquid crystal systems” *European Physical Journal E,* **24**, 119-127 (2007).

[32] Jarvis, D. A.; Hutchinson, I. J.; Bower, D. I.; Ward, I. M. “Characterization of biaxial orientation in poly(ethylene-terephthalate) by means of refractive index

measurements and Raman and infrared spectroscopies" *Polymer*, **21**, 41-54 (1980).

[33] Jones, W. J.; Thomas, D. K.; Thomas, D. W.; Williams, G. "Raman scattering studies of homogeneous and twisted-nematic liquid crystal cells and the determination of < P2 > and < P4 > order parameters" *Journal of Molecular Structure*, **614**, 75-85 (2002).

CHAPTER 3

DETERMINATION OF ORIENTATIONAL ORDER PARAMETERS IN A UNIAXIAL NEMATIC LIQUID CRYSTALLINE PHASE

3. 1 Introduction

3.1.1 Orientation in a Nematic Phase of Liquid Crystals

Liquid crystals (LCs) constitute an archetype category of soft matter [1-4], sometimes referred to as structured fluids with thermodynamically stable states, or intermediate phases (mesophases) between the crystalline solids and an ordinary isotropic liquid. The structure arises from the self-organizations of anisotropically shaped molecules or of aggregates of amphiphilic molecules or components with anisotropic shape in a solvent. Generally, components in liquid crystals consist of a hard mesogenic group coupled to a flexible chains and the overall structure is thought to be rigid rod-like or disk-like [5, 6]. Anisotropy in the shape of components causes anisotropic electrostatic interactions between components, which makes the orientational order in liquid crystals.

Nematic LC is the simplest mesophase in which the molecules preferably oriented in a specific direction, referred to as the director ***n*** (Figure 3.1). The degree of orientation in nematic LCs is defined by the thermodynamic fluctuations of the director, ***n***. In a uniaxial nematic (N_u) phase in which the molecules possess a cylindrical symmetry along the molecular axis, the ordering is purely orientational and the corresponding distribution function describes the angular distribution of the director about a defined coordinate axis (*Z-axis*). Thus, the orientation distribution function (ODF) consists of order parameters concerning only polar angle (β) dependence (see Figure. 2.7 (b)). Due to the microscopic orientational order of nematic LCs, most macroscopic tensor properties show anisotropy, which endows liquid crystals with distinct electro-optical and dynamic phenomena in response to applied external fields [6]. Knowledge and understanding of the orientational behavior is, therefore, of prime importance for the characterization of physical properties of nematic LCs.

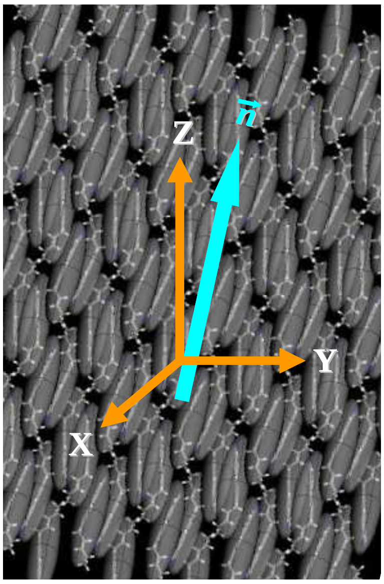

Figure 3.1 The arrangement of rod-like molecules in the nematic phase: the direction of blue arrow is the statistically averaged preferred direction of molecules, the director, ***n***.

For nematic LCs, any phenomenological quantity (electric/magnetic susceptibility, optical absorption, etc.) can be used to obtain the degree of orientation as long as these phenomena depend on the pair distribution of director ***n*** [6-8]. Measurements of the anisotropy in the refractive indices [9, 10], of anisotropy of the spin interactions (nuclear magnetic resonance, NMR) [11, 12], and of absorption anisotropy at infra-red wavelength by specific atomic or molecular units (polarized infra-red (IR) spectroscopy) [13] enable one to obtain orientational order parameters. However, these phenomenological quantities are second rank tensorial properties so that these experiments usually yield the order parameters up to $L=2$. The only method to construct ODF with the full expansion of coefficients, in principle, is small angle x-ray [14, 15] and neutron scattering [16, 17]. With negligible interference effects among molecules due to much shorter wavelength of incident radiation sources, it is, in principle, possible to deduce entire orientational order parameters (*i.e.*, $L=\infty$) to construct the full ODF. However, order parameters up to only the fourth rank ($L=4$) are usually considered in the expansion of ODF [18].

3.1.2 Conventional Raman Approach to Quantify the Orientational Order Parameters

Polarized Raman spectroscopy is one of a few methods that can provide orientational order parameters up to $L=4$ as described in chapter 2. Notably Jen and co-workers [19, 20] first pointed out that $\langle \cos^4 \beta \rangle$ terms in ODF can be obtained by measuring polarized Raman intensities from room temperature nematic liquid crystal, N-(*p*'-methoxybenzylidene)-*p*-n butylaniline) (MBBA). In their extensive studies, comprehensive formula to calculate the values of $\langle \cos^2 \beta \rangle$ and $\langle \cos^4 \beta \rangle$ were established in terms of two depolarization ratios, R as [19, 20]:

$$R_1 = \frac{I_\perp(\theta = 0^\circ)}{I_{//}(\theta = 0^\circ)},\ \mathrm{R}_2 = \frac{I_\perp(\theta = 90^\circ)}{I_{//}(\theta = 90^\circ)} \tag{3-1}$$

$$\begin{aligned} \langle \cos^2 \beta \rangle &= \frac{3R_2(2R_1+1)}{8R_1+3R_2+12R_1R_2} \\ \langle \cos^4 \beta \rangle &= \frac{3R_2}{8R_1+3R_2+12R_1R_2} \end{aligned} \tag{3-2}$$

where R_1 and R_2 is equal to the value of depolarization ratio measured at the configuration of $\theta = 0^\circ$ and $\theta = 90^\circ$ in our geometry (Figure 2.6), respectively. This approach was successful in exploring the temperature dependence of $\langle P_{200} \rangle$ values that was in good agreement with those obtained from other independent measurements [21-23] as well as the predicted values from widely accepted mean-field theory [24, 25].

The main criticism of utilizing polarized Raman spectroscopy to date, however, is the discrepancy of $\langle P_{400} \rangle$ values with respect to theoretical predictions [24, 25]. In general, the magnitude of $\langle P_{400} \rangle$, obtained from the conventional Raman approach was far below the predicted values from the mean field theory, and even had negative values

[19, 26, 27] in the vicinity of nematic-isotropic transition temperature, T_{NI} , which was not explainable by mean-field theories [28].

Further studies considering the influence of molecular biaxiality [26, 29] and non-rigidity [30] have been carried out and interactions between pairs of molecules were proposed to be responsible for the discrepancy from the results of mean-field theory since mean-field theory did not consider the interactions. While these possibilities seem reasonable, there is no independent evidence yet. Moreover, the measurements of electron paramagnetic resonance (EPR) for various nematic compounds [31] and small angle neutron scattering [32] for 4,4'-dimethoxyazoxybenzene (PAA) yield $\langle P_{400} \rangle$ values that were found to be in close agreement with theory whereas those from the Raman approach showed unexplainable results. Notwithstanding the necessity of revising the conventional methodology, many groups have followed the way that Jen *et al.* proposed to obtain orientational order parameters of nematic LCs [27, 33-36] since $\langle P_{200} \rangle$ is the primary expansion coefficient to construct ODF. However, in order to construct ODF accurately, knowledge of $\langle P_{400} \rangle$ values is required.

Recently, Jones and coworkers [37, 38] discussed the benefit of the measurements of polarized Raman intensities over the entire range of θ angles (0° to 360°). They described how to derive more reliable value of $\langle P_{200} \rangle$ and $\langle P_{400} \rangle$ using polarized Raman spectroscopy. Rather than utilizing Raman intensities obtained at only three selected configurations, *i.e.,* $I_{ll}\left(\theta = 0°\right)$, $I_{ll}\left(\theta = 90°\right)$, $I_{\perp}\left(\theta = 0°\right)$, they considered polarized Raman intensities at more configurations of polarization direction of incident beam with respect to the director, ***n***. Jones and coworkers obtained $\langle P_{200} \rangle$ and $\langle P_{400} \rangle$ as well as the Raman tensor ratio, $r = {\alpha'_{yy}}\big/{\alpha'_{zz}}$ by fitting the measured Raman intensities over the entire range of θ angles (0° to 360°) as variables. With the new Raman approach, they were able to obtain $\langle P_{400} \rangle$ values much higher than those reported in previous literature at a given T/T_{NI} in a nematic phase. There are two significant points in the literature reported by Jones *et al.* [38]. One is that the more data points one takes into account, the more abundant information about the orientation distribution one can obtain. The other is that Raman tensor ratio, $r = {\alpha'_{yy}}/{\alpha'_{zz}}$ is neither zero nor a constant value as previously assumed in the literature in which r was obtained from the depolarization ratio at isotropic state R_{iso} as [29];

$$R_{iso} = \frac{(1-r)^2}{3+4r+8r^2} \tag{3-3}$$

Following the methods by Jones *et al.*, Southern *et al.* [39] in 2007 explored the thermal evolution of orientational order parameters, $\langle P_{200} \rangle$ and $\langle P_{400} \rangle$, of a thermotropic nematic liquid crystal, 4'-octyl-4-cyanobiphenyl (8CB, see the details in Experimental Section).

While this new methodology was proposed several years ago, few experiments have been carried out to obtain orientational order parameters for soft matter systems. Thus, this chapter seeks to validate the quantification of orientational order using this new approach of polarized Raman measurement. We will obtain temperature dependence of $\langle P_{200} \rangle$ and $\langle P_{400} \rangle$ of two different thermotropic LCs (5CB and 8CB) in the nematic phase and the results will be compared with those from other methods and the predictions from mean-field theory. Details about instrumentation and experimental set-up for the quantification of orientational order parameters are described in this chapter.

3.2 Experiments

3.2.1 Instrumentation

The micro-Raman spectroscope (*RAMANRXN2*, Kaiser Optical Systems) used in our experiments consists of four major components: the excitation source, the microscope, the spectrograph, and the detector. A schematic of the apparatus is shown in Figure 3.2. The excitation source for Raman spectroscopy is usually a laser since it provides intensity strong enough to generate sufficient Raman signals, and a monochromatic light. The excitation source used in our instrument is 785 *nm* diode laser. Optical fiber carries the laser excitation onto the sample through a light microscope. The laser spot is focused on the sample by using the high-magnification microscope objective, which requires sample specimen as small as tens of ㎛ across. In addition, more Raman scattered light from the sample can be collected through the objective. Thus, it requires a short measuring time, normally a few seconds, which enables one to monitor chemical reactions or processing in essentially real time [40]. Back scattered light is collimated by optical lenses and is carried into a spectrometer in which the scattered photons are separated. Scattered photons pass through a holographic notch filter that cuts off photons with the same frequency as the incident radiation (*i.e.* Rayleigh scattering) prior to entering the spectrometer. As a result, remaining photons have different frequencies from incident radiation and then a monochromator containing a diffraction grating (1200 grooves/*mm*) disperses Raman signals by their wavelengths and transfers them to the detector.

Since the number of photons from Raman scattering is low (1 over 10^6 scattered photons), a very sensitive detector is required to measure the Raman signals. The charge-coupled device (CCD), which scientific achievement was chosen for a Nobel Prize in Physics (2009), has revolutionized the read-out of Raman signals. In our instrument, CCD detector consisting of a rectangular two-dimensional array of independent, integrating pixels on a silicon chip is used. Each pixel in the CCD detector is 26 ㎛ × 26 μm and there are 1024 pixels × 128 pixels in the CCD photoactive area. The spectral resolution of the CCD detector is 4 cm^{-1}. The amount of photo-generated charge is linearly proportional to both the intensity of radiation and the exposure time. Photo-generated charge from each pixel is transferred from pixel to pixel until the charge reaches an on-chip output amplifier. The quality of Raman spectra is determined by signal-to-noise ratio (S/N). The most common noises arising from the detection are read-noise, dark-noise, and shot-noise. Read-noise, created in accumulating charge in each CCD pixel, and dark noise, caused by charge other than photoelectrons, are negligible at –40℃, the typical operating temperature for the *RAMANRXN2* CCD. The dominant source of noise from a CCD is usually shot-noise that is a consequence of the statistical nature of light. Shot noise increases linearly with the square root of accumulation time. Since photo-generated charge for Raman signal is linearly proportional to exposure time, S/N of Raman spectra will increase linearly with the square root of accumulation time. More details about the instrument can be found at the website of manufacturer, www.kosi.com.

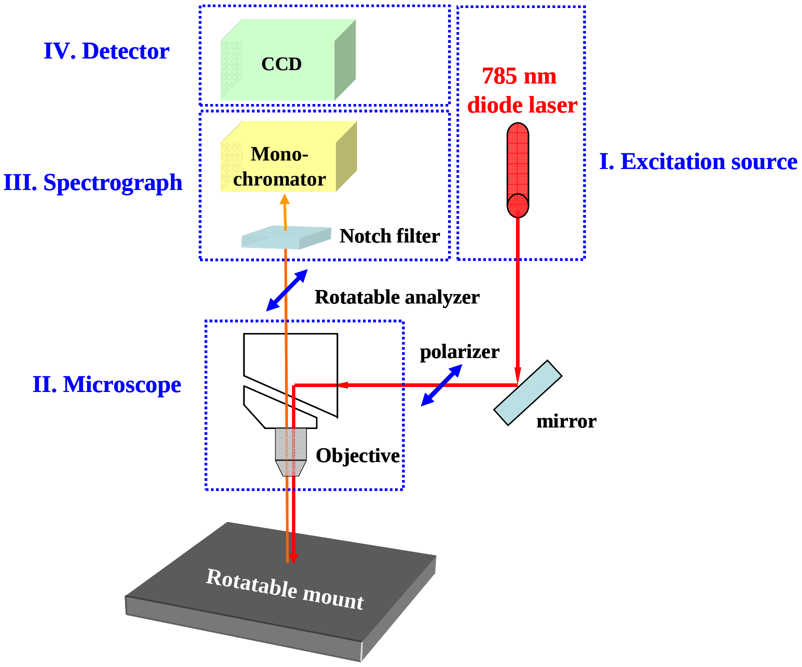

Figure 3.2 A schematic diagram of the major components in micro-Raman spectrometer.

3.2.2 Sample Preparation

Two thermotropic nematic LCs, 4’-pentyl-4-cyanobiphenyl (5CB, *Sigma-Aldrich*$^{@}$) and 4’-octyl-4-cyanobiphenyl (8CB, *Merck EMD*) were chosen to verify the quantification of orientational order using polarized Raman spectroscopy since their orientational order parameters have already been extensively studied by various experimental methods [26, 29, 31]. Molecular structures, phase sequences, and transition temperatures for these two compounds are shown in Figure 3.3. As mentioned earlier, the extent of orientational order in a nematic phase is defined as thermal fluctuations of director in a bulk state. In order to explore the degree of orientation induced by director fluctuations, we removed topological defects of samples influencing the anisotropy of polarized Raman intensity apart from thermal fluctuations of director. Indeed, polarized Raman intensity measured from multi-domains with inhomogeneous director configurations or defects formed by discontinuity of director configurations in a focused area can induce incorrect information about the orientational order defined by the thermal fluctuations of director. Thus, we prepared a mono-domain sample using mechanically rubbed substrates of a cell, in which the long axis of molecules, equivalent to director ***n*** for 5CB and 8CB, lie on the substrate and orient toward the rubbing direction.

Homogeneous configuration of directors ***n*** was achieved under sufficiently strong boundary conditions, called ‘*strong anchoring*’ [6]. The two bounding glasses were coated with polyimide and then were mechanically rubbed in one direction using velvet. Rubbed polymer strands on the surface promoted the alignments of the molecular axis, *i.e.* director of 5CB and 8CB, along the plane of the substrate [41]. Then, we assembled these two glasses in a way that the rubbing directions were parallel to each other and separated by 25 μm spacers. LCs were filled into the cell by the capillary action close to the isotropic-nematic transition temperature, T_{NI} and then annealed at T_{NI} + 5 ℃ for 20 minutes to remove the residual flow effects during the capillary action. The temperature was controlled using a *Linkam* hot stage that provides relative temperature accuracy at ± 0.1℃.

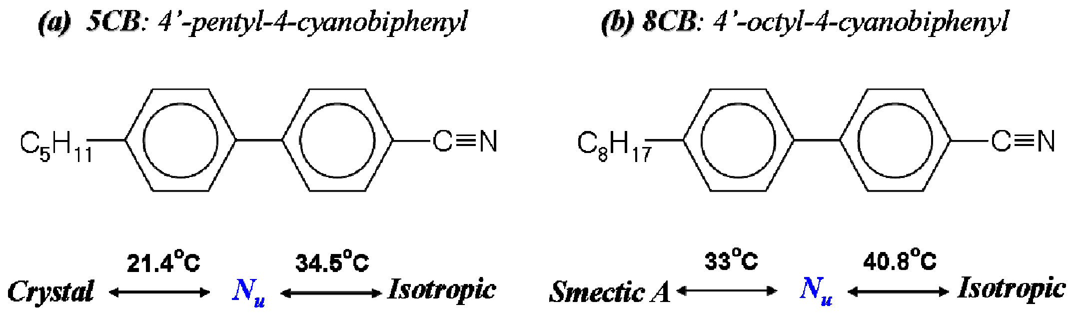

Figure 3.3 Molecular structures, phases, and transition temperatures for compounds (a) 5CB and (b) 8CB.

The achievement of homogeneously aligned mono-domain was confirmed by polarized optical microscopy. Under crossed polarizers, when the rubbing direction was parallel or perpendicular to the incident polarization direction, the LC samples looked completely dark, while the maximum intensity of transmitted light appeared when rotating the rubbing direction to 45° with respect to the polarization direction of incident light without any defects. This indicates that the optic axis of the molecules, usually thought to be identical with the molecular long axis of these compounds, thus director ***n***, is aligned along the rubbing direction. After the achievement of a mono-domain sample, we examined sample purity/quality by checking T_{NI} of 5CB and 8CB. Should impurities be added, T_{NI} of LCs in the sample cells is supposed to drop from that of pure LCs [42] . Judging from the absence of any drop of T_{NI}, we neglected any contamination in the sample.

It is noteworthy that widely used glass made of *soda-lime-silica* cause a significant fluorescence background problem. Figure 3.4 (a) shows that the strong fluorescence background of soda-lime-silica glass masks the Raman signal from 5CB. It is unknown where this strong fluorescence background comes from, but it is likely due to the many impurities and ions in glasses. In order to reduce fluorescence background, we used quartz to make the cells. Figure 3.4 (b) shows the remarkable reduction of fluorescence background when using a quartz plate compared to the result of Figure 3.4

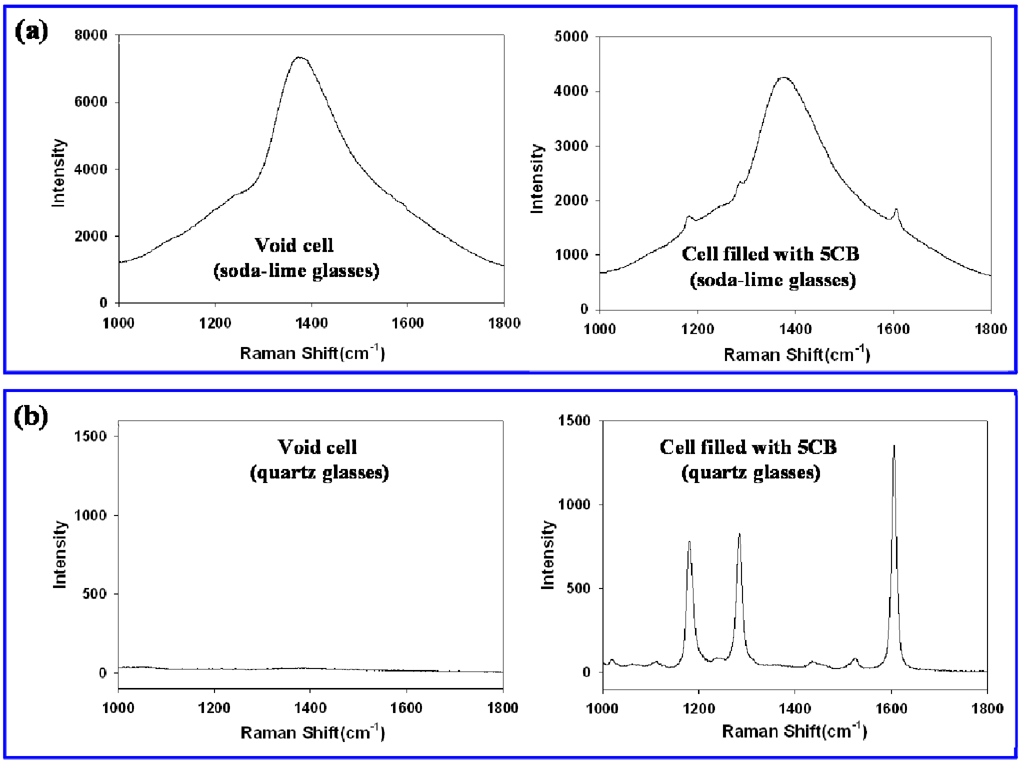

Figure 3.4 Raman spectrum of (a) void cell made of soda-lime glasses (left) and 5CB filled in the soda-lime glass cell (right), and (b) void cell made of quartz glasses (left) and 5CB filled in the quart glass cell (right) at a given laser intensity (50 *mW*).

3.2.3 Measurements of Raman Spectra

By placing homogenously aligned specimens inside the hot stage flat on the rotatable mount, we were able to make director ***n*** lie in the polarization plane of incident light. We then locate the rubbing direction parallel to the *Z-axis* in Figure 2.6 and set this configuration as $\theta = 0^\circ$. The polarized, $I_{//}$ and depolarized component, $I_{\perp}$ was resolved by setting the polarization direction of analyzer parallel and perpendicular to that of the incident beam, respectively. According to the denotation of I_{ij} as shown in Eq. (2-27), $I_{//}$ and $I_{\perp}$ are essentially I_{ZZ} and I_{ZY} in our geometry, respectively. 50× objective (N.A =

0.55, Working Distance = 8 *mm*) was used and focusing area was about 7 ㎛ in diameter. Each Raman spectrum was recorded for 30 seconds (10 seconds exposure time × 3 accumulation times) under the output laser power of 50 *mW*.

Any combination of θ can be carried out by rotating either the sample on the mount or polarizer/analyzer. In our experiments, we rotated the sample on the rotatable mount and recorded a series of Raman spectra over the entire range of 0° to 360° at 10° intervals. Figure 3.5 presents the polarized and depolarized components, $I_{//}$ and $I_{\perp}$, of 5CB, measured at the configuration of $\theta = 0°$. The Raman spectrum from the cyanobiphenyl compound exhibits four strong Raman peaks [26, 36, 43]: a peak at 1180 cm^{-1} assigned to *C-H* deformation in benzene ring, a peak at 1283 cm^{-1} attributed to the stretching of biphenyl link, the most intense peak at 1606 cm^{-1} corresponding to the symmetric *C-C* stretching in benzene ring along molecular axis, and a peak due to the *C≡N* stretching at 2225 cm^{-1}. In our present studies, we analyzed the most intense peak at 1606 cm^{-1} to calculate orientational order parameters of molecules from the polarized intensities. It is because the symmetric C-C stretching along the molecular axis in a benzene ring is thought to be highly anisotropic and the symmetry of stretching is collinear with the molecular axis so that the orientation information of this vibrational band can represent that of molecules [29].

In order to explore the temperature dependence of orientational order parameters, we repeated the measurements described above by changing the temperature in the nematic range of each LC. We controlled the temperature of the sample using a hot stage that has an accuracy of temperature within ±0.1℃. After the first measurement of angular dependence of polarized intensities close to T_{NI}, we slowly cooled the sample at a rate of -0.1℃/min to the next measurement temperature. On reaching the next measurement temperature, we held the temperature and waited for 20 minutes in order to remove any thermal history and for the sample to attain thermal equilibrium. We also checked the heating effect from the laser power, but depolarization ratios obtained from 20 *mW* to 100 *mW* of laser output did not make any difference in the angular dependence of depolarization ratio. It is likely that fluctuating components of LCs scatter the incident laser source rather than absorb it, so that the thermal energy on the focused area is not strong enough to affect director fluctuation significantly. Thus, we ruled out the heating effect from the laser power on the thermal fluctuation of the director ***n*** for these compounds. However, for the sample that absorbs the energy of the laser with visible wavelength such as colored samples, or for the sample that is easily damaged even by weak external energy, special care should be taken not to make the sample heated or damaged by the laser.

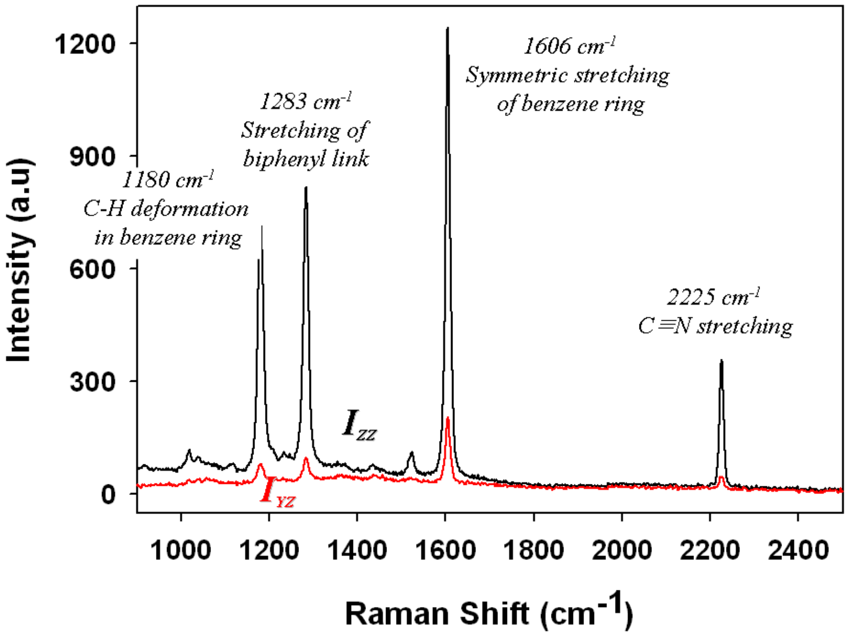

Figure 3.5 Raman spectrum recorded using 5CB, showing 4 intense signal within the range of frequency 1000 ~ 2400 *cm*$^{-1}$. The most intense peak at 1606 *cm*$^{-1}$ is attributed to symmetric stretching of *C-C* in a benzene ring along the molecular axis.

3.2.4 Data Analysis

Peak intensities were quantified from the integrated area of resolved peaks using commercial software package, GRAMS (*Galactic Inc.*). If we are aware of the number of peaks and band shape, it is possible to obtain the integrated area of peaks through a numerical fitting of observed spectra. If unknown number of peaks is mixed or the intensity of the probe peak is too weak to be resolved clearly, the situation will be more complicated and will require meticulous care to yield the intensity of peak of interest. Accordingly, the criteria of selecting Raman peak for the orientation information of molecules are twofold in addition to the prerequisite of totally symmetric vibration, *i.e.*, $0 \le R_{iso} \le 3/4$ as explained in chapter 2. First, vibration symmetry should be collinear with the molecular main axis so that the orientational ordering obtained from Raman intensities of the peak can represent that of molecules in a system. Second, the Raman peak should be strong enough so that one can easily analyze the integrated area. From this point of view, the peak at 1606 cm^{-1} is appropriate as an indicator to use in order to quantify the molecular orientation.

In fitting the peak using the software, we adopted the mixed *Gaussian-Lorentzian* function as a peak shape and reproducible results were obtained with regression coefficient R^2 greater than 0.99. While natural line broadening follows Lorentizan-shape in character [44], there may also be several factors that broaden the discrete spectral lines that are Gaussian in character as described in chapter 2. It is noteworthy that bandwidths of the Raman peak for 5CB and 8CB are more or less constant independent of the angle, θ, and even of the temperature in the nematic range. Therefore, the peak height can be taken to be linearly proportional to the integrated area of peaks and we can simply replace the peak area with the peak height to calculate the depolarization ratios.

As 5CB and 8CB are well known to possess a uniaxial nematic (N_u) phase, the orientational order is considered to be only β angle dependent and only $\langle P_{200} \rangle$ and $\langle P_{400} \rangle$

are expected to be nonzero terms in expanding the equation of ODF (Eq. 2-28). Therefore, a series of depolarization ratios (37 points) obtained from the measured intensities, $I_{ll}(\theta)$ and $I_{\perp}(\theta)$, were fitted to a simplified formula, Eq. (3-4), resulting in the extractions of only non-zero expansion coefficients of $\langle P_{200}\rangle$, $\langle P_{400}\rangle$, and r [45].

$$
\begin{aligned}
R(\theta) &= \frac{I_{\perp}(\theta)}{I_{ll}(\theta)} = \frac{I_{YZ}(\theta)}{I_{ZZ}(\theta)} \\
&= \frac{(-1+r)^2\left\{56+40\langle P_{200}\rangle+(9-105\cos 4\theta)\langle P_{400}\rangle\right\}}{\left\{\begin{array}{l} 56\left(8r^2+4r+3\right) \\ -40\left(4r^2-r-3\right)(1+3\cos 2\theta)\langle P_{200}\rangle \\ +3(r-1)^2\left(9+20\cos 2\theta+35\cos 4\theta\right)\langle P_{400}\rangle \end{array}\right\}}
\end{aligned}
\qquad (3\text{-}4)
$$

3.3 Results

3.3.1 Angular Dependence of Polarized Raman Intensity and Depolarization Ratio

Polarized (I_{ll}) and depolarized intensities ($I_{\perp}$) of the Raman peak at 1606 cm^{-1} of 5CB measured at T-T_{NI} = -0.7℃ are plotted as a function of the sample rotating angle, θ, in Figure 3.6. We obviously observe strong θ-angle dependence of both I_{ll} and $I_{\perp}$, which indicates there is a strong anisotropic ordering in 5CB. The most intense peak was I_{ll} at $\theta = 0°$ as expected from Eq. (2-17). While polarized intensity, I_{ll} at $\theta = 90°$ and depolarized intensity, $I_{\perp}$ at $\theta = 0°$ and $\theta = 90°$ are expected to be zero in a single component system (Eq. (2-17)), it is a multi-molecular system in practice and director fluctuations produce a non-negligible quantity of I_{ll} at $\theta = 90°$ and of $I_{\perp}$ at $\theta = 0°$ and $\theta = 90°$.

Peak intensities normalized by the most intense peak, *i.e.*, $I_{ll}(\theta = 0°)$ are plotted as a function of angle, θ, in Figure 3.7 (a) where the plot reaches its maximum at $\theta = 0°$

and smoothly decreases with increasing θ before reaching the peak again at $\theta = 180°$ reflecting the symmetry of the phase. The blue open circles for I_{II} components and the red triangles for $I_{\perp}$ components show twofold rotational symmetry, C_2, and fourfold rotational symmetry, C_4, respectively as the sample is rotated from 0° to 360°. The pattern of twofold and fourfold rotational symmetry of I_{II} and $I_{\perp}$ with respect to rotating angle, θ are conformable to trigonometric periodicities of Eq. (2-17) similar to those reported by Jones *et al.* [38]. However, we have to consider a multi-atomic system and director fluctuations so that the “scrambling” effect induces non zero values of peak intensities over the entire angle θ [29]. However the trigonometric periodicity should be valid, thus we fit the intensity profiles $I_{II}(\theta)$ and $I_{\perp}(\theta)$ to the analytical formula in considering the scrambling effect as arbitrary background expressed as a parameter, ***a*** in Eq. (3-5) [37];

$$\begin{aligned} I_{II}(\theta) &= a + b\cos^4\theta \\ I_{\perp}(\theta) &= c + d\cos^2\theta\sin^2\theta \end{aligned} \tag{3-5}$$

Analyzed peak intensities were fit to Eq. (3-5) as a function of rotating angle, θ and we obtained fitting results with R^2 values of 0.995 and 0.950 for all sets of $I_{II}(\theta)$ and $I_{\perp}(\theta)$ measurements, respectively. The relatively low R^2 value from fitting $I_{\perp}(\theta)$ will be addressed in the discussion section.

Depolarization ratios, $R(\theta)$, corresponding to ${}^{I_{\perp}(\theta)}\!\big/\!{}_{I_{II}(\theta)}$ are plotted in Figure 3.7 (b). Using a χ^2 minimization routine, we numerically fitted 37 values of depolarization ratios at a given temperature to Eq. (3-4). This fit allows the extraction of the parameters, $\langle P_{200}\rangle = 0.4176$ and $\langle P_{400}\rangle = 0.2185$, and $r = -0.2114$, respectively, at a temperature of $T\text{-}T_{NI} =$ -0.7 ℃.

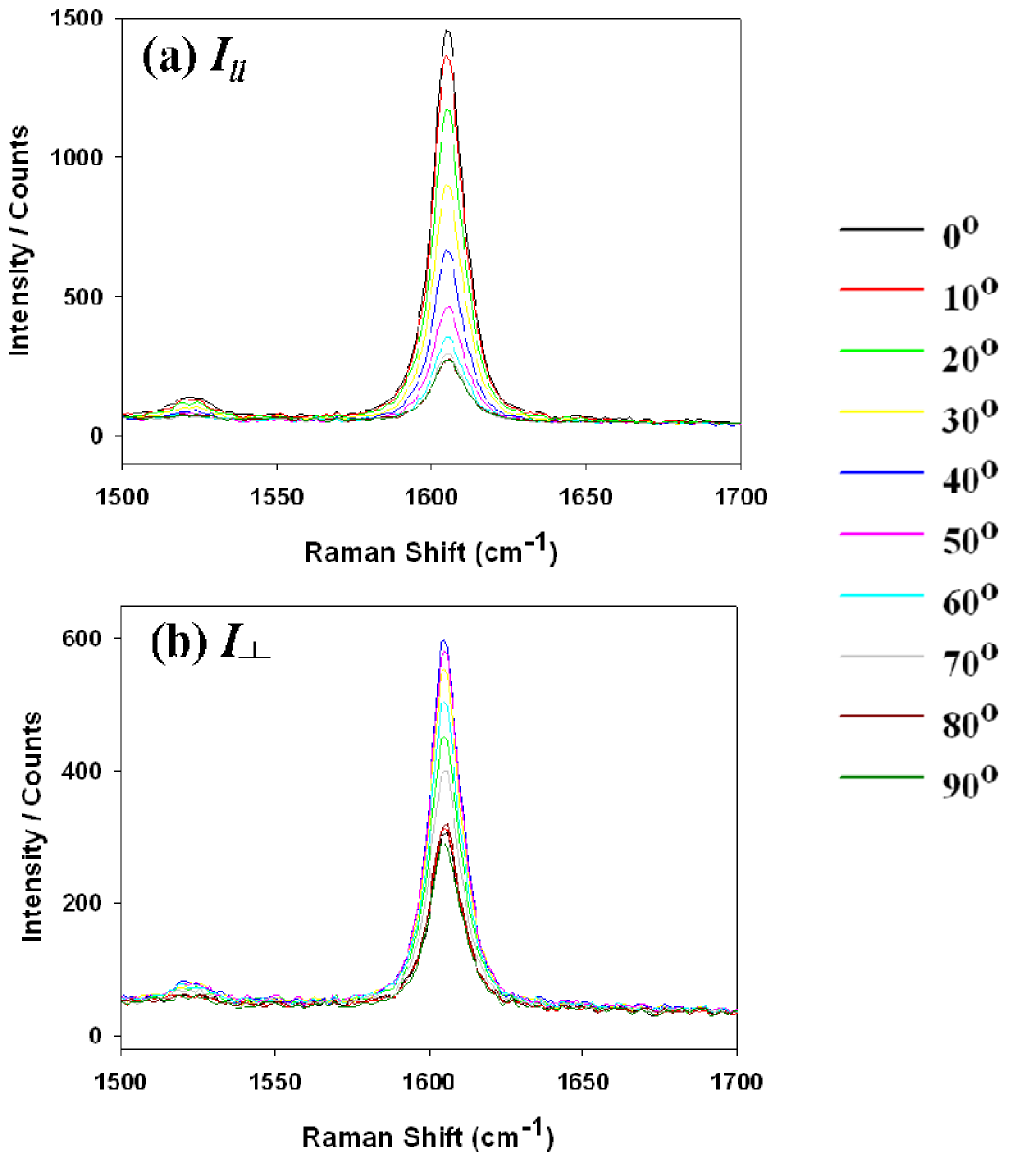

Figure 3.6 θ-angle dependence of Raman peak for benzene ring stretching (1606 cm^{-1}) measured at T-T_{NI} =-0.7 ℃. a) Raman spectra measured with parallel ($I_{//}$) and b) perpendicular ($I_{\perp}$) configuration between polarizer and analyzer.

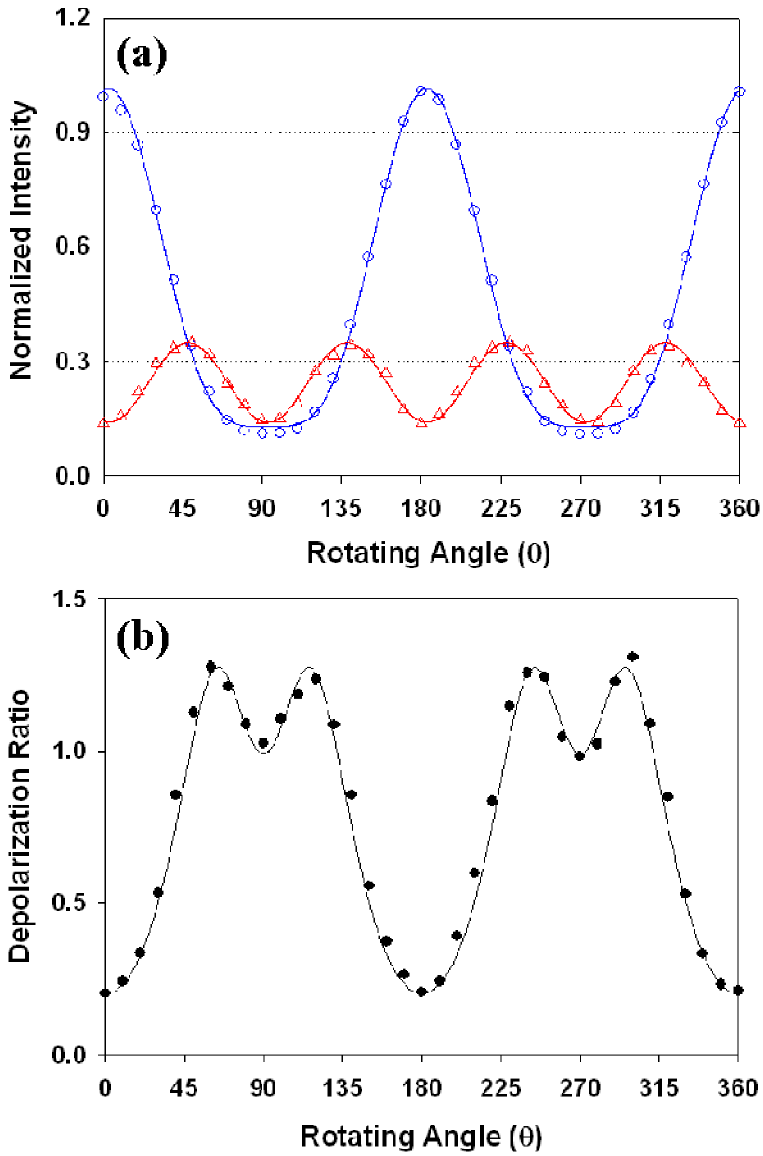

Figure 3.7 Angular dependences of Raman intensities and depolarization ratio. (a) Dotted marks, (○) and (Δ), are measured intensities, $I_{//}(\theta)$ and $I_{\perp}(\theta)$. Solid lines are the results from the numerical fitting of measured intensities to Eq. (3-5). (b) The corresponding depolarization ratio profile to the measured intensities; measured (●) and numerical fit to Eq. (3-4) (solid line), resulting in $\langle P_{200} \rangle = 0.4176$, $\langle P_{400} \rangle = 0.2185$, and $r = -0.2114$.

3.3.2 Temperature Dependence of Polarized Raman Intensity and Depolarization Ratio

In order to explore the thermal evolution of orientational order in a nematic phase of thermotropic LCs, we repeated the measurements of angular dependence of polarized Raman spectra at various temperatures in the nematic range. Figure 3.8 presents the variation of $I_{//}(\theta=0^\circ)$ and $I_{//}(\theta=90^\circ)$ of the Raman peak at 1606 cm^{-1} of 5CB according to the measured temperatures, in which $I_{//}(\theta=0^\circ)$ increases as temperature decreases, whereas $I_{//}(\theta=90^\circ)$ follows the reverse trend. This linear manner of variation in $I_{//}(\theta=0^\circ)$ and $I_{//}(\theta=90^\circ)$ with different temperatures suggests qualitative evidence that more population of scattering unit distributed along *Z-axis* (i.e., rubbing direction in our experiment) as temperature decreases.

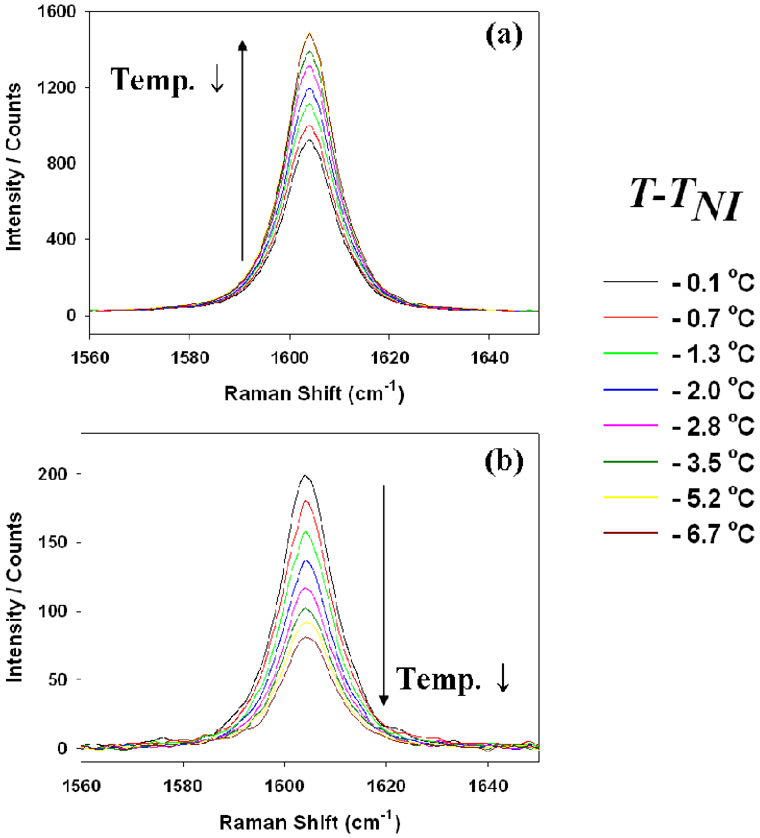

Figure 3.8 Temperature dependence of $I_{//}$ for Raman peak at 1606 cm^{-1} measured at the configuration of (a) $\theta=0^\circ$ and (b) $\theta=90^\circ$.

Fitting the results of polarized Raman intensities, $I_{//}(\theta)$ and $I_{\perp}(\theta)$, for the measurements at various temperatures are displayed in Figure 3.9 (a) and (b) in which peak intensities are normalized by $I_{//}(\theta = 0°)$ at each temperature measured. It is clear that the curves of both $I_{//}(\theta)$ and $I_{\perp}(\theta)$ show gradually increasing peak-to-peak amplitude as temperature decreases (it is easier to compare the peak-to-peak amplitude from the plot of renormalized $I_{\perp}(\theta)$ by the most intense $I_{\perp}$, *i.e.* $I_{\perp}(\theta = 45°)$, at each temperature (Figure 3.9 (c)). However, the manner of the evolution of curve shapes is different. In the case of $I_{//}(\theta)$, anisotropic distribution of intensities becomes less in the sections of ca. $(\theta = 60° \sim 120°)$ and $(\theta = 240° \sim 300°)$ as temperature decreases. In the case of $I_{\perp}(\theta)$, no flattening of the curve shape was observed, but the width of curve becomes narrower, which is attributed to the fact that the decreasing rate of $I_{\perp}$ with temperature decrease differs according to rotating angle, θ. One comparison was shown in Figure 3.9 (b) where the gap between solid horizontal lines means the extent of the intensity decrease with temperature decrease (T-T_{NI} = -1 ℃ → -6.7 ℃). The intensity difference (normalized values) is 0.1158 at $\theta = n\pi \pm 45°$ and that at $\theta = \frac{n\pi}{2}$ is 0.0961. Depolarization ratios, $R(\theta)$ corresponding to $I_{//}(\theta)$ and $I_{\perp}(\theta)$ according to various temperatures are plotted in Figure 3.10. We observed significant variations in depolarization ratio profiles of different temperatures. Above-mentioned results pertain in the case of 8CB with more or less the same manner.

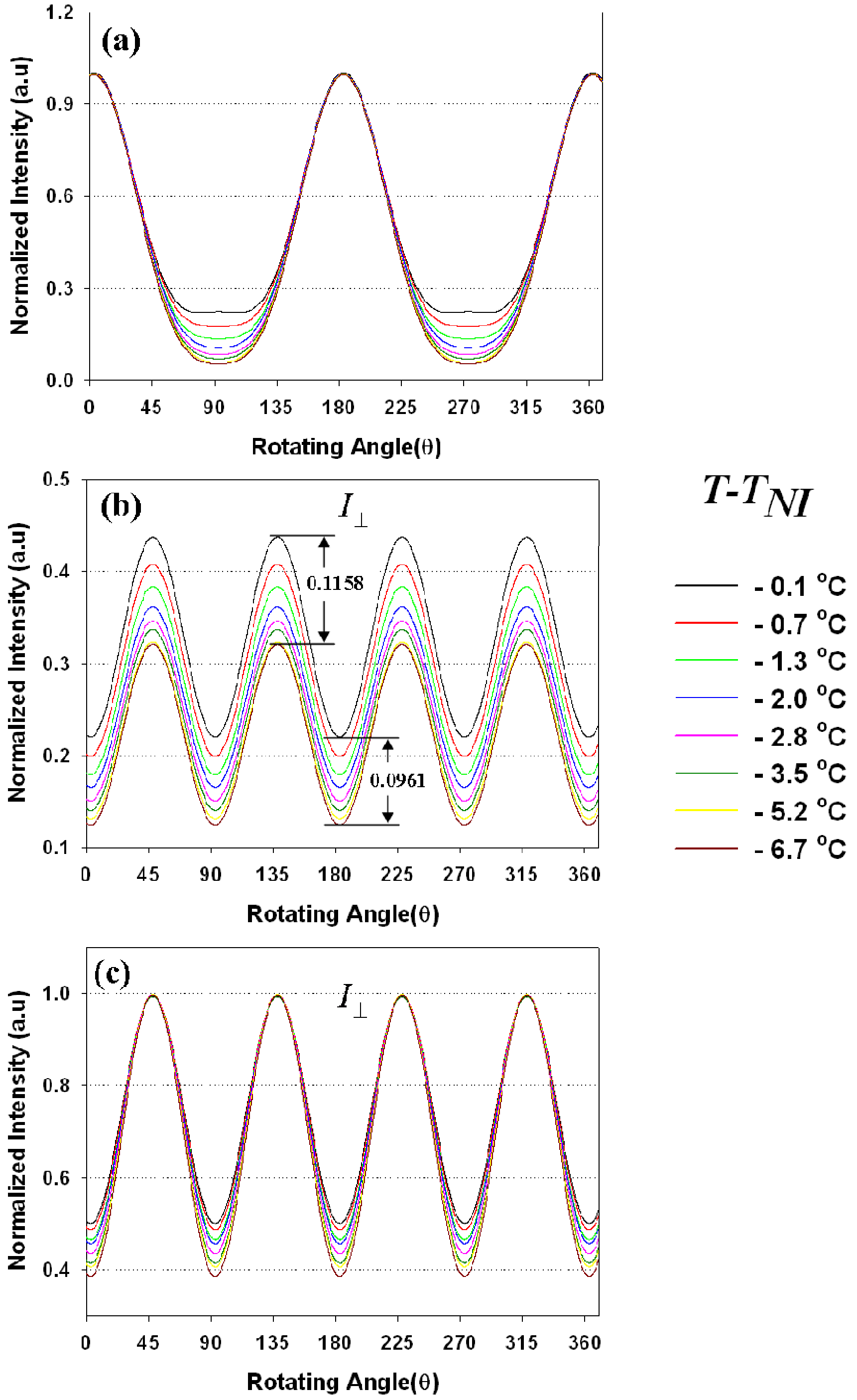

Figure 3.9 Numerical fitting results of measured intensities, (a) $I_{//}(\theta)$ and (b) $I_{\perp}(\theta)$, normalized to $I_{//}(\theta = 0°)$ at various temperatures. (c) Numerical fitting results of $I_{\perp}(\theta)$ normalized to $I_{\perp}(\theta = 45°)$

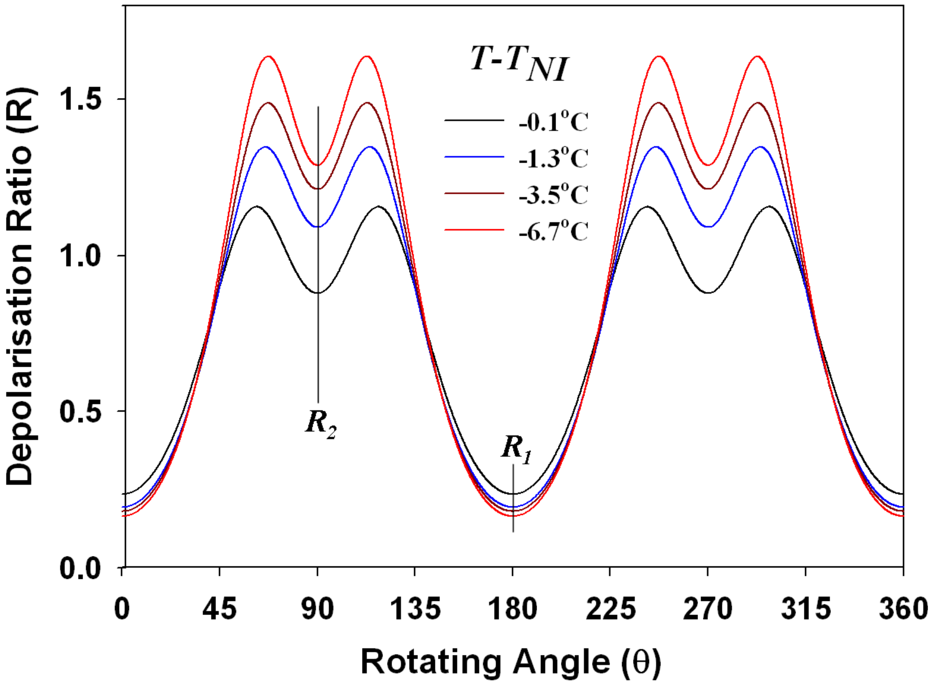

Figure 3.10 Numerical fitting results of measured depolarization ratios, $R(\theta)$ to Eq. (3-4) at several temperatures.

3.3.3 Orientational Order Parameters, $\langle P_{200} \rangle$ *and* $\langle P_{400} \rangle$

We obtained three unknown coefficients, r, $\langle P_{200} \rangle$, and $\langle P_{400} \rangle$ for 5CB and 8CB samples as results of the numerical fitting of measured depolarization ratios, $R(\theta)$ to Eq. (3-4). Temperature dependence of orientational order parameters, $\langle P_{200} \rangle$ and $\langle P_{400} \rangle$, through the measured temperature range upon cooling from isotropic phase is shown in Figures 3.11 and 3.12 for 5CB and 8CB, respectively. For many low molecular weight nematogens, $\langle P_{200} \rangle$, often denoted as S, was considered to be a universal function of T/T_{NI} (K), which is in good agreement with the experimental result [46], using the Haller approximation by [47];

$$\langle P_{200} \rangle = \tau \left(1 - {T}/{T_{NI}} \right)^{\eta} \tag{3-6}$$

where both τ and η are fitting parameters.

As shown in Figure 3.11 (a) and Figure 3.12 (a), the thermal evolution of $\langle P_{200} \rangle$ values for both 5CB and 8CB, marked as ○, are in excellent agreement with the prediction by Eq. (3-6). We also calculated the values of $\langle P_{200} \rangle$ from $R_1 = \frac{I_\perp(\theta = 0°)}{I_{//}(\theta = 0°)}$ and $R_2 = \frac{I_\perp(\theta = 90°)}{I_{//}(\theta = 90°)}$ using Eq. (3-2) as Jen *et al.* proposed [19] and plotted them, marked as Δ. For the thermal evolution of $\langle P_{200} \rangle$ values, both results are quite consistent with each other for 5CB sample. While there are small deviations for 8CB, $\langle P_{200} \rangle$ values obtained using Eq. (3.2) are comparable with those obtained by fitting 37 depolarization ratios to Eq. (3.4).

The values of $\langle P_{400} \rangle$ obtained by fitting measured 37 depolarization ratios to Eq. (3-4) are plotted according to T/T_{NI} (K) in Figure 3.11 (b) and 3.12 (b). These obtained values are much larger than the results of previous literature [26, 29], marked as ×, and are positive over the entire temperature range measured, even in the vicinity of T_{NI} . The values of $\langle P_{400} \rangle$ calculated using Eq. (3-2) with only R_1 and R_2 are plotted with ▼ marks along with above results. On the contrary to the results of $\langle P_{200} \rangle$, $\langle P_{400} \rangle$ values calculated using Eq. (3-2) with only R_1 and R_2 values, as done in many previous literature [26, 29], appear far lower than those obtained by fitting 37 points of depolarization ratios to Eq. (3-4). Interestingly, $\langle P_{400} \rangle$ calculated from only R_1 and R_2 exhibits a negative value at close T_{NI}, which had been a criticism of the Raman approach to obtain orientational order parameters. Figure 3.13 compare the relations between $\langle P_{200} \rangle$ and $\langle P_{400} \rangle$ obtained by fitting 37 depolarization ratios to Eq. (3-4), marked as ○ and Δ for 5CB and 8CB sample, respectively. It is clearly seen that the results from the fit are closer to the result of mean-field theory [24], as marked by the solid line, than the results in previous literature [26, 29], which may be due to the consideration of more data of depolarization ratio for obtaining $\langle P_{200} \rangle$ and $\langle P_{400} \rangle$. The relation between $\langle P_{200} \rangle$ and $\langle P_{400} \rangle$ for 5CB measured at a specific temperature by NMR in previous literature was marked as ★.

Along with $\langle P_{200} \rangle$ and $\langle P_{400} \rangle$, the differential polarizability ratio, $r = {\alpha'_{yy}}/{\alpha'_{zz}}$ was deduced from the data fit and obtained r values at measured temperatures are shown in Figure 3.14, in which r values obtained as a fitting parameter quite differ from the value calculated from measured depolarization ratio at isotropic phase, R_{iso} using Eq. (3-3). The r value calculated from measured R_{iso} was -0.0725 and -0.0685 for 5CB and 8CB, respectively, whereas r values as the result of fitting measured data to Eq. (3-4) have values within the range of ca. -0.15 ~ -0.25. Details about the effect of the difference in r value on the orientational order parameters, $\langle P_{200} \rangle$ and $\langle P_{400} \rangle$, is not clearly known yet and it needs to be studied further.

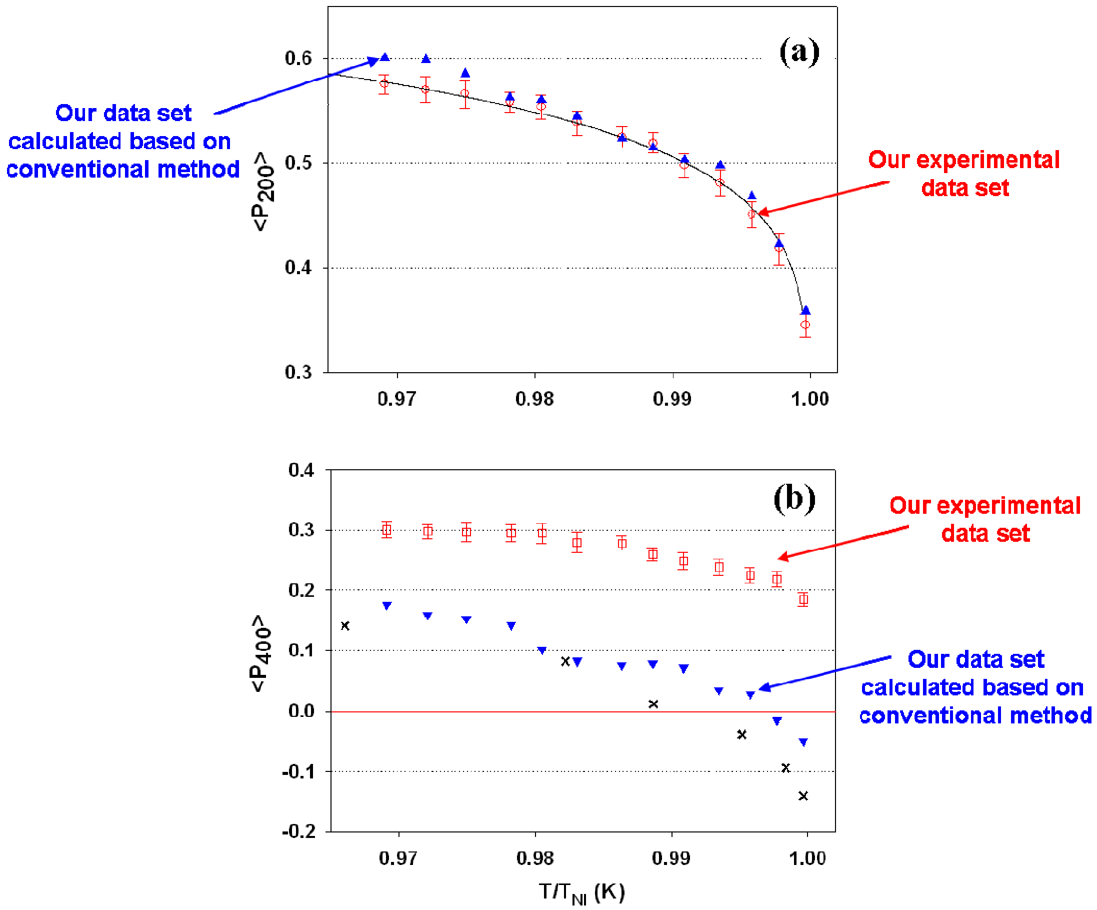

Figure 3.11 Thermal evolutions of orientational order parameters of 5CB. (a) (○): $\langle P_{200} \rangle$ values obtained by fitting 37 measured values of R to Eq. (3-4), (Δ): $\langle P_{200} \rangle$ values calculated using Eq. (3-2) with R_1 and R_2, and solid line: fitting the $\langle P_{200} \rangle$ values, (○), to Haller approximation, Eq. (3-6), resulting $\eta = 0.138$. (b) (□): $\langle P_{200} \rangle$ values obtained by fitting 37 measured values of R to Eq. (3-4), (▼): $\langle P_{400} \rangle$ values calculated using Eq. (3-2) with R_1 and R_2, and (×): $\langle P_{400} \rangle$ values for 5CB from Raman approach by Miyano et al. [26].

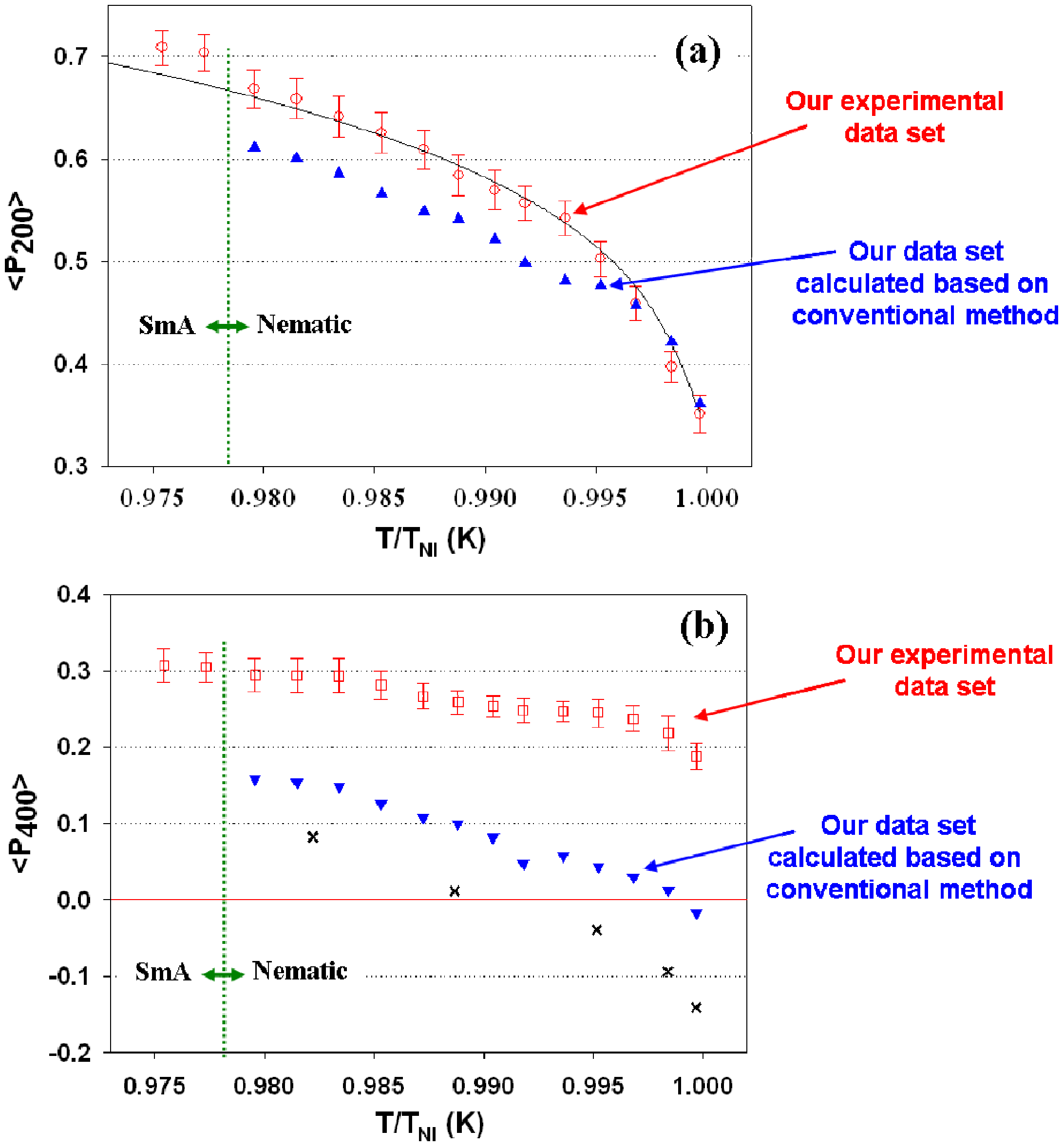

Figure 3.12 Thermal evolutions of orientational order parameters of 8CB. (a) (○): $\langle P_{200} \rangle$ values obtained by fitting 37 measured values of R to Eq. (3-4), (Δ): $\langle P_{200} \rangle$ values calculated using Eq. (3-2) with R_1 and R_2, and solid line: fitting the $\langle P_{200} \rangle$ values, (○), to Haller approximation, Eq. (3-6), resulting $\eta = 0.1770$. (b) (□): $\langle P_{200} \rangle$ values obtained by fitting 37 measured values of R to Eq. (3-4), (▼): $\langle P_{400} \rangle$ values calculated using Eq. (3-2) with R_1 and R_2, and (×): $\langle P_{400} \rangle$ values for 5CB from Raman approach by Miyano et al. [26].

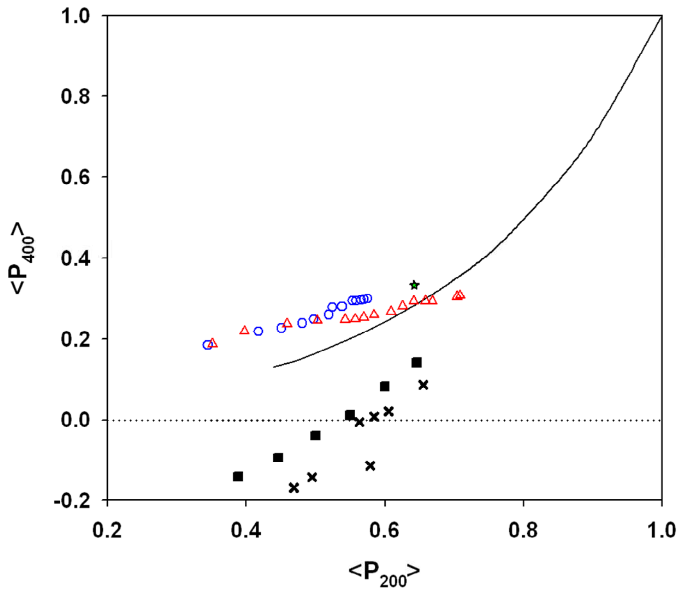

Figure 3.13 The dependence of $\langle P_{400} \rangle$ on $\langle P_{200} \rangle$; the solid curve is the prediction from mean-field theory [24]. The points correspond to the results by fitting measured data to Eq. (3-4) for 5CB (○) and 8CB (Δ), the results for 5CB by conventional Raman approach in ref. [29] (■), in ref. [26] (×) , and NMR measurements in ref.[31] (★).

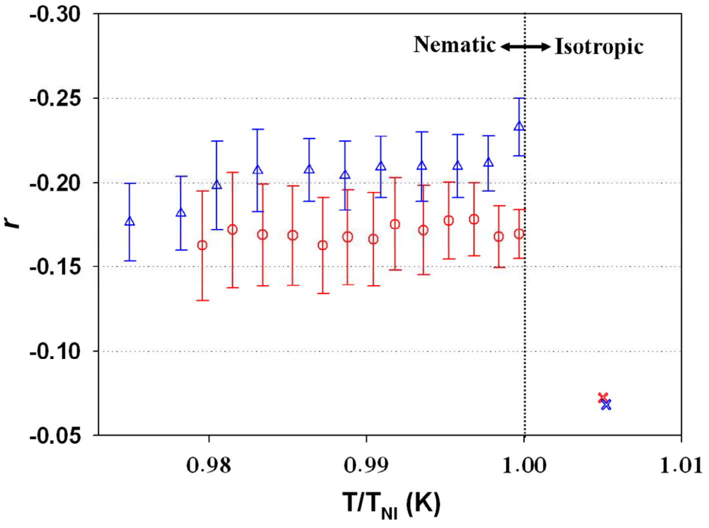

Figure 3.14 Temperature dependence of Raman tensor ratio, $r = \dfrac{\partial \alpha'_{zz}}{\partial \alpha'_{yy}}$, for *C-C* stretching in benzene ring for 5CB (Δ) and 8Cb (○) in a nematic phase. The r value from R_{iso} is -0.0685 for 5CB (×) and -0.0725 for 8CB (×).

3.4 Discussion

3.4.1 Relatively low R^2 from the fit of $I_{\perp}(\theta)$

We found that the R^2 value (*>0.95*) from the fit of the measured $I_{\perp}(\theta)$ to Eq. (3-5) is relatively lower than that from the fit of $I_{//}(\theta)$ (*>0.995*). It seems that two factors are responsible. First, the range between the maximum intensity, $I_{\perp}(\theta = n\pi \pm 45°)$ and the minimum intensity, $I_{\perp}\left(\theta = \frac{n}{2}\pi\right)$, *i.e.* peak-to-peak amplitude, is much narrower than that of $I_{//}$, such that even the same extent of deviations on the numerical fitting may produce relatively lower R^2 value from fitting $I_{\perp}(\theta)$.

Another reason is the twisted director configuration. Under '*strong anchoring*' at the surface of substrates, the director arrangement is distorted due to the elastic character of LCs when rubbing directions on both substrate are not parallel [6]. When the director on substrate 1 is tilted to the director on substrate 2 by an angle ϕ_1, directors successively rotate to adjust to the rubbing directions on substrates as shown in Figure 3.15 (a). Then, the twisting angle ϕ_1 should be taken into consideration on $I_{//}(\theta)$ and $I_{\perp}(\theta)$. Jones *et al.* [38] discussed the effect of 90° twist of directors, *i.e.* $\phi_1 = 90°$, on the $I_{//}(\theta)$ and $I_{\perp}(\theta)$ of a nematic LC and reported that the profiles of $I_{//}(\theta)$ and $I_{\perp}(\theta)$ keep C_2 and C_4 rotational symmetry in the backscattering geometry. However, it is not the case for a slightly tilted sample, *i.e.* $\phi_1 \neq 90°$. While we tried to make the rubbing directions on both substrates parallel to each other, there may be slight misalign between the two rubbing directions ($\phi_1 < 1 \sim 3°$). Should the directors be anchored on the each surface with slightly twisted angle ϕ as drawn in Figure 3.15 (b), Eq. (3-5) should be corrected to adjust the effect of the averaged tilt angle ϕ in bulk by replacing $\cos(\theta)$ and $\sin(\theta)$ with

$\cos(\theta \pm \phi)$ and $\sin(\theta \mp \phi)$, respectively. It is based on the similar manner of Eq. (2-17) in chapter 2. Thus, corresponding polarized intensities are expressed by [38]:

$$\begin{aligned} I_{II}(\theta) &= a + b\cos^4(\theta \pm \phi) \\ I_{\perp}(\theta) &= c + d\cos^2(\theta \pm \phi)\sin^2(\theta \mp \phi) \end{aligned} \tag{3-7}$$

From Eq. (3.7) we can recognize that C_4 rotational symmetry no longer exists in the equation for $I_{\perp}(\theta)$ because of the different angles in the sine and cosine terms, whereas the C_2 rotational symmetry of $I_{II}(\theta)$ is independent of twisting angle, ϕ. This was observed frequently when analyzing measured Raman intensities.

Figure 3.16 shows 3 data set of $I_{\perp}(\theta)$ obtained from 2 different samples, one is the sample with almost parallel alignment (Figure 3.16 (a)) and the other is the sample with twist angle, $\phi \approx 2.5°$ (Figure 3.16 (b) and (c)). Figure 3.16 (a) is the data set measured using the sample with almost parallel rubbing directions so that the profile of $I_{\perp}$ shows C_4 symmetry and fit very well to Eq. (3-5) (R^2 *=0.993*). On the contrary, Figure 3.16 (b) displays the plot of measured $I_{\perp}$ as a function of rotating angle, θ, which does not follow C_4 rotation symmetry and thus the R^2 value from the fit to Eq. (3-5) is quite low (R^2*= 0.832*). When the data set in Figure 3.16 (b) was fitted, however, to Eq. (3-7) with $\phi \approx 2.5°$, it yielded an excellent fitting result (R^2 *=0.996*). While we tried to use the data set obtained from well-assembled sample, a slight tilt angle could take place and induce a small deviation in C_4 rotational symmetry, which may be responsible for the relatively lower R^2 value from fitting measured $I_{\perp}(\theta)$. It is noteworthy that the result by Jones *et al.* [38], no change of C_4 symmetry for $I_{\perp}(\theta)$ from a 90° twisted cell, makes sense in that $\cos^2(\theta \pm 90°)$ and $\sin^2(\theta \mp 90°)$ is converted to $\sin^2(\theta)$ and $\cos^2(\theta)$, respectively and thus, Eq. (3-7) equals to Eq. (3-5) for $I_{\perp}(\theta)$.

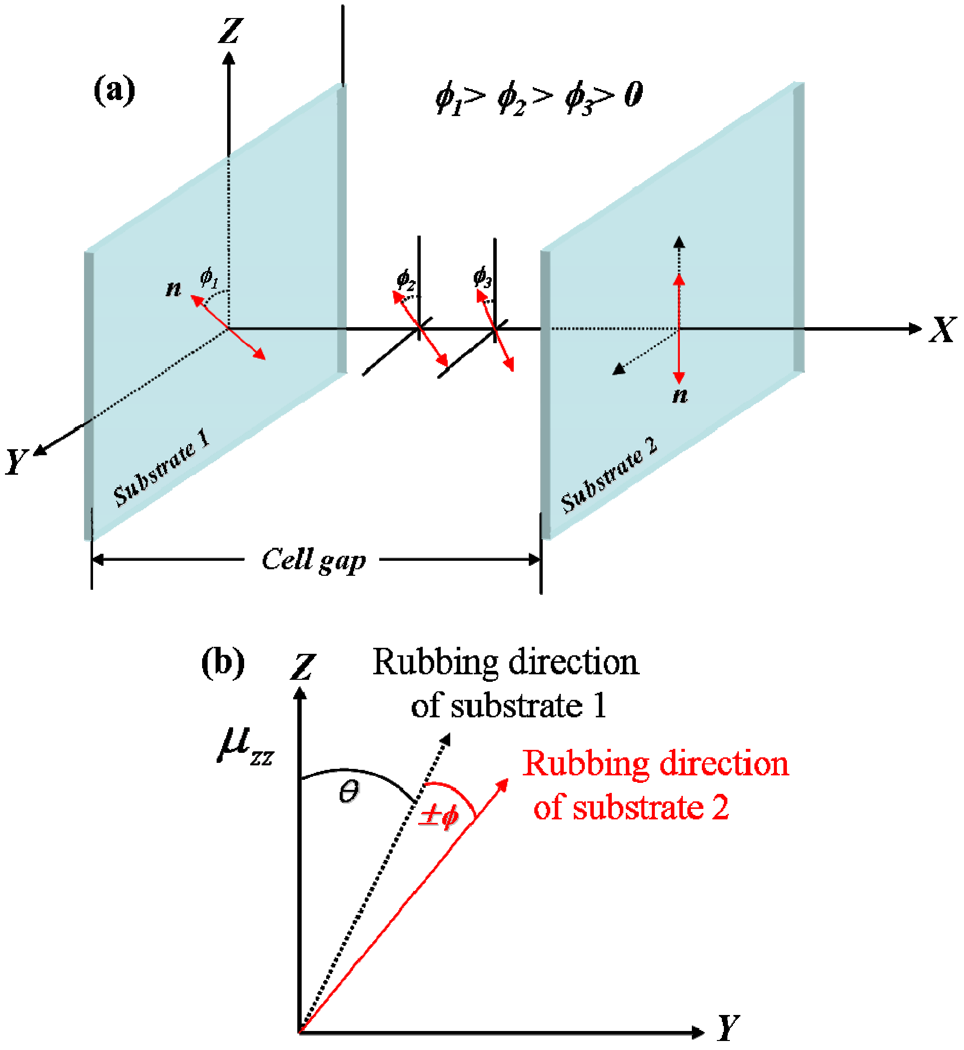

Figure 3.15 (a) twisted director configuration between two substrates with strong anchoring force and (b) twist angle effect on dipole moments.

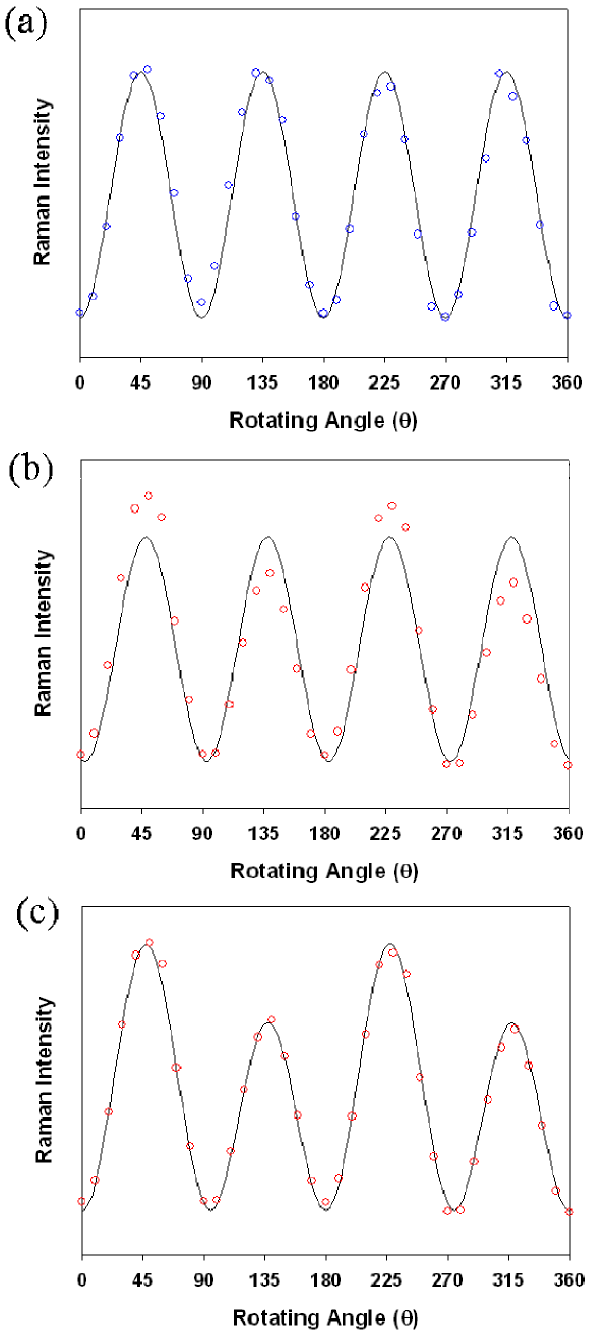

Figure 3.16 (a) Fitting result of measured $I_{\perp}(\theta)$ from the sample with parallel rubbing directions; (○): measured $I_{\perp}(\theta)$, solid line: the result from the fit to Eq. (3-5) (R^2 =*0.993*). Points (○) in (b) and (c) are measured $I_{\perp}(\theta)$ from the sample in which rubbing directions are slightly twisted, $\phi = 2.5°$, but solid lines are the results from the fit (b) to Eq. (3-5) (R^2 =*0.832*) and (c) to Eq. (3-7) (R^2 =*0.996*).

3.4.2 Determination of the Fourth-rank Order Parameter, $\langle P_{400} \rangle$

The increase of $\langle P_{200} \rangle$ values with decreasing temperature obtained from 5CB and 8CB are due to decreasing thermal fluctuations of molecules resulting in increasing anisotropic interactions between components. The observation of different $\langle P_{200} \rangle$ and η values at the same *T/T_{NI}* between 5CB and 8CB samples may be acceptable in that even two different nematogens, yet having the same T_{NI}, may have different $\langle P_{200} \rangle$ values at a given T/T_{NI}. While MBBA has the same T_{NI} as E2 (5CB-host-LC mixture, BDH, Ltd) does, for example, $\langle P_{200} \rangle$ was reported to be 0.55 and 0.64, respectively, at 24.5 ℃ which results in $\eta = 0.218$ for MBBA and $\eta = 0.164$ for E2 [48]. While the fitting parameter, η, is different each other ($\eta = 0.138$ for 5CB and for $\eta = 0.177$ 8CB), the temperature dependence of $\langle P_{200} \rangle$ values for both 5CB and 8CB (Figure 3.11 (a) and Figure 3.12 (a)) follows the manner of the Haller approximation (Eq. 3-6) through the entire temperature measured in a nematic phase. It means that the temperature dependent order parameters for a nematic LC obtained by polarized Raman spectroscopy can be predicted using a universal function based on selective measured data points.

Our attempts to interpret the significantly low values of $\langle P_{400} \rangle$ reported in previous literature were made. As shown in Figure 3.11 (b) and Figure 3.12 (b), $\langle P_{400} \rangle$ values calculated using Eq. (3-2) with measured R_1 and R_2 only are even lower than those obtained by fitting 37 data set of depolarization ratios to Eq. (3-4) and have negative values in the vicinity of T_{NI} as previous literature reported [19, 26, 27]. Two important factors that conventional methods did not consider seem to be mainly responsible for the low or negative values of $\langle P_{400} \rangle$. First, only 2 data points, *i.e.* R_1 and R_2, do not provide sufficient information about the degree of molecular orientation in a system so that exact $\langle P_{400} \rangle$ may not be extracted. Indeed, the shape of 37 depolarization ratios profile as a function of angle, θ, appear doublet peaks in the range of $\theta = 0 \sim 180°$ through entire temperatures measured as shown in Figure 3.10. However, it is likely that conventional works proposed by Jen *et al.* [19] assume that depolarization ratios have the maximum at $\theta = \pm \frac{(2n+1)}{2}\pi$ and the minimum at $\theta = \pm n\pi$, thus depolarization ratio profile about θ may exhibit the shape with singlet peak in the range of $\theta = 0 \sim 180°$. This seems reasonable in the case of a single component with axial symmetry of Raman tensor. When polarized light is scattered by a single scattering unit, the depolarization ratio is minimized at $\theta = 0, \pi, 2\pi ...$ because the scattered light is totally polarized at $\theta = 0, \pi, 2\pi ...$ and thus $I_{//}$ is maximized and $I_{\perp}$ is minimized. On the contrary, the depolarization ratio has its largest value at $\theta = \frac{\pi}{2}, \frac{3\pi}{2}, \frac{5\pi}{2} ....$ because the single component at this configuration scatters most depolarized light. However, when considering the system consisting of multi-components, especially fairly fluctuating components, it may not be the case. Distributions in a system and fluctuations of components can make a considerable amount of depolarized light scattering at $\theta = 0, \pi, 2\pi ....$

In order to check the influence of the values of $\langle P_{400} \rangle$ on the shape of $R(\theta)$ profile, we simulated the plots of $R(\theta)$ by applying various $\langle P_{400} \rangle$ values to Eq. (3-4). In Figure 3.17 (a), the solid curve with red color is the fitting results of the 37 measured depolarization ratios in Eq. (3-4) at $T/T_{NI} = 0.9977$, which results in $\langle P_{200} \rangle = 0.4176$, $\langle P_{400} \rangle = 0.2185$, and $r = -0.2114$. The others display the simulated $R(\theta)$ plots from the assumption of 4 different $\langle P_{400} \rangle$ values with keeping $\langle P_{200} \rangle$ and r fixed as 0.4176 and -0.2114, respectively. We can see that decreasing $\langle P_{400} \rangle$ makes $R(\theta)$ plots exhibit singlet peak from doublet peaks in the range between $\theta = 0 \sim 180°$. Accordingly, we can suppose that low values of $\langle P_{400} \rangle$ from the conventional method using Eq. (3-2) with only R_1 and R_2 reflects the distribution of depolarization ratios exhibiting a monotonic increase from $\theta = 0°$ to $\theta = 90°$ and a monotonic decrease from $\theta = 90°$ to $\theta = 180°$, which may induce significant deviation of $\langle P_{400} \rangle$ values from reality. However, it is also seen that R_1 and R_2 values simulated from the decreasing $\langle P_{400} \rangle$ keep increasing far from the measured R_1 and R_2. Apart from the assumption of singlet distribution, therefore, there seems to be another factor involved.

We hypothesize that the consideration of $r = \frac{\partial \alpha'_{yy}}{\partial \alpha'_{zz}}$ as either zero [19] or of constant value [26] obtained from R_{iso} (Eq. (3.4)) may cause the problem. Indeed, r values obtained as a fitting parameter (*ca.* $r = -0.15 \sim -0.25$) were not constant and very different from zero or obtained from R_{iso} ($r = -0.0685$ for 5CB and $r = -0.0725$ for 8CB) as shown in Figure 3.14. The simulations of $R(\theta)$ using Eq. (3-4) also explored the effect of r values on the plot of $R(\theta)$, and the results are plotted in Figure 3.17 (b). We chose constant $\langle P_{200} \rangle$ and $\langle P_{400} \rangle$ values corresponding to the $R(\theta)$ plot to exhibit the singlet peak with various r values (0, -0.05, -0.1, -0.15, -0.2). Figure 3.17 (b) shows that R_1 and R_2 values are decreasing as the r value approaches zero. Herein, the negative sign of r is rationalized that r is related to the gradient in the polarizability about the oscillation at the equilibrium position in the normal coordinate, not the polarizability itself. As Jones *et al.* already noted [38], the symmetric *C-C* stretching in a benzene ring along the molecular axis may decrease polarizability along the axis perpendicular to molecular axis. Therefore, the derivatives of the polarizability with respect to normal coordinate can take either a positive or a negative sign.

We simulated the $R(\theta)$ plot by letting $\langle P_{400} \rangle = -0.0160$, the value obtained by the conventional method using only measured R_1 and R_2, and $r = 0$ in Eq. (3-4) and compared the simulated result with experimentally obtained 37 depolarization ratios and the fitting result to Eq. (3-4). Figure 3.17 (c) demonstrates that the combination of low $\langle P_{400} \rangle$ with $r = 0$ produces the similar value of R_1 and R_2 with those of 37 depolarization ratio profile at $T\text{-}T_{NI}$ = -0.7 ℃. Therefore, it implies that taking into consideration only the measured R_1 and R_2 and zero or low r values can lead to erroneous $\langle P_{400} \rangle$ values.

Finally, as shown in Figure 3.13, while the relations between $\langle P_{400} \rangle$ and $\langle P_{200} \rangle$ obtained from the 37 depolarization ratios deviate from the prediction of mean-field theory, the extent of deviation is smaller than those obtained from the conventional Raman approach. We speculate that the change in molecular packing density induced by thermal fluctuation, which was neglected in the Maier-Saupe theory, may be responsible for the slight deviation between experimental results and the theoretical prediction.

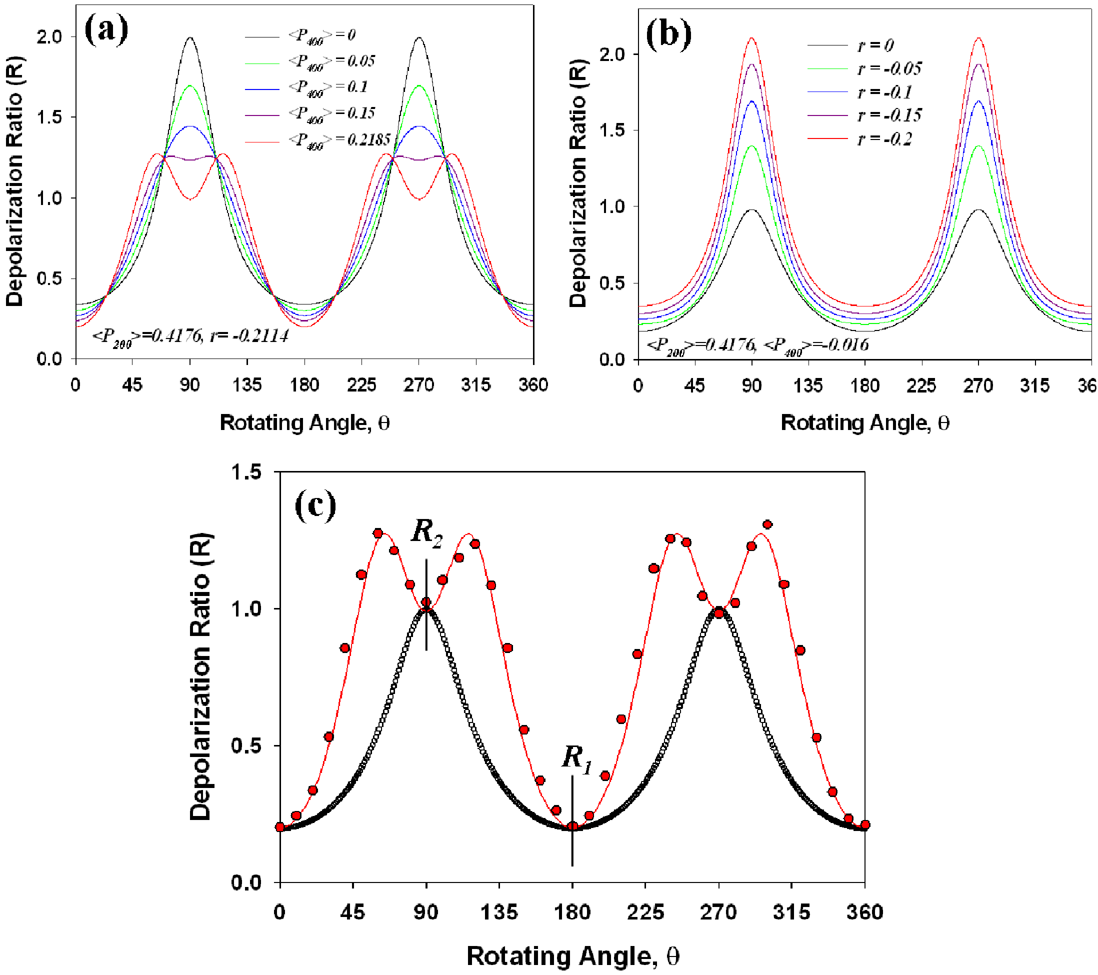

Figure 3.17 (a) Variations of $R(\theta)$ plots according to different $\langle P_{400}\rangle$ values with $\langle P_{200}\rangle = 0.4176$ and $r = -0.2114$. (b) Variations of $R(\theta)$ plots according to different r values with $\langle P_{200}\rangle = 0.4176$ and low $\langle P_{400}\rangle = -0.016$ on purpose. (c) Comparison of the $R(\theta)$ plot by applying $\langle P_{200}\rangle = 0.4176$, $\langle P_{400}\rangle = -0.016$, and $r = 0$ to Eq. (3-4) with the plots from experimentally measured data, (●) and fitting results of measured data to Eq. (3-4) (red solid curve).

3.5 Conclusions

The measurements over the complete range from $\theta = 0 \sim 360°$ provide more reliable information about the orientational distribution of scattering units than the Raman measurements at 3 selected configurations, *i.e.* $I_{ll}\left(\theta = 0°\right)$, $I_{ll}\left(\theta = 90°\right)$, and $I_{\perp}\left(\theta = 0°\right) = I_{\perp}\left(\theta = 90°\right)$ as the conventional Raman approach used. We have demonstrated that the method proposed by Jones *et al.* [37, 38] provides a sensitive criterion for the determination of the $\langle P_{400} \rangle$ of which inexplicably small values, or even negative values in the vicinity of T_{NI} have been a criticism about the conventional Raman approach established by Jen *et al.* [19]. Taking into consideration only a few depolarization ratios seems to be based on a problematic assumption of depolarization ratio distribution with respect to angle, θ. In addition, the assumption of zero or constant $r = \frac{\partial \alpha'_{yy}}{\partial \alpha'_{zz}}$ value also caused erroneous results. Therefore, the method proposed by Jones *et al.* and we adopted is reliable and applicable to quantify the orientation degree for systems possessing orientational order.

3.6 References

[1] Witten, T. A. “Insights from soft condensed matter” *Reviews of Modern Physics*, **71**, 367-373 (1999).

[2] Daoud, M.; Williams, C. E., Eds., *Soft Matter Physics*. Berlin: Springer, pp. 289-314, 1999.

[3] Jones, R. A. L. *Soft Condensed Matter*. Oxford: Oxford University Press, pp. 104-126, 2004.

[4] de Gennes, P. G. “Soft Matter” *Nobel Lecture*,1991.

[5] Collings, P. J.; Hird, M. *Introduction to liquid crystals chemistry and physics*. New Yokr: Taylor & Francis, pp. 1-79, 1997.

[6] de Gennes, P. G.; Prost, J. *The Physics of Liquid Crystals*, 2nd ed. Oxford: Clarendon Press, Chapter 1-3, 1993.

[7] Stephen, M. J.; Straley, J. P. “Physics of liquid-crystals” *Reviews of Modern Physics*, **46**, 617-704 (1974).

[8] de Gennes, P. G. “Phenomenology of short-range-order effects in isotropic phase of nematic materials” *Physics Letters A*, **A 30**, 454-455, (1969).

[9] Zeminder, A. K.; Paul, S.; Paul, R. “Refractive-indexes and orientational order parameter of 5 liquid-crystals in nematic phase” *Molecular Crystals and Liquid Crystals*, **61**, 191-205 (1980).

[10] Chirtoc, I.; Chirtoc, M.; Glorieux, C.; Thoen, J. “Determination of the order parameter and its critical exponent for nCB (n=5-8) liquid crystals from refractive index data” *Liquid Crystals*, **31**, 229-240 (2004).

[11] Emsley, J. W.; Luckhurst, G. R.; Stockley, C. P. “The deuterium and proton-(deuterium) NMR-spectra of the partially deuteriated nematic liquid-crystal 4-n-pentyl-4’-cyanobiphenyl” *Molecular Physics*, **44**, 565-580 (1981).

[12] Emsley, J. W.; Hamilton, K.; Luckhurst, G. R.; Sundholm, F.; Timimi, B. A.; Turner, D. L. “Orientational order in the nematic phase of 4-methyl-4’-cyanobiphenyl- A deuterium NMR-study” *Chemical Physics Letters,* **104**, 136-142 (1984).

[13] Ceasar, G. P.; Levenson, R. A.; Gray, H. B. “Polarized infrared spectroscopy of molecules oriented in a nematic liquid crystal. Application to MN2(CO)10 and RE2(CO)10” *Journal of the American Chemical Society,* **91**, 772-774 (1969).

[14] Leadbetter, A. J.; Norris, E. K. “Distribution functions in 3 liquid-crystals from x-ray-diffraction measurements” *Molecular Physics,* **38**, 669-686 (1979).

[15] Davidson, P.; Petermann, D.; Levelut, A. M. “The measurements of the nematic order-parameter by x-ray-scattering reconsidered” *Journal De Physique Ii,* **5**, 113-131 (1995).

[16] Richardson, R. M.; Allman, J. M.; McIntyre, G. J. “Neutron-scattering from mixtures of isotropically labeled molecules. A new method for determining the orientational distribution function in liquid-crystals” *Liquid Crystals,* **7**, 701-719 (1990).

[17] Date, R. W.; Hamley, I. W.; Luckhurst, G. R.; Seddon, J. M.; Richardson, R. M. “Orientational ordering in liquid-crystals - Isotope labeling neutron-diffraction experiments” *Molecular Physics,* **76**, 951-977 (1992).

[18] Deutsch, M. “Orientational order determination in liquid-crystals by x-ray-diffraction” *Physical Review A,* **44**, 8264-8270 (1991).

[19] Jen, S.; Clark, N. A.; Pershan, P. S.; Priestley, E. B. “Raman scattering from a nematic liquid crystal: Orientational statistics” *Physical Review Letters,* **31**, 1552-1556 (1973).

[20] Priestley. E. B.; Pershan, P. S. “Investigation of nematic ordering using Raman-scattering” *Molecular Crystals and Liquid Crystals,* **23**, 369-373, (1973).

[21] Madusudana, N. V.; Shashidhar, R.; Chandrasekhar, S. “Orientational order in anisaldazine in nematic phase” *Molecular Crystals and Liquid Crystals,* **13**, 61-67 (1971).

[22] Haller, I. “Elastic constants of nematic liquid crystalline phase of para. Methoxybenzylidene-p-n-butylaniline (MBBA)” *Journal of Chemical Physics,* **57**, 1400-405 (1972).

[23] Sigaud, G.; Gasparou. H. “Compared magnetic properties of para-(para'-methoxybenzylidene) amino-butyl benzene (MBBA) showing different temperatures for nematic phase-isotropic phase-transition” *Journal De Chimie Physique Et De Physico-Chimie Biologique,* **70**, 699-700 (1973).

[24] Maier, W.; Saupe, A. “Eine einfache molekulare theorie des nematischen kristallinflussigen zustandes’’ *Zeitschrift Fur Naturforschung Part a-Astrophysik Physik Und Physikalische Chemie,* **13**, 564-566 (1958); “Eine einfache molekular-statistische theorie der nematischen kristallinflussigen phase’’ *Zeitschrift Fur Naturforschung Part a-Astrophysik Physik Und Physikalische Chemie,* **14**, 882-889 (1959).

[25] Humphries, R. L.; James, P. G.; Luckhurst. G. R. “Molecular field treatment of nematic liquid-crystals” *Journal of the Chemical Society-Faraday Transactions Ii,* **68**, 1031-1044 (1972).

[26] Miyano, K. “Raman depolarization ratios and order parameters of a nematic liquid-crystal” *Journal of Chemical Physics,* **69**, 4807-4813 (1978).

[27] Sidir, M.; Farhi, R. “On the determination of orientational order parameters in liquid-crystals from Raman scattering - CB9 revisited” *Liquid Crystals,* **19**, 573-579 (1995).

[28] Priestley, E. B.; J., W. P.; Sheng, P., Eds., *Introduction to Liquid Crystals*. New York: Plenum Press, Chapter 1, 3, 4, and 6, 1974.

[29] Jen, S.; Clark, N. A.; Pershan, P. S.; Priestley, E. B. “Polarized Raman scattering studies of orientational order in uniaxial liquid-crystalline phases” *Journal of Chemical Physics,* **66**, 4635-4661 (1977).

[30] Luckhurst, G. R.; Viloria, F. R. “The relationship between the 2nd and 4th rank order parameters for liquid-crystals composed of non-rigid molecules” *Molecular Crystals and Liquid Crystals,***72**, 201-209 (1982).

[31] Luckhurst, G. R.; Yeates, R. N. “Orientational order of a spin probe dissolved in nematic liquid-crystals – electron resonance investigation” *Journal of the Chemical Society-Faraday Transactions Ii*, **72**, 996-1009 (1976).

[32] Hamley, I. W.; Garnett, S.; Luckhurst, G. R.; Roskilly, S. J.; Pedersen, J. S.; Richardson, R. M.; Seddon, J. M. “Orientational ordering in the nematic phase of a thermotropic liquid crystal: A small angle neutron scattering study” *Journal of Chemical Physics*, **104**, 10046-10054 (1996).

[33] Bhattacharjee, B.; Paul, S.; Paul, R. “Order parameter and the orientational distribution function for 4-cyanophenyl-4’-n-heptyl benzoate in the nematic phase” *Molecular Physics*, **44**, 1391-1398 (1981).

[34] Prasad, S. N.; Venugopalan, S. “Molecular flexibility and orientational statistics of liquid-crystals – Raman study of 7-CB and 8-OCB” *Journal of Chemical Physics*, **75**, 3033-3036 (1981).

[35] Constant, M.; Decoster, D. “Raman scattering investigation of nematic and smectic ordering” *Journal of Chemical Physics*, **76**, 1708-1711 (1982).

[36] Dalmolen, L. G. P.; Dejeu, W. H. “Order parameters of some nematic para, para’ substituted tolanes as determined by polarized Raman scattering” *Journal of Chemical Physics*, **78**, 7353-7361 (1983).

[37] Jones, W. J.; Thomas, D. K.; Thomas, D. W.; Williams, G. “Raman scattering studies of homogeneous and twisted-nematic liquid crystal cells and the determination of < P2 > and < P4 > order parameters” *Journal of Molecular Structure*, **614**, 75-85 (2002).

[38] W. J. Jones, *et al.*, “On the determination of order parameters for homogeneous and twisted nematic liquid crystals from Raman spectroscopy” *Journal of Molecular Structure*, **708**, 145-163 (2004).

[39] Southern, C. D.; Gleeson, H. F. “Using the full Raman depolarisation in the determination of the order parameters in liquid crystal systems” *European Physical Journal E*, **24**, 119-127 (2007).

[40] Amer, M. S. *Raman sepctroscopy for soft matter applications*. New Jersey: John Wiley & Sons. Inc., pp. 33-62 and references therein, 2009.

[41] Bahadur, B. *Liquid Crystals: Applications and Uses*. Singapore: World Scientific, pp. 14-35, 1996.

[42] Denolf, K.; Cordoyiannis, G.; Glorieux, C.; Thoen, J. “Effect of nonmesogenic impurities on the liquid crystalline phase transitions of octylcyanobiphenyl” *Physical Review E,* **76**, 051702 (2007).

[43] Lin-Vien, D.; Colthup, N. B.; Fateley, W. G.; Grasselli, J. G. *The Handbook of Infrared and Raman Characteristic Frequencies of Organic Molecules*. San Diego: Academic Press, pp. 277-291, 1991.

[44] Sindhu, P. S. *Fundamentals of Molecular Spectroscopy*. Delhi: New Age International Ltd., Publishers, pp. 153-175, 2006.

[45] Park, M. S.; Wong, Y. S.; Park, J. O.; Venkatraman, S. S.; Srinivasarao, M. “A simple mMethod for obtaining the information of orientation distribution using polarized Raman spectroscopy: Orientation study of structural units in poly(lactic acid)” *Macromolecules,* **44**, 2120-2131 (2011).

[46] Cladis, P. E.; Palffy-Muhoray, Eds., *Dynamics and Defects in Liquid Crystals: A Festschrift in Honer of Alfred Saupe*. Amsterdam: Gordon and Breach Science Publishers, p 149, 1998.

[47] Haller, I. “Thermodynamic and static properties of liquid crystals” *Progress in Solid State Chemistry,* **10**, 103-118 (1975).

[48] Wu, S. T. “Infrared markers for determining the order parameters of uniaxial liquid-crystals” *Applied Optics,* **26**, 3434-3440 (1987)

CHAPTER 4

RAMAN SCATTERING STUDY OF PHASE BIAXIALITY IN A THERMOTROPIC BENT-CORE NEMATIC LIQUID CRSYTAL

4.1 Introduction

4.1.1 What is a Biaxial Nematic (N_b) Phase?

The term "*biaxial*" stems from optics and strictly indicates that there are two principle optic axes, whereas "*uniaxial*" crystals have only one direction along which a plane polarized light beam can travel with the state unchanged [1], defined as *optic axis*. In liquid crystals, the terms of '*uniaxial*' and '*biaxial*' embrace the symmetry of anisotropy in various phenomenological quantities such as electric/magnetic susceptibility, as well as optical anisotropy, which originate from anisotropic ordering of components in the liquid crystalline phases.

While the shape of molecules composing conventional nematic phase are usually not strictly axisymmetric but show slight asymmetry, the asymmetry of molecular shape is averaged out by the rotations of the molecules about their molecular axis in uniaxial nematic ($\boldsymbol{N_u}$) phase, resulting in the rotational symmetry ($D_{\infty h}$) about the director $\boldsymbol{n}$. In some nematics, however, the rotational freedom along the director $\boldsymbol{n}$ is restricted and the continuous rotational symmetry about director $\boldsymbol{n}$ is broken, which gives rise to additional orientational order along the second director $\boldsymbol{m}$ mutually perpendicular to $\boldsymbol{n}$ (Figure 4.1). This is referred to as "*biaxial orientation*". A nematic phase that exhibits biaxial orientation of molecules is "*biaxial nematic (N_b) phase*" and possesses reduced symmetry (D_{2h}). In other words, the molecules in the $\boldsymbol{N_u}$ phase are rotationally disordered along the director $\boldsymbol{n}$ whereas in the $\boldsymbol{N_b}$ phase, molecules possess preferred direction about this rotation.

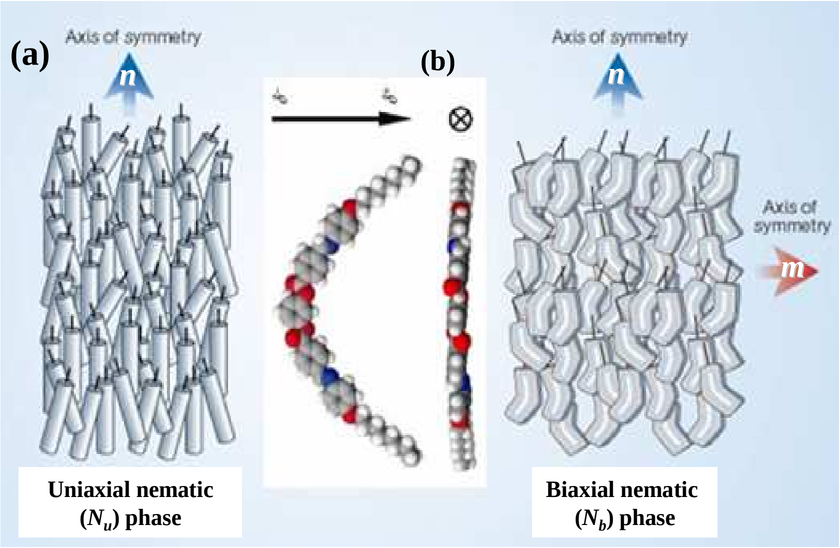

Figure 4.1 Left: uniaxial nematic phase in which the molecules line up along a single axis (axis of symmetry, ***n***). Right: the molecules align along the primary symmetry axis (***n***) and along another axis of symmetry (***m***) perpendicular to the primary one. [Reprinted from ref. [2] with permission]

4.1.2 Researches on a Biaxial Nematic Phase in a Thermotropic System

The biaxial nematic, N_b, phase has been one of the most elusive liquid crystalline phases since its prediction by Freiser [3] in 1970 based on his generalization of the Maier-Saupe model [4] of the N_u phase. This prediction was followed by a number of important microscopic [5-7] and phenomenological models [8-10], and by simulations [11] which yield interesting phase diagrams with one biaxial nematic, N_b, phase and two (prolate and oblate) uniaxial nematic, $N_u^-/\ N_u^+$ (or, $N_u^{\pm})_u$, phases. In the microscopic models, the biaxiality was either due to molecular shape biaxiality [5-7] or a consequence of mixing rod-like and plate-like objects [6]. The transitions between the isotropic (I) and the $N_u^-/\ N_u^+$ (or, $N_u^{\pm}$) phases are predicted to be first order while the transitions from the $N_u^{\pm}$ to the N_b phase form lines of second order transitions.

Encouraged by the success of the work of Saupe and coworkers in discovering the N_b phase in a lyotropic liquid crystalline system [12], several attempts were made to verify its existence in thermotropic systems [13-15], which were proved unsuccessful [16]. However, recent discoveries of the $\boldsymbol{N_b}$ phase using x-ray diffraction [17] and NMR [2] have rekindled the scientific interest in nematic biaxiality. These discoveries have inspired theorists [18, 19] as well as experimentalists [20-23] to inquire into the physics of this hitherto elusive but scientifically interesting phase. At the transition to the $\boldsymbol{N_b}$ phase, the growth of (biaxial) orientational order in a direction perpendicular to director $\boldsymbol{n}$ occurs, which results in a rich phenomenology. A good understanding of the origin of such compelling phenomena is, however, still in an early state of development. Therefore, comprehensive information on the thermodynamic properties, the rheological behavior, and aligning properties need to be accumulated. From this point of view, exploring the degrees of orientational order and its evolution as a function of temperature in a biaxial nematic phase is definitely an essential step toward understanding their rich phenomenology since the distinct behaviors of molecular orientation lies at the root of unique phenomenology in $\boldsymbol{N_b}$ phase.

In this chapter, we report the results of Raman scattering study of thermal evolution of orientational order of bent-core compound that has been reported to possess both $\boldsymbol{N_u}$ and $\boldsymbol{N_b}$ phases, thereby permitting measurements of thermal evolution of distinct orientation modes associated with the uniaxial and biaxial orientational order parameters. The valuable information presented here will help explain the phase biaxiality and dynamics of thermotropic biaxial nematic liquid crystals.

4.2 Experiments

4.2.1 Sample Preparation and Raman Measurements

An achiral bent-core mesogen, 4-((4-dodecylphenyl)diazenyl)phenyl 2-methyl-3-(4-(4-octylbenzoyloxy)benzylideneamino)benzoate (A131) was synthesized [24] and provided by our collaborator (Prof. Satyendra Kumar at Kent State University). Molecular structures, phase sequences, and transition temperatures for this compound (A131) are reprinted from ref. [25] in Figure 4.2.

A homogenously planar-aligned cell with 15 ㎛ spacer was obtained as described in the Experiments part of chapter 3. Since the melting point of A131 is much higher (82.8℃) than room temperature, we placed the crystallized powder of A131 in front of fill-hole of the assembled cell and heated over the nematic-isotropic transition temperature, T_{NI} + 5℃. We checked T_{NI} of A131 filled into the cell using optical microscope with crossed polarizations by slowly cooling down the temperature (0.2℃/min) until angular dependence of transmitted light intensity appeared, *i.e.*, the entrance into a nematic phase. T_{NI} of A131 in our sample was 176.1±0.3℃, which is almost identical to the transition temperature reported in ref. [25]. A sample of A131 was cooled down from T_{NI} + 5℃ through the nematic and into the smectic C phases (118.5℃). In order to determine the changes in the order parameters in the vicinity of the phase transition temperature ($\boldsymbol{N_u} \rightarrow \boldsymbol{N_b}$) reported in ref. [26], we especially recorded the anisotropy in polarized Raman intensities at small temperature intervals near the phase transition temperature.

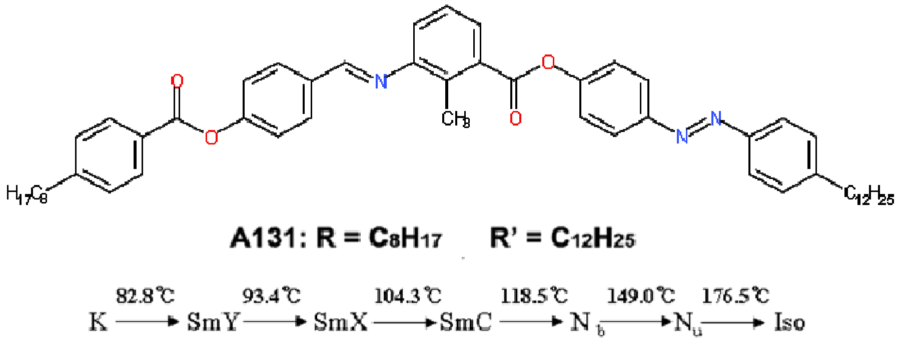

Figure 4.2 Molecular structure, phase, and transition temperatures for compound A131 [Reprinted from ref. [25] with permission].

The procedure for measuring the angular dependence of polarized Raman intensities is same as described in chapter 3. Figure 4.3 shows the polarized Raman spectrum $(I_{//})$ of A131 measured at $T = T_{NI} + 5$℃. In the spectrum, two strong Raman signals at 1141 cm^{-1} and 1460 cm^{-1} are thought to come from the asymmetric stretching of COC and $N{=}N$ stretching, respectively [27]. We used the most intense peak at 1141 cm^{-1} for calculating the orientational order parameter of A131. It is because Raman signal with strong Raman activity usually corresponds to internal vibrations of the mesogenic units, of which the symmetry of dipole moment is likely to be parallel to the long molecular axis, thus the assumption of collinearity of the principal axis of Raman tensor with the molecular axis is persuasive.

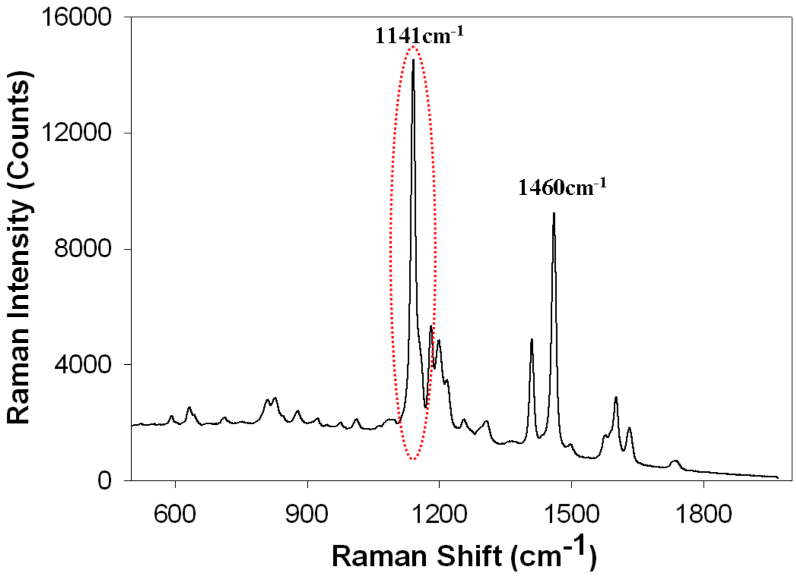

Figure 4.3 Polarized Raman spectrum ($I_{//}$) of A131 measured at T=T$_{NI}$+5℃ with $\theta = 0°$. Two strong peaks at 1141 *cm*$^{-1}$ and 1460 *cm*$^{-1}$ are attributed to asymmetric stretching of *COC* and *N=N* stretching mode, respectively [27].

4.2.2 Fitting Process

As described earlier, it is usually assumed that the Raman probe is axially symmetric. It should be noted that this does not necessarily mean that the molecular elements have an axial symmetry, while it does mean that a rotation about their long axis does not affect the orientational distribution function (ODF). Thus, one may assume a random rotation about the Euler angle, γ. There is, however, no reason to ignore α angle dependence of ODF (see Figure 4.4) unless the molecules possess cylindrical symmetry along director ***n***. Thus, we did take the α angle dependence into consideration on constructing the ODF and 5 orientational order parameters, $\langle P_{200} \rangle$, $\langle P_{400} \rangle$, $\langle P_{220} \rangle$, $\langle P_{420} \rangle$, and $\langle P_{440} \rangle$ were obtained by fitting measured depolarization ratios, $R(\theta)$ to Eq. (2-28). Note that the two parameters, $\langle P_{200} \rangle$ and $\langle P_{400} \rangle$, commonly recognized as the *uniaxial orientational order parameters*, provide information about the average orientation of molecules distributed along the *Z*-direction with dependence only on the angle, β. In contrast, $\langle P_{220} \rangle$, $\langle P_{420} \rangle$, and $\langle P_{440} \rangle$ characterize the symmetry breaking with respect to both α and β angle; thus nonzero values of these *biaxial orientational order parameters*, are indicative of the existence of biaxial symmetry (See Figure 4.4 for the experimental configuration).

It is necessary to note that the fitting procedure was carried out with some constraints. Since there are 6 fitting parameters in Eq. (2-28), 5 order parameters and $r = \alpha'_{yy} / \alpha'_{zz}$, on trying to get these values from fitting measured $R(\theta)$ to Eq. (2.28) at once, sometimes outrageous values, *e.g.*, $\langle P_{200} \rangle > 1$ were obtained. Thus, first we assumed that the biaxial terms are negligible in the estimation of the uniaxial order parameters and Raman tensor ratio, r, as the same manner of calculating uniaxial order parameters for conventional nematic LC in chapter 3. Based on these approximations, biaxial order terms play a role in a meticulous numerical fitting for maximum χ^2 value.

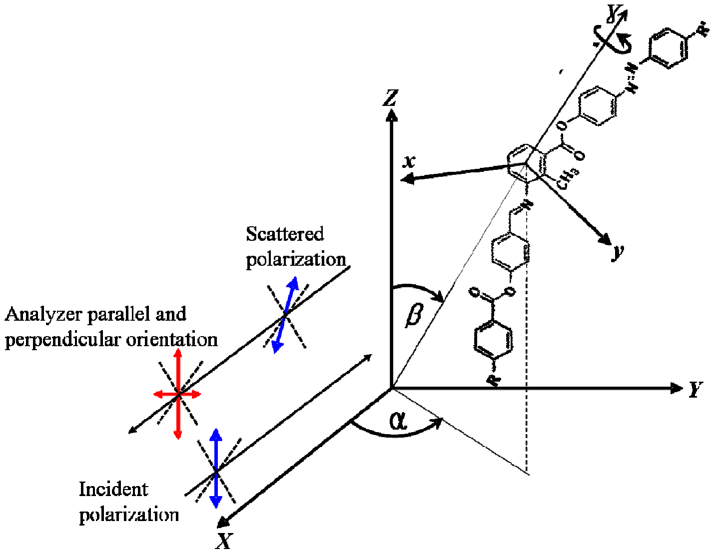

Figure 4.4 Euler angles α, β, γ are defined with molecular axes O-xyz in a macroscopic (laboratory) system of axes O-XYZ. The polarization of the Raman scattered light is resolved by the different direction of the analyzer [Reprinted from ref. [26] with permission].

4.3 Results

4.3.1 Uniaxial and Biaxial Orientational Order Parameters

Figure 4.5 is an example of experimental data set for $I_{//}(\theta)$, $I_{\perp}(\theta)$ and $R(\theta)$ of A131 sample. $I_{//}(\theta)$ and $I_{\perp}(\theta)$ are normalized to unity at the peak of $I_{//}(\theta = 0°)$. The pattern of twofold and fourfold rotational symmetry of $I_{//}(\theta)$ and $I_{\perp}(\theta)$ conforms to the trigonometric periodicities resulting from Eq. (3-5). From the results of numerical fitting to Eq. (2-28), we obtained 5 orientational order parameters. Figure 4.6 displays a plot of various order parameters as a function of reduced temperature (T/T_{NI} (K)), in which $\langle P_{200} \rangle$ and $\langle P_{400} \rangle$ values increase with decreasing temperature as expected and $\langle P_{400} \rangle$ values are positive in the entire range of the nematic phase. Two features need to be pointed out. First, the manner of order parameters evolving as a function of temperature looks quite different from that of conventional nematic LCs (5CB and 8CB) shown in Figure 3.11 (a) and 3.12 (a) in chapter 3. In order to compare the temperature dependence of $\langle P_{200} \rangle$ for A131, we fitted experimentally obtained $\langle P_{200} \rangle$ values to the Haller approximation [28], Eq. (3-6) (Figure 4.7). The result clearly shows that the thermal evolution of $\langle P_{200} \rangle$ follows the manner of conventional nematic LCs evolving up to about T/T_{NI}=0.9388 (T-T_{NI}= -27.5℃), and then starts to deviate from the theoretical fitting curve of Eq. (3-6). Another interesting observation is that the value of $\langle P_{200} \rangle$(~0.275) in A131 at very close to T_{NI} is smaller than the measured values of conventional nematic LCs (0.35~0.37).

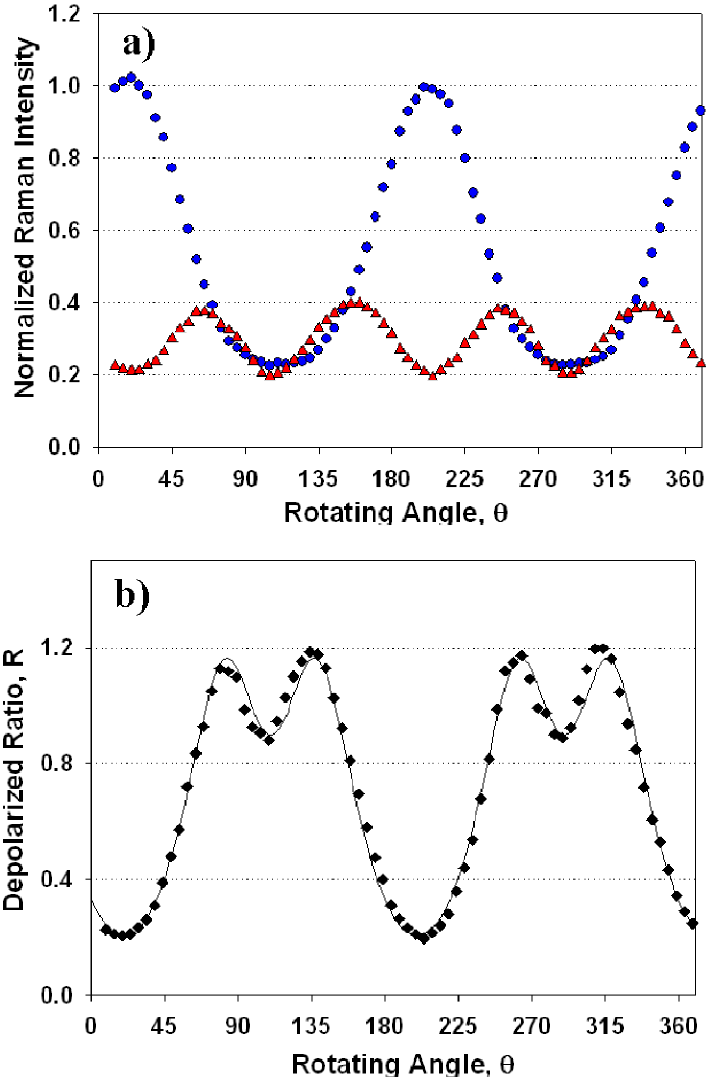

Figure 4.5 (a) Polarized (●) and depolarized (▲) Raman scattering intensity profiles for A131 at 166.5℃ and (b) the corresponding depolarization ratio profile; measured (◆) and theoretical fit (solid line) to Eq. (2-28). [Reprinted from ref. [26] with permission]

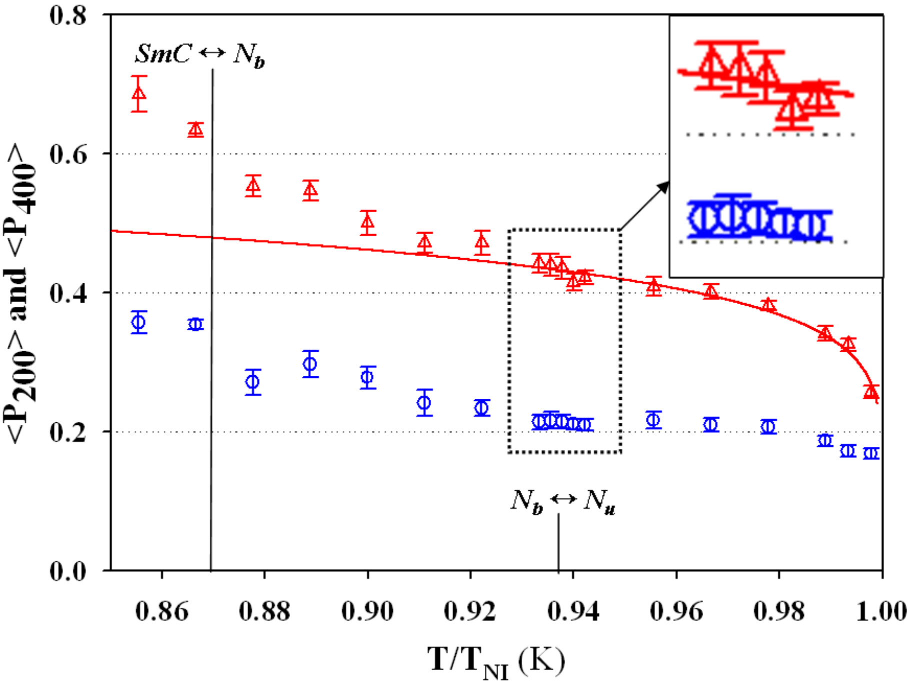

Figure 4.6 Temperature dependence of uniaxial order parameters; $\langle P_{200}\rangle$ (△) and $\langle P_{400}\rangle$ (○). Red solid line is the fitting of $\langle P_{200}\rangle$ values to Haller approximation, Eq. (3-6). Vertical solid line indicates temperatures of phase transitions (***N_u***↔***N_b*** and ***N_b***↔***SmC***) that is based on the result of ref. [25].

We also obtained 3 biaxial orientational order parameters, $\langle P_{220}\rangle$, $\langle P_{420}\rangle$, and $\langle P_{440}\rangle$ as a function of reduced temperature in Figure 4.7. From the plots of these biaxial terms, we can observe that the magnitude of biaxial orientational order parameters increase as temperature decreases. For comparison, we obtained biaxial order parameters for the conventional LCs (5CB and 8CB) with the same fitting procedure for deducing biaxial terms using Eq. (2-28) and obtained $\langle P_{220}\rangle$, $\langle P_{420}\rangle$, and $\langle P_{440}\rangle$ for 5CB and 8CB were too small to be meaningful (order of ~10^{-2}) as expected through the entire nematic range we measured. (see the values of $\langle P_{220}\rangle$ for 5CB and 8CB over the entire nematic ranges we measured in Figure 4.8). Thus, the gradual increase of the magnitude of biaxial order parameters of A131 indicates that A131 possesses a different orientation behavior in a nematic phase compared to the conventional nematic LCs, likely to have biaxial ordering in nematic phase.

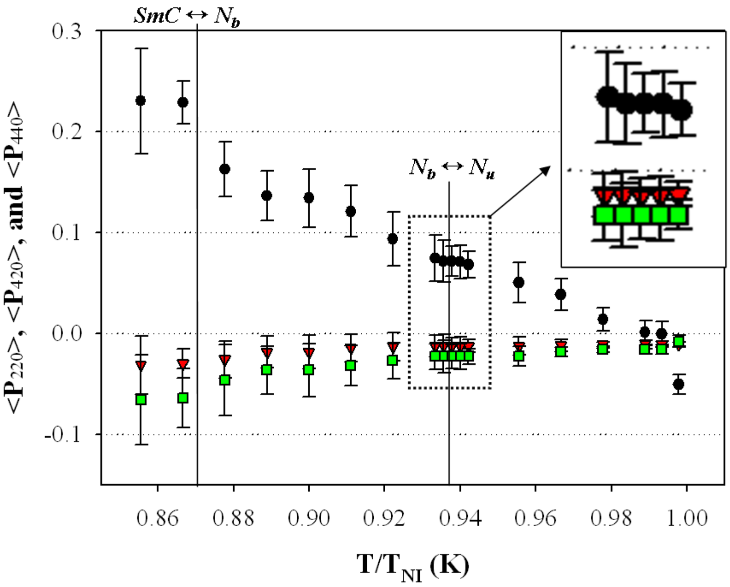

Figure 4.7 Temperature dependence of biaxial order parameters; $\langle P_{220} \rangle$ (●), $\langle P_{420} \rangle$ (▼), and $\langle P_{440} \rangle$ (■) obtained by fitting results. [Reprinted from ref. [26] with permission] Vertical solid line indicates temperatures of phase transitions (***$N_u \leftrightarrow N_b$*** and ***$N_b \leftrightarrow SmC$***) that is based on the result of ref. [25].

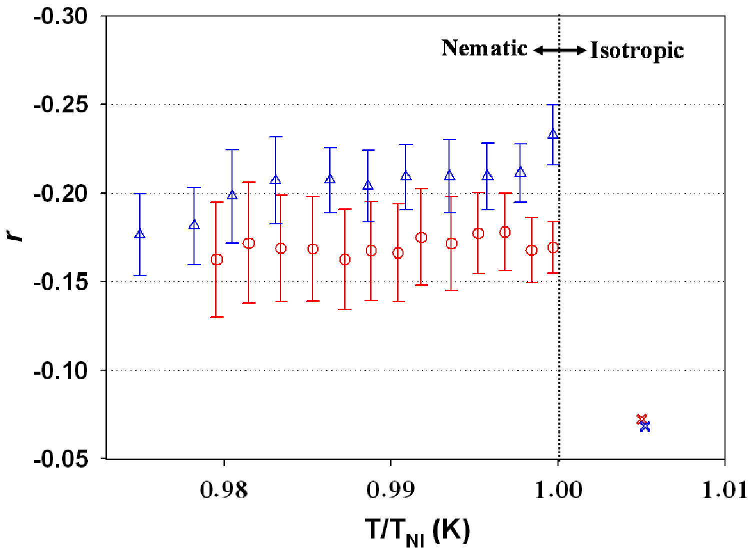

Figure 4.8 Temperature dependence of biaxial order parameters; $\langle P_{220} \rangle$ for 5CB (◆) and 8CB (▼) obtained by fitting results.

4.3.2 Construction of Orientational Distribution Function (ODF)

A conventional way to interpret these measured order parameters is to model their effect on the ODF. In order to construct ODF perfectly, however, it is necessary to be aware of all expansion coefficients in the equation of ODF (Eq. 2-20), but we obtained only 5 coefficients of the truncated function. One of the most common methods to construct ODF with a few expansion coefficients from the truncated ODF is "the most probable" approximation using maximum entropy theory [29]. Most probable ODF, $f_{mp}(\alpha,\beta)$ is described as [30]:

$$f_{mp}(\alpha,\beta) = A\exp(\omega_1 P_{200} + \omega_2 P_{220} + \omega_3 P_{400} + \omega_4 P_{420} + \omega_5 P_{440}) \qquad (4\text{-}1)$$

where A is normalized constant and ω_i are Lagrange multipliers.

$$A = 1 \Big/ \int_\alpha \int_\beta \exp(\omega_1 P_{200} + \omega_2 P_{220} + \omega_3 P_{400} + \omega_4 P_{420} + \omega_5 P_{440}) \sin\beta d\beta d\alpha \qquad (4\text{-}2)$$

It should be noted that we failed to obtain above 5 Lagrange multipliers. Lagrange multipliers associated to 4th rank order parameters, i.e., $\omega_3, \omega_4,$ and ω_5. Thus, we just used second rank order parameters, i.e., $\langle P_{200} \rangle$ and $\langle P_{220} \rangle$ to construct most probable ODF and the results at various temperatures are plotted in Figure 4.9.

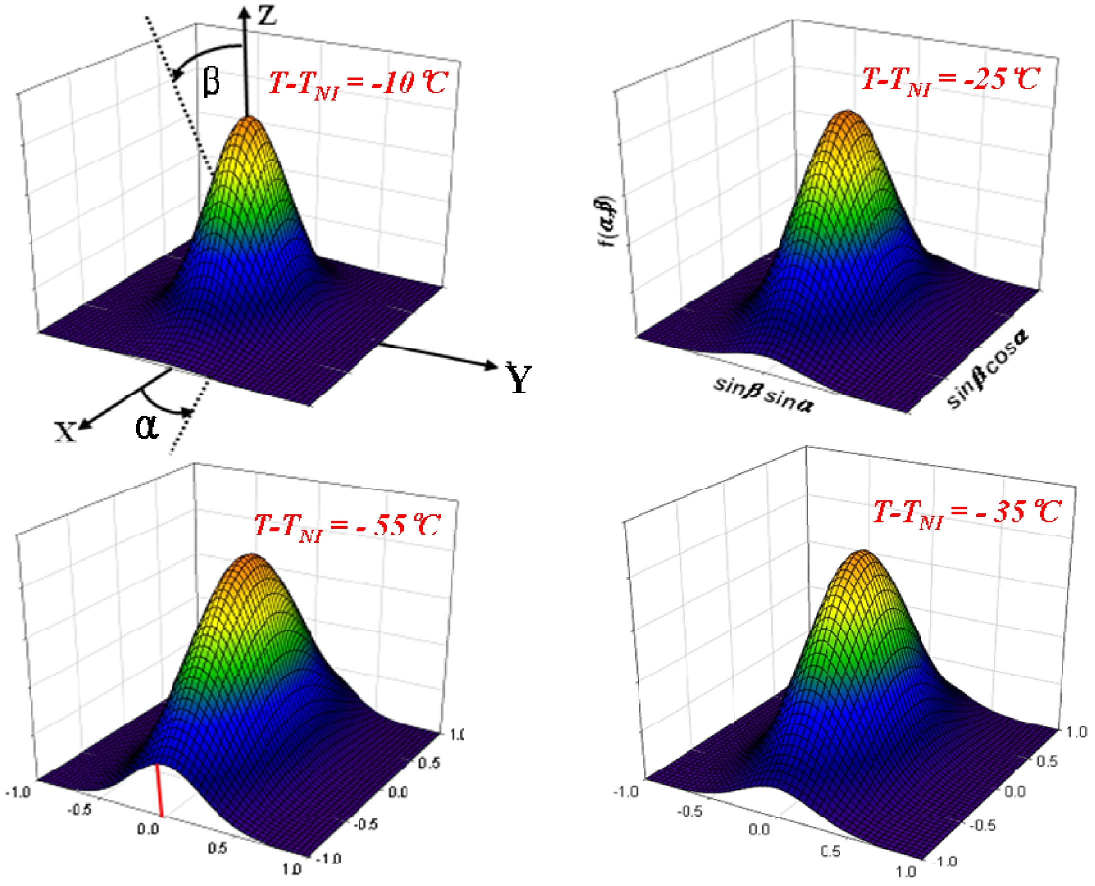

Figure 4.9 Distribution functions, $f_{mp}(\alpha,\beta)$ constructed with maximum entropy formalism, Eq. (4-1) from calculated second rank values, $\langle P_{200}\rangle$ and $\langle P_{220}\rangle$: (a) $\langle P_{200}\rangle$ = 0.381, $\langle P_{220}\rangle$ = 0.0138 at T-T_{NI} = -10℃ (T/T_{NI} = 0.9782), (b) $\langle P_{200}\rangle$ = 0.421, $\langle P_{220}\rangle$ = 0.068 at T-T_{NI} = -25℃ (T/T_{NI} = 0.9448), (c) $\langle P_{200}\rangle$ = 0.471, $\langle P_{220}\rangle$ = 0.0934 at T-T_{NI} = -35℃ (T/T_{NI} = 0.9926) , and (d) $\langle P_{200}\rangle$ = 0.553, $\langle P_{220}\rangle$ =0.1625 at T-T_{NI} = -55℃ (T/T_{NI} = 0.8781). The macroscopic axes X, Y, and Z are indicated as $\sin\beta\cos\alpha$, $\sin\beta\sin\alpha$, and normalized magnitude of $f_{mp}(\alpha,\beta)$, respectively.

4.4 Discussion

4.4.1 Physical Meaning of Non-zero Biaxial Order Parameters

The absolute limits for the 3 biaxial order parameters can be easily calculated, as was done by Javis *et al*. [31] and can be written as:

$$\begin{aligned} &\left|\langle P_{220}\rangle = \frac{1}{4}\left\langle\left(1-\cos^2\beta\right)\cos 2\alpha\right\rangle\right| \le \frac{1}{4} = 0.25 \\ &\left|\langle P_{420}\rangle = \frac{1}{24}\left\langle\left(-1+8\cos^2\beta-7\cos^4\beta\right)\cos 2\alpha\right\rangle\right| \le \frac{3}{56} = 0.0536 \\ &\left|\langle P_{440}\rangle = \frac{1}{16}\left\langle\left(1-2\cos^2\beta+\cos^4\beta\right)\cos 4\alpha\right\rangle\right| \le \frac{1}{16} = 0.0625 \end{aligned} \tag{4-3}$$

Among the biaxial orientational order parameters in Figure 4.7, especially $\langle P_{220}\rangle$ is the dominant biaxial term, of which the high value provides quantitative evidence that one of the molecular short axes is preferentially aligned perpendicular to the ZY plane. The orientation distributions with non-zero $\langle P_{220}\rangle$ values at various temperatures were visualized in Figure 4.9, in which the uniaxial symmetry of orientational distribution is gradually broken into biaxial shape as the magnitude of $\langle P_{220}\rangle$ continuously increases. While we just used the second rank order parameters to truncate most probable ODF, it is sufficient to show the broken symmetry of direction orientation.

The fourth rank order parameters, $\langle P_{420}\rangle$ and $\langle P_{440}\rangle$, have a more complicated physical interpretation. The observed negative values, in particular for $\langle P_{440}\rangle$, indicate that the direction of the molecular axis is projected onto the *XY* plane at approximately $\pm 45°$ to the *X* or *Y* axis, rather than collinear with them, since the value of $\left(1-2\cos^2\beta+\cos^4\beta\right)$ is positive for all β. From the result that biaxial order parameters for conventional nematic LCs (5CB and 8CB) were almost zero over the entire nematic range, the gradual increase of magnitude of biaxial order parameters indicates that A131 possesses an orientation behavior quite distinct from those of conventional LCs in a nematic phase. It is worth noting that our results for the biaxial terms, displayed in Figure 4.7, lie well within the absolute limits of the values throughout the temperature range studied, while some previous reports show value beyond these limits [32, 33].

4.4.2 Transition between $\boldsymbol{N_u}$ *and* $\boldsymbol{N_b}$ *Phases and Fluctuation Behavior of A131*

Temperature dependence of orientational order parameters provides both qualitative and quantitative evidence of phase transitions. From the insets of Figure 4.6 and Figure 4.7, it is clear that an abrupt change in order parameters does not occur in the vicinity of transition ($\boldsymbol{N_u} \rightarrow \boldsymbol{N_b}$) temperature based on the result of ref. [26]. Should A131 undergo phase transition ($\boldsymbol{N_u} \rightarrow \boldsymbol{N_b}$) as reported in ref. [25], the continuity of thermal evolution of order parameters rules out a first order transition. However, there is a qualitative change in the temperature dependence of order parameters. Especially, the manner of $\langle P_{200} \rangle$ evolution as a function of temperature shows distinct orientational behavior of A131, which follows a universal function of T/T_{NI} (Haller approximation based on mean-field theory, Eq. (3-6)) until ca. $T/T_{NI} = 0.9388$ ($T\text{-}T_{NI}$=27.5℃), and then starts to deviate from this approximation. This deviation may be because biaxiality parameter was ignored in the mean-field theory [34] and thus the existence of biaxiality in a phase is likely to exhibit an unexpected behavior with temperatures.

Judging from the changes in the slope of $\langle P_{200} \rangle$ and non-zero values of biaxial order parameters, we conclude that the orientational behavior of A131 at $T/T_{NI} < 0.9388$ may differ from that at $T/T_{NI} > 0.9388$ in a uniaxial nematic phase of A131. Therefore, it may be an evidence of the phase transition between $\boldsymbol{N_u}$ and $\boldsymbol{N_b}$ phases. It should be noted that the distinction of temperature ranges by $T/T_{NI} = 0.9388$ is arbitrary in that physical quantities usually vary continuously for 2nd order transition and thus clear distinction between two phases is not easy. Interestingly, however, this temperature ($T/T_{NI} = 0.9388$) is quite similar to the transition ($\boldsymbol{N_u} \leftrightarrow \boldsymbol{N_b}$) temperature reported in ref. [25].

Recently, one group in the UK has raised issues [33] that the biaxial order parameters at $T/T_{NI} < 0.9388$ reported in ref. [26] should ideally vanish as it is a uniaxial nematic phase at $T/T_{NI} < 0.9388$. However, literature is replete with reports showing that molecular fluctuations in a phase affect the molecular orders in a sequent phase [35-37]. This has been attributed to "*pretransitional*" and "*field*" effects: (a) Pretransitional increase in the smectic order parameter was reported in many experiments including the pioneering work of McMillan [35], where the smectic order parameter has a finite value in the nematic phase and it leads to smectic order fluctuation. (b) Melnik *et al*. [36] reported a phase shift (proportional to biaxiality) in the $\boldsymbol{N_u}$ phase of a lyotropic system, whose magnitude depends on the applied magnetic field. Similarly, de Gennes [37] has shown that small values of the order parameter in the isotropic phase are observable under the influence of external fields. In our Raman experiments, the surfaces impose an orienting field on the order parameter fluctuations and it is quite possible that close to one such transition point of A131 will yield a finite value of the order parameter on the other side of the transition, which may be responsible for nonzero values of biaxial order parameter, though not significantly large.

This additional biaxial ordering fluctuations in the $\boldsymbol{N_u}$ phase may be responsible for smaller value of $\langle P_{200} \rangle$ of A131 close to T_{NI} than the common value of 0.35~0.4 for conventional uniaxial nematics. Hence, we compared the thermal fluctuations of A131 with those of conventional nematic LC (E7) close to their T_{NI} and observed much more pronounced fluctuations in the case of A131. This is consistent with the results of the study of the order parameter and director fluctuations by Olivares *et al*. [38], in which they revealed the evidence of weak biaxial fluctuation using polarized light scattering.

4.5 Conclusions

The quantitative and qualitative analyses of orientational order parameters in the nematic phase provides the evidence of different orientational behaviors of A131 in a nematic phase, which may support the existence of the biaxial nematic phase in A131 from ~27.5 to 58℃ below T_{NI} ($0.87<T/T_{NI}<0.9388$). We have demonstrated the power of the polarized Raman scattering technique in reliably measuring nematic order parameters and revealing their thermal evolution across the second order uniaxial to biaxial nematic phase transition. The technique and the results presented here have a significant impact on our ability to quantitatively understand orientational order in nematic fluids and test theoretical prediction of shear flow aligning behavior and calculations of viscosities and elastic constants [39, 40], the thermodynamic properties, and the rheological behavior of anisotropic fluids.

4.6 References

[1] Bloss, F. D. *Optical Crystallography,* Washington: Mineralogical Society of Amer, Chapter 6-7, 1999.

[2] Madsen, L. A.; Dingemans, T. J.; Nakata, M.; Samulski, E. T. “Thermotropic biaxial nematic liquid crystals” *Physical Review Letters,* **92**, 145505, (2004).

[3] M. J. Freiser, M. A. “Oordered states of a nematic liquid” *Physical Review Letters,* **24**, 1041-1043 (1970).

[4] Maier, W.; Saupe, A. “Eine einfache molekulare theorie des nematischen kristallinflussigen zustandes’’ *Zeitschrift Fur Naturforschung Part a-Astrophysik Physik Und Physikalische Chemie,* **13**, 564-566 (1958); “Eine einfache molekular-statistische theorie der nematischen kristallinflussigen phase’’ *Zeitschrift Fur Naturforschung Part a-Astrophysik Physik Und Physikalische Chemie,* **14**, 882-889 (1959).

[5] Alben, R. “Phase-transitions in a fluid of biaxial particles” *Physical Review Letters,* **30**, 778-781 (1973).

[6] Alben, R. “Liquid-crystal phase-transitions in mixtures of rodlike and platelike molecules” *Journal of Chemical Physics,* **59**, 4299-4304 (1973).

[7] Straley, J. P. “Ordered phases of a liquid of biaxial particles” *Physical Review A,* **10**, 1881-1887, 1974.

[8] Allender, D. W.; Lee, M. A.; Hafiz, N. “Landau theory of biaxial and uniaxial nematic liquid-crystals” *Molecular Crystals and Liquid Crystals,* **124**, pp. 45-52 (1985).

[9] Vissenberg, M.; Stallinga, S.; Vertogen, G. “Generalized Landau-de Gennes theory of uniaxial and biaxial nematic liquid crystals," *Physical Review E,* **55**, 4367-4377 (1997).

[10] Toledano, P.; Martins, O. G.; Neto, A. M. F. “Coupling between tilt and polar orders in liquid crystal phases formed from achiral bent shaped molecules” *Physical Review E,* **62**, 5143-5153 (2000).

[11] Frenkel, D.; Eppenga, R. “Monte-Carlo study of the isotropic-nematic transition in a fluid of thin hard disks” *Physical Review Letters,* **49**, 1089-1092 (1982).

[12] Yu, L. J.; Saupe, A. “Observation of a biaxial nematic phase in potassium laurate-1-decanol-water mixtures” *Physical Review Letters,* **45**, 1000-1003 (1980).

[13] Chandrasekhar, S.; Sadashiva, B. K.; Ratna, B. R.; Raja, V. N. “A biaxial nematic liquid-crystal” *Pramana,* **30**, L491-L494 (1988).

[14] Praefcke, K.; Kohne, B.; Singer, D.; Demus, D.; Pelzl, G.; Diele, S. “Liquid-crystalline compounds. 56. Thermotropic biaxial nematic phases with negative optical character” *Liquid Crystals,* **7**, 589-594 (1990).

[15] Chandrasekhar, S.; Nair, G. G.; Rao, D. S. S.; Prasad, S. K.; Praefcke, K.; Blunk, D. “Schlieren textures in free-standing nematic films: evidence of biaxiality” *Liquid Crystals,* **24**, 67-70 (1998).

[16] Luckhurst, G. R. “Biaxial nematic liquid crystals: fact or fiction?” *Thin Solid Films,* **393**, 40-52 (2001).

[17] Acharya, B. R.; Primak, A.; Kumar, S. “Biaxial nematic phase in bent-core thermotropic mesogens” *Physical Review Letters,* **92**, 145506 (2004).

[18] Longa, L.; Pajak, G. “Luckhurst-Romano model of thermotropic biaxial nematic phase” *Liquid Crystals,* **32**, 1409-1417 (2005).

[19] Allender, D.; Longa, L. “Landau-de Gennes theory of biaxial nematics reexamined” *Physical Review E,* **78**, 011704 (2008).

[20] Merkel, K.; Kocot, A.; Vij, J. K.; Korlacki, R.; Mehl, G. H.; Meyer, T. “Thermotropic biaxial nematic phase in liquid crystalline organo-siloxane tetrapodes” *Physical Review Letters,* **93**, 237801 (2004).

[21] Figueirinhas, J. L.; Cruz, C.; Filip, D.; Feio, G.; Ribeiro, A. C.; Frere, Y.; Meyer, T.; Mehl, G. H. “Deuterium NMR investigation of the biaxial nematic phase in an organosiloxane tetrapode” *Physical Review Letters,* **94**, 107802, (2005).

[22] Neupane, K.; Kang, S. W.; Sharma, S.; Carney, D.; Meyer, T.; Mehl, G. H.; Allender, D. W.; Kumar, S.; Sprunt, S. "Dynamic light scattering study of biaxial ordering in a thermotropic liquid crystal" *Physical Review Letters,* **97**, 207802 (2006).

[23] Dong, R. Y.; Kumar, S.; Prasad, V.; Zhang, J. "High nematic ordering in a bent-core smectogen showing a biaxial nematic phase: A C-13 NMR study" *Chemical Physics Letters,* **448**, 54-60 (2007).

[24] Prasad, V.; Kang, S. W.; Kumar, S., "Novel examples of achiral bent-core azo compounds exhibiting B-1 and anticlinic-antiferroelectric B-2 mesophases" *Journal of Materials Chemistry,* **13**, 1259-1264 (2003); Prasad, V.; Jakli, A. "Achiral bent-core azo compounds: observation of photoinduced effects in an antiferroelectric tilted smectic mesophase" *Liquid Crystals,* **31**, 473-479 (2004).

[25] Prasad, V.; Kang, S. W.; Suresh, K. A.; Joshi, L.; Wang, Q. B.; Kumar, S. "Thermotropic uniaxial and biaxial nematic and smectic phases in bent-core mesogens" *Journal of the American Chemical Society,* **127**, 17224-17227 (2005).

[26] Park, M. S.; Yoon, B. J.; Park, J. O.; Prasad, V.; Kumar, S.; Srinivasarao, M. "Raman scattering study of phase biaxiality in a thermotropic bent-core nematic liquid crystal" *Physical Review Letters,* **105**, 027801 (2010).

[27] Lin-Vien, D.; Colthup, N. B.; Fateley, W. G.; Grasselli, J. G. *The Handbook of Infrared and Raman Characteristic Frequencies of Organic Molecules*. San Diego: Academic Press, pp. 61-64, 1991.

[28] Haller, I. "Thermodynamic and static properties of liquid crystals" *Progress in Solid State Chemistry,* vol. 10, pp. 103-118, 1975.

[29] Mead, L. R.; Papanicolaou, N. "Maximum-entropy in the problem of moments" *Journal of Mathematical Physics,* **25**, 2404-2417 (1984).

[30] Bower, D. I. "Orientation distribution-functions for biaxially oriented polymers" *Polymer,* **23**, 1251-1255 (1982).

[31] Jarvis, D. A.; Hutchinson, I. J.; Bower, D. I.; Ward, I. M. "Characterization of biaxial orientation in poly(ethylene-terephthalate) by means of refractive-index measurements and Raman and infrared spectroscopies" *Polymer,* **21**, 41-54 (1980).

[32] Southern, C. D.; Brimicombe, P. D.; Siemianowski, S. D.; Jaradat, S.; Roberts, N.; Gortz, V.; Goodby, J. W.; Gleeson, H. F. “Thermotropic biaxial nematic order parameters and phase transitions deduced by Raman scattering” *Europhysics Letters*. **82**, 56001 (2008).

[33] Gleeson, H. F.; Brimicombe, P. D. “Comment on "Raman scattering study of phase biaxiality in a thermotropic bent-core nematic liquid crystal” *Physical Review Letters*, **107,** 109801 (2011).

[34] Cladis, P. E.; Palffy-Muhoray, P., Eds., *Dyanmics and Defects in Liquid Crystals: A Festschrift in Honor of Alfred Saupe*. Amsterdam: Gordon and Breach Science Publishers, pp. 141-149, 1998.

[35] McMillan, W. L. “X-ray scattering from liquid-crystals. 1. Cholesteryl nonanoate and myristate” *Physical Review a-General Physics,* **6**, 936-947 (1972).

[36] Melnik, G.; Photinos, P.; Saupe, A. “Critical properties of the uniaxial biaxial transition in micellar nematic phases” *Journal of Chemical Physics,* **88**, 4046-4051 (1988).

[37] de Gennes, P. G. “Phenomenology of short-range-order effects in isotropic phase of nematic materials” *Physics Letters A,* **A 30**, 454-455 (1969).

[38] Olivares, J. A.; Stojadinovic, S.; Dingemans, T.; Sprunt, S.; Jakli, A. “Optical studies of the nematic phase of an oxazole-derived bent-core liquid crystal” *Physical Review E,* **68**, 041704 (2003).

[39] Archer, L. A.; Larson, R. G. “A molecular theory of flow-alignment and tumbling in sheared nematic liquid-crystals” *Journal of Chemical Physics,* **103**, pp. 3108-3111 (1995).

[40] Fialkowski, M. “Viscous properties of nematic liquid crystals composed of biaxial molecules” *Physical Review E,* **58**, 1955-1966 (1998).

CHAPTER 5

PREDICTION OF FLOW ALIGNING PROPERTY IN LOW MOLECULAR NEMATIC LIQUID CRYSTALS BASED ON ORIENTATIONAL ORDER PARAMETERS

5.1 Introduction

5.1.1 Flow Alignment of Nematics

The behavior of nematic liquid crystals (LCs) in a shear flow exhibits complex flow properties due to the transient response of the director which strongly depends on the relative orientation of the director, the directions of the flow and the flow gradient relative to the nematic director [1-3]. Complexities of LCs in flow result in several instabilities [4-7] that are not only the unique interesting phenomena from a scientific viewpoint, but also critical for commercial applications, e.g., liquid crystal display (LCD) requiring the absence of instabilities resulting from filling LCs into the cell.

Two classes of behavior of nematic director have been classified to describe the influence of shear flow on the director response; "*Flow-aligning*" and "*Non-flow aligning*". The former is the ability for nematics to align in the shear plane (plane containing $\vec{v}$ and $\nabla\vec{v}$) with a specific angle known as *Leslie angle* [8] in the shear plane. (see the angle ς in Figure 5.1 (a)) On the other hand, non-flow aligning nematics have no preferred alignment angle, and the director experiences a viscous torque forcing it to rotate, leading a number of instabilities.

Since discontinuities in the director configuration typically cause a variety of instabilities such as irregular defects [9], much effort has been devoted to determine whether or not stable alignment exists in a shear flow both by experiments [7, 10-13] and by theoretical studies [3, 14, 15]. Knapp et al. [10, 11] and Srinivasarao and Berry [16], for instance, obtained information about two of the Leslie viscosity coefficients, α_2 and α_3 [2, 17] (see *Figure* 5.1 (b)), from viscosity measurements for low molecular nematic LCs and from rheo-optical studies for nematic liquid crystalline polymers, respectively. They interpreted their experimental observations in the framework of Ericksen-Leslie theory [18, 19].

Although extensive experimental studies for flow-aligning properties in a shear-flowing nematic LCs have been carried out [5, 13, 20-22], the flow-aligning properties of many nematic LCs are still unknown. As mentioned earlier, flow properties in a flowing nematic LC depends strongly on the orientation of the director, ***n***, the coupling between molecular orientation and flow behavior is quite attractive. In the following section, a simple molecular theory [23, 24] coupling the orientation degree of nematic LCs in equilibrium state with their flow properties will be introduced.

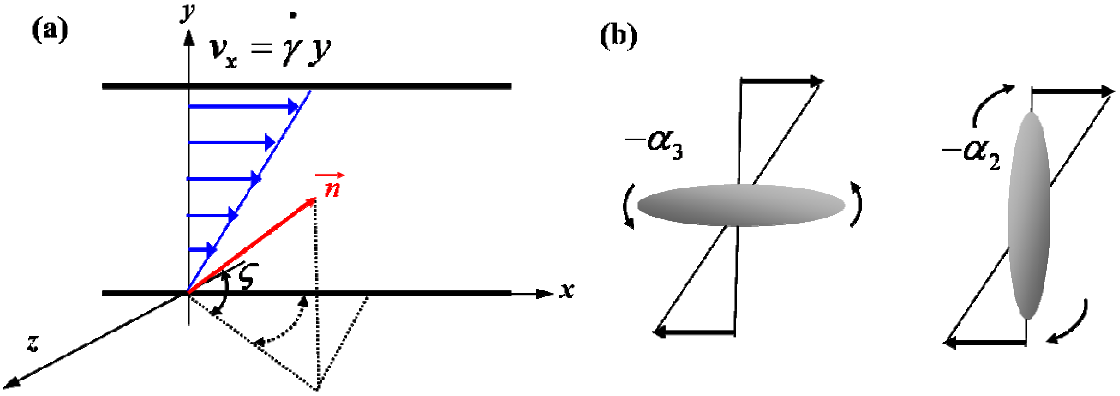

Figure 5.1 (a) Diagram showing directions of stable alignment of a flow-aligning nematic with flow-alignment angle θ in a steady shearing flow, with *x* the flow direction and *y* the velocity gradient direction. (b) The Leslie viscosities α_3 and α_2 determine the direction and rate of rotation of the director (represented by the cylinders) in the orientations shown. For negative values of α_3 and α_2, the rotation directions are shown by the arrows.

5.1.2 A Molecular Theory of Flow Alignment

In 1995, a simple mathematical approximation [23, 24] was derived to express the shear flow dynamics of low molecular nematic LCs based on Ericksen-Leslie continuum theory. It was proposed that the flow behavior can be more explicit from the measurement of $\langle P_{200} \rangle$ and $\langle P_{400} \rangle$, and effective aspect ratio of molecular shape, *p* as [23];

$$\xi = L(p)\frac{\left(5\langle P_{200}\rangle + 16\langle P_{400}\rangle + 14\right)}{35\langle P_{200}\rangle} \tag{5-1}$$

where $L(p) = {\left(p^2 - 1\right)} \big/ {\left(p^2 + 1\right)}$ and $\xi = {(\alpha_2 + \alpha_3)} \big/ {(\alpha_2 - \alpha_3)}$ is the so called *tumbling parameter*. When $|\xi| \geq 1$, the shear flow is stable with a finite Leslie angle, with no stable solution. When $|\xi| < 1$, in contrast, the director rotates in response to an imposed flow. The validity of this simple prediction was shown from the qualitative agreement between experimentally obtained ξ values for a few low molecular nematic LCs and the calculated values from the Eq. (5-1) using $\langle P_{200} \rangle$ and $\langle P_{400} \rangle$ values by Maier-Saupe theory [25] and using estimated *p* values based on the bond length and bond angle data. Despite the fact that a qualitative advance has been made, it has not been generalized for flow behavior of all nematic LCs according to the molecular theory from first principles in that the orientation behavior always depends on molecules building nematic phase, and the shape of composing molecules and their intermolecular interactions are different for each LC.

In this chapter, using measured values of $\langle P_{200} \rangle$ and $\langle P_{400} \rangle$, we compute the tumbling parameter, ξ, of two different low molecular weight nematic LCs studied in chapter 3, 4’-pentyl-4-cyanobiphenyl (5CB) and 4’-octyl-4-cyanobiphenyl (8CB). Based on the calculated ξ values, we predict the flow behavior of these LCs and compare it with the experimental results for 5CB and 8CB [10-13, 26-29]. In addition, an achiral bent-core azo compound, A131 [30], was also used to study the effect of molecular shape deviating from rod-type on the prediction results of ξ values.

5.2. Approach for Molecular Shape

The molecular shape was determined by calculating the principal axes of inertia through diagonalizing the moment of inertia tensor [31] by Dr. S. S. Jang and Dr. S. G. Lee at School of Materials Science and Engineering in Georgia Tech.

$$I = \begin{bmatrix} I_1 & 0 & 0 \\ 0 & I_2 & 0 \\ 0 & 0 & I_3 \end{bmatrix} \tag{5-2}$$

where I_1, I_2, I_3 are the components of the principal moment of inertia tensor, representing the three principal axes. Semi axes lengths of this equivalent ellipsoid are calculated in terms of principal moment of inertia tensor and the total mass of the object, m. Rotational center of the ellipsoid is the center of mass of the object.

Optimized structures of 5CB and 8CB are determined through the geometry optimization using Generalized Gradient Approximation (GGA) in the DMol3 [32], a modeling program using density functional theory (DFT) to simulate chemical processes and predict properties of materials, with the Perdew-Burke-Ernzerhof (PBE) function [33]. We used all electron Kohn-Sham wave functions and TNP (Triple Numerical plus Polarization) numerical basis sets with a polarization function on all atoms in DMol3 code for the spin-unrestricted DFT computation. Self-consistent field (SCF) convergence, 10^{-6} Ha (Hartree, $E_h = 27.2\ eV$) was used.

5.3 Results and Discussion

$\langle P_{200} \rangle$ and $\langle P_{400} \rangle$ values obtained for 5CB, 8CB and A131 in chapter 3 and 4 are tabulated (Table 5.1). Optimized structures and generated ellipsoids of 5CB and 8CB are shown in Figure 5.2. The conformation of the aliphatic chain is given by an all-*trans* Conformation. In our results, the inter-ring bond length between the phenyl rings and torsional angle between phenyl rings was 1.48Å and 32.27° obtained from the geometry optimization using DFT, respectively. These results were in agreement with the results for 5CB obtained by NMR [34]. Considering the rotational freedom in the nematic phase, we approximate that p value of 5CB and 8CB is 4.8 and 5.13, respectively. However, an aspect ratio, p of A131 was chosen as a variable rather than fixing it to be a constant due to the ambiguity in the shape and we applied various numbers of p (>4) to Eq. (5-1) to calculate ξ values. Estimates of the molecular aspect ratios of A131 result from bond length and bond angle data from DFT.

We predicted the flow behaviors of 3 different nematics: 5CB and 8CB in mostly ellipsoidal shape without/with a phase transition to smectic phase, respectively, and A131 in bent-core shape with a phase transition to smectic phase. Hence, we aim at exploring the effect of a phase transition to smectic phase and molecular shape on the predicted results of flow-alignment based on a molecular theory (Eq. 5-1).

Table 5.1 $\langle P_{200} \rangle$ and $\langle P_{400} \rangle$ values for 3 LCs (5CB, 8CB and A131) obtained from the measurement of polarized Raman intensities.

5CB			**8CB**			**A131**		
T_{NI}(K)	**$\langle P_{200} \rangle$**	**$\langle P_{400} \rangle$**	**T_{NI}(K)**	**$\langle P_{200} \rangle$**	**$\langle P_{400} \rangle$**	**T_{NI}(K)**	**$\langle P_{200} \rangle$**	**$\langle P_{400} \rangle$**
0.9997	0.3448	0.1844	0.9997	0.3514	0.1877	0.9978	0.2570	0.1681
0.9977	0.4176	0.2185	0.9984	0.3972	0.2183	0.9933	0.3250	0.1718
0.9958	0.4506	0.2257	0.9968	0.4590	0.2375	0.9889	0.3406	0.1864
0.9935	0.4806	0.2382	0.9952	0.5025	0.2449	0.9778	0.3810	0.2068
0.9909	0.4974	0.2483	0.9936	0.5425	0.2475	0.9666	0.4009	0.2092
0.9886	0.5188	0.2595	0.9918	0.5568	0.2483	0.9555	0.4089	0.2161
0.9863	0.5246	0.2779	0.9904	0.5695	0.2533	0.9422	0.4215	0.2096
0.9831	0.5382	0.2797	0.9888	0.5842	0.2588	0.9399	0.4250	0.2104
0.9805	0.5533	0.2940	0.9872	0.6088	0.2669	0.9377	0.4351	0.2135
0.9782	0.5582	0.2946	0.9853	0.6256	0.2813	0.9355	0.4397	0.2157
0.9750	0.5658	0.2959	0.9834	0.6415	0.2936	0.9333	0.4422	0.2135
0.9721	0.5698	0.2977	0.9815	0.6585	0.2938	0.9221	0.4717	0.2339
0.9691	0.5752	0.3002	0.9796	0.6685	0.2942	0.9110	0.4712	0.2407
			0.9773	0.7037	0.3049	0.8999	0.4998	0.2778
			0.9754	0.7085	0.3069	0.8888	0.5465	0.2967
						0.8776	0.5532	0.2708
						0.8665	0.6340	0.3538
						0.8554	0.6852	0.3567

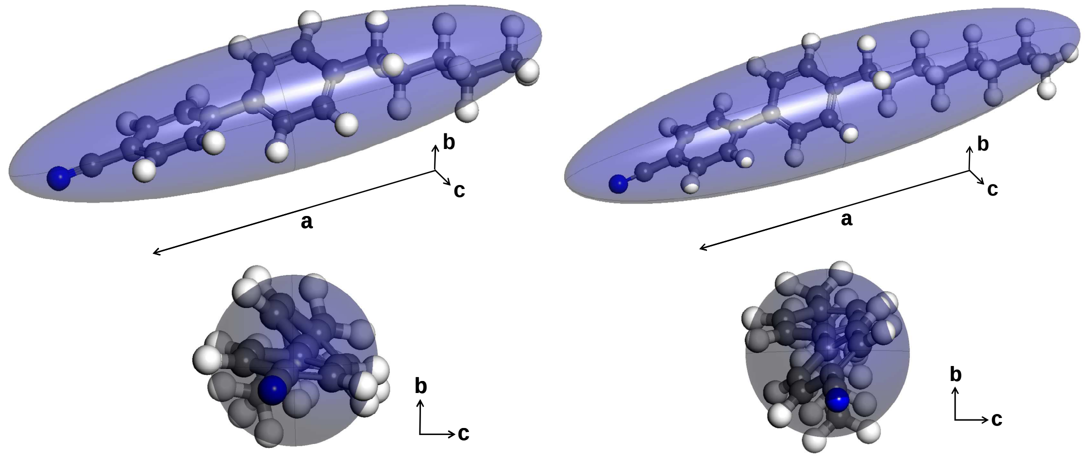

Figure 5.2 Optimized structures and generated ellipsoids of conventional nematic LCs: (a) 5CB with a/b/c=0.663/1.32/1.00 and (b) 8CB with a/b/c=7.38/1.44/1.

5.3.1 Effect of the Transition to Smectic Phase

From the measurements of $\langle P_{200} \rangle$ and $\langle P_{400} \rangle$ values using polarized Raman spectroscopy and p values, we quantified the tumbling parameter, ξ, using Eq. (5-1) as a function of T/T_{NI} (K) and made plots for 5CB and 8CB in Figure 5.3. The values of ξ is $\xi > 1$ for 5CB over the entire temperature measured, which indicates the director of 5CB tends to be stable at a flow-aligning angle in the shear plane under shear flow. This result is consistent with the experimental observations that 5CB has negative α_3, thus exhibiting flow-aligning tendency in the entire nematic range [10-12, 27].

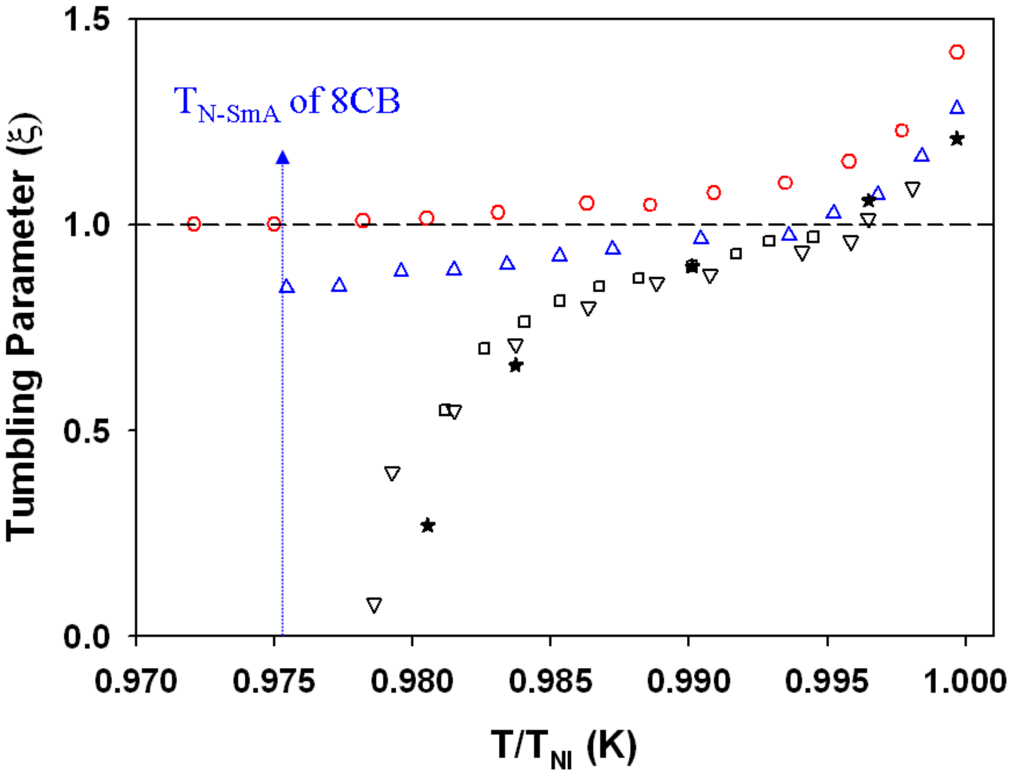

Figure 5.3 Evolution of tumbling parameter (ξ) of 5CB (○) (p=4.8), and 8CB (△) ★ (p=5.13) obtained from the measurements of $\langle P_{200} \rangle$ and $\langle P_{400} \rangle$ at various temperatures. Calculated ξ values of 8CB are compared to experimental results of ξ determined by the rheological method [29] (□), by obtaining Leslie viscosities by Gu and Jamieson [27] (▽), and by Kneppe et. al. [11] (★)

On the other hand, ξ for 8CB is tending towards values less than 1, with decreasing temperature, which implies that the director is predicted to undergo a transition from flow-aligning to non-flow aligning. Such a transition from flow-aligning to non-flow aligning was interpreted to imply that α_3 changes sign, becoming positive at a critical point and the director experiences a viscous torque tending to rotate it [10, 11, 27, 29]. This non-flow aligning behavior of 8CB subjected to torsional shearing flow was shown in rheological studies by Gu et al. [26, 27] and in microscopic visualization studies by Mather et al. [13, 20].

Unlike the case of 5CB, the plot of ξ for 8CB obtained from our calculation in Figure 5.3 clearly illustrates that ξ value of 8CB exhibits more than unity implying flow-aligning behavior at $T_{NI} > T > 38.5\text{C}^{o}$ (i.e., $0.9933 < T/T_{NI} < 1$), while it exhibit less than unity meaning a non-flow aligning nematic at temperatures below 38.5 C^{o}. The observation of ξ being less than unity at temperatures far from a nematic-smectic A phase transition point ($T_{N\text{-}SmA}$ = 33 C^{o}) can be interpreted by pretransitional effect [35]. Gahwiller [35] identified that not all nematics exhibit a stable shear flows, but the flow of nematics can turn abruptly from a uniform configuration to many irregular rotating domains even at temperatures far from a nematic-smectic phase transition. This drastic change of flow-aligning properties in 8CB has been reported and such behavior has been attributed to pretransitional smectic fluctuations [36] [29]. Another factor that we should consider is the possibility of form factor, *p,* being temperature dependent. We applied the form factor, *p*, for 8CB as a constant value so that *L*(*p*) was adopted as constant value through entire temperature of measurements. If the geometry of structure varies, however, L(*p*) should be temperature-dependent. Thus, one may obtain more realistic results with consideration of both pretransition effect and temperature-dependent *p* value on calculating tumbling parameter.

In an attempt to verify our result for 8CB, we re-plotted temperature dependences of ξ value obtained by the rheological method [29], and using the values of Leslie viscosities measured by Gu and Jamieson [27], and Kneppe et al. [11] (Figure 5.3). The critical point at which the transition between flow-aligning and non-flow aligning is predicted to take place in our result (*i.e.*, ca. T/T_{NI} =0.9933) is quite similar with those experimentally observed in previous literature [11, 27, 29]. Especially, the curve of ξ values in the range of $T/T_{NI} > 0.9933$ is in a good agreement with experimental results both qualitatively and quantitatively. At temperatures of $T/T_{NI} < 0.9933$, however, the temperature dependence of ξ from our results is quite different from the results in previous literature although all of them have ξ values less than unity indicating non-flow alignment in a shear flow. Based on the comparisons, a simple analytical expression of ξ appears valid for predicting flow-aligning property of rod-type nematics (5CB) or in a nematic region far from $T_{N\text{-}SmA}$ where pretransitional effect does not influence significantly ($T/T_{NI} > 0.9933$).

5.3.2 Effect of the Molecular Shape

Since it is not easy to define the form factor of bent-core molecules, we just applied possible p values from 4 ($L(p)$ = 0.88) to 10 ($L(p)$ = 0.9802) based on the geometry optimization to calculate λ values from measured $\langle P_{200} \rangle$ and $\langle P_{400} \rangle$ of A131. Temperature dependence of ξ for A131 in a nematic phase is plotted considering various aspect ratios in Figure 5.4. It is interesting that all ξ values are larger than unity when $p > 4$ over the entire temperature range in a nematic phase. While A131 possesses a nematic phase followed by a smectic phase with decreasing temperature as 8CB does, the temperature dependence of ξ of A131 is different from that of 8CB. From $\xi > 1$ in the entire nematic range (Figure 5.4), A131 is supposed to be a flow-aligning nematic LC. Should pretransition effect be universal phenomena in a nematic phase followed by smectic phases, there may be two plausible interpretations: (1) Pretransitional fluctuation of A131 in a nematic phase is not likely to affect the director rotation significantly. (2) Orientational order parameters, $\langle P_{200} \rangle$ and $\langle P_{400} \rangle$, that are obtained from the measurements of polarized Raman intensities at non-flowing state, may not reflect pretransitional fluctuations of orientation degree. If so, Eq. (5-1) may not be an appropriate method to represent flow-aligning behaviors of directors suffering from pretransitional fluctuation occurred in a shear flow using measured $\langle P_{200} \rangle$ and $\langle P_{400} \rangle$ values. A study of whether the orientation degree resulting from polarized Raman approach reflects the pretransition effect is required prior to conclude above interpretations, which will be future works to be done.

Nevertheless, we guess the possibility of the second scenario from the consideration of why temperature dependence of ξ values obtained from our Raman approach in Figure 5.3 quantitatively differ from those obtained by other experiments in literature [11, 27, 29] under T/T_{NI} = 0.9933. Since temperature dependence of ξ values in literature [11, 27, 29] is analogous to our result qualitatively and quantitatively until T/T_{NI} = 0.9933, it is likely that the orientation degree obtained from Raman approach is valid in predicting flow behavior at least in the nematic range far from $T_{N\text{-}SmA}$. However, it should be pointed out that discrepancy between ξ values from our results and those from other experimental observations becomes larger as temperature decreases under T/T_{NI} = 0.9933 at which pretransitional fluctuations were thought to influence dynamics of the director. Since pretransitional fluctuation is thought to increase as temperature decreases to $T_{N\text{-}SmA}$ [27, 29, 35, 36], it is rational to think that ξ values calculated using $\langle P_{200} \rangle$ and $\langle P_{400} \rangle$ obtained from Raman approach do not reflect pretransition effect sufficiently.

Due to the absence of experimental observations of flow behavior of A131, it remains to carry out the determination of whether the predicted flow behavior of A131 corresponds to real flow behavior under shear force for future efforts.

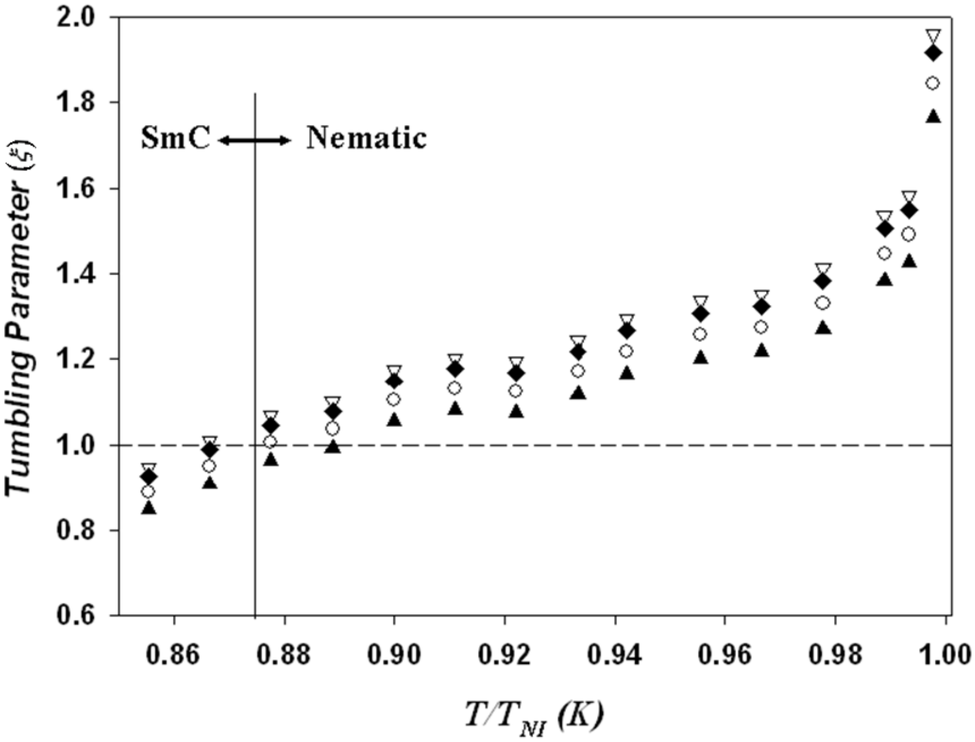

Figure 5.4 Temperature evolution of tumbling parameter of A131 with various possible aspect ratios: *p*=4 (▲), *p*=5 (○), *p*=7 (◆), and *p*=10(▽).

5.4 Conclusions

We predicted flow behaviors of low molecular thermotropic LCs in a nematic phase by means of thermal evolutions of tumbling parameter, ξ, calculated from $\langle P_{200} \rangle$ and $\langle P_{400} \rangle$ values at equilibrium state and molecular aspect ratio, *p*. A number of anisotropic data from polarized intensities facilitate accurate and reliable information about the degree of orientation in a nematic phase. From the result of $\xi > 1$ in the entire nematic range we measured, we predict the director alignment of 5CB in its nematic phase under shear flow, which is in an excellent agreement with experimental observations [10-13, 27]. In the case of 8CB possessing both a nematic and a smectic phase, judging from the evolution of ξ, a transition from flow-alignment to non-flow alignment of the director is predicted to occur at 38.5℃, and overall extend of flow-aligning behaviors qualitatively follow the way of experimental results in literature [11, 27, 29] . Thermal evolution of ξ between T_{NI} and 38.5℃ follows the experimental results both qualitatively and quantitatively, and then start to quantitatively deviate from experimental results as temperature decreases. Predicted results for A131 show a flow-alignment of the director in entire nematic phase and open questions about validity of a molecular theory to nematogens with a shape deviated from rod-type.

Although molecular theories valid for flow behaviors in nematic mixtures [37] or polymeric LCs [38] are not identical with that for a single component low molecular nematics, it is very possible in that dynamics of orientations in nematic phase is a key factor to explain hydrodynamics of LCs from a theoretical point of view. Thus, we expect a better representation of orientation change in nematic phase improves the accuracy of a molecular theory and provides a guide into how to tailor flow dynamics to suit shear processing for various nematic liquid crystalline materials.

5.5 References

[1] de Gennes, P. G.; Prost, J. *The Physics of Liquid Crystals*, 2nd ed. Oxford: Clarendon Press, pp. 198-255, 1993.

[2] Larson, R. G. *The Structure and Rheology of Complex Fluids*. New York: Oxford University Press, pp. 443-495, 1999.

[3] Rey, A. D.; Tsuji, T. "Recent advances in theoretical liquid crystal rheology" *Macromolecular Theory and Simulations,* **7**, 623-639 (1998).

[4] Pieranski, P.; Guyon, E. "Two Shear-Flow Regimes in Nematic p-n-Hexyloxybenzilidene-p'-aminobenzonitrile" *Physical Review Letters,* **32**, 924 (1974); "Instability of certain shear flows in nematic liquids" *Physical Review A,* **9**, 404-417 (1974).

[5] Cladis, P. E.; Torza, S. "Stability of nematic liquid-crystals in couette flow" *Physical Review Letters,* **35**, 1283-1286 (1975).

[6] Alderman, N. J.; Mackley, M. R. "Optical textures observed during the shearing of thermotropic liquid-crystal polymers" *Faraday Discussions,* **79**, 149-160 (1985).

[7] Larson, R. G.; Mead, D. W. "The Ericksen number and Deborah number cascades in sheared polymeric nematics" *Liquid Crystals,* **15**, 151-169 (1993).

[8] Leslie, F. M. "Theory of flow phenomena in liquid crystals" *Advances in Liquid Crystals,* **4**, 1 (1979).

[9] Kleman, M. "Defects in liquid-crystals" *Reports on Progress in Physics,* **52**, 555-654 (1989).

[10] Kneppe, H.; Schneider, F.; Sharma, N. K. "A Ccomparative study of the viscosity coefficients of some nematic liquid crystals" *Berichte Der Bunsen-Gesellschaft-Physical Chemistry Chemical Physics,* **85**, 784-789 (1981).

[11] Kneppe, H.; Schneider, F.; Sharma, N. K. "Rotational viscosity -gamma-1 of nematic liquid crystals" *Journal of Chemical Physics,* **77**, 3203-3208 (1982).

[12] Mather, P. T.; Pearson, D. S.; Larson, R. G. "Flow patterns and disclination-density measurements in sheared nematic liquid crystals .1. Flow-aligning 5CB" *Liquid Crystals,* **20**, 527-538 (1996).

[13] Mather, P. T.; Pearson, D. S.; Larson, R. G. “Flow patterns and disclination-density measurements in sheared nematic liquid crystals .2. Tumbling 8CB” *Liquid Crystals,* **20**, 539-546 (1996).

[14] Carlsson, T. “Theoretical investigation of the shear-flow of nematic liquid crystals with the Leslie viscosity alpha-3 greater than 0 – Hydrodynamic analog of 1st-order phase transitions” *Molecular Crystals and Liquid Crystals,* **104**, 307-334 (1984).

[15] Zuniga, I.; Leslie, F. M. “Shear-flow instabilities in non-flow-aligning nematic liquid crystals” *Liquid Crystals,* **5**, 725-734 (1989).

[16] Srinivasarao, M.; Berry, G. C. “Rheooptic studies on aligned nematic solutions of a rodlike polymer” *Journal of Rheology,* **35**, 379-397 (1991).

[17] Skarp, K.; Lagerwall, S. T.; Stebler, B. “Measurements of hydrodynamic parameters for nematic 5CB” *Molecular Crystals and Liquid Crystals,* **60**, 215-236 (1980).

[18] Ericksen, J. L. “Anisotropic fluids” *Archive for Rational Mechanics and Analysis,* **4**, 231-237 (1960).

[19] Leslie, F. M. “Some constitutive equations for anisotropic fluids” *Quarterly Journal of Mechanics and Applied Mathematics,* **19**, 357-370 (1966).

[20] Mather, P. T.; Pearson, D. S.; Larson, R. G.; Gu, D. F.; Jamieson, A. M. “The origin of stress-oscillation damping during start-up and reversal of torsional shearing of nematics” *Rheologica Acta,* **36**, 485-497 (1997).

[21] Pieransk.P; Guyon, E. “Instability of certain shear flows in nematic liquids” *Physical Review A,* **9**, 404-417 (1974).

[22] Carlsson, T.; Skarp, K. “Observation of the tumbling instability in torsional shear-flow of a nematic liquid crystal with $\alpha_3 > 1$” *Liquid Crystals,* **1**, 455-471 (1986).

[23] Archer, L. A.; Larson, R. G. *J.* “A molecular theory of flow-alignment and tumbling in sheared nematic liquid-crystals” *Journal of Chemical Physics,* **103**, 3108-3111 (1995).

[24] Kroger, M.; Sellers, H. S. “Viscosity coefficients for anisotropic, nematic fluids based on structural theories of suspensions” *Journal of Chemical Physics,* **103**, 807-817 (1995).

[25] Maier, W.; Saupe, A. “Eine Einfache Molekulare Theorie des Nematischen Kristallinfussigen Zustandes,“ *Zeitschrift Fur Naturforschung Part a-Astrophysik Physik Und Physikalische Chemie*, **13**, 564-566 (1958); “Eine Einfache Molekular-Statistische Theorie Der Nematischen Kristallinflussigen Phase .1,“ *Zeitschrift Fur Naturforschung Part a-Astrophysik Physik Und Physikalische Chemie,* **14**, 882-889 (1959); “Eine Einfache Molekular-Statistische Theorie Der Nematischen Kristallinflussigen Phase .2,“ *Zeitschrift Fur Naturforschung Part a-Astrophysik Physik Und Physikalische Chemie,* **15**, 287-292 (1960).

[26] Gu, D. F.; Jamieson, A. M.; Wang, S. Q. “Rheological characterization of director tumbling induced in a flow-aligning nematic solvent by dissolution of a side-chain liquid crystal polymer” *Journal of Rheology,* **37**, 985-1001 (1993).

[27] Gu, D. F.; Jamieson, A. M. “Shear deformation of homeotropic monodomains – Temperature-dependence of stress-response for flow-aligning and tumbling nematics” *Journal of Rheology,* **38**, 555-571 (1994).

[28] Han, W. H.; Rey, A. D. “Orientation symmetry breakings in shearing liquid crystals” *Physical Review E,* **50**, 1688-1691 (1994).

[29] Ternet, D. J.; Larson, R. G.; Leal, L. G. “Flow-aligning and tumbling in small-molecule liquid crystals: pure components and mixtures” *Rheologica Acta,* **38**, 183-197 (1999).

[30] Prasad, V.; Kang, S. W.; Suresh, K. A.; Joshi, L.; Wang, Q. B.; Kumar, S. “Thermotropic uniaxial and biaxial nematic and smectic phases in bent-core mesogens” *Journal of the American Chemical Society,* **127**, 17224-17227 (2005).

[31] Jang, S. S.; Jang, Y. H.; Kim, Y. H.; Goddard, W. A.; Choi, J. W.; Heath, J. R.; Laursen, B. W.; Flood, A. H.; Stoddart, J. F.; Norgaard, K.; Bjornholm, T. “Molecular dynamics simulation of amphiphilic bistable 2 rotaxane Langmuir monolayers at the air/water interface” *Journal of the American Chemical Society,* **127**, 14804-14816 (2005).

[32] Delley, B. “From molecules to solids with the DMol(3) approach” *Journal of Chemical Physics,* **113**, 7756-7764 (2000); “DMol(3) DFT studies: from molecules and molecular environments to surfaces and solids” *Computational Materials Science,* **17**, 122-126 (2000).

[33] Perdew, J. P.; Burke, K.; Ernzerhof, M. “Generalized gradient approximation made simple” *Physical Review Letters,* **77**, 3865-3868 (1996).

[34] Sinton, S.; Pines, A. “Study of liquid-crystal conformation by multiple quantum NMR - Normal-pentyl cyanobiphenyl” *Chemical Physics Letters,* **76**, 263-267 (1980).

[35] Gahwiller.C. “Temperature dependence of flow alignment in nematic liquid-crystals” *Physical Review Letters,* **28**, 1554-1556 (1972).

[36] Bruinsma, R. F.; Safinya, C. R. “Landau theory of the nematic smectic-A phase-transition under shear-flow” *Physical Review A,* **43**, 5377-5404 (1991).

[37] Rey, A. D. “Flow-alignment and viscosity rules for single-phase binary mesomorphic mixtures” *Liquid Crystals*, **20**, 147-159 (1996).

[38] Kuzuu, N.; Doi, M. “Constitutive equation for nematic liquid-crystals under weak velocity gradient derived from a molecular kinetic equation” *Journal of the Physical Society of Japan,* **52**, 3486-3494 (1983); “Constitutive equation for nematic liquid-crystals under weak velocity gradient derived from a molecular kinetic equation .2. Leslie coefficients for rodlike polymers” *Journal of the Physical Society of Japan,* **53**, 1031-1038 (1984).

CHAPTER 6

MOLECULAR ORIENTATION IN POLYMERS WITH COMPLEX STRUCTURES: STUDY OF STRUCTURAL UNITS IN POLY(LACTIC ACID)

6.1 Introduction

6.1.1 Molecular Orientation of Semi-crystalline Polymers

Molecular orientation plays a significant role in determining mechanical performance of processed polymer and fiber products. Since there is broad distribution of chain conformations, most ordered polymers exhibit semi-crystalline phases consisting of alternating crystalline and amorphous regions that respond differently at the structural level to macroscopic deformation. This difference in orientation behaviors of polymer chains between in crystalline and amorphous phase is critical in determining the final performance of products [1-3]. Therefore, characterization of orientation of polymer chains in crystalline and especially amorphous region is necessary so that physical properties of the products may be more fully understood and usefully modified.

While diffraction methods such as X-ray diffraction are capable of elucidating the crystalline structure [4, 5], few deterministic methods allow us to describe the transformation of an isotropic to anisotropic amorphous polymer chains in semi-crystalline polymer due to the complex conformation and absence of long-range coherence. Raman spectroscopy, however, is informative in providing valuable orientation properties of amorphous polymer chains in that they enable the detection of localized structures at the molecular scale and the separation of vibration of polymer chains in amorphous region from those of the crystalline region [6-9]. Since Bower [10] first developed the quantification of the molecular orientation in a polymeric system using polarized Raman spectroscopy, there have been numbers of studies analyzing molecular orientation of several semi-crystalline polymers [11-13].

In this chapter, we explore the orientational behaviors of poly (*L*-lactic acid) (PLLA), which exhibit a semi-crystalline phase. Our interest in orientation effects in this polymer stems from a rich variety of applications [14, 15] as a biomaterial. Recently, Tanaka *et al*. have introduced a good way to use polarized Raman spectroscopy for obtaining the degree of molecular orientation between the amorphous and crystalline regions in semi-crystalline polymers [16, 17] including PLLA [18]. In their publications, they reported a methodology for separating the degree of orientation of polymer chains in the amorphous and crystalline regions by combining $\langle P_{400} \rangle$ and $\langle P_{200} \rangle$ for the cylindrical symmetry axis of Raman tensor with orientation information from XRD and birefringence techniques. We will expand the way of using polarized Raman spectroscopy to quantify the degree of orientation of structural units in semi-crystalline polymer, PLLA as well as to obtain qualitative information about responsive behaviors of both amorphous and crystalline chains with quite different approaches. Rather than simply reproducing the orientation degrees in both crystalline and amorphous chains, the present work aims at shedding light on the coupling between the analysis of the anisotropy of polarization intensities of various vibrational modes and deformation histories of molecules.

6.1.2 Mutual Consistency of $\langle P_{200} \rangle$ and $\langle P_{400} \rangle$

In the case of polymer chains, the orientation distribution does not necessarily occur with a monotonic pattern, but can have more complicated patterns. Nomura *et al.* [19] and Bower *et al.* [20] reported the graphical representation of the state of orientation in polymer system using plots of $\langle P_{400} \rangle$ against $\langle P_{200} \rangle$ for several types of distribution under uniaxial deformation. They simulated the mutual relations between $\langle P_{200} \rangle$ and

$\langle P_{400} \rangle$ determined from the boundary equations of trigonometric functions. Using the relationship between $\langle \cos^2 \beta \rangle$ and $\langle \cos^4 \beta \rangle$ by the Schwarz inequality, the variation of $\langle P_{400} \rangle$ should be in the limited area of the following formula if the value of $\langle P_{200} \rangle$ is known as [19, 21]:

$$\frac{1}{18}\left(35\langle P_{200} \rangle^2 - 10\langle P_{200} \rangle - 7\right) \le \langle P_{400} \rangle \le \frac{1}{12}\left(5\langle P_{200} \rangle + 7\right) \tag{6-1}$$

where $\langle P_{200} \rangle = \frac{1}{2}\left(3\left\langle \cos^2 \beta - 1 \right\rangle\right)$ and $\langle P_{400} \rangle = \frac{1}{8}\left(3 - 30\left\langle \cos^2 \beta \right\rangle + 35\left\langle \cos^4 \beta \right\rangle\right)$.

In their graphical representations, there are four types of orientation distribution functions: monotonically increasing or decreasing function that has a single maximum at $\beta = 0°$ and $\beta = 90°$ respectively, bimodal shape that has two maximum peaks at $\beta = 0°$ and $90°$, and one minimum at specific angle. Each of the orientation models is illustrated in Figure 6.1, and the domain of the variation of $\langle P_{200} \rangle$ against $\langle P_{400} \rangle$ for each model is depicted in Figure 6.2. Model I represents a monotonic decrease of the orientation distribution function $f(\beta)$ with increasing β, while model II represents a monotonic increase of the population with increasing β. For model III, the function of $f(\beta)$ has at least one maximum at β where $0° < \beta < 90°$, and the function $f(\beta)$ has at least one minimum at β where $0° < \beta < 90°$ for model IV. By comparing the obtained values of $\langle P_{200} \rangle$ and $\langle P_{400} \rangle$ with four domains in Figure 6.2, we can predict a type of orientation distribution of polymer chains exhibiting in a system under the uniaxial deformation.

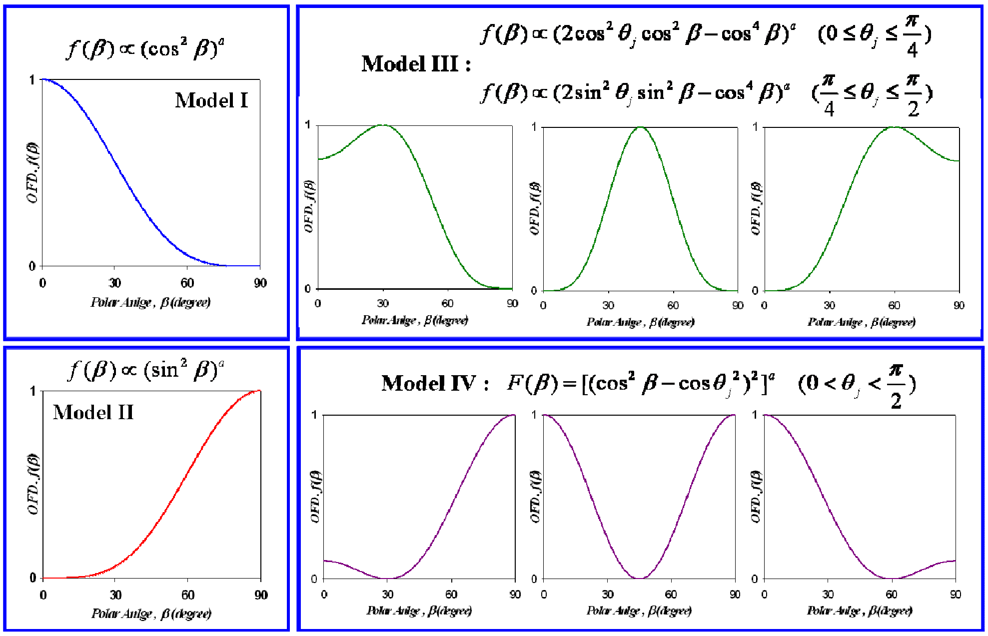

Figure 6.1 Different types of orientation distribution functions of polymer chain corresponding to the equation of Nomura *et al.* [21]: Model I: monotonic decrease with a single maximum at $\beta = 0°$, Model II: monotonic increase with a single maximum at $\beta = 90°$, Model III: bimodal function with a single minimum at specific angle, Model IV: unimodal function with a single maximum at specific angle.

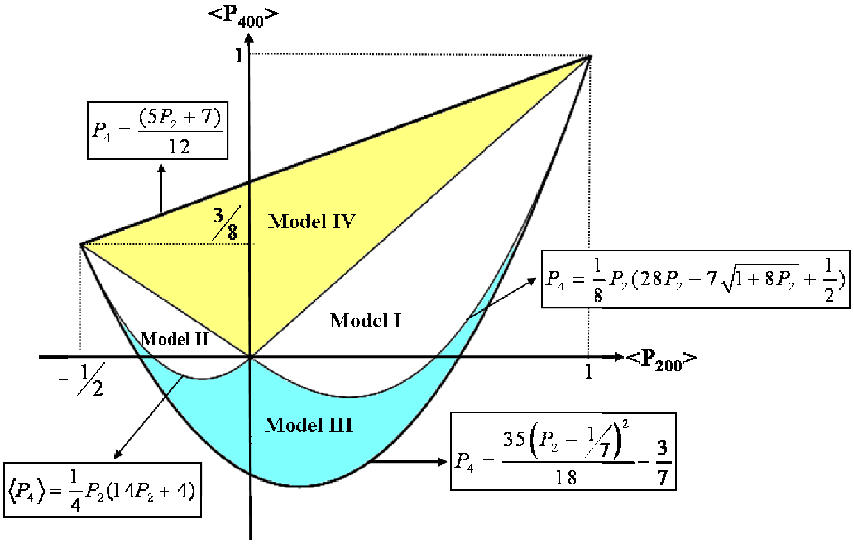

Figure 6.2 Possible four planes for the relation of $\langle P_{200} \rangle$ and $\langle P_{400} \rangle$ according to the type of ODF; solid line is bounds on the Eq. (5-1); inner solid lines are plotted to divide the $\langle P_{200} \rangle$ and $\langle P_{400} \rangle$ planes according to types of ODF [20]. [Reprinted from ref. [22] with permission]

6.2 Experiments

6.2.1 Sample Preparation

Poly (L-lactic acid) (PLLA) ($M_w = 1.9\times10^5$) was purchased from *Purac Biochem* and was used as received. A collaborator (Prof. Subbu S. Venkatraman at Nanyang University, Singapore) prepared film specimen by casting them from an isotropic solution of PLLA in dichloromethane. Solutions were cast onto glass plates using an automatic film applicator. The solvent are evaporated, and films with a uniform thickness of 0.1 *mm* were obtained. Drawing the solution cast film at 85℃ yielded some degree of uniaxial orientation of chains in the film and then quenched to room temperature. (Stretch ratios, $\varepsilon = l/L = 2,\ 3,\ 4$ where l: the final length and L: the initial length) The crosshead speed of the machine was 10 *mm*/min. Figure 6.3 shows molecular structure of PLLA and transition temperatures (glass transition/melting) of PLLA with α-helix structure.

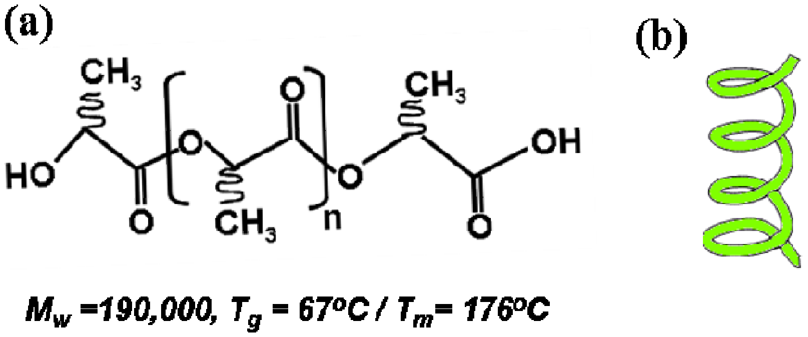

Figure 6.3 (a) Molecular structure of PLLA and its transition temperature (glass transition (T_g) and meting (T_m)) and (b) simple scheme of α-helix structure.

Uniaxial orientation in stretched films on a macroscopic scale was observed by polarized optical microscope (POM). Under crossed polarization, optical microscopic images of stretched the films appeared with 2-fold rotational symmetry of sample in birefringence. When drawing direction was parallel or perpendicular to polarization direction of incident light, it became dark, while the maximum intensity of transmitted light was obtained when rotating the drawing direction is 45° with respect to the polarization direction of incident light. This indicates that polymer chains in stretched films are aligned uniaxially on a macroscopic scale [23, 24].

6.2.2 Measurements of Raman Spectra

The procedure to obtain the anisotropy of polarized Raman intensity from stretched samples was the same with experimental set-up described in chapter 3. Right after drawing the samples, we placed the sample on the rotating stage at the configuration that drawing direction is collinear with ZY plane (see Figure 2.6). Since amorphous regions in semi-crystalline polymer coexist with crystalline regions [25], the difficulty in analyzing the orientation of both amorphous and crystalline chain using polarized Raman spectra is the separation of morphology effects on the scattering intensity. If the crystallinity of a sample can be varied substantially as temperature changes, it should be possible to assign some peaks to the crystalline chains by heat treatments. Thus, in order to evaluate the contribution of the crystalline and amorphous regions to peak intensities, polarized Raman spectra of isotropic crystalline PLLA film was measured at various temperature from 25℃ to 200 ℃ at which the crystalline phase effect can be eliminated since the melting temperature of PLLA with α-helix form is known to be 175℃ [26]. Differentiation of band assignments between crystalline and amorphous regions was carried out by measuring the polarized Raman spectra of undrawn PLLA over the melting temperature (T_m). Temperature of the film was controlled using a hot stage (*Linkam*) that provides a relative accuracy in temperature of ±0.1℃.

6.3 Results

6.3.1 Temperature Dependence of Raman Spectra of PLLA

Figure 6.4 (a) are optical images of undrawn film with 30% crystallinity with different temperatures ($T < T_g$, $T_g < T < T_m$, $T > T_m$), in which we observed that the optical image of the sample became out of focus when temperature reached its glass transition temperature (T_g) and that grains disappear when the sample was melted. Figure 6.4 (b) presents the peak changes in detail over the frequency regions studied as temperature changes. It is clearly seen that the peaks at 520 cm^{-1}, 708 cm^{-1}, and 919 cm^{-1} disappear after the temperature rises above T_m.

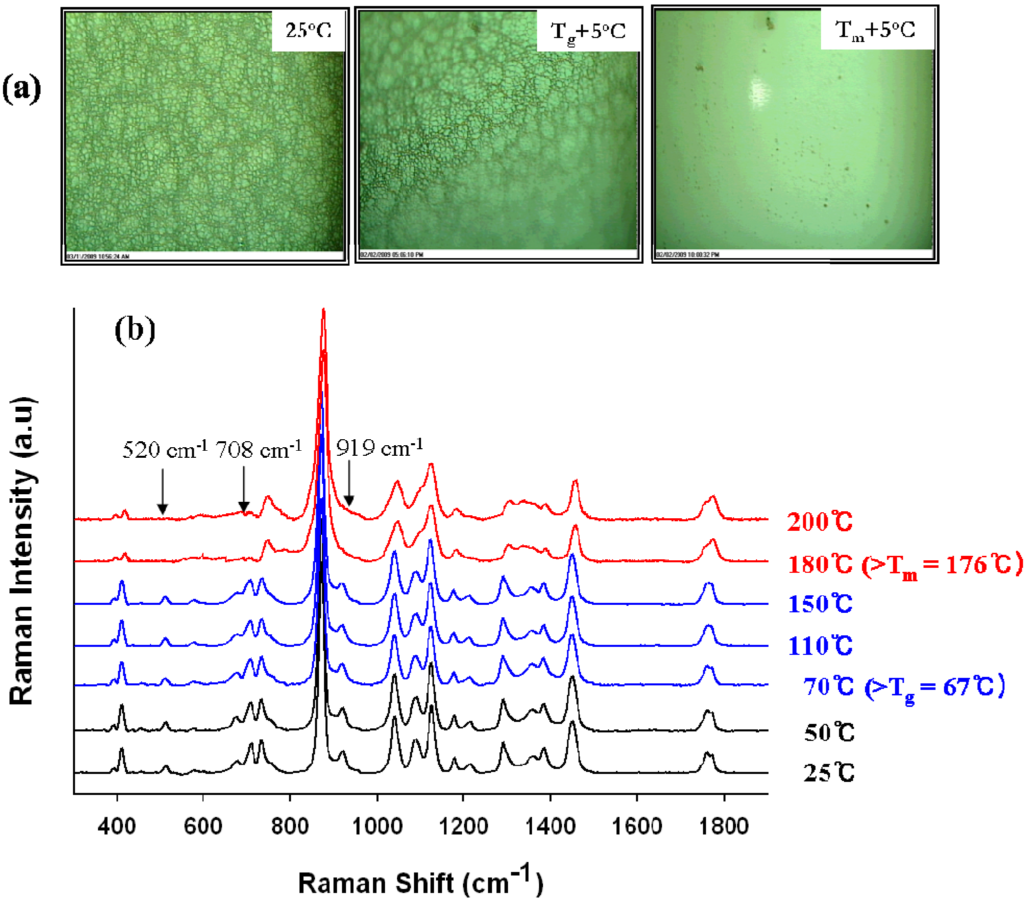

Figure 6.4 (a) Optical microscopic images at various temperature; left (25℃), middle (T_g+5℃) and right (T_m+5℃). (b) Polarized Raman spectra, $I_{//}$, of undrawn PLLA at various temperatures. [Reprinted from ref. [22] with permission]

Other peaks are present in the melt state, but there are some changes of the full width at half-maximum (FWHM) of peaks as temperature changes. Figure 6.5 shows temperature evolution of the bandwidth of various Raman peaks normalized to the width of each peak at 25℃. There are two features of interest in Figure 6.5: first, there is relatively slow increase of FWHM ratio with temperature up to T_m followed by a sharp increase to a constant value. The extent of broadening of other peaks is different for different peaks. For example, FWHM of the peak at 873 cm^{-1} slowly increases over T_g and then abruptly jump at above T_m, whereas that of peak at 1454 cm^{-1} looks independent of temperatures.

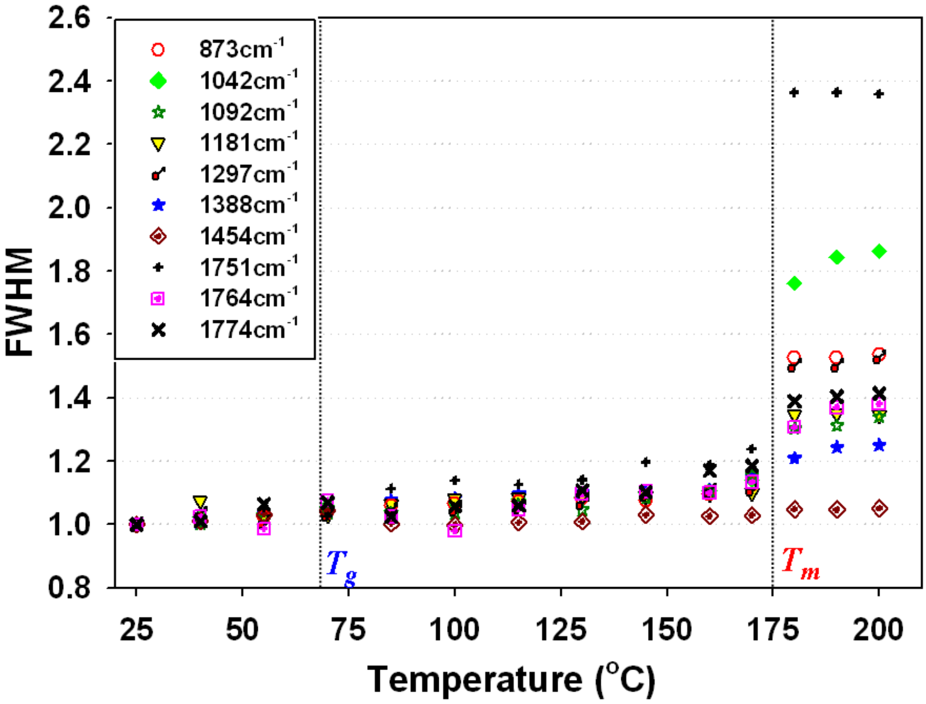

Figure 6.5 Temperature evolution of full width at half-maximum (FWHM) of various Raman bands normalized to the width of each band at 25℃. [Reprinted from ref. [22] with permission]

6.3.2 Raman Tensor Form and Symmetry of Vibration

As discussed in chapter 2, it is necessary to determine the form of the Raman tensor prior to the study of orientation using Raman peaks by measuring depolarization ratio in the isotropic state, $R_{iso} = I_{\perp} / I_{ll}$. Figure 6.6 shows the measured polarized Raman spectra of an undrawn PLLA film and deconvolution of mixed peaks. The value of R_{iso} for each peak is annotated in Figure 6.6. The number of peaks used to fit the overlapped peak was determined based on the literature [2, 18, 27].

According to R_{iso} values of each band, the tensor form is classified to be totally symmetric if R_{iso} is smaller than 0.75. In this case, the off-diagonal components of the Raman tensor are zero. If the R_{iso} value equals 0.75, on the other hand, the Raman tensor is non-totally symmetric, in which case the diagonal components of Raman tensor are zero. It is noteworthy that peaks with symmetric Raman tensor are appropriate to quantify the uniaxial ordering with simplified expression of the ODF as described in chapter 2.

6.3.3 Angular Dependence of Polarized Raman Intensity

All peaks attributed to each band were analyzed over the whole range of rotating angle, θ in detail, and its intensity profiles, I_{ll} for the four peaks of drawn film $(\varepsilon = 4)$ are shown in Figure 6.7. Interesting observation is that there are four types of angular dependence of polarized intensity, $I_{ll}(\theta)$ which are very similar to four types of orientation distribution functions as plotted in Figure 6.1.

The pattern of intensity profile of peak at 1388 cm^{-1} has a single maximum at $\theta = 0°$ and monotonically decreases until $\theta = 90°$. The intensity of peak at 1092 cm^{-1} and 1454 cm^{-1} monotonically increases as the rotating angle increases and has a single maximum at $\theta = 90°$. The intensity profile of the peak at 919 cm^{-1} follows the manner of unimodal variation. Angular dependence of Raman intensities of the other peaks such as that at 873 *cm*$^{-1}$ appear to be bimodal shape having two maxima at $\theta = 0°$ and $90°$, and one minimum at specific angle. Herein it is important to differentiate polar angle β form the rotating angle, θ. The intensity profiles are constructed as a function of the rotating angle, θ and the plots of orientation distribution are made as a function of polar angle β.

Since the pattern of the intensity profile follows different ODF types, experimentally obtained intensity profiles at different stretch ratios are fit to the ODF models of Nomura *et al.* [19], and fitting results as a function of stretch ratios are presented in Figure 6.8. From Figure 6.8, we can see significant changes of the shape of intensity profiles under the deformation of films.

6.3.4 $\langle P_{200} \rangle$ and $\langle P_{400} \rangle$ of the Scattering Units

Uniaxial orientational order parameters, $\langle P_{200} \rangle$ and $\langle P_{400} \rangle$, by fitting experimentally obtained depolarization ratios, $R(\theta)$, to Eq. (3-4). Obtained $\langle P_{200} \rangle$ are plotted against stretch ratios in Figure 6.9. It is observed that the $\langle P_{200} \rangle$ values for Raman peaks at 919, 1042, 1297, and 1388 *cm*$^{-1}$ increase positively as the stretch ratio becomes high; this implies the measured axis of symmetry has a tendency to align toward the drawing direction. In contrast, decreasing $\langle P_{200} \rangle$ values for bands at 1751-1764-1774 *cm*$^{-1}$ with increasing stretch ratio imply that the molecular chains align toward the drawing direction since the *C=O* stretching vibration is thought to occur in a direction perpendicular to the polymer backbone.

Interesting information on the shape of the ODF comes from the relation between $\langle P_{200} \rangle$ and $\langle P_{400} \rangle$ of the principal axis of Raman tensor of each peak. $\langle P_{200} \rangle$ and $\langle P_{400} \rangle$ values obtained for each Raman peak are plotted in the $\langle P_{200} \rangle \langle P_{400} \rangle$ plane which is theoretically limited by Nomura *et al.* [19] and Bower [20] in Figure 6.10. We can clearly see that the $\langle P_{200} \rangle$ and $\langle P_{400} \rangle$ values of each band are divided to be well inside each domain; values for 1388 cm^{-1} in domain I, those for 1092 cm^{-1} in domain II, values from the peak at 919 cm^{-1} in domain III, and those for peaks at other frequencies in domain IV.

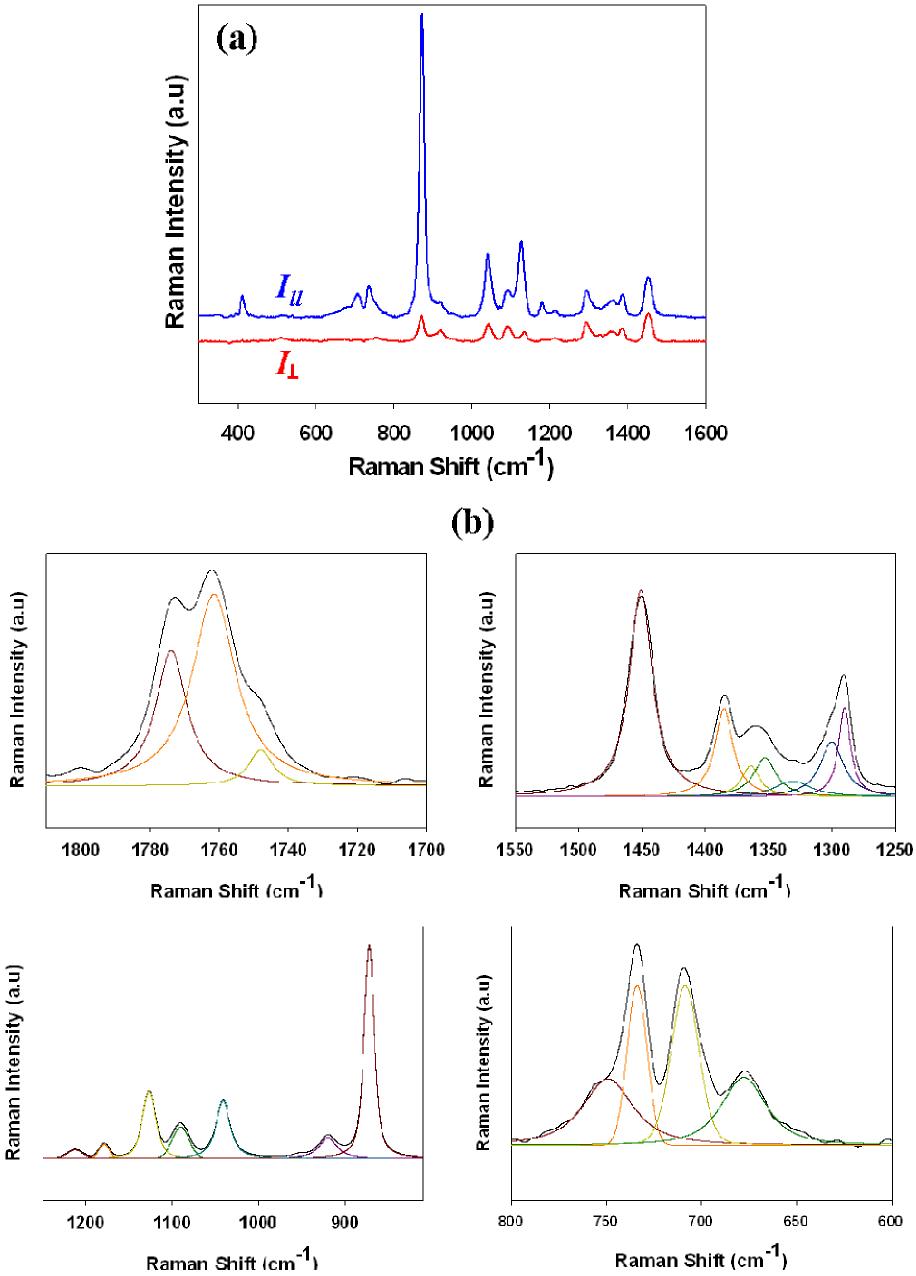

Figure 6.6 Polarized Raman spectra of undrawn PLLA (30% crystallinity) measured at room temperature: (a) $I_{//}$ and $I_{\perp}$ (b) decomposition of spectra over the range from 600 to 1800 cm^{-1}. [Reprinted from ref. [22] with permission]

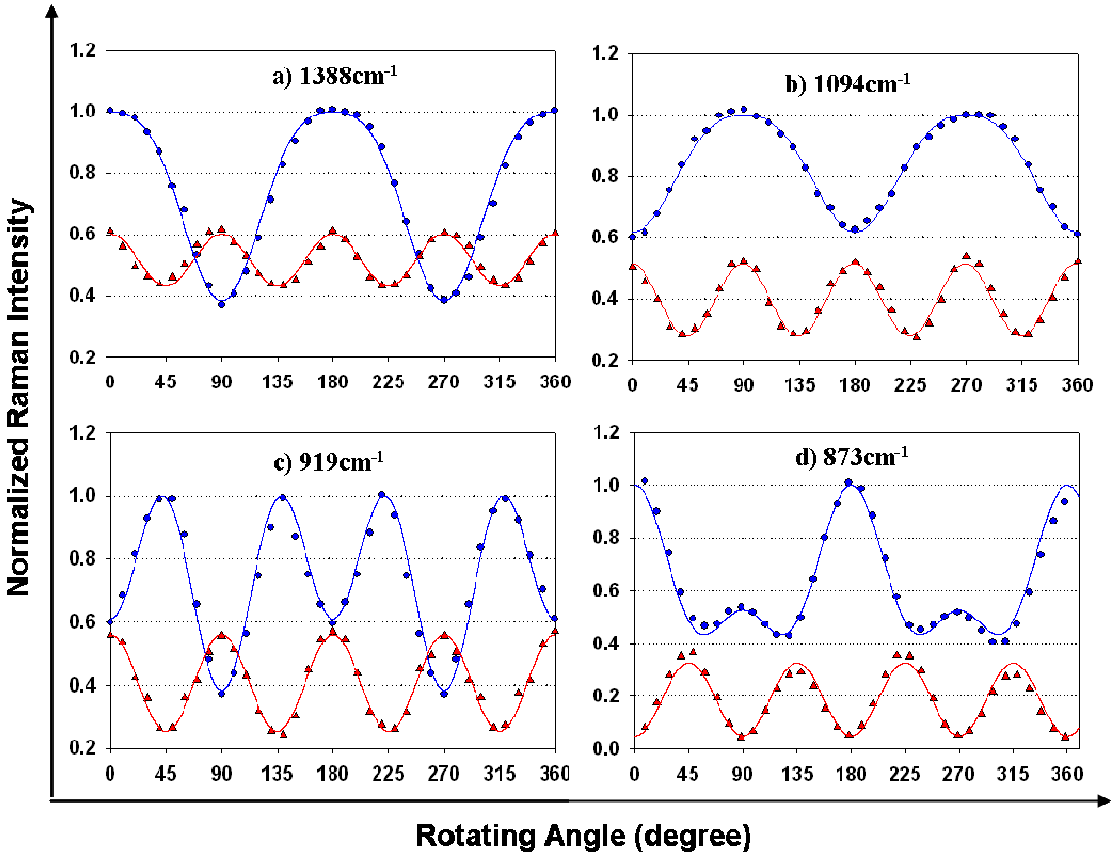

Figure 6.7 Angular dependence of polarized Raman intensities of drawn film $(\varepsilon = 4)$: (●) measured $I_{//}$, (▲) measured $I_{\perp}$, and solid lines are their fitting results. (a) Monotonic decrease of $I_{//}$, (b) Monotonic increase of $I_{//}$, (c) Unimodal shape of $I_{//}$ profile and (d) Bimodal shape of $I_{//}$ profile. [Reprinted from ref. [22] with permission]

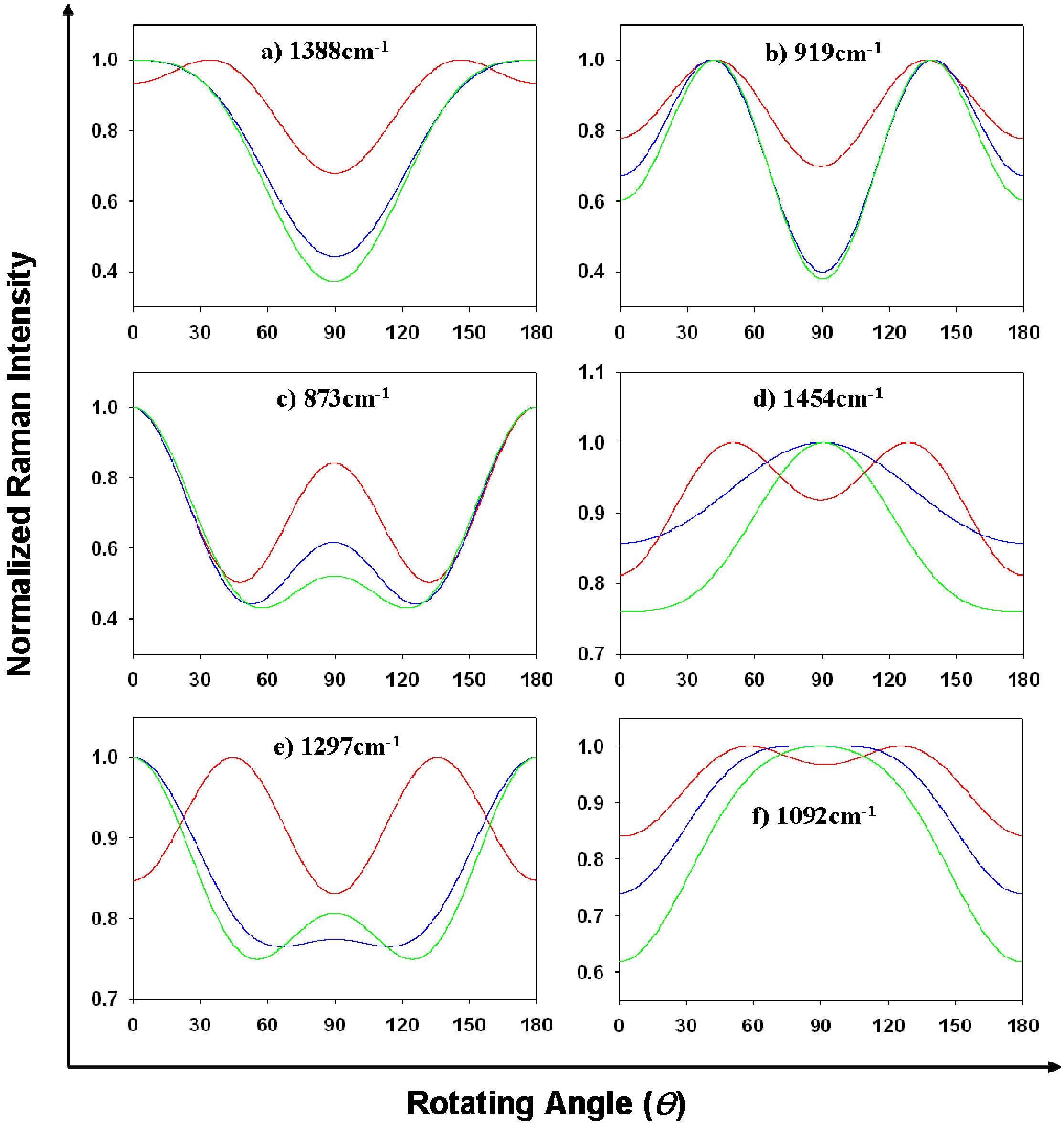

Figure 6.8 Angular dependence of $I_{//}$ for various bands of samples with different stretch ratios: red lines are fitting results of $I_{//}(\theta)$ at $\varepsilon = 2$, blue lines are fitting result of $I_{//}(\theta)$ at $\varepsilon = 3$, and green lines are fitting results of $I_{//}(\theta)$ at $\varepsilon = 4$. [Reprinted from ref. [22] with permission]

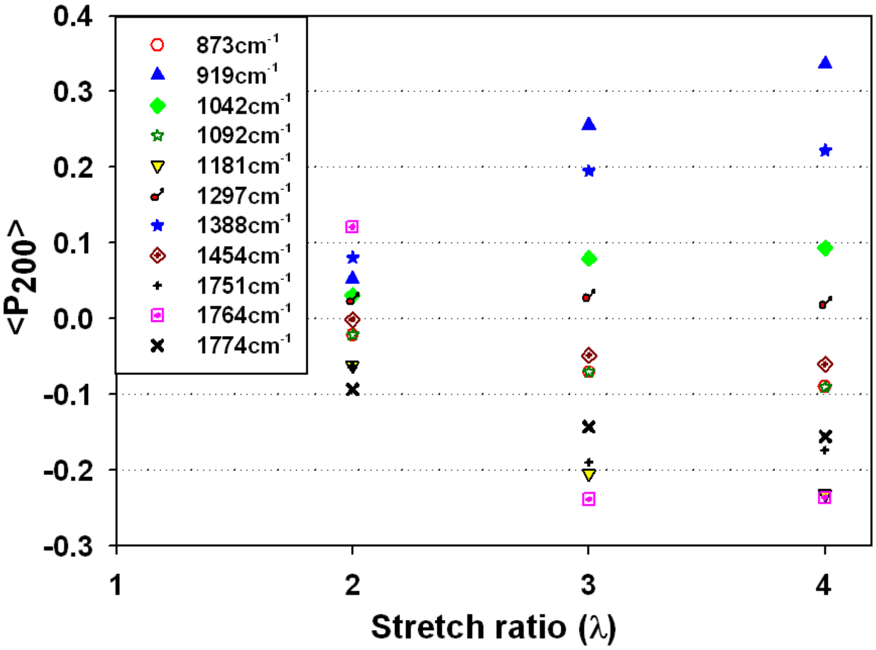

Figure 6.9 Plots of calculated values of $\langle P_{200} \rangle$ of vibration bands as a function of stretch ratio. [Reprinted from ref. [22] with permission]

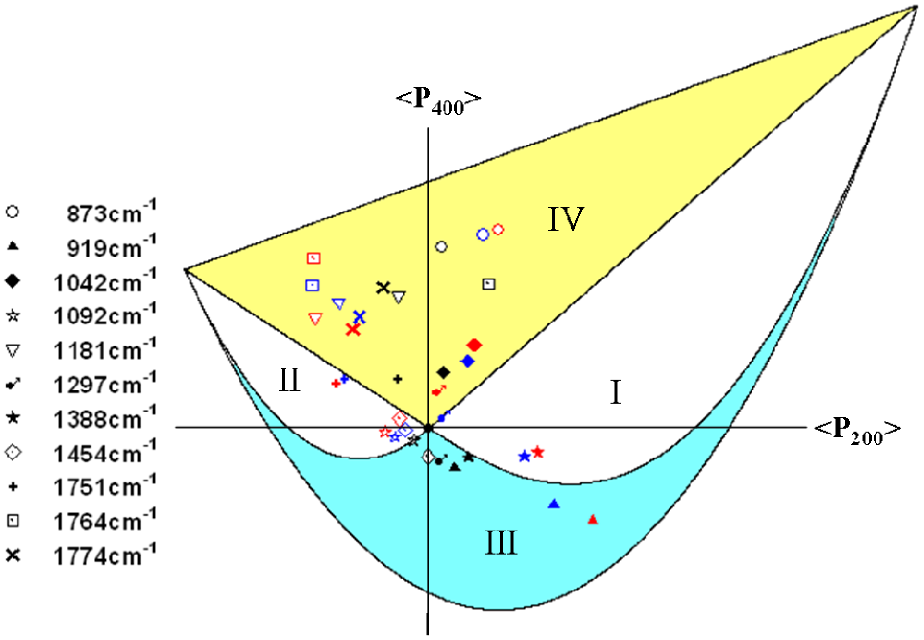

Figure 6.10 Plots of $\langle P_{400} \rangle$ against $\langle P_{200} \rangle$ for various vibration bands; each mark corresponds to each Raman band, and different colors with the same mark indicate the values obtained at different stretch ratios (black ones at $\varepsilon = 2$, blue ones at $\varepsilon = 3$, and red ones $\varepsilon = 4$). [Reprinted from ref. [22] with permission]

6.4 Discussion

6.4.1 Morphology Effect on Polarized Raman Spectra and Peak Assignments

From Figure 6.4 (b), peaks disappearing at above T_m (peaks at 520/708/919 cm^{-1}) were assigned to the vibration modes attributed to only crystalline nature since they were absent from the spectrum of the molten PLLA. This agrees with the result of previous studies reporting that bands at there frequencies are attributed only or mostly to the vibrations of chains in a crystalline region [2, 18, 27]. Thus, it is possible to identify orientation of scattering units in crystalline phases by analyzing Raman scattered intensity of these bands. Other peaks detected at above T_m may be the result of the overlap of peaks belonging to both phases. We can roughly estimate the contribution of the crystalline and amorphous phases to peak intensity from the changes of bandwidth of peaks. Increase of FWHM occurs when the chain conformations change from well-ordered states to random states. It is because the structure of disordered chains encompasses a broad distribution of chain conformation, and thus their vibrational transitions have broad bandwidth. The sharp increase of FWHM at over T_m was interpreted as occurring at the order-disorder phase transition. The slow broadening of peak width under T_m corresponds that a broad distribution of chain conformation without order-disorder phase transition occurring as temperature increases.

Therefore, the degree of change of FWHM gives qualitative information about how the morphology contributes to the peak intensity. For instance, the increase of FWHM of the peak at 1751 cm^{-1} becomes even greater at T_m than that of the peak at 1454 cm^{-1}. With these comparisons, it is plausible to conclude that the assigned band at 1751 cm^{-1} is significantly related to the chain vibration in amorphous regions. Little change of bandwidth at 1454 cm^{-1} even at the temperatures above T_m may indicate that the shape of the peak is not dominated by the vibrations of crystalline chains and does not change much over T_m due to disappearance of crystalline phase. For other bands, each has different degree of FWHM changes as a function of temperature, which indicates each band may have different contribution from both phases.

Since it has been known that PLLA has α-helix structure [25, 28], and the structure is also likely to be preserved in the amorphous regions, the tensor forms were classified into two symmetry types, A- and E-mode [16, 29]. In addition, we assume that any deformation in our study does not affect the helical structure of PLLA since the peak at 919 cm^{-1}, which reflects 10_3-helix structure [27], does not shift under the deformation.

Based on the temperature dependence of Raman peaks and previous literature [2, 18, 27], band assignments and morphology effects on the major bands are tabulated in Table 6.1.

Table 6.1 Raman Band Assignments and Morphology Effects on the Peak[a]

Raman shift (cm^{-1})	Morphology Effect	R_{iso}	Bands Assignments
- 398M–411M	Cr/Am	0.721–0.152	- *δCCO*
- 520w	Cr	/	- *δC-CH3+ δCCO*
- 708M	Cr >> Am	0.089	- *γC=O*
- 736M	Cr/Am	0.062	- *δC=O*
- 873VS	Cr/Am	0.095	- *νC–COO*
- 919M	Cr	0.841	- *rCH3 + νCC*
- 1042S	Am > Cr	0.267	- *ν C–CH3*
- 1092S	Cr/Am	0.501	- *ν (COC)s*
- 1128S	Cr/Am	0.109	- *r (CH3)as*
- 1181M	Cr/Am	0.086	- *ν (COC)as + r (CH3)as*
- 1297M	Cr/Am	0.577	- *δ CH*
- 1388M	Cr > Am	0.673	- *δ(CH3)s*
- 1454S	/	0.741	- *δ(CH3)as*
- 1751M	Am >> Cr	0.463	- *ν C=O*
- 1765M–1774M	Cr/Am	0.182–0.146	

[a] VS = very strong; S = strong; M = medium; w = weak; s = symmetric; as = asymmetric, Cr; crystalline nature, Am; amorphous nature, A>; more attribution to A rather than B, A>> B; even more attribution to A rather than B, Cr/Am; mixed attribution to both phases but portion of effect from morphology is not clear, /; difficult to decide.

6.4.2 Evolution of Intensity Profiles, $I_{ll}\left(\theta\right)$, corresponding to Deformation

In previous works about uniaxially drawn PLLA [18, 30], the pseudo-affine deformation model [31] was proposed for the deformation of polymer chains in the amorphous regions while the degree of chain orientation in crystalline region increases slowly at low stretch ratios followed by a rapid rise because of crystal rotation and slip along the stretching direction at high drawing ratio. This proposed deformation mechanism accounts for the variation of intensity profile with various stretch ratios in Figure 6.8 based on the knowledge about morphology contribution to the peak intensity qualitatively concluded in Table 6.1. For the peaks at 1092 cm^{-1}, 1297 cm^{-1}, and 1454 cm^{-1}, for instance, Raman peaks are assigned to the vibration of chains both in the crystalline region and in the amorphous region. This mixed contribution of morphology to peak intensity can explain the difference in intensity profiles according to stretch ratios. For the above three Raman peaks, Figure 6.8 shows remarkable changes of profile shape when stretch ratio changes from $\varepsilon = 2$ into $\varepsilon = 3$, but profile shape is more or less the same between $\varepsilon = 3$ and $\varepsilon = 4$. This suggests that scattering units in both the amorphous part and the crystalline part are involved in the orientation process while the sample is being deformed to low stretch ratio $\left(\varepsilon = 2\right)$. However, at high stretch ratio, $\varepsilon \geq 3$, the crystal orientation increases dramatically and then levels off due to the essentially complete micro-fibrillar transformation, and any further increase in orientation is confined to the amorphous regions. Thus, it results in the change of profile shape.

This approach is interpreted as evidence for a clear segregation of the crystalline and amorphous phases. Additional evidence is shown in the intensity profile of the crystalline peak at 919 cm^{-1}, where angular dependence of peak intensity increases abruptly from $\varepsilon = 2$ to $\varepsilon = 3$, but it almost level off at higher stretch ratios. These behaviors are in accord with previous results [18, 30]. With the profile changes at other peaks, however, it is difficult to explain the deformation mechanism of PLLA because angular dependence of the peak intensity is dependent on not only the mixed contribution of morphology but also the arbitrary angle of tilt that the symmetry axis of Raman tensor makes against molecular chain axis.

The result in Figure 6.10 is consistent with the matches between the profile shapes of $I_{II}(\theta)$ and those of ODF as shown in Figure 6.8 and Figure 6.1, respectively. It is clearly seen in the case of 1297 cm^{-1} for which $\langle P_{200} \rangle$ and $\langle P_{400} \rangle$ ranges from domain III to domain IV as stretch ratio increases. As shown in Figure 6.8, the pattern of $I_{II}(\theta)$ of this varies from unimodal to bimodal function, which is thought for the type of ODF to change in the same way. Thus, values of $\langle P_{200} \rangle$ and $\langle P_{400} \rangle$ at $\varepsilon = 3$ and $\varepsilon = 4$ are supposed to be in domain IV, whereas those of $\langle P_{200} \rangle$ and $\langle P_{400} \rangle$ at $\varepsilon = 2$ remain in domain III. The same explanation can be applied to the case of the Raman peak at 1454 cm^{-1}. The Raman peak at 1454 cm^{-1} is assigned to CH_3 asymmetric deformation modes, and CH_3 groups in PLLA are perpendicular to the molecular chain. Assuming that the Raman tensor is oriented along the direction of the CH_3 bond, our results show that the molecular chains are aligned along the deformation direction with a Gaussian distribution at high stretch ratio (refer to Figure 6.8). Therefore, we are able to predict the approximate pattern of ODF of polymer chains by measuring the intensity profile as a function of sample rotating angle.

However, it does not necessarily mean that these derived values of $\langle P_{200} \rangle$ and $\langle P_{400} \rangle$ reflect accurately the ODFs of polymer chains in the amorphous and crystalline region, respectively. This is because the analyzed scatterings have contributions from both phases, of which polymer chains respond differently to macroscopic deformation. Consequently, ODFs of the principal axis of Raman tensors averaged over both phases have a unimodal or bimodal function although the ODF of chains in each phase in fact may change monotonically. Furthermore, the tilt angle, Ψ between the symmetry axis of

Raman tensor and the helix axis should be considered to calculate ODF of molecular chains unless $\Psi = \pm n\pi,\ n = 0,\ \pm 1,\ \pm 2.....$

From the above discussion, we propose that plotting the intensity profiles, $I_{ll}(\theta)$ of Raman scattering of properly selected bonds can provide valuable information about the response of amorphous and crystalline chains separately under the deformation if the band is attributed to only one phase and the symmetry axis of Raman tensor is collinear with chain backbone axis.

6.4.3 Orientation of Amorphous Polymer Chains

Since the orientation information on crystalline chains in PLLA can be obtained using X-ray diffraction as shown in the result part, we would focus on discussing the orientation of amorphous chains in PLLA under deformation.

As discussed above, experimentally obtained $\langle P_{200} \rangle$ and $\langle P_{400} \rangle$ values represent the orientation distribution of the principal axis of the Raman tensor in a given coordinate system. In order to quantify the orientation degree of chains in the amorphous region, not only the contribution of vibration in both amorphous and crystalline chains to Raman peak should be separated but also the tilting angle, Ψ should be considered. Although we could qualitatively approximate the morphology effect on Raman intensity based on the variations of Raman bandwidth according to the temperature, exact quantification is still unclear. Moreover, an accurate knowledge of Ψ is quite complicated, perhaps impossible, only with analysis of experimentally measured Raman spectra unless quantum mechanical calculations of polarizability change during vibration are carried out in parallel.

Recently, Tanaka *et al*. reported an approach to obtain the tilt angle Ψ by combining $\langle P_{200} \rangle$ and $\langle P_{400} \rangle$ for the cylindrical symmetry axis of Raman tensor with those from wide-angle X-ray diffraction (WAXRD) and birefringence measurements [17, 18]. Once the tilt angle, Ψ has been determined, the orientational order parameters of amorphous chains, $\langle P_{200,a} \rangle$ were obtained from $\langle P_{200} \rangle$ for the Raman peak that is contributed from both crystalline and amorphous phase. $\langle P_{200,a} \rangle$ was calculated from Eq. (5-4) with the knowledge of the degree of crystallinity, χ_c and sample birefringence, Δn [18, 32, 33]·

$$\Delta n = \chi_c \langle P_{200,c} \rangle \Delta n_c + (1 - \chi_c) \langle P_{200,a} \rangle \Delta n_a \qquad (6\text{-}2)$$

where subscript *a* and *c* indicates amorphous and crystalline phase, respectively.

Herein lies the difficulty of decoding the individual contributions from the amorphous and crystalline regions. This equation can be applied for separating the orientation degree of amorphous and crystalline chains from the averaged values if the contribution of vibration of chains in amorphous and crystalline regions to Raman intensity is equal. Although qualitative separation of the contribution of morphology to Raman intensity is possible as shown in the discussion dealing with the FWHM in Figure 6.5, quantifying those exactly is quite difficult and not obvious. It would be quite useful to be able to figure out how to separate these contributions both qualitatively and, more importantly, quantitatively and merits further attention.

Free from the degree of contribution, the band at 1751 cm^{-1} may be used for the orientation of amorphous chains. It can be assumed that the contribution of crystalline chains to the peak intensity of band at 1751 cm^{-1} is so small that it can be ignored. In addition, the depolarization ratio, 0.463 obtained for this peak of the undrawn sample is again an indication that the Raman tensor of this band is symmetric, and hence a good approximation to simple ODF will be valid to apply Eq. (3-4). However, we were not able to obtain the orientational order parameters of amorphous chains due to the lack of tilting angle for the Raman band at 1751 cm^{-1}. Although the direction of transition moment of $C{=}O$ stretching was reported to be tilted about $53 \pm 3^\circ$ from the molecular chain axis in α-helix system [34], using this information may also product another assumption. Thus, rather than obtaining exact values of orientation degree for amorphous chains, what we propose is a new way to analyze polarized Raman spectra to characterize anisotropic behavior of semi-crystalline polymer under deformation.

6.5 Conclusions

The complex behavior of chain orientation in the semi-crystalline PLLA system was studied by means of polarized Raman spectroscopy. The present paper employed a simple approach to the use of polarized Raman, which seeks to provide additional information on the orientation distribution from examining the complete range of orientation of the symmetry axis of Raman tensor in relation to the polarizations. The measurements of the angular dependence of the scattered intensity of assignable vibration bands were performed to determine the orientational order parameters of scattering units. Comparison of calculated values, $\langle P_{200} \rangle$ and $\langle P_{400} \rangle$, with predicted ones was made according to types of ODF, and the results suggest that measurement of polarization of scattered intensity as a function of rotating angle can allow the orientation distribution function to be determined with a good accuracy without the use of information of entropy theory.

In order to characterize the orientation degree of crystalline chains and amorphous chains separately, we assigned Raman bands according to the effect of morphology on Raman intensity of the bands. The peak at 1751 cm^{-1} was mostly attributed to amorphous chain and could be directly used to obtain the orientation degree of amorphous chains. The molecular orientation distribution in the amorphous regions can be determined if the tilt angle, Ψ, is known. Using this approach, we found that most of the development of molecular orientation in the crystalline regions of uniaxially oriented PLLA film was complete after λ=3. The molecular orientation in the amorphous regions is much lower than that in the crystalline regions but seemed to be increased continually even after the molecular orientation in the crystalline regions was completed. These findings have implications for optimizing the recovery of semi-crystalline polymers, as crystalline orientation generally is less recoverable compared to amorphous orientation. In turn, this finding has implications for optimization of the processes used to incorporate shape memory effects in such polymers.

6.6 References

[1] Burg, K. J. L.; LaBerge, M.; Shalaby, S. W. "Change in stiffness and effect of orientation in degrading polylactide films" *Biomaterials*, **19**, 785-789 (1998).

[2] Smith, P. B.; Leugers, A.; Kang, S. H.; Hsu, S. L.; Yang, X. Z. "An analysis of the correlation between structural anisotropy and dimensional stability for drawn poly(lactic acid) films" *Journal of Applied Polymer Science*, **82**, 2497-2505, (2001).

[3] Murugan, R.; Ramakrishna, S. "Design strategies of tissue engineering scaffolds with controlled fiber orientation" *Tissue Engineering*, **13**, 1845-1866, (2007).

[4] Alexander, L. E. *X-ray Diffraction Methods in Polymer*. New York: Wiley-Interscience, 1969.

[5] Lapersonne, P.; Tassin, J. F.; Monnerie, L.; Beautemps, J. "Uniaxial-planar deformation of poly(ethylene-terephthalate) films. 1. Characterization of the crystalline phase" *Polymer*, **32**, 3331-3339 (1991).

[6] Jarvis, D. A.; Hutchinson, I. J.; Bower, D. I.; Ward, I. M. "Characterization of biaxial orientation of in poly(ethylene-terephthalate) by means of refractive-index measurements and Raman and infrared spectroscopies" *Polymer*, **21**, 41-54 (1980).

[7] Cunningham, A.; Ward, I. M.; Willis, H. A.; Zichy, V. "An infra-red spectroscopic study of molecular orientation and conformational changes in poly(ethylene terephthalate)" *Polymer*, **15**, 749-756 (1974).

[8] Bower, D. I.; Maddams, W. F. *The Vibrational Spectroscopy of Polymers*. Cambridge: Cambridge University Press, pp. 107-161, 1989.

[9] Kausch, H. H.; Zachmann, H. G., Eds., *Advances in Polymer Science* (Determination of Molecular Orientation by Spectroscopic Techniques. Berlin: Springer-Verlag, 1985 .

[10] Bower, D. I. "Investigation of molecular orientation distributions by polarized Raman-scattering and polarized fluorescence" *Journal of Polymer Science Part B-Polymer Physics*, **10**, 2135-2153 (1972).

[11] Maxfield, J.; Stein, R. S.; Chen, M. C. "Polarized Raman studies of crystalline and amorphous orientation in polyethylene" *Journal of Polymer Science Part B-Polymer Physics,* **16**, 37-48 (1978).

[12] Robinson, M. E. R.; Bower, D. I.; Maddams, W. F. "Molecular orientation in polyvinyl-chloride) studied by Raman spectroscopy and birefringence measurements" *Journal of Polymer Science Part B-Polymer Physics,* **16**, 2115-2138 (1978).

[13] Pigeon, M.; Prudhomme, R. E.; Pezolet, M. "Characterization of molecular orientation in polyethylene by Raman spectroscopy" *Macromolecules*, **24**, 5687-5694 (1991).

[14] Freed, L. E.; Marquis, J. C.; Nohria, A.; Emmanual, J.; Mikos, A. G.; Langer, R. "Neocartilage formation invitro and invivo using cells cultured on synthetic biodegradable polymers" *Journal of Biomedical Materials Research*, **27**, 11-23 (1993).

[15] Spenlehauer, G.; Vert, M.; Benoit, J. P.; Boddaert, A. "Invitro and invivo degradation of poly(D, *L*-lactide glycolide) type microspheres made by solvent evaporation method" *Biomaterials,* **10**, 557-563 (1989).

[16] Tanaka, M.; Young, R. J. "Molecular orientation distributions in the crystalline and amorphous regions of uniaxially oriented isotactic polypropylene films determined by polarized Raman spectroscopy" *Journal of Macromolecular Science-Physics*, **B44**, 967-991 (2005).

[17] Tanaka, M.; Young, R. J. "Polarised Raman spectroscopy for the study of molecular orientation distributions in polymers" *Journal of Materials Science,* **41**, 963-991 (2006).

[18] Tanaka, M.; Young, R. J. "Molecular orientation distributions in uniaxially oriented poly(L-lactic acid) films determined by polarized Raman spectroscopy" *Macromolecules,* **39**, 3312-3321 (2006).

[19] Nomura, S.; Nakamura, N.; Kawai, H. "Graphical representation of state of orientation of polymer systems" *Journal of Polymer Science Part a-2-Polymer Physics,* **9**, 407-420 (1971).

[20] Bower, D. I. “Orientation distribution functions for uniaxially oriented polymers” *Journal of Polymer Science Part B-Polymer Physics,* **19**, 93-107 (1981).

[21] Nomura, S.; Kawai, H.; Kimura, I.; Kagiyama, M. “General description of orientation factors in terms of expansion of orientation distribution function in a series of spherical harmonics” *Journal of Polymer Science Part a-2-Polymer Physics,* **8**, 383-400 (1970).

[22] Park, M. S.; Wong, Y. S.; Park, J. O.; Venkatraman, S. S.; Srinivasarao, M. “A Simple method for obtaining the information of orientation distribution using polarized Raman spectroscopy: Orientation study of structural units in poly(lactic acid)” *Macromolecules,* **44**, 2120-2131 (2011).

[23] Born, M.; Wolf, E. *Principles of Optics*, 5th ed. Oxford: Pergamon Press Ltd., 1975.

[24] Mattoussi, H.; Srinivasarao, M.; Kaatz, P. G.; Berry, G. C. “Refractive-indexes dispersion and order of lyotropic liquid-crystal polymers” *Macromolecules,* **25**, 2860-2868 (1992).

[25] Vasko, P. D.; Koenig, J. L. “Raman scattering and polarization measurements of isotactic polypropylene” *Macromolecules,* **3**, 597-601 (1970).

[26] Hoogsteen, W.; Postema, A. R.; Pennings, A. J.; Tenbrinke, G.; Zugenmaier, P. “Crystal-structure, conformation, and morphology of solution-spun poly(L-lactide) fibers” *Macromolecules,* **23**, 634-642 (1990).

[27] Kister, G.; Cassanas, G.; Vert, M. “Effects of morphology, conformation and configuration on the IR and Raman spectra of various poly(lactic acid)s” *Polymer,* **39**, 267-273 (1998).

[28] Bailey, R. T.; Hyde, A. J.; Kim, J. J. “The Raman spectra of uniaxially oriented isotactic polypropylene” *Spectrochimica Acta Part A: Molecular Spectroscopy,* **30**, 91-98, (1974).

[29] Bower, D. I. “Raman-scattering from an assembly of partially oriented scatterers” *Journal of Physics B-Atomic Molecular and Optical Physics,* **9**, 3275-3293 (1976).

[30] Wong, Y. S.; Stachurski, Z. H.; Venkatraman, S. S. “Orientation and structure development in poly(lactide) under uniaxial deformation” *Acta Materialia*, **56**, 5083-5090 (2008).

[31] Ward, I. M. *Mechanical Properties of Solid Polymer*, 2nd ed. New York: John Wiley & Sons, 1983.

[32] Stein, R. S.; Norris, F. H. “The x-ray diffraction, birefringence, and infrared dichroism of stretched polyethylene” *Journal of Polymer Science,* **21**, 381-396 (1956).

[33] Samuels, R. J. “Morphology of deformed polypropylene. Quantitative relations by combined x-ray, optical and sonic methods” *Journal of Polymer Science Part a-General Papers,* **3**, 1741-1763 (1965).

[34] Tsuboi, M. “Infrared dichroism and molecular conformation of alpha-form poly-gamma-benzyl-L-glutamate” *Journal of Polymer Science,* **59**, 139-153 (1962).

CHAPTER 7

SOLVENT EVAPORATION INDUCED LIQUID CRYSTALLINE PHASE IN POLY(3-HEXYLTHIOPHENE)

7.1 Introduction

Polymeric semiconductors are particularly attractive candidates for electronic devices because of their compatibility with high through-put and low cost processing techniques [1, 2]. When precisely functionalized through the techniques of organic synthesis, they afford desired performance attributes [3-5]. Their use, however, is restricted to opto-electronic devices because of their relatively low charge mobility [6-8]. The limitation of charge mobility in polymeric electronics is mostly due to both imperfect local order and macroscopic barriers such as grain boundaries, which behave as defect sites for charge hopping [9]. Therefore, understanding the morphology development of conducting films is of great importance for the enhancement of performance in device applications. As charge mobility strongly depends on the packing of chains and the degree of chain ordering, extensive research has been carried out to understand the structure-morphology-property relationships. These have focused on parameters dealing with molecular weight [10], regio-regularity [11, 12], and processing using various solvents [13], all of which affect the final morphology of the conjugated film, resulting in increased charge mobility.

Along with the study of structure-property relations, solution-processing techniques that facilitate a higher degree of macroscopic order in conjugated polymer films have been studied to improve the viability of conjugated polymers [14, 15]. Various groups have been trying to achieve the highly ordered alignment of conjugated polymers using various techniques such as using rubbed substrates [16, 17], Langmuir-Blodgett technique [18], friction transfer [19, 20], and directional solidifications [21].

In a separate study, we made a drop-casted film using regio-regular poly(3-heyxl thiophene) (P3HT), one of the most widely used conjugated polymers due to the self-organizing characteristic into highly ordered microstructure [15]. Interestingly, we observed clear birefringence at the periphery of casted P3HT film on a glass under crossed polarizers using an optical microscope (see Figure 7.1). It makes us recall the optical anisotropy that is the direct result of the drying process produced in the plane orientation of the dominating polarizable group, relative to the chain backbone in the solvent plasticized melt [22, 23]. This orientation reflects the molecular conformations that are frozen into the film during the drying process, and the magnitude of birefringence reflects both the optical anisotropy of the group and the steric constrains to its free rotation.

We are interested in elucidating the mechanism of the chain alignments at the border of the film formed by the evaporation of sessile drop. It has been reported that the conformation of polymer chains keep evolving in an evaporating solution droplet and the behavior of polymer chains in the solvents play a crucial role in determining the final morphology [24-26]. Despite the importance, a coherent picture of the morphology and the role of polymer relaxation in the solution process is incomplete. Thus, in the present work, in an effort to characterize how P3HT chains behave from an evaporating solution, we monitored the change in the orientation of the polymer chains as the solvent evaporated using polarized Raman spectroscopy. In addition, we report on the time dependence of vibration frequency and bandwidth of specific peak that is known to be very sensitive to structural changes at the molecular level, which provides the extent of intermolecular interactions and structural order of P3HT chains. (The works described in chapter 7, 8, and 9 have been done in collaboration with Prof. Elsa Reichmanis' group at Georgia Institute of Technology.)

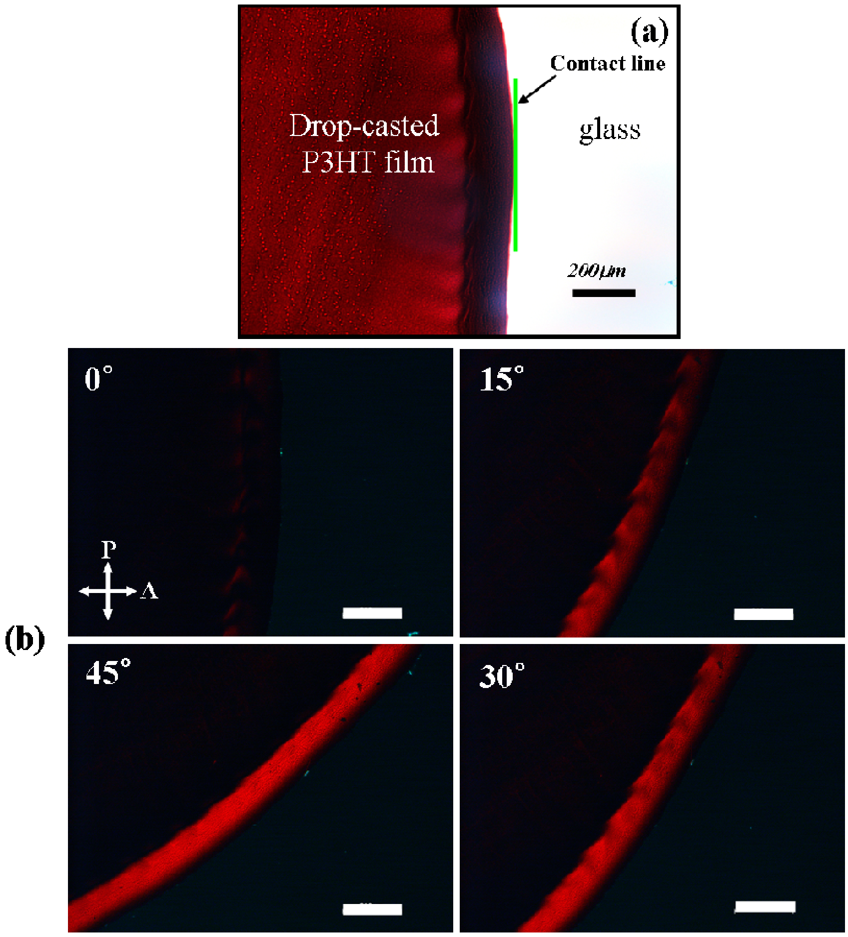

Figure 7.1 (a) Optical microscopic image of P3HT film drop casted from P3HT in chloroform on a glass without polarizer and analyzer. (b) Optical microscopic images under crossed polarizers; angles (0°, 15°, 30°, 45°) mean the tilt angle between the polarization direction (denoted as **P**) and the direction of contact line of the film. Scale bar is 200 μm. The sample stage was rotated with respect to the fixed crossed polarizers.

7.2 Experiments

7.2.1 Sample Preparation

The P3HT used for this study was purchased from *Sigma-Aldrich* and used without further purification. This material has a M_n of 24kD and M_w of 47.7 kD (from GPC in tetrahydrofuran calibrated with polystyrene standards using a Waters 15115 Isotropic HPLC system with a Water 2489 UV/Vis detector, using a Styragel HR 5E column) and a head to tail regio-regularity of 92~94% (as estimated from the ^{1}H NMR spectrum obtained from a solution of the polymer in deuterated chloroform at 293K recorded using a *Bruker DSX 300* NMR spectrometer). P3HT solution with a concentration of 3mg/mL were prepared using 1,2,4-trichlorobenzene (1,2,4-TCB) (boiling point =218-219˚C) as a solvent in order to monitor the changes of Raman spectra accurately with long enough evaporation time. The structures of P3HT and 1,2,4-TCB are depicted in Figure 7.2.

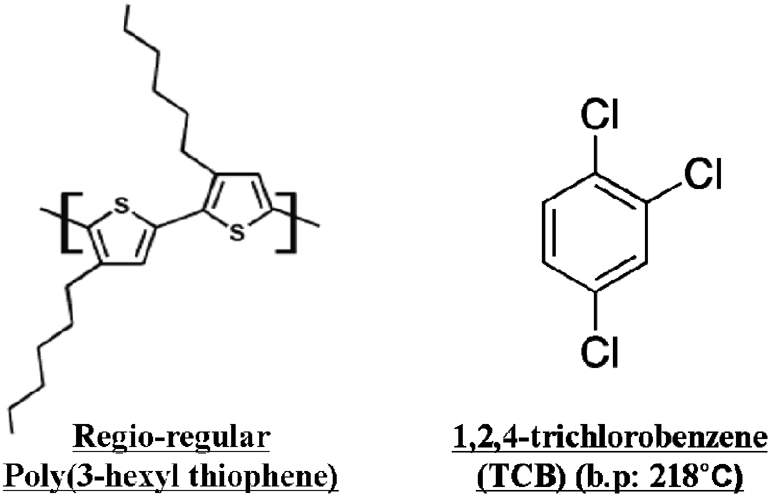

Figure 7.2 Structures of head-to-tail regio-regular poly(3-hexyl thiophene) (P3HT) and 1,2,4-trichlorobenzene (TCB)

7.2.2 In-Situ Polarized Raman Measurements

In order to monitor the change of Raman spectra as a function of solvent evaporation time, we carried out *in-situ* polarized Raman measurements. As shown in Figure 7.3, right after we deposited P3HT solution (2 *μL*, 3*mg*/*mL*) on a 200 *nm* thick SiO$_2$ coated silicon wafer, we continuously measured the polarized Raman spectra near the periphery of the solution drop by accumulating a Raman signal for 5 seconds with 6 time repetitions (that is, it took 30 seconds to obtain a Raman spectrum) using a 10× objective until the solvent evaporation was completed. In order to avoid local degradation of the sample, the laser power was limited to 30*mW* of laser output.

The development of anisotropy of P3HT chains was monitored by recording a series of polarized Raman spectra, $I_{//}$ as a function of the angle, θ, between the arbitrary direction in the *YZ*-plane and the polarization direction of the incident light (see Figure 2.5). Angular dependence was detected by measuring polarized Raman spectra in 15° intervals from 0° to 90° one after another by rotating sample stage while measuring *in-situ* Raman spectra. We arbitrarily defined $\theta = 90^\circ$ as the angle at which polarized Raman peak is strongest. While each polarized Raman spectrum was obtained from the accumulation of Raman signal for 30 seconds, *i.e.*, not simultaneously, this time interval (30 seconds) was so short in comparison to the time scale for complete solvent evaporation (> 12 hrs) that we ignored the influence of the time difference on polarized Raman spectra measured in a sequence.

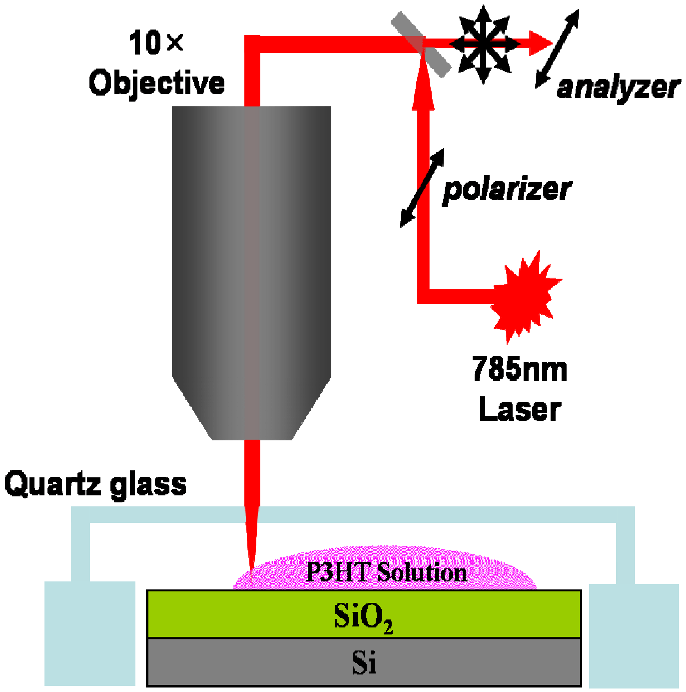

Figure 7.3 Experimental setup for *in-situ* polarized Raman measurement in the back scattering geometry. Deposited solution on the substrate was covered with quartz glass in order to protect the objective lens from the evaporated solvent and was placed on a rotatable stage. [Reprinted from ref. [27] with permission]

7.3 Results

7.3.1 Raman Spectrum of regio-regular P3HT

Polarized Raman spectrum measured for pure regio-regular P3HT powder, which is known to be semi-crystalline, are plotted within 600~1800 cm^{-1} range in Figure 7.4 (a) and the Raman spectrum of pure 1,2,4-TCB is plotted along with that of P3HT solution (P3HT+TCB) in Figure 7.4 (b). From the comparisons of the Raman spectra in Figure 7.4, Raman peaks from 1,2,4-TCB, distinct from those of pure P3HT, are highlighted with star marks (★). Especially, the most intense peak at 677 cm^{-1} attributed to *C-Cl* stretching vibration [28] can be used as an indicator of the existence of solvent in an evaporating P3HT solution.

It is always complicated and not definite to assign vibration bands for poly-atomic species based on the experimentally obtained spectrum unless quantum mechanical calculations are carried out in parallel. Nevertheless, we assigned the most intense peak for P3HT at c.a. 1445 cm^{-1} to symmetric *C=C* stretching in thiophene rings [29-33], a characteristic band that is sensitive to the structural change of molecules and to the intermolecular interactions based on the results of previous literature. (1) Raman spectra of both polythiophene without alkyl substitution and poly(3-alkylthiophene) exhibit very strong peak at near 1450 cm^{-1}, implying that this peak comes from the vibrational band independent of alkyl substitution [29]. (2) The frequency of this peak varies significantly according to the number of thiophene rings, *i.e.*, the extent of conjugation length, which was determined by experimental observations as well as quantum calculations of vibration frequencies of oligothiophenes [30-32]. (3) Oxidative doping of polythiophenes [33] and a poly(3-alkylthiophene) [32] shows obvious changes in both the position and shape of this peak, which means this peak is attributed to the vibration in the π bonding system. (4) The positions of strong Raman peaks coming from *C-H* stretching and skeletal stretching of *C-C* are usually known to be in the regions of 2800~3000 cm^{-1} and under 1200 cm^{-1}, respectively [34-36]. (5) The literature is replete with results showing that this peak for P3HT is sensitive to structural order [32, 37-40]. Dispersions of vibration frequencies of this peak under different resonant excitation conditions (*i.e.*, under different laser source) indicate peak position of this peak is strongly affected by the degree of molecular order [32, 38, 39]. The position of this peak of polythiophenes shift with high temperature at which structural order changes [37, 40].

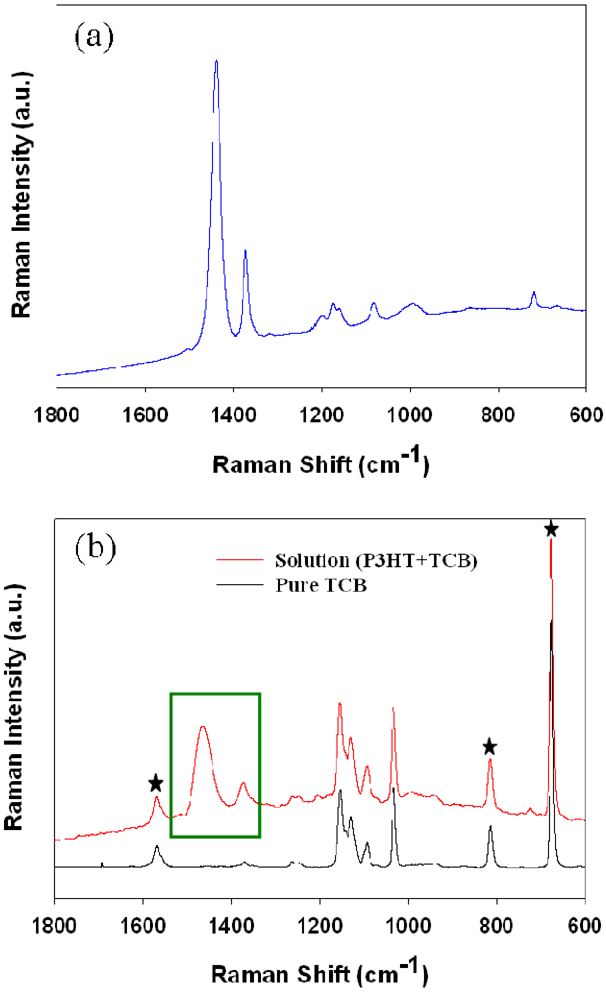

Figure 7.4 (a) Polarized Raman spectra of pure P3HT powder, and (b) polarized Raman spectra of P3HT solution (P3HT+TCB) along with pure TCB, under parallel polarization mode $(I_{//})$ at 30℃. Peaks highlighted with star mark (★) are characteristic Raman peaks coming from pure solvent, 1,2,4-TCB and peaks in green square are contributed to the vibrations of P3HT. [Reprinted from ref. [27] with permission]

7.3.2 Angular Dependence of Polarized Raman Spectra

Figure 7.5 shows anisotropic angular dependence of Raman spectra of P3HT solution for specific time duration (approximately 645~700 minutes after solution deposition). While the extent of anisotropy is different according to measured time, it is clear that polarized Raman spectra show anisotropic angular dependence. Especially, the intensity of peak at 1445 cm^{-1} varies significantly with the rotation angle. Another notable observation is that the fluorescence background of the polarized Raman spectra also displays a strong angular dependence. Intensity variation of the peak at 1445 cm^{-1} at this time duration is plotted with numerical values of peak intensity in Figure 7.6.

It was only for the period of approximately 645 to 720 minutes after solution deposition that we were able to detect the angular dependence in the polarized Raman spectra relative to the entire elapsed time during which measurements were obtained (0-1200 minutes). It is noteworthy that in the Raman spectra measured up to 675 minutes after the deposition, we were able to detect characteristic peaks of pure solvent that were distinct from the peaks coming from P3HT. In particular, the peak at 667 cm^{-1} was clearly seen in those spectra. (see Figure 7.7). It required a meticulous peak fitting to detect Raman signal at 667 cm^{-1} after 675 minutes due to the continuous loss of solvent amount and strong fluorescence background of which noise bury the Raman signal. However, meticulous spectra analysis enabled us to differentiate the peak at 667 cm^{-1} from the noise of fluorescence background even up to 720 minutes.

No angular dependence was discernible before the time period noted above (645~720 minutes after the deposition) for both the Raman peak at 1445 cm^{-1} and fluorescence background. Figure 7.8 shows no angular dependence of polarized Raman spectra measured at 630 minutes and 800 minutes after the deposition. (We intentionally shifted Raman spectra in consecutive order for the easy view. Otherwise, all spectra are almost identical one another.) It should be noted that Raman spectrum shown in Figure 7.8 (a) and 7.8 (b) looks very different. Raman spectrum in Figure 7.8 (a) consists of weak and broad peak at ca. 1445 cm^{-1}, whereas that in Figure 7.8 (b) show very strong and sharp peak at ca. 1445 cm^{-1} that looks similar to the Raman spectrum for regio-regular P3HT powder, which consists of polycrystalline domains embedded in amorphous matrix (Figure 7.4 (a)).

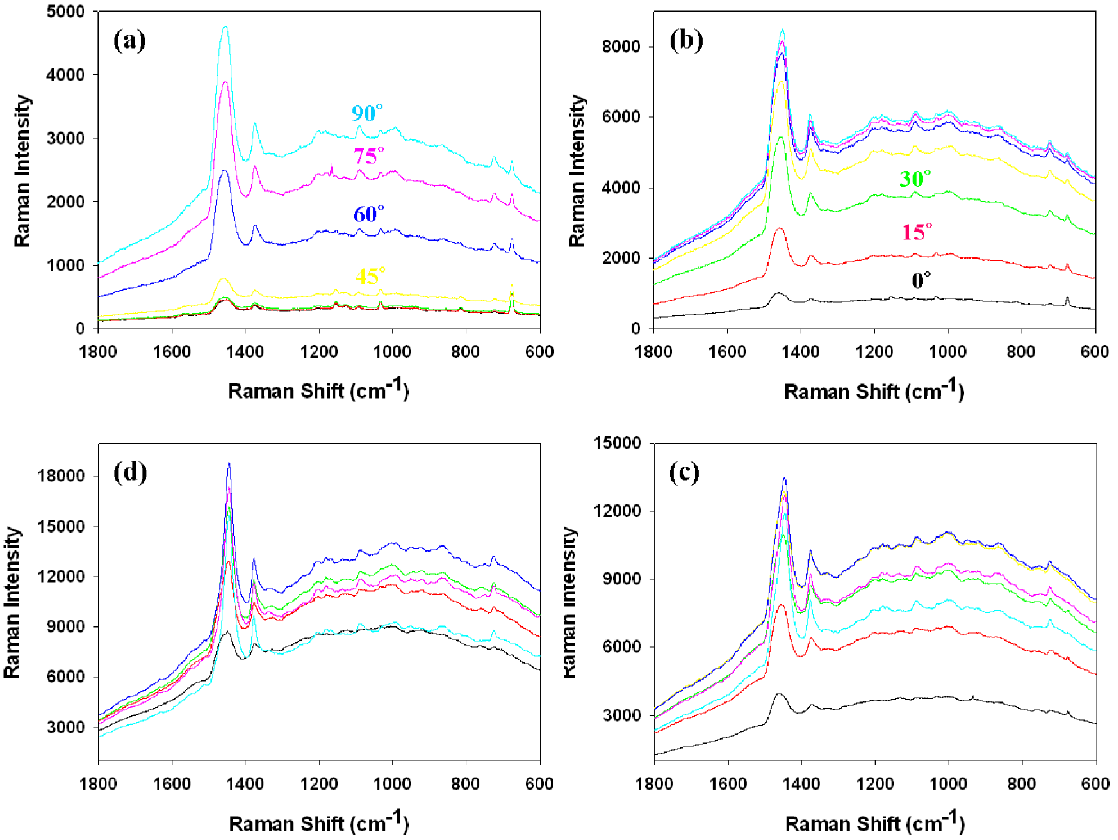

Figure 7.5 Angular dependence of polarized Raman spectra measured at various evaporation times at room temperature; (a) 645 minutes, (b) 660 minutes, (c) 675 minutes, and (d) 690 minutes after the deposition. Angle highlight with each color corresponds with Raman spectrum with the same color.

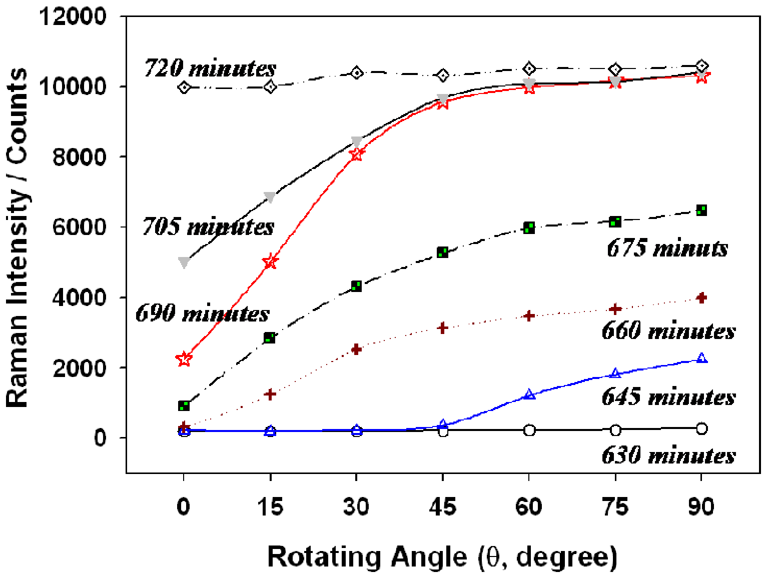

Figure 7.6 Time evolution of angular dependence of the peak intensity from *C=C* stretching between 630 minutes and 720 minutes after deposition. Outside of these time scale, *i.e.*, for ca. 0~630 minutes and ca. 720~1200 minutes, there is no angular dependence. [Reprinted from ref. [27] with permission]

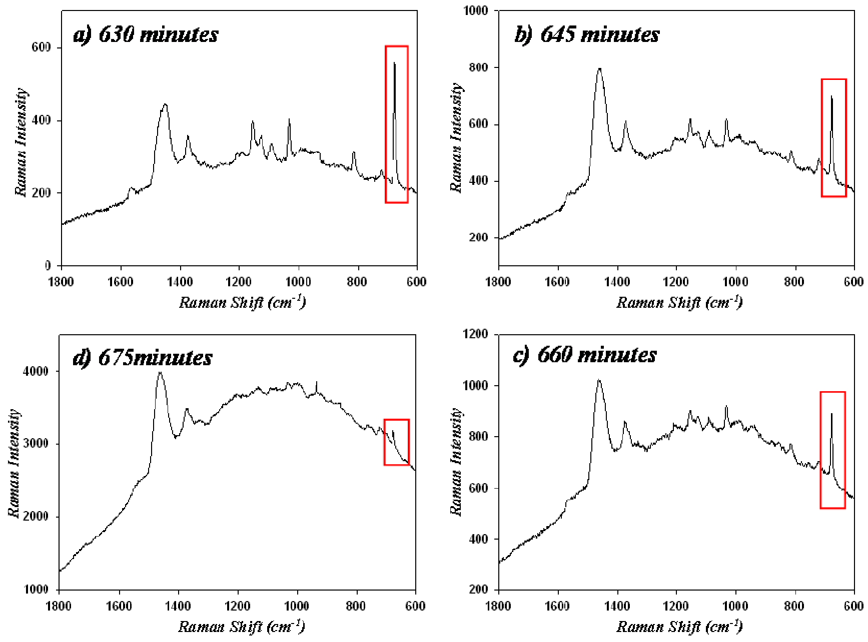

Figure 7.7 Polarized Raman spectra measured at 630~675 minutes, during which polarized Raman spectra exhibit angular dependence. In all spectra, a distinct peak at 667 *cm*$^{-1}$ is clearly detected as shown within red squares. [Reprinted from ref. [27] with permission]

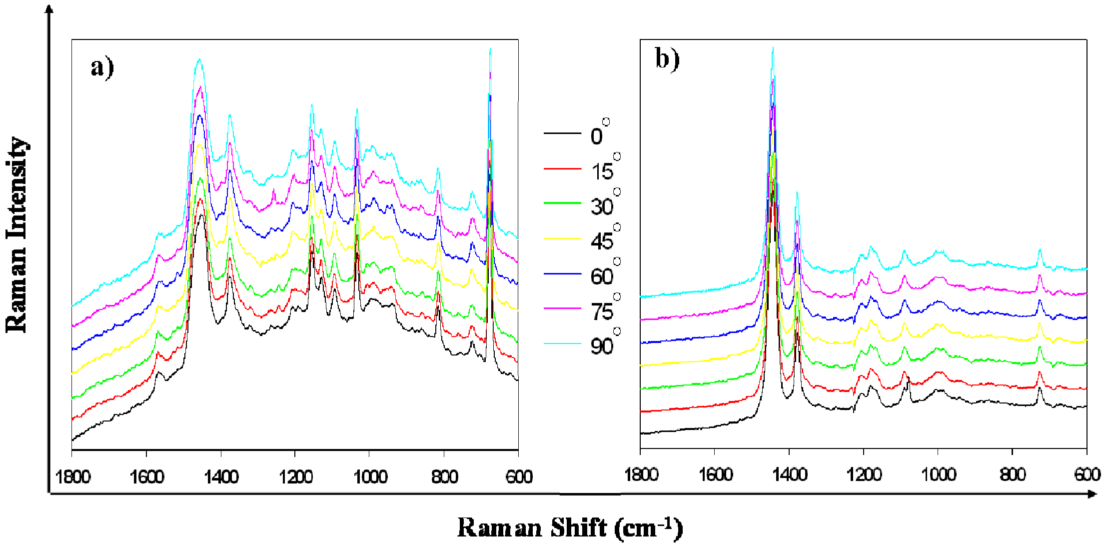

Figure 7.8 Plots of polarized Raman spectra consecutively measured by rotating sample stage at (a) 600 minutes, and (b) 800 minutes after deposition, respectively. Spectra in each figure are intentionally shifted for a lucid comparison. Otherwise, all spectra in each state are almost identical. [Reprint from ref. [27] with permission]

7.3.2 Time Evolution of Peak Position and Peak Width

We fitted the peak at ca 1445 cm^{-1} using GRAMS (*Galactic Inc.*) for all spectra measured for the entire time duration (0 ~ 1200 minutes), which resulted in obtaining numerical values of the peak position (Raman shift) and the peak width (FWHM). Figure 7.9 presents the time evolution of the vibrational frequency of the $C=C$ stretching mode, showing that the peak frequency of this band does not vary significantly until about 600 minutes followed by significant decrease with the continuous manner by 15 cm^{-1} until about 800 minutes. Then, the frequency keeps slowly decreasing to its saturation.

The time evolution of the full width at half-maximum (FWHM) of this peak during the same time frame is depicted in Figure 7.9. Similarly, FWHM does not vary significantly until about 600 minutes, and then sharply decrease in a discontinuous fashion. After about 800 minutes, FWHM is increasing until it saturates to about 29 cm^{-1}.

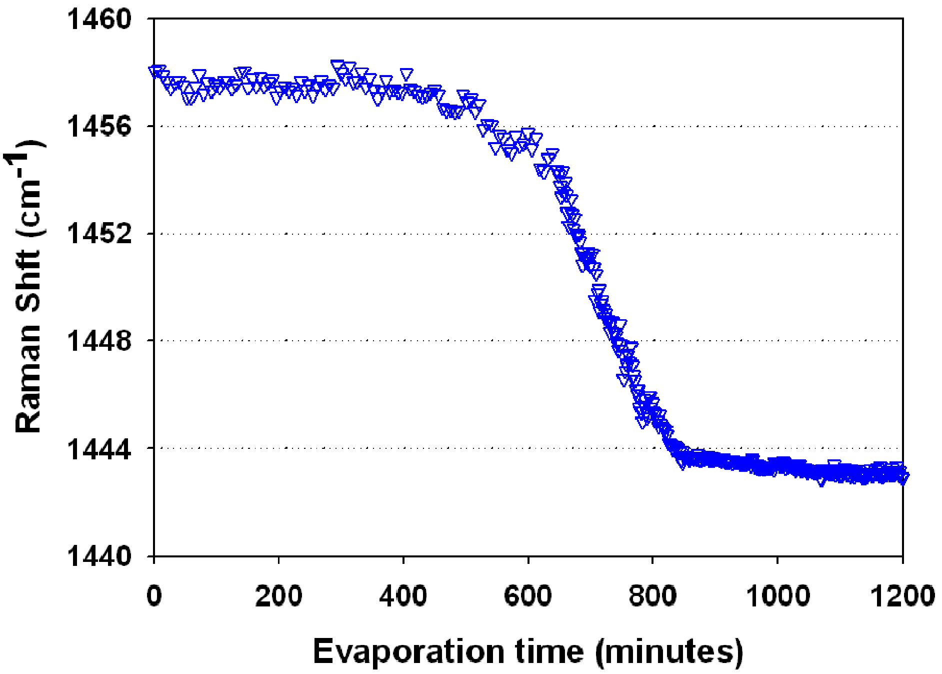

Figure 7.9 Time evolution of the frequency of the peak from C=C stretching in the thiophene rings. [Reprinted from ref. [27] with permission]

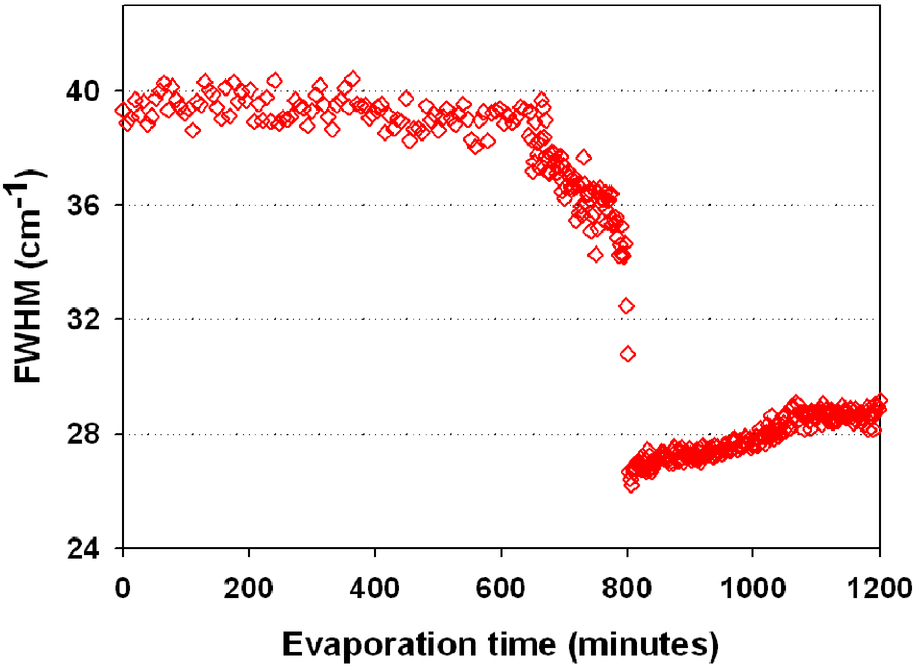

Figure 7.10 Time evolution of the FWHM of the Raman peak assigned to C=C stretching in the thiophene ring. [Reprinted from ref. [27] with permission]

7.4 Discussion

7.4.1 Phase Transitions in an Evaporating P3HT Solution Droplet

From the definite difference of peaks shape in Figure 7.8 (a) compared with those in Figure 7.8 (b), we can assume that phase transition takes place as solvent evaporates between 600 minutes and 800 minutes after the deposition. In principle, vibration motion in a crystal lattice (so called "*phonon*") is not random, but superimposed by collective vibrations of atoms [41]. A superposition of these elementary vibrations enables us to distinguish Raman peaks from the vibration modes of P3HT in a crystalline state from those in an amorphous state. This is supported by the comparison of Raman spectra obtained from P3HT solutes that exhibit different ordered phases. Figure 7.11 shows polarized Raman spectra ($I_{//}$) for two different pure-P3HT solutes; one has 94% regio-regularity that is known to have crystalline domains embedded in amorphous matrix (red solid line) and the other has regio-regularity of 50% (regio-random) forming amorphous state (black solid line). While the amount of two P3HT solutes measured was similar, relative intensity and sharpness is completely different, which results from the existence of crystalline domains. Therefore, it is rationalized that the Raman spectrum consisting of relatively quite strong and sharp peaks results from the collective vibrations in crystalline domains of P3HT, whereas spectrum consisting of weak and broad peaks arises from the vibration modes in a phase without crystalline domains.

No angular dependence in Figure 7.8 provides other information about chain orderings in different phases. As described above, no angular dependence was discernible before 630 minutes and after 720 minutes from the solution deposition. It is likely that considerable mobility of the polymer chains is responsible for the former case. As shown in Figure 7.7 (a), we could detect quite strong Raman peak at 667 cm^{-1} assigned to C-Cl stretching of 1,2,4-TCB at 630 minutes, which implies a non-negligible amount of solvent remaining. Consequently, P3HT chains may have too much conformational and configurational freedom to be ordered, thus exhibiting no ordering in macroscopic scale.

At longer times, it is thought that continued solvent evaporation produced semi-crystalline state consisting of polycrystalline domains embedded in amorphous matrix. However, the size of crystalline domains of casted P3HT films is reported to be tens of *nm* scale [13, 15, 26] and the orientation of crystals are randomly distributed [42]. In order to check the morphology of the area for Raman measurements, we visualized the microstructure of the film surface at the periphery of P3HT film using atomic force microscopy (AFM) micrographs. As seen from Figure 7.12, the P3HT polymer chains organize into nano-size (<~ 100 *nm* in width) fibrils that constitute crystalline-like domains, orientation of which exhibit no preferred direction. Accordingly, the anisotropic nature of the nano-scale domains was statistically averaged out because the polarized intensities were recorded from a micrometer-sized area (the diameter of the focused laser spot was about 15μm). Above observations provide an evidence that P3HT chains undergoes phase transition from isotropic phase in solution (before 630 minutes) to crystalline phase in dried film (after 720 minutes) with solvent evaporation.

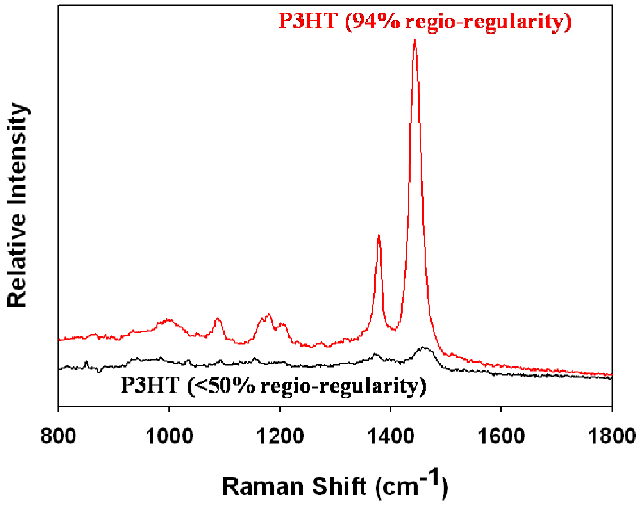

Figure 7.11 Polarized Raman spectra measured from P3HTs with different regio-regularity; high regio-regularity (94%) form a semi-crystalline phase and regio-random (50% head-to-tail content of side chains) form an amorphous phase.

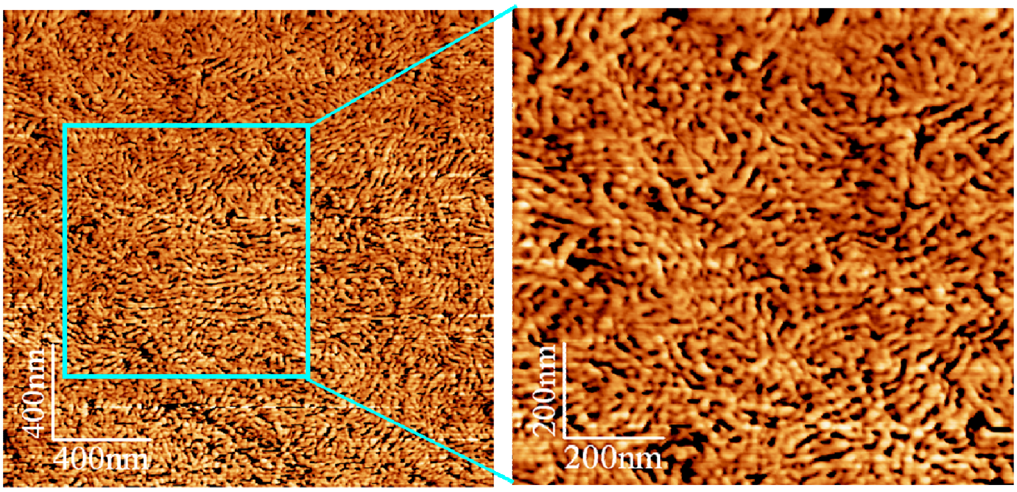

Figure 7.12 Tapping mode AFM phase images of P3HT films obtained by drop-casting from 1,2,4-TCB solution. The measured area was the border of drop-cast film.

The results in Figure 7.5, however, imply different ordered state different from both that of isotropic solution and that in morphology of dried P3HT film. It is not sure to correlate the angle, θ, with the tilting angle between the P3HT backbone axis and polarization direction of incident beam because we are not aware of chain configuration in an evaporating droplet. Nevertheless, clear angular dependence of polarized Raman spectra stands for the anisotropy in macroscopic orientation of P3HT chains. Another evidence of the anisotropic ordering of P3HT chains comes from the observations that the fluorescence background of the Raman spectra, the origin of which may be related to the structure of P3HT, also displays a strong angular dependence.

It can be questioned that the differences of polarized Raman spectra as a function of sample rotating angle may result from the different concentrations of P3HT because solvent was continuously evaporating while we measured in consecutive order. However, we ruled out the possibility that the continuous concentration changes may cause the angular dependence of polarized Raman spectra. We believe the concentration does not vary significantly during the time interval (15 seconds) for consecutively measured spectra so that concentration effect on the Raman spectra is rare. Should the concentration variation be responsible for, peak intensity should linearly increase with evaporation time regardless of rotating angle. However, this is not the case. For instance, although the concentration must become higher and higher due to the solvent evaporation, the peak intensity at $\theta = 90^\circ$ measured in the data set of 660 minutes is stronger than that at $\theta = 0^\circ$ in the data set of 690 minutes.

We suppose that the volume of the coating decreases and the film becomes thinner as the solvent evaporates. Consequently, the polymer chains were contracting from their solvated dimensions resulting in the emergence of long-range interchain interactions. While some amount of solvent in this time period (645~720 minutes) remains as shown by the solvent peak in Figure 7.7, interchain interactions may dominate the arrangements of P3HT chains in an ordered manner due to the self-organization nature of regio-regular P3HT [15]. However, it seems likely that remaining solvent may plasticize the P3HT chains so that the ordering stands between disordered isotropic solution and the strongly organized solid state, similar to nematic ordering in liquid crystalline phase.

7.4.2 Evidence of Liquid Crystalline Phase

The existence of a liquid-crystalline phase during solvent evaporation is supported by P3HT backbone peak analysis: the vibrational features observed for structural units in molecules are significantly affected by the presence of interchain interactions in π-conjugated systems such as a change in the extent of π-π overlap [43-45]. It has been reported that the vibrational frequency of the $C{=}C$ stretching mode of the thiophene ring is the principal feature supporting extended conjugation in thiophene-based conducting materials [30-32]. In this respect, the variation in peak frequency of the $C{=}C$ stretching mode is an effective indicator of the presence of P3HT interchain interactions. Significant red shift (by ca. $15 cm^{-1}$) of this peak shown in Figure 7.10 can be interpreted as the extension of conjugation upon solvent evaporation, on the basis of literature reporting that the position of the Raman peak associated with $C=C$ stretching is very sensitive to the extent of conjugation and that its wave number decreases as the conjugation is extended [30, 31]. A distinct characteristic of the frequency shifts, therefore, may show the change in the magnitude of intermolecular interactions between different phases. It should be noted that the time duration for a significant change in frequencies to occur is comparable with the time scale during which we was able to detect the anisotropy in the polarization intensity of Raman scattering.

The time evolution of the full width at half-maximum (FWHM) also provides additional indirect evidence of a phase transition. A significant increase in peak width for a polymeric system is observed when the chain conformation changes from a well-defined ordered state to a random state. This is because the structure of disordered chains encompasses a broad distribution of chain conformations, and thus, their vibrational transitions have broad bandwidths. Therefore, the significant decrease in FWHM as evaporation proceeds can support the conjecture that the interchain interactions force the P3HT backbone thiophene rings to be planar as the packing density increases via solvent evaporation. In contrast, in the dilute-solution state, internal twisting about ring-to-ring bonds may induce a deviation from planarity; thereby increase conformational entropy of P3HT chains. This torsional mode may break up the long π-π overlap [46] and broaden the bandwidth because of the large distribution of conjugations. Therefore, the decreasing slopes observed upon solvent evaporation (Figure 7.9 and Figure 7.10) represent a different state associated with the evolution of vibrational behavior with time, which characterizes a phase behavior distinct from that for either an isotropic solution or the crystalline state, namely, that of a liquid crystal.

These peak analyses, combined with the anisotropic nature of the peak intensity, provide firm evidence of a plausible model involving phase transitions from an isotropic solution to a liquid liquid-crystalline phase and then to a polycrystalline phase via solvent evaporation. It is quite rationalized by "*coffee ring effect*" proposed by Deegan [47].

When a drop of solution deposited on a solid surface and dries with the pinned three-phase contact line (see Figure 7.13), solvent evaporate faster at the edge and outward solution flux to replenish the loss of solvent drive solutes to the edge, which increases the solute concentration. Since regio-regular P3HT has rigid backbone, it is thought to be rigid-rod polymer with anisotropic shape in highly dense state. Thus, it is highly possible to form a lyotropic liquid crystalline phase at a critical concentration as Onsager predicted [48] and experimentally demonstrated for rod-like particle [49, 50], stiff virus [51, 52] and polymers [53-55].

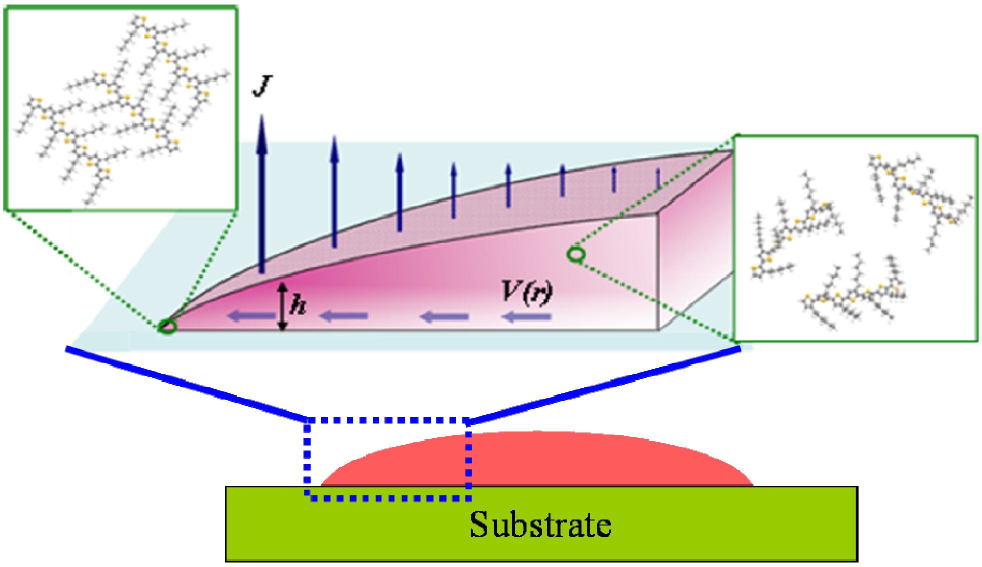

Figure 7.13 Mechanism of outward flow in an evaporating solution deposited on solid substrate. ***J*** is the evaporative flux, ***h*** is the height and ***v*** is the flow velocity [47]. Outward solution flux increases the concentration of P3HT at the 3-phase contact line.

Despite the fact that we successfully detected the same trend of time evolution of peak shape and anisotropic nature in polarized Raman spectra from five separate trials, it should be noted that experimental factors such as the evaporation rate and the initial amount of solute in a given droplet of different volume may result in different time scales for the phase transition from one sample to the next. For instance, in the case of a higher evaporation rate under stronger air circulation, the isotropic solution may undergo the phase transition to the liquid crystalline phase earlier, and the time duration when the sample exhibits the liquid crystalline phase may be shorter. In an effort to understand these dynamic phenomena, systematic studies of the film formation mechanism and control of relevant experimental factors needs to be carried out.

7.5 Conclusions

We have used polarized Raman spectroscopy to demonstrate that P3HT can form a lyotropic liquid-crystalline phase beyond a critical concentration via solvent-evaporation induced self-assembly. These phase transitions can be clearly understood by analyzing the vibrational frequency and bandwidth (FWHM) as the material changes from an isotropic solution to a solidified film. The gradually decreasing region in the evolution of the vibrational frequency and FWHM of the $C=C$ stretching mode in the thiophene ring is attributed to the liquid crystalline phase intermediate between the isotropic solution and the solidified crystalline phase.

We are unaware of any study that has reported a lyotropic liquid crystalline phase in the P3HT system at room temperature. Hence, our result will open a new paradigm for creating a long-range ordered structure with fewer defects in a simple, controllable, and cost-effective manner via solvent-evaporation-induced self-assembly under external field to maintain the well ordered polymer chains even in a fully dried state.

7.6 References

[1] Sirringhaus, H.; Kawase, T.; Friend, R. H.; Shimoda, T.; Inbasekaran, M.; Wu, W.; Woo, E. P. "High-resolution inkjet printing of all-polymer transistor circuits" *Science,* **290**, 2123-2126 (2000).

[2] Huebler, A. C.; Doetz, F.; Kempa, H.; Katz, H. E.; Bartzsch, M.; Brandt, N.; Hennig, I.; Fuegmann, U.; Vaidyanathan, S.; Granstrom, J.; Liu, S.; Sydorenko, A.; Zillger, T.; Schmidt, G.; Preissler, K.; Reichmanis, E.; Eckerle, P.; Richter, F.; Fischer, T.; Hahn, U. "Ring oscillator fabricated completely by means of mass-printing technologies" *Organic Electronics,* **8**, 480-486, (2007).

[3] McCullough, R. D. "The chemistry of conducting polythiophenes" *Advanced Materials*, **10**, 93-116, (1998).

[4] Katz, H. E. "Recent advances in semiconductor performance and printing processes for organic transistor-based electronics" *Chemistry of Materials*, **16**, 4748-4756 (2004).

[5] Kelley, T. W.; Baude, P. F.; Gerlach, C.; Ender, D. E.; Muyres, D.; Haase, M. A.; Vogel, D. E.; Theiss, S. D. "Recent progress in organic electronics: Materials, devices, and processes" *Chemistry of Materials,* **16**, 4413-4422 (2004).

[6] Pei, Q. B.; Yu, G.; Zhang, C.; Yang, Y.; Heeger, A. J. "Polymer light-emitting electrochemical-cells" *Science,* **269**, 1086-1088 (1995).

[7] Hide, F.; DiazGarcia, M. A.; Schwartz, B. J.; Heeger, A. J. "New developments in the photonic applications of conjugated polymers" *Accounts of Chemical Research,* **30**, 430-436 (1997).

[8] Friend, R. H.; Gymer, R. W.; Holmes, A. B.; Burroughes, J. H.; Marks, R. N.; Taliani, C.; Bradley, D. D. C.; Dos Santos, D. A.; Bredas, J. L.; Logdlund, M.; Salaneck, W. R. "Electroluminescence in conjugated polymers" *Nature,* **397**, 121-128 (1999).

[9] Salleo, A.; Chen, T. W.; Volkel, A. R.; Wu, Y.; Liu, P.; Ong, B. S.; Street, R. A. "Intrinsic hole mobility and trapping in a regioregular poly(thiophene)" *Physical Review B,* **70** (2004).

[10] Kline, R. J.; McGehee, M. D.; Kadnikova, E. N.; Liu, J. S.; Frechet, J. M. J. “Controlling the field-effect mobility of regioregular polythiophene by changing the molecular weight” *Advanced Materials,* **15**, 1519-1522 (2003).

[11] Sirringhaus, H.; Tessler, N.; Friend, R. H. “Integrated optoelectronic devices based on conjugated polymers” *Science,* **280**, 1741-1744 (1998).

[12] Bao, Z.; Dodabalapur, A.; Lovinger, A. J. “Soluble and processable regioregular poly(3-hexylthiophene) for thin film field-effect transistor applications with high mobility” *Applied Physics Letters,* **69**, 4108-4110 (1996).

[13] Chang, J. F.; Sun, B. Q.; Breiby, D. W.; Nielsen, M. M.; Solling, T. I.; Giles, M.; McCulloch, I.; Sirringhaus, H. “Enhanced mobility of poly(3-hexylthiophene) transistors by spin-coating from high-boiling-point solvents” *Chemistry of Materials,* **16**, 4772-4776 (2004).

[14] Grell, M.; Bradley, D. D. C. “Polarized luminescence from oriented molecular materials” *Advanced Materials,* **11**, 895-905 (1999).

[15] Sirringhaus, H.; Brown, P. J.; Friend, R. H.; Nielsen, M. M.; Bechgaard, K.; Langeveld-Voss, B. M. W.; Spiering, A. J. H.; Janssen, R. A. J.; Meijer, E. W.; Herwig, P.; de Leeuw, D. M. “Two-dimensional charge transport in self-organized, high-mobility conjugated polymers” *Nature,* **401**, 685-688 (1999).

[16] Culligan, S. W.; Geng, Y. H.; Chen, S. H.; Klubek, K.; Vaeth, K. M.; Tang, C. W. “Strongly polarized and efficient blue organic light-emitting diodes using monodisperse glassy nematic oligo(fluorene)s” *Advanced Materials,* **15**, 1176-1180 (2003).

[17] Whitehead, K. S.; Grell, M.; Bradley, D. D. C.; Jandke, M.; Strohriegl, P. “Highly polarized blue electroluminescence from homogeneously aligned films of poly(9,9-dioctylfluorene)” *Applied Physics Letters,* **76**, 2946-2948 (2000).

[18] Xu, G. F.; Bao, Z. A.; Groves, J. T. “Langmuir-Blodgett films of regioregular poly(3-hexylthiophene) as field-effect transistors” *Langmuir,* **16**, 1834-1841 (2000).

[19] Wittmann, J. C.; Smith, P. “Highly oriented thin-films of poly (tetrafluoroethylene) as a substrate for oriented growth of materials” *Nature,* **352**, 414-417 (1991).

[20] Nagamatsu, S.; Takashima, W.; Kaneto, K.; Yoshida, Y.; Tanigaki, N.; Yase, K. “Backbone arrangement in "friction-transferred" regioregular poly(3-alkylthiophene)s” *Macromolecules,* **36**, 5252-5257 (2003).

[21] Brinkmann, M.; Aldakov, D.; Chandezon, F. “Fabrication of oriented and periodic hybrid nanostructures of regioregular poly(3-hexylthiophene) and CdSe nanocrystals by directional epitaxial solidification” *Advanced Materials,* **19**, 3819-3823 (2007).

[22] Prest, W. M.; Luca, D. J. “Origin of the optical anisotropy of solvent cast polymeric films” *Journal of Applied Physics*, vol. 50, pp. 6067-6071, 1979.

[23] Prest, W. M.; Luca, D. J. “The alignment of polymers during the solvent-coating process” *Journal of Applied Physics*, **51**, 5170-5174 (1980).

[24] Nguyen, T. Q.; Doan, V.; Schwartz, B. J. “Conjugated polymer aggregates in solution: Control of interchain interactions” *Journal of Chemical Physics,* **110**, 4068-4078 (1999).

[25] Zen, A.; Pflaum, J.; Hirschmann, S.; Zhuang, W.; Jaiser, F.; Asawapirom, U.; Rabe, J. P.; Scherf, U.; Neher, D. “Effect of molecular weight and annealing of poly (3-hexylthiophene)s on the performance of organic field-effect transistors” *Advanced Functional Materials,* **14**, 757-764 (2004).

[26] Surin, M.; Leclere, P.; Lazzaroni, R.; Yuen, J. D.; Wang, G.; Moses, D.; Heeger, A. J.; Cho, S.; Lee, K. “Relationship between the microscopic morphology and the charge transport properties in poly(3-hexylthiophene) field-effect transistors” *Journal of Applied Physics,* **100**, 033712 (2006).

[27] Park, M. S.; Aiyar, A.; Park, J. O.; Reichmanis, E.; Srinivasarao, M. “Solvent evaporation induced liquid crystalline phase in poly(3-hexylthiophene)” *Journal of the American Chemical Society,* **133**, 7244-7247 (2011)

[28] Scherer, J. R.; Evans, J. C. “Vibrational spectra and assignments for 16 chlorobenzenes” *Spectrochimica Acta,* **19**, 1739-1775 (1963).

[29] Louarn, G.; Mevellec, J. Y.; Buisson, J. P.; Lefrant, S. “Comparison of the vibrational properties of polythiophene and polyalkylthiophenes” *Synthetic Metals,* **55**, 587-592 (1993).

[30] Furukawa, Y.; Akimoto, M.; Harada, I. “Vibrational key bands and electrical-conductivity of polythiophene” *Synthetic Metals,* **18**, 151-156 (1987).

[31] Navarrete, J. T. L.; Zerbi, G. “Lattice-dynamics and vibrational-spectra of polythiophene. 1. Oligomers and polymer” *Journal of Chemical Physics,* **94**, 957-964 (1991).

[32] Louarn, G.; Trznadel, M.; Buisson, J. P.; Laska, J.; Pron, A.; Lapkowski, M.; Lefrant, S. “Raman spectroscopic studies of regioregular poly(3-alkylthiophenes)” *Journal of Physical Chemistry,* **100**, 12532-12539 (1996).

[33] Louarn, G.; Buisson, J. P.; Lefrant, S.; Fichou, D. “Vibrational studies of a series of alpha-oligothiophenes as model systems of polythiophene” *Journal of Physical Chemistry,* **99**, 11399-11404 (1995).

[34] Snyder, R. G.; Scherer, J. R. “Band-structure in the C-H stretching region of the extended polymethylene chain – influenece of fermi resonance” *Journal of Chemical Physics,* **71**, 3221-3228 (1979).

[35] Snyder, R. G.; Strauss, H. L.; Elliger, C. A. “C-H stretching modes and the structure of normal alkyl chains. 1. Long, disordered chains” *Journal of Physical Chemistry,* **86**, 5145-5150 (1982).

[36] Lin-Vien, D.; Colthup, N. B.; Fateley, W. G.; Grasselli, J. G. *The Handbook of Infrared and Raman Characteristic Frequencies of Organic Molecules*. San Diego: Academic Press, pp. 9-18 (1991).

[37] Zerbi, G.; Chierichetti, B.; Inganas, O. “Vibrational-spectra of oligothiophenes as model of polythiophenes” *Journal of Chemical Physics,* **94**, 4637-4645 (1991).

[38] Tsoi, W. C.; James, D. T.; Kim, J. S.; Nicholson, P. G.; E., N. C.; Bradley, D. D. C.; Nelson, J.; Kim, J.-S. “The nature of in-plane skeleton Raman modes of P3HT and their correlation to the degree of molecular order in P3HT:PCBM blend thin films” *Journal of the American Chemical Society,* **133**, 9834-9843 (2011).

[39] Gao, Y. Q.; Grey, J. K. “Resonance chemical imaging of polythiophene/fullerene photovoltaic thin films: mapping morphology-dependent aggregated and unaggregated C=C species” *Journal of the American Chemical Society,* **131**, 9654-9662 (2009).

[40] Zerbi, G.; Chierichetti, B.; Inganas, O. “Thermochromism in polyalkylthiophenes – molecular aspects from vibrational spectroscopy” *Journal of Chemical Physics,* **94**, 4646-4658 (1991).

[41] Quinn, J. J.; K-S., Y. *Solid State Physics: Principles and Modern Applications*. New York: Springer, pp. 37-79, 2009.

[42] Kline, R. J.; McGehee, M. D.; Toney, M. F. “Highly oriented crystals at the buried interface in polythiophene thin-film transistors” *Nature Materials,* **5**, 222-228 (2006).

[43] Brown, P. J.; Sirringhaus, H.; Harrison, M.; Shkunov, M.; Friend, R. H. “Optical spectroscopy of field-induced charge in self-organized high mobility poly(3-hexylthiophene)” *Physical Review B,* **63**, 125204 (2001).

[44] Osterbacka, R.; Jiang, X. M.; An, C. P.; Horovitz, B.; Vardeny, Z. V. “Photoinduced quantum interference antiresonances in pi-conjugated polymers” *Physical Review Letters,* **88**, 226401 (2002).

[45] Brown, P. J.; Thomas, D. S.; Kohler, A.; Wilson, J. S.; Kim, J. S.; Ramsdale, C. M.; Sirringhaus, H.; Friend, R. H. “Effect of interchain interactions on the absorption and emission of poly(3-hexylthiophene)” *Physical Review B,* **67**, 064203 (2003).

[46] Ong, B. S.; Wu, Y. L.; Liu, P.; Gardner, S. “High-performance semiconducting polythiophenes for organic thin-film transistors” *Journal of the American Chemical Society,* **126**, 3378-3379 (2004).

[47] Deegan, R. D.; Bakajin, O.; Dupont, T. F.; Huber, G.; Nagel, S. R.; Witten, T. A. “Capillary flow as the cause of ring stains from dried liquid drops” *Nature,* **389**, 827-829 (1997).

[48] Onsager, L. “The effects of shape on the interaction of colloidal particles” *Annals of the New York Academy of Sciences,* **51**, 627-659 (1949).

[49] Maeda, Y.; Hachisu, S. “Schiller layers in beta-ferric oxyhydroxide sol as an order-disorder phase separating system” *Colloids and Surfaces,* **6**, 1-16 (1983).

[50] Sharma, V.; Park, K.; Srinivasarao, M. “Colloidal dispersion of gold nanorods: Historical background, optical properties, seed-mediated synthesis, shape separation and self-assembly” *Materials Science & Engineering R-Reports,* **65**, 1-38 (2009).

[51] Bawden, F. C.; Pirie, N. W.; Bernal, J. D.; Fankuchen, I. “Liquid crystalline substances from virusinfected plants” *Nature,* **138**, 1051-1052 (1936).

[52] Bawden, F. C.; Pirie, N. W. “The isolation and some properties of liquid crystalline substances from solanaceous plants infected with three strains of tobacco mosaic virus” *Proceedings of the Royal Society of London Series B-Biological Sciences,* **123**, 274-320 (1937).

[53] Robinson, C. “Liquid-crystalline structures in solutions of a polypeptide” *Transactions of the Faraday Society,* **52**, 571-592 (1956).

[54] Morgan, P. W. “Synthesis and properties of aromatic and extended chain polyamides” *Macromolecules,* **10**, 1381-1390 (1977).

[55] Kwolek, S. L.; Morgan, P. W.; Schaefgen, J. R.; Gulrich, L. W. “Synthesis, anisotropic solutions, and fibers of poly(1,4-benzamide)” *Macromolecules,* vol. 10, pp. 1390-1396, 1977.

CHAPTER 8

UNDULATION INSTABILITY IN DROP-CAST POLY(3-HEXYLTHIOPHENE) FILM

8.1 Introduction

It is widely recognized that self-organization in liquid crystalline (LC) phase is a potential strategy to control the order and packing of organic semiconductors [1-3]. A key advantage of the self-organizing nature in LC phase is the ability to reduce defects caused by grain barriers between neighboring liquid crystalline domains through self-healing process. These materials possessing LC phase may be annealed in the mesophase, so that the high degree of uniform molecular alignment is obtained via self-healing, and then locked in by subsequent crystallization [4, 5].

There is much literature reporting that some poly(3-alkyl thiophenes) (P3ATs) such as poly (3-dodecylthiopene) undergo thermotropic transitions to a LC phase [6-8]. For P3ATs with alkyl side-chain lengths long enough to interdigitate with side chains of adjacent polymer backbones, the secondary structural ordering at alkyl-chain ends have been known to induce an LC phase in thermotropic system [7, 8]. However, there are no reports of poly(3-hexylthiophene) (P3HT), one of the best performing semi-conducting polymers [9-11], forming a thermotropic LC phase. The absence of a thermotropic LC phase in P3HT was interpreted as a result of the end-to-end structure of P3HT where the short side chains do not interpenetrate [12]. Recently, however, Segalman and coworkers [13, 14] reported a thermotropic LC phase in poly(3-(2’-ethyl)hexylthiophene) (P3EHT). While P3EHT has a functionalized side chain, its length is analogous to that of P3HT. Thus, it is likely that a steric hindrance as well as the length of side chain play an important role in forming a thermotropic LC phase. While there have been numerous studies of phase transition into LC phases in a thermotropic system, the study of a lyotropic system of P3HT is rare. In practice, most polymeric conducting layers are fabricated via solution process and most solution processible semiconducting polymers are thought to be more rigid than coil-like polymers such as polystyrene (PS) [15, 16] because of its π-conjugated structure and stiff units in backbone. Since solutions of rod-like macromolecules often exhibit liquid crystalline phases at high concentrations [17-23], therefore, we cannot rule out the possibility of lyotropic LC phases in rr-P3HT solution as proposed in chapter 7.

In this chapter, we propose further evidences that concentrated P3HT solutions can exhibit a lyotropic LC phase, supporting the results described in chapter 7. We prepared rr-P3HT films via drop-casting and observed interesting patterns formed in the periphery of casted film, which originate from undulating instabilities. We focus our effort on interpreting the formation of undulating instability in a casted film, showing a periodic optical oscillation based on the undulation pattern attributed to layered structure in LC phase of DNA. In addition, the optical characterization of highly concentrated rr-P3HT solution will also provide an evidence to support the existence of LC phase of rr-P3HT in a lyotropic system.

8.2 Experiments

8.2.1 Optical and Topographic Characterization

We used regio-regular P3HT (rr-P3HT) (a M_n of 24kD and M_w of 47.7 kD with 94% head-to-tail, Sigma-Aldrich), and the solutions were prepared in air, by dissolving the rr-P3HT in 3 different solvents, chloroform ($CHCl_3$), thiophene, and toluene. The initial concentration of solutions was ca. 0.3 wt%. Films of rr-P3HT were made by drop-casting on a glass at room temperature.

Modulation of birefringence in cast films was observed with rotating crossed polarizers against the sample stage that was kept fixed, instead of rotating samples, using an optical microscope (Leica RDX). The AFM measurements were performed to characterize the topography of the film surface in the solid state with a Veeco Digital Instruments Dimension 3100 scanning probe microscope in tapping mode with a silicon tip.

8.3 Results and Discussion

8.3.1 Periodic Modulation of Birefringence and Molecular Orientations

As shown in Figure 8.1, from the drop-cast P3HT film (circular shape with 15mm diameter) from 10 ㎕ solution ((rr-P3HT + $CHCl_3$), 4.5 *mg/mL* (0.3wt%)) on a glass substrate, periodic stripe patterns are observed at the edge of the film. Under crossed polarizers, these patterns exhibit alternating dark and bright striated patterns with a periodicity of 40 ~ 45 ㎛ as shown in Figure 8.1 (b)-(d).

It is interesting that the birefringence periodically changes upon rotating the crossed polarizers with respect to the direction parallel to the contact line of cast film. The area behind the contact line, which is followed by the emergence of striated patterns, shows a gradual change in brightness according to the polarization direction of light with respect to the direction of contact line. It is darkest when the polarization direction is parallel or perpendicular to the direction of contact line (Figure 8.2 (b) and (h)) and gradually becomes brighter as we rotate crossed polarizeres. When the angle between contact line direction and the polarization direction becomes 45°, the brightest birefringence occurs (Figure 8.2 (e)) under crossed polarizers. This modulation of birefringence shows 4-fold symmetry through the entire rotation of crossed polarizers (360°). This indicates that the distribution of optic axis coming from P3HT chains has anisotropic nature and that the preferred direction of chain alignment, ***n***, is either parallel or perpendicular to the contact line direction.

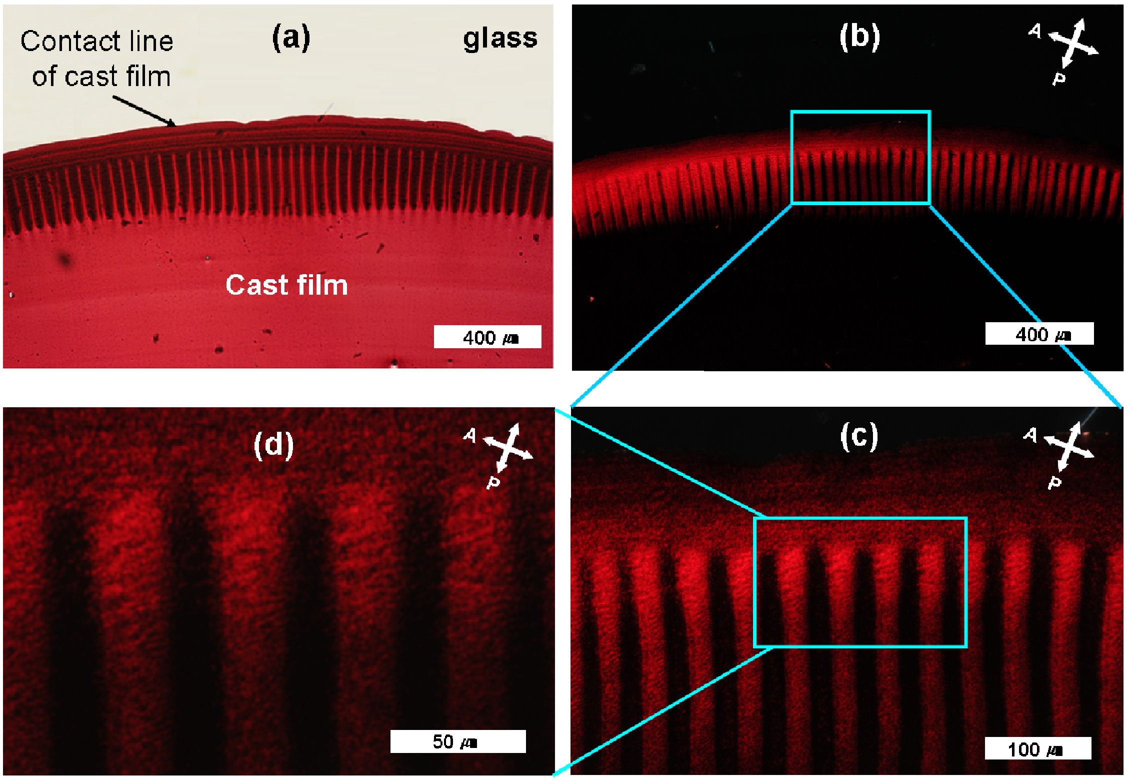

Figure 8.1 Optical images of drop-cast film with rr-P3HT dissolved in $CHCl_3$; (a) optical image without polarizers, (b)-(d) Optical images of the area with striated patterns under crossed polarizers (the direction of polarizers is presented with white crosses, **P**; polarizer, **A**: analyzer). The diameter of deposited film (circular shape) from 10 *μℓ* solution drop was ca. 15 *mm*.

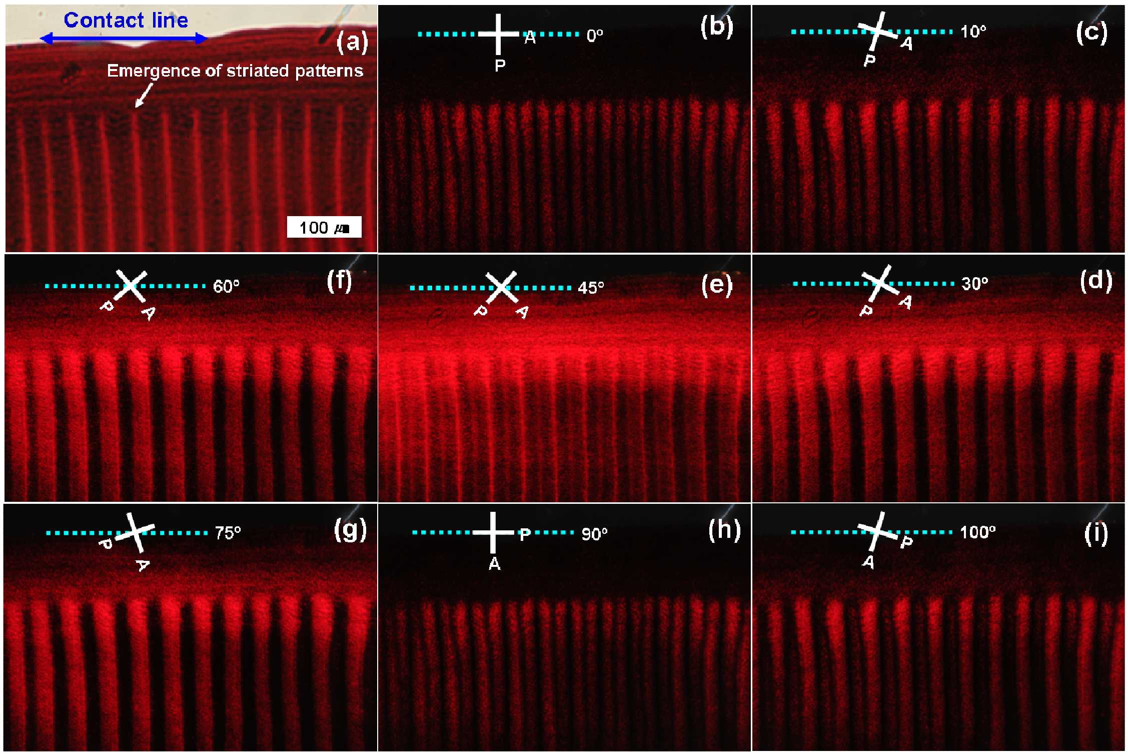

Figure 8.2 Optical images at the area of striated patterns; (a) without polarizers, (b)-(j) under crossed polarizers, of which direction is tilted in consecutive order from 0° to 100 °. Optical images under crossed polarizers, (b)-(i), has the same magnification with (a).

Birefringence of striated patterns appears as the bright regions interrupted by thin dark parallel lines (Figure 8.2 (b) and (h)) when the direction of polarizers is parallel or perpendicular to the direction of contact line. They transform into an alternation of bright and dark bands (Figure 8.2 (d)) with the rotation of crossed polarizers. This modulation of birefringence also exhibit 4-fold symmetry upon the rotation of 360° and is reminiscent of the modulation of birefringence coming from the undulating pattern in the columnar hexagonal phase of DNA solution [24, 25]. Livolant and coworkers illustrated multiple textures depending on the orientation of undulated molecules with respect to the projection plane under crossed polarizers. Different situations of the undulation textures in the columnar hexagonal phase of DNA are illustrated in Figure 8.3. They represented a modulation of molecular orientation as solid lines for the simplicity. They supposed the presence of disclination lines (δ) due to the undulation of layers and reported that molecular orientations follow sinusoidal paths in the projection onto the observation plane when these disclination lines are normal to the plane (Figure 8.3 (a)). In this situation, birefringence texture from top view yields the modulation leading to thin dark lines (left in Figure 8.3 (a’)) which extend and move when the crossed polarizers is slightly rotated (middle in Figure 8.3 (a’)). Further rotation makes the thin dark lines transform into broad dark bands whose number is reduced by a factor of 2, which alternate with light bands (right in Figure 8.3(a’)). When the concentration of DNA increases, the regular curvature of the layers in Figure 8.3 (a) disappears and there are discontinuity walls as shown Figure 8.3 (b). In this situation, alternating dark and bright bands are still observed, but the extinguished lines do not move the position continuously anymore upon rotating crossed polarizers. Instead, fully extinguished bands occur when the molecular orientation directions are parallel to one of the polar directions (Figure 8.3 (b’)).

The former (Figure 8.3 (a’)) is the case of the variation observed in our birefringence texture upon rotating crossed polarizers. Figure 8.4 shows the modulation of birefringence (left) and their schematic representation of birefringence patterns resulting from molecular orientations with respect to the polar directions (right). The observations are exactly the same with the case of undulation textures of the columnar hexagonal phase with sinusoidal patterns, that is, patterns with thin dark lines (Figure 8.4 (a)) is moving and widening when polar directions slightly changes (Figure 8.4 (b)) and then transform into alternating dark and light bands with further rotation (Figure 8.4 (c)). It is in agreement with that the number of extinguished lines reduce by a factor of 2 (4 in (b) → 2 in (c)) as previously reported [24]. The change of birefringence in striated bands is easily understood from the relation of molecular orientation and the polar directions.

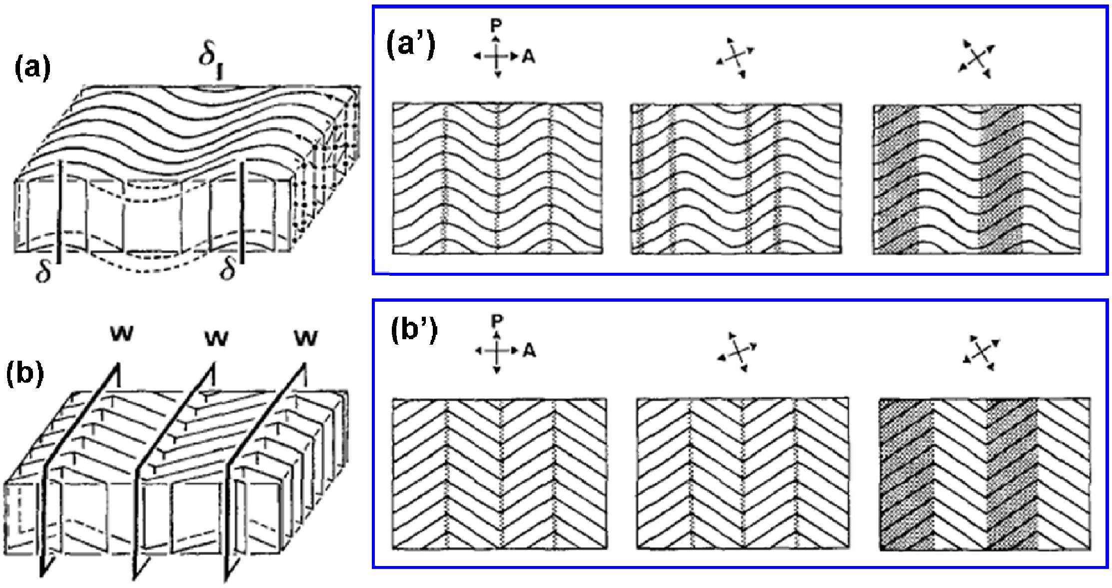

Figure 8.3 Undulation textures of the columnar hexagonal phases and the corresponding representations of birefringence texture from top view; (a) Undulations of the planes of molecules, represented with solid lines, around disclination lines (δ). (a') Birefringence textures from top view illustrate that the domain appears bright except the thin lines along where molecules are aligned parallel to one of the polar directions (left) and these lines extend and move with slight rotation of crossed polarizers (middle), which transform into alternate dark and light bands upon rotating further (right). (b) The increase of concentration of DNA straighten the sinusoidal pattern of molecular orientation and (b') the corresponding birefringence textures exhibit no movement of extinguished lines. [Reprinted from ref. [25] with permission]

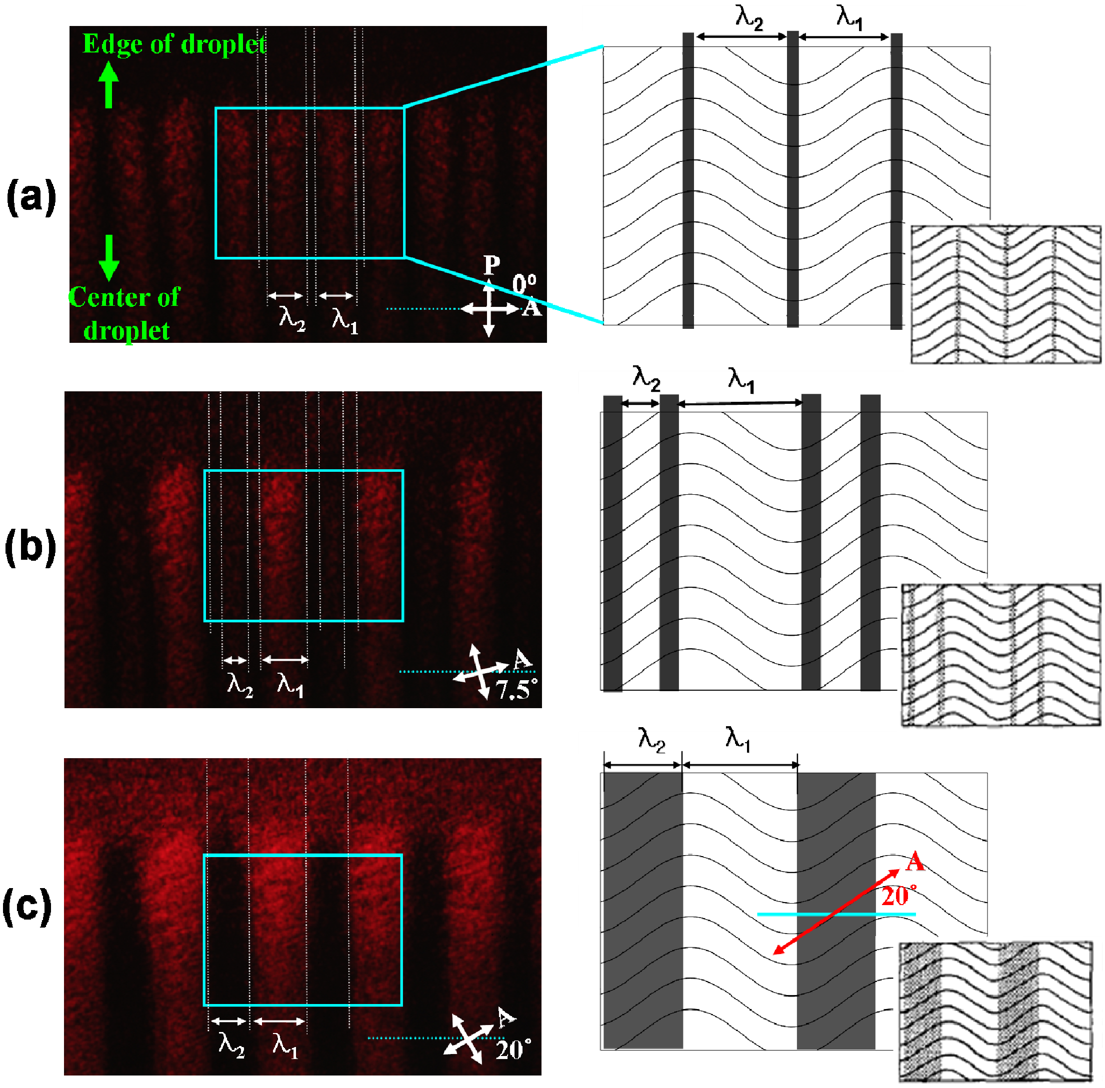

Figure 8.4 Optical images under crossed polarizers (left) and their schematic representations with respect to the molecular orientation for the area highlighted with light-blue box (right). (a) Thin dark lines appear when one of the polar directions parallel to stripe direction, (b) dark lines extend and move with slight rotation of crossed polarizers, and (c) when one of polar directions is tilted with ca. 20°, the number of dark lines reduce by factor of 2 (4 → 2) and broad alternating (dark and bright) bands show up. In order to compare our schematic representations (right column) corresponding to optical observations (left column) with the representation by Livolant and Leforestier, insets in right column were reprinted from ref. [25] with permission.

Figure 8.5 presents thin darkest (Figure 8.5 (a)) and brightest stripe lines (Figure 8.5 (b)) that appears when polar directions are parallel and are 45° with respect to the stripe lines direction, respectively. It also shows the 4-fold symmetry through the entire rotation of 360 °. Accordingly, it seems that the distribution of optic axes, ***n***, projected on the plane in these stripe lines, is preferred either parallel or perpendicular to the direction of stripe. From the birefringence pattern in Figure 8.6 that the darkest and brightest broad bands appear when the angle between polar directions and contact line direction becomes 17.5° and 62.5°, respectively, we can approximate the sinusoidal pattern of projected ***n*** on the plane, in which the projected direction of ***n*** is tilted with 17.5° with respect to the direction of contact line.

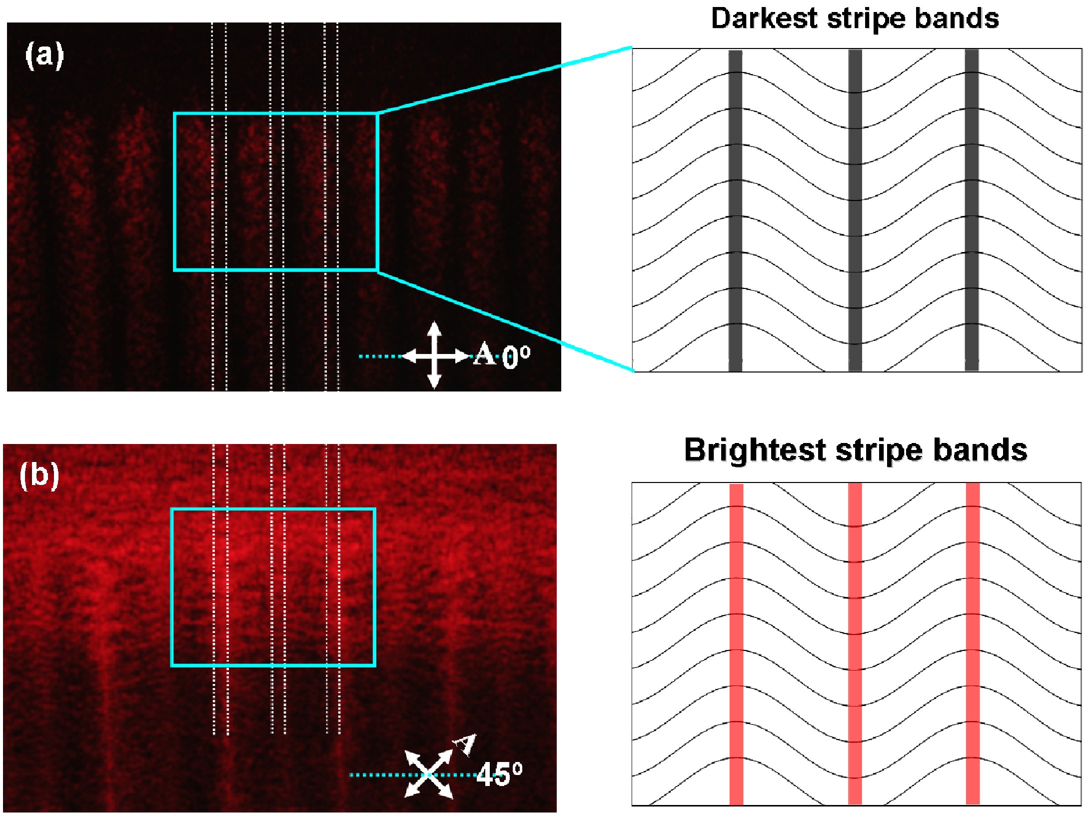

Figure 8.5 (a) The darkest stripe lines appear when one of polar directions is parallel to the stripe direction. (b) Stripe lines show brightest birefringence when polar directions are tilted at ± 45° with respect to the stripe direction.

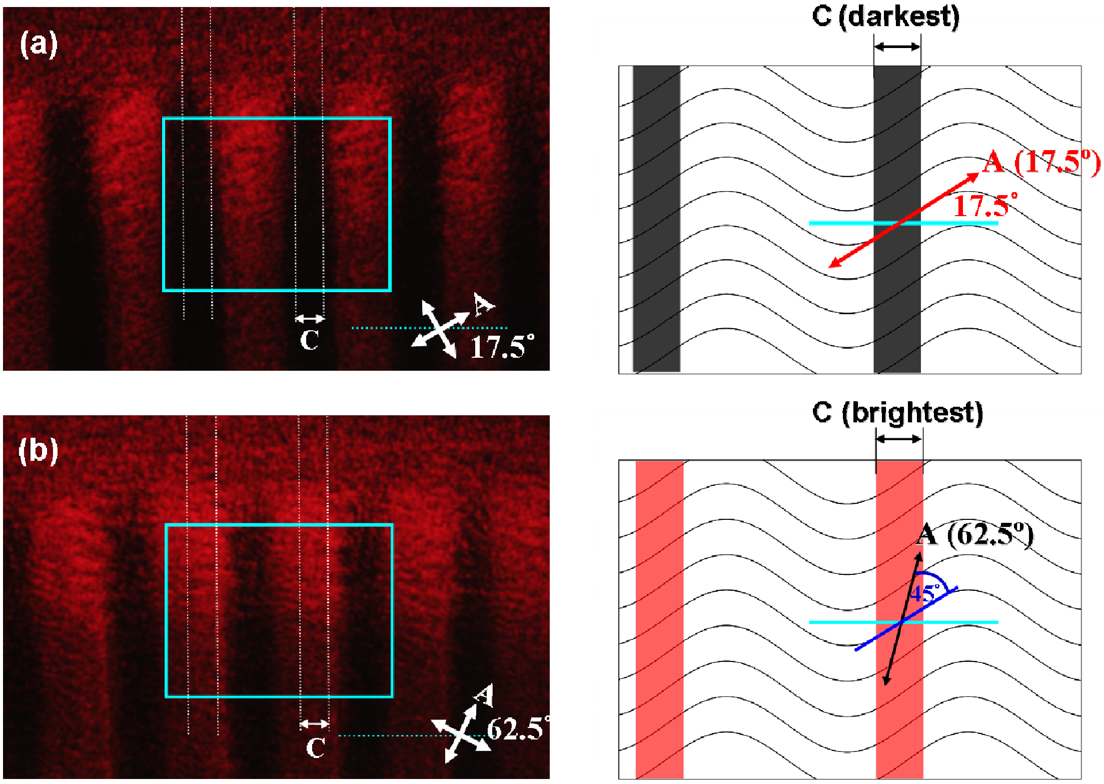

Figure 8.6 (a) The darkest broad bands appear when one of polar directions is tilted at 62.5° with respect to stripe direction (or 17.5 ° with respect to the contact line direction). (b) Stripe bands show the brightest birefringence when one of polar directions is tilted at 17.5° with respect to the stripe direction (or 17.5 ° with respect to the contact line direction).

Another interesting observation is the existence of pattern similar to defects occurring in undulating patterns of columnar hexagonal phases of biopolymer [24]. Livolant and Bouligand illustrated three possible defects (see Figure 8.7 (a)); two stripe pattern are added simultaneously either at a point of maximum curvature (I and II in Figure 8.7 (a)) or at an inflexion point (III in Figure 8.7 (b)), yielding branched patterns (I and II in Figure 8.7 (a)) or flame patterns (III in Figure 8.7 (a)), respectively under crossed polarizers [24]. In their literature, only the first (I) and the third (III) ones were reported to be observed from the texture of layered systems of biopolymer. We compared optical images of striated patterns in P3HT film and their schematic representation of defects. Defect-like stripe patterns, which composed of 5 stripe patterns are added into 3 stripe patterns, observed in rr-P3HT film (Figure 8.7 (b)) resembles the third one (III) in Figure 8.7 (a).

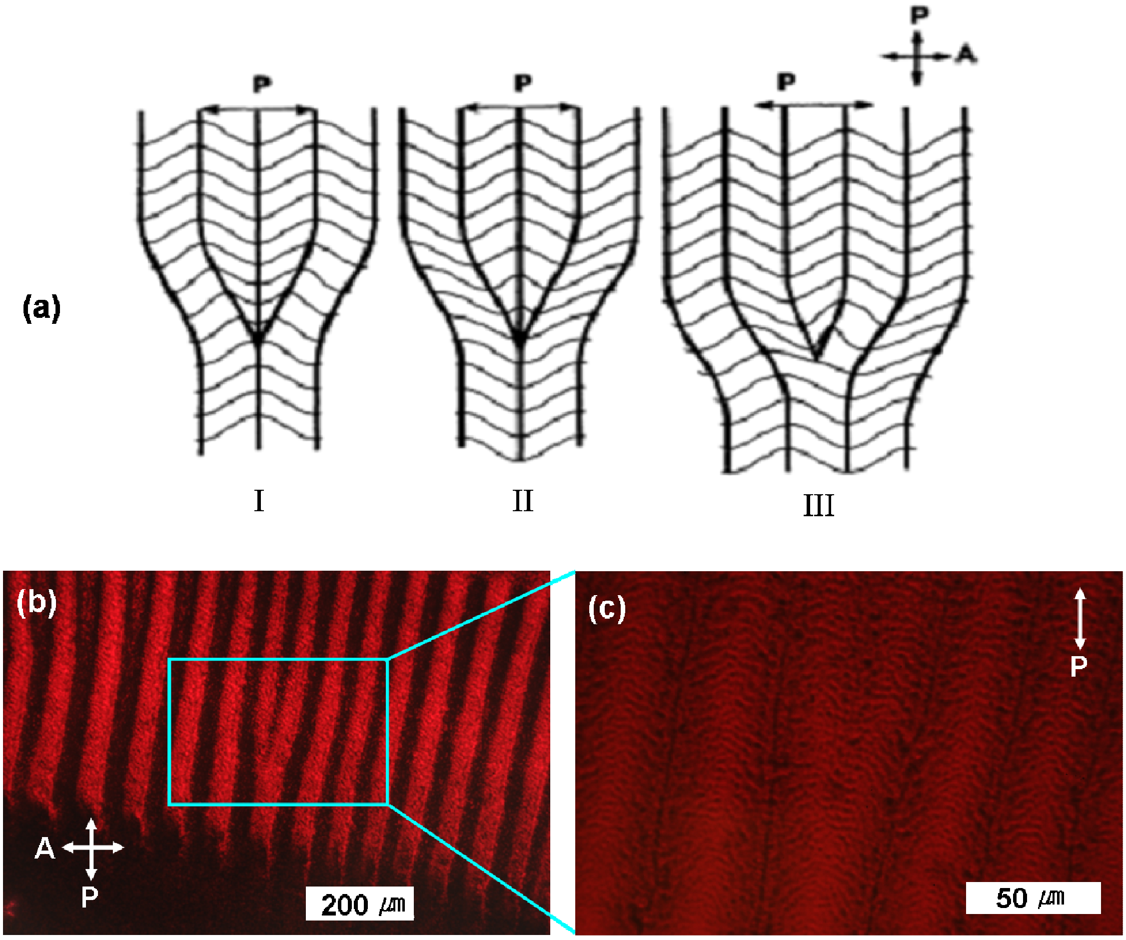

Figure 8.7 (a) Defects occurring in columnar hexagonal phase of DNA solution reprinted from ref. [16] with permission. (b) Optical image of defect in the striated patterns under crossed polarizers and (c) optical image under the polarization of incident beam without analyzer within the area highlighted with light-blue box in (b).

8.3.2 Undulation Instability

As described above, the birefringent patterns at the edge of rr-P3HT film closely resembles that of undulating structure seen for concentrated DNA solutions in their columnar hexagonal phase [24, 25]. Hence, we characterized the topography of the patterned region using AFM. Figure 8.8 presents the AFM images (2D: Figure 8.8 (b) and 3D: Figure 8.8 (c)) and depth profile (Figure 8.8 (d)) that show the undulating topography with the amplitude of 500 ~ 600 *nm* and 40 ~ 45 *µm* periodicity. Figure 8.9 visualizes the topographies of the area where the instability appears (Figure 8.9 (b) and of the area where the instability decays (Figure 8.9 (c)). The propagating length of undulation is 200~240 ㎛ (Figure 8.9 (a)). We also measured the thickness of the edge of the film including undulating regions using a profilometer (Figure 8.10). As shown in Figure 8.10, the thickness of the patterned area is 1.0~1.6 ㎛, and the thickness inside film is decreased into 0.4 ㎛. Hence, it is likely that the amplitude of undulation (500 ~ 600 *nm*) conforms to about 1/3 of the film thickness of corresponding area.

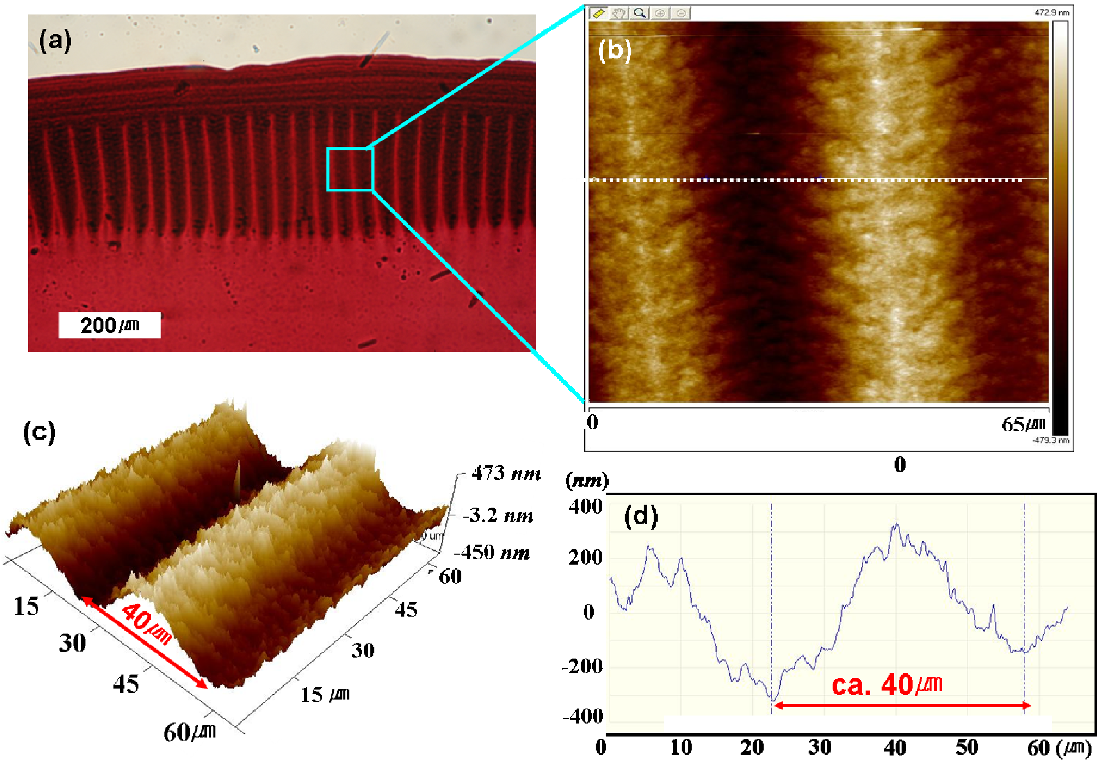

Figure 8.8 (a) Optical image of drop-cast film shows p (b) 2D and (c) 3D AFM image of the striated patterned area highlighted with light-blue box in (a), and corresponding depth profile for the undulation with ca. 600 nm amplitude and 40 ㎛ periodicity.

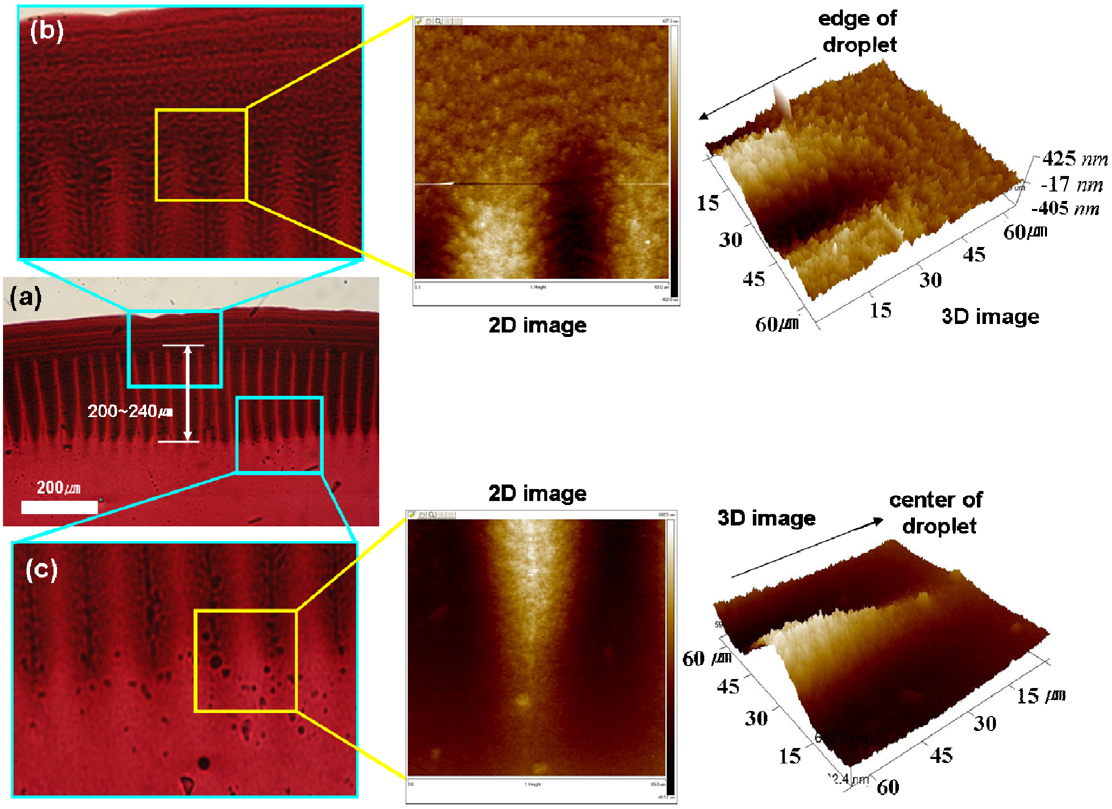

Figure 8.9 Optical images of drop-cast film: (a) the length of undulation is 200~240 ㎛. (b) the emergence of the ripple of undulation, which propagates inward the radial direction and (c) decay at the length of 200~240 ㎛. AFM (2D and 3D) images clearly show the emergence and decay of undulation.

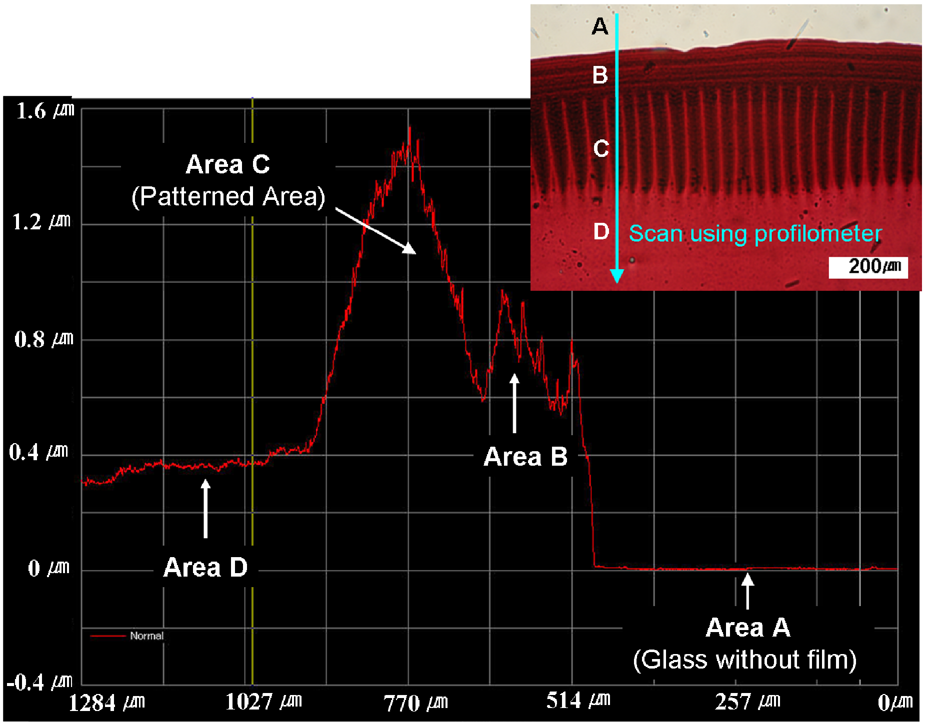

Figure 8.10 Profile of film thickness using a profilometer. **A-D** corresponds to the measurement areas shown in the inset of optical image.

This wavy undulation shown in AFM images is also very similar to the undulation formed in drying droplet of DNA through liquid crystalline phase [26]. (see Figure 8.11) Smalyukh et al. showed the periodic undulating pattern formed in the edge of drying DNA solution drop on glass and explained it based on the model of liquid crystal (LC) nature appearing at high concentration. The mechanism of the undulation formation they proposed was explained by the hydrodynamics in the formation of coffee ring, as in colloidal suspensions [27]. Faster solvent evaporation at the contact line induces outward solution flux in order to replenish the lost solvent, which transports DNA and increases DNA concentration at the edge of drop. DNA at high concentration forms a liquid crystalline phase and the drop at this stage has a birefringent wedge-shaped LC ring with optic axis, ***n***, parallel to the contact line, which is still pinned at the initial location. The orientation of DNA is reported to be parallel to the contact line direction, *i.e.*, perpendicular to radial direction, and Rey rationalized this counterintuitive alignment in terms of minimum elastic deformation energy of liquid crystal nature [28].

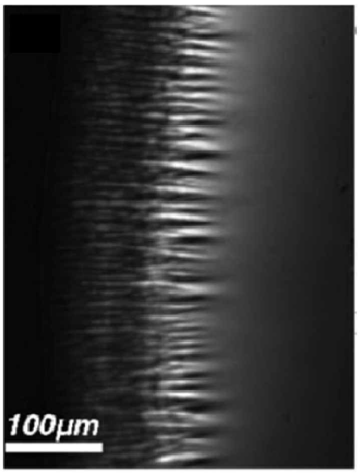

Figure 8.11 (a) Undulating pattern image of drying DNA solution droplet under crossed polarizers. The crossed polarizer and analyzer are at 30º to the vertical and horizontal directions of the image [Reprinted from ref. [26] with permission].

It has been well known that highly concentrated DNA can form layered LC phases such as columnar hexagonal and cholesteric phases [25, 29, 30], and in many layered systems (smectic [31, 32], columnar hexagonal LCs [25, 26], lamellar phase of diblock copolymers [33, 34]), curvature deformation appears as the undulation instability responding to the field-induced stress. In the evaporating sessile drop, contact-line pinning and the receding contact line may be the primary physical processes corresponding to the relaxation of the field-induced stress. During the evaporating process, outward solution flux transports solutes to the edge of drop and the concomitant increase in concentration results in pinning of the solution edge and forms a LC phase [35]. Should this LC phase have a layered structure, the imposed stress on pinned area may be relaxed by the contact line retraction and may induce a dilatation of layers [26]. Thus, the undulation instability observed in drying DNA-solution drop was attributed to the layered structure in an LC phase at high concentration and radial dilatation via pinning/retraction of contact line.

Returning to the appearance of wavy undulation of rr-P3HT film, let us consider the possibility of liquid crystalline phase of rr-P3HT solution at its high concentration. According to the report by Heffner and Pearson [36], a persistence length of regio-random P3HT (40K <Mw< 220K in THF and in $CHCl_3$) is 2.4±0.3 nm, which may not reach the inherent chain stiffness to form anisotropic liquid crystal phases in solution [18, 22]. Despite the fact that we are not able to find any report that characterizes the persistence length of rr-P3HT as a function of its concentration upon the formation of film, we can presume the persistence length of highly rr-P3HT (HT, >94%) longer than that of regio-random P3HT, *i.e.*, 2.4±0.3 nm. It is because ordering of the side chains can increase the stiffness of the polymer backbone. In addition, upon solvent evaporating, concomitant concentration increase may induce the polymer backbone to be more planar by chain crowding effect, thus makes it significantly stiffer. Thus, it is presumed that rigidity of rr-P3HT backbone increases with the increasing concentration via solvent evaporation. Should the rigidity of rr-P3HT become high enough to form anisotropic liquid crystal orderings, at its high concentration, the undulating instability and the periodic oscillation of director orientation observed from the birefringence texture may support the existence of a liquid crystalline phase before solidification.

Another noticeable observation is that undulating patterns occur several times at different location by pinning process in the drop-cast film from P3HT+$CHCl_3$ solution. In Figure 8.12 (a), we observed several pinning of contact lines pointed with arrows, which leave more deposited P3HT at these lines and make them look darker red in optical image. While the intensity modulation is weak, the modulation of birefringence for these striated patterns (Figure 8.12 (b)) upon rotating crossed polarizers follows the same manner explained in section 8.3.1. AFM analysis in Figure 8.12 (c) shows that there is still weak undulation (amplitude of 200~250 *nm*, wavelength of about 22 ㎛, and length of ~ 45 ㎛) in these secondary patterns. It is noteworthy that periodicity of undulating pattern and propagating distance becomes narrower and shorter than those of primary ones (periodicity of 40~45 ㎛ and length of 200~240 ㎛). This is consistent with the fact that a periodicity of undulation from the smectic/lamellar LCs is proportional to the sample thickness [26, 37, 38]. Thus, it may be thought that liquid crystalline nature and the contact line pinning process are responsible for the formation of these undulations with periodic variation in the intensity under crossed polarizers.

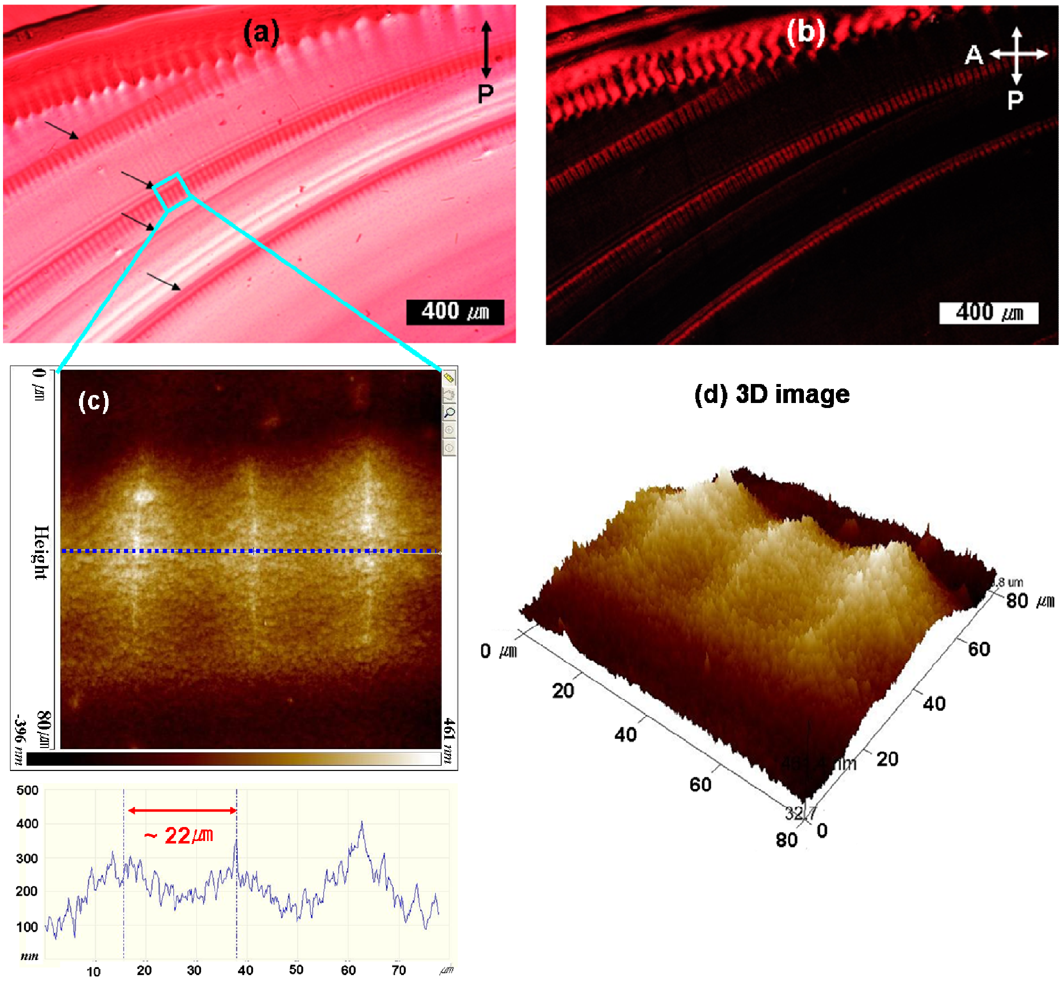

Figure 8.12 Optical image of the area where several pinning processes occur in the drop-cast film (rr-P3HT+$CHCl_3$) (a) without polarizer and (b) under crossed polarizers. Lines pointed with arrows in (a) are the pinned contact lines. The modulation of birefringence of patterns in each contact line follows the same manner of the modulation described in Figure 8.4 and 8.5. (c) and (d) presents 2D and 3D topography of the area highlighted with light-blue box in (a), respectively. Amplitude, periodicity, and the length of the undulation is 200~240 *nm* and ~22 ㎛, 40~50 ㎛ respectively.

8.3.3 Solvent Evaporation Rate Effect on the Formation of Undulation

Although we proposed the relevance of LC phases with the formation of periodic undulating instability, the results of optical and topographic analysis are limited to a dried film, not a liquid crystal itself. Should an equilibrium LC phase, however, exist before the evaporation-induced solidification, it is highly possible that liquid crystalline ordering would be frozen into the solid state by fast evaporation. The optical images in Figure 8.13 show the effect of solvent evaporation rate on the pattern formation. Using 3 different solvents, of which evaporating rates at room temperature are different one another, ($CHCl_3$ (b.p: 61.2℃), thiophene (b.p: 84℃) and toluene (b.p: 110.6℃)), we prepared rr-P3HT film via drop-casting. Except the kinds of solvent, we kept other factors, such as the initial concentration of solution (0.3 wt%), volume of drop (10 $\mu\ell$) and substrate, fixed. Figure 8.13 shows the definite difference in the formation of undulating patterns: (a) drop-cast film using $CHCl_3$, of which evaporation rate is fastest, exhibits a clear formation of undulating pattern as described in previous section, (b) the evaporation rate of thiophene is in the middle between those of chloroform and toluene, and undulating pattern is observed from the cast film. However, the patterns show a narrow periodicity and the sharpness is a little bit blurry compared with those obtained using chloroform. (c) For toluene, no patterns are observable through optical microscope, but circumferential birefringent bands are remained. (see the bands along the contact line pointed with white arrow in Figure 8.13 (c))

In an evaporating droplet deposited on the substrate, the faster solvent evaporation at the edge with a pinned contact line leads to the faster solution radial flow [27]. Hu and Larson studied that the stretching behavior of polymer chains, which is coiled DNA chains in dilute solution, is strongly affected by the evaporation rate of droplet in the flow field [39]. Experiment and simulation of DNA solution drop, for example, show that DNA molecules deposited at the edge of the droplet are more highly stretched under fast evaporation conditions than under slow ones [39, 40]. The strong Stokes drag may extend the DNA chains [41, 42], which may reinforce the chain ordering at the rim. Hu and Larson [39] developed a finite element method (FEM) model to solve the vapor concentration distribution and the evaporation flux above a sessile DNA droplet. In their literature, the evaporation flux along the droplet surface is not uniform and becomes singular at the edge of the droplet as suggested by Deegan et al.[27]. Hence, different evaporation rate of solvent may drive different evaporation flux on the surface, which affects the amount of solute deposited, concomitant local viscosity, and receding rate of contact line. As a result, the stress imposed on the pinning and its relaxation from the retraction of contact line must be affected by evaporation rate. In order to elucidate the mechanism of pattern formation, systematic studies of the effect of hydrodynamics in evaporating droplet on the pattern formation need to be performed for the future study.

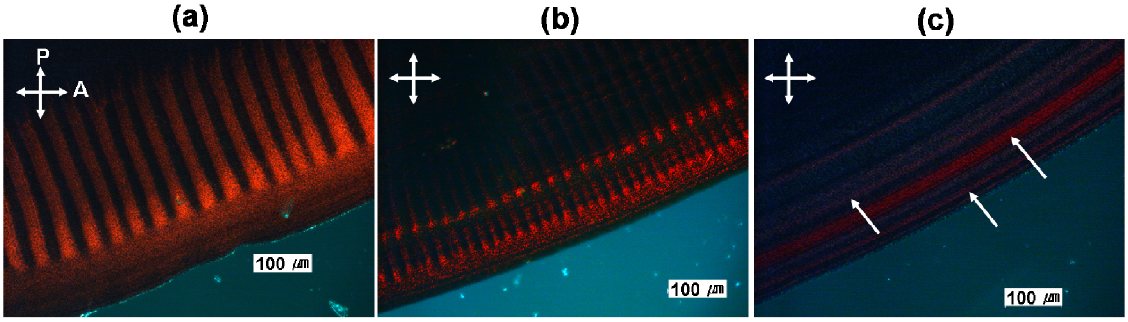

Figure 8.13 Optical images under crossed polarizers of drop-cast film using (a) $CHCl_3$, (b) thiophene, and (c) toluene as a solvent. White arrows in (c) point the circumferential birefringent bands along contact line of the film.

Optical images of the center area of cast film under crossed polarizers supports the effect of evaporation rate on chain alignments and the freezing of aligned chains. Figure 8.14 show the optical images of the center area of cast films that show maltese cross-like texture. A maltese cross rotates parallel to the polar directions upon rotating crossed polarizers (see Figure 8.15 for the case of the sample using chloroform), which means that alignments of P3HT chains were induced during the film formation. Since, in an evaporating sessile drop, a radial flow of solution is expected, the P3HT chains might be stretched along the same direction, which corresponds to the rotation of dark brush. It is noticed that the extent of birefringence and the sharpness of brush depends on the evaporation rate. As the evaporation rate increases (chloroform > thiophene > toluene), the feature of maltese cross-like texture becomes clear. The difference of the extent of birefringence and the sharpness of maltese cross-like texture may support that flow induced stretched P3HT chains can be frozen into solidification due to the fast evaporation.

Chain alignments and freezing effect of evaporation, responsible for the formation of dark brush, is demonstrated also by changing evaporation rate with the same solvent. Figure 8.16 shows POM images of center area of drop-cast rr-P3HT film using the same solvent, 1,2,4-trichlorobenzne (1,2,4-TCB, b.p. 214.4 °C), when the evaporation rate was changed by circulating air with heat. Figure 8.16 (a) is POM image of drop-cast film at room temperature, thus it took over 12 hours for complete evaporation. So, at very slow flux, weak or no stretching effect is expected. In addition, there may be enough time for polymer to relax to disorder, even though weak alignment of P3HT occurs via weak radial flow. Whereas the drop-cast film under the air-circulation with heating (it took 5 minutes for complete evaporation) exhibited a dark brush parallel to polarizer/analyzer directions.

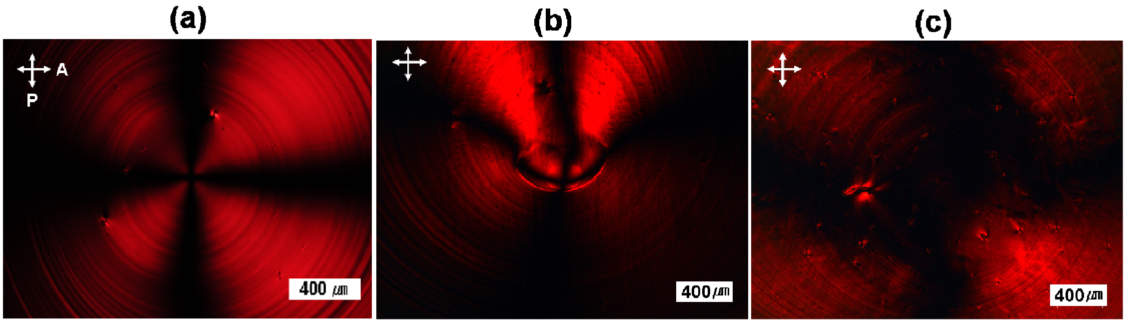

Figure 8.14 Optical images under crossed polarizers of the center area in drop-cast film using (a) $CHCl_3$, (b) thiophene, and (c) toluene. White arrow in each image points the area where the solution evaporated last.

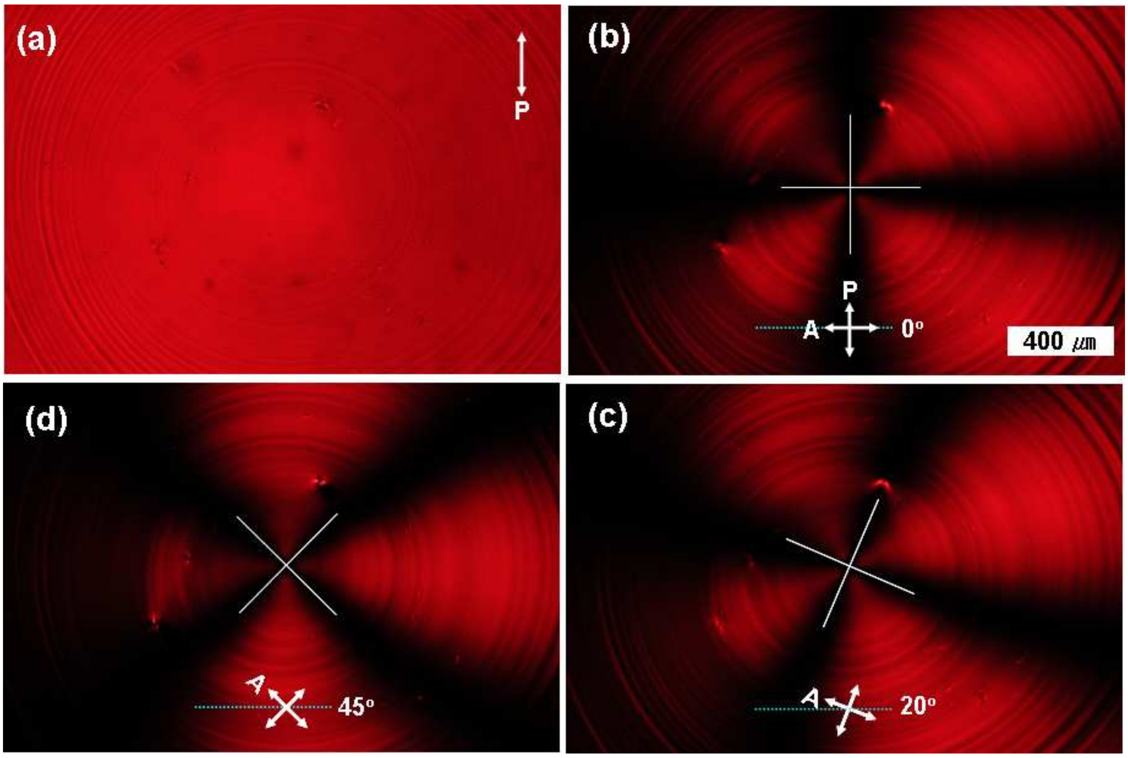

Figure 8.15 Optical images of the center area in drop-cast film using $CHCl_3$, (a) featureless texture using only polarizer, and (b)-(d) POM texture under crossed polarizers with different rotating angles of crossed polarizers.

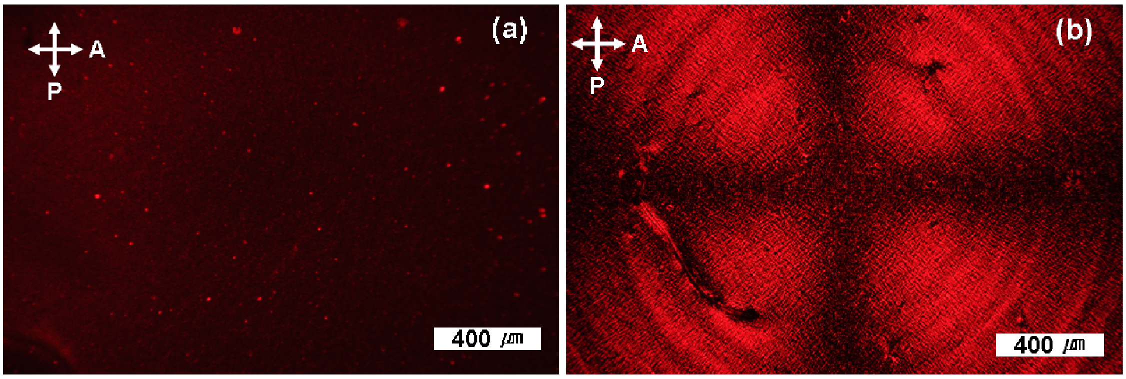

Figure 8.16 POM images of drop-cast film using 1,2,4-TCB at different evaporation environment; (a) room temperature without air-circulation and (b) under strong air circulation with heating. Time for the complete evaporation was over 12 hours (a) and 5 minutes (b).

As seen from these results, the formation of undulating patterns strongly depends on the solvent evaporation rate. Should fast evaporating solvent extend polymer chains and their stacking occur at the edge of droplet, it may be possible to think of forming liquid crystalline order. While it is too early to conclude, it is plausible scenario that the formation of undulating instability with periodic optic oscillation is originated from the liquid crystalline order and radial dilatation in the evaporation-induced flow field, of which structure is frozen by fast solvent evaporation.

8.3.4 Observation of POM Textures of Highly Concentrated rr-P3HT Solution

The results from Raman measurement in chapter 7 and the observation of the undulating patterns with oscillating director alignment support the existence of a lyotropic liquid crystalline phase of rr-P3HT. Thus, we attempted to prepare rr-P3HT solution using 1,2,4-TCB with different concentrations in order to observe the critical concentration for LC phases. When we increase the initial concentration of rr-P3HT (M_n of 24kD and M_w of 47.7 kD) dissolved in 1,2,4-TCB at temperature, a small fraction of the polymer precipitated out. So, we prepared 3 wt% rr-P3HT solution dissolved in 1,2,4-TCB and constantly stirred the solution using a magnetic bar at high temperature (130ºC). We allowed the solvent to evaporate by opening the bottle of solution while constantly stirring it at high temperature. By doing this process, we could obtain the solution with higher concentration without precipitation observed, but we failed to calculate the concentration variation. We filled the solution into a flat capillary (inner dimension is 100 ㎛ (depth) × 1000 ㎛ (width)) as a function of time. Since it was quite viscous, the solution was not filled into the entire space by capillary action, but into a part of the capillary. After filling the viscous solution, the ends of the capillary were sealed with epoxy in order to prevent further solvent evaporation.

Figure 8.17 presents a series of optical images of the capillary filled with concentrated rr-P3HT solution. (Again, we do not know the concentration) Optical image without polarizers in Figure 8.17 (a) is featureless except the absorption color. Under crossed polarizers, however, we could detect the periodic change of birefringence over large areas, and observe 4-fold symmetry for rotation under crossed polarizers (360°) (Figure 8.17 (b) ~ (h) with 15° intervals).

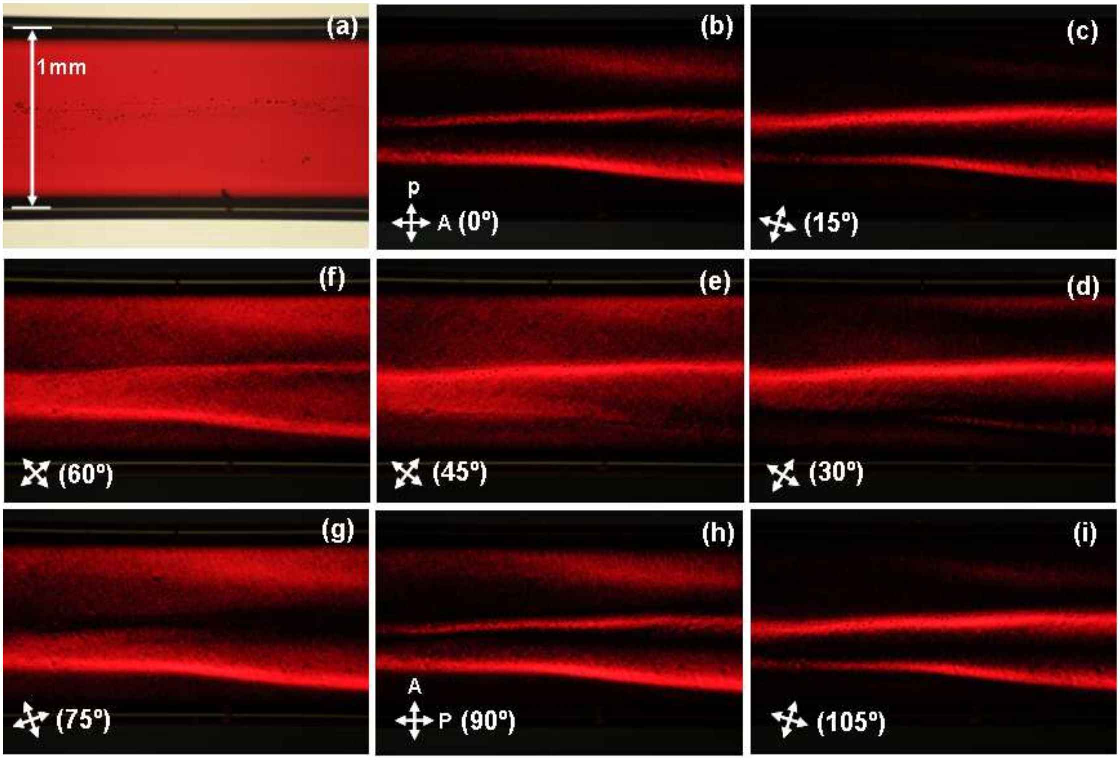

Figure 8.17 Optical images of a capillary filled with concentrated rr-P3HT solution in 1,2,4-TCB; (a) without polarizers and (b)-(i) POM images with the rotation of crossed polarizers with 15° intervals.

While POM images do not show a perfect mono-domain within the entire area of the sample, there exists macroscopic orientation of rr-P3HT in several parts of areas with hundreds of μm^2, which is much larger than the molecular scale. One may doubt that this periodic birefringence has nothing to do with liquid crystalline ordering, but is originated from the shear induced chain alignments when the solution was filled by capillary action.

Should it result from only the chain alignment by shear effect, however, the aligned structure is not an equilibrium state, thus it must relax into disordered state with time. However, we could observe the same birefringent texture at even 5 months after the first observation. In addition, there remained the fluidity of sample inside the capillary when we poked the sealed capillary using tweezers. It means the periodic birefringence results from an equilibrium ordered state of rr-P3HT with remaining solvent, *i.e.,* liquid crystalline phase.

Although these optical observations point to a liquid crystalline phase, we do not know the critical concentration for the formation of liquid crystalline phase of rr-P3HT. Therefore, the elucidation of the critical concentration for LC phases and a phase diagram needs to be mapped out.

8.4 Conclusions

In this chapter, we summarized the undulating pattern with periodic optic oscillation at the edge of drop-casted rr-P3HT film. Optical and topographic characterizations were compared with the undulating pattern originated from columnar hexagonal phase of DNA, which is closely reminiscent of our sample. We proposed that the undulating pattern can be attributed to the existence of liquid crystalline phase of rr-P3HT and a radial dilatation by pinning/retraction process of contact line in an evaporating drop may play a role in forming the undulating pattern. The formation of the undulating patterns strongly depends on the rate of solvent evaporation; using fast evaporating solvent ($CHCl_3$) its formation is much clearer and the periodicity of undulation is wider than that using slow evaporating solvent (thiophene and toluene). Finally, we observed characteristic features of POM textures in capillary tubes filled with highly condensed solution, which looks similar to a schlieren texture of nematic liquid crystal. These features were observable even after long time (5 months) and the sample still show its fluidity. Direct observations of the characteristic features of LC phase combined with the formation of undulating patterns support the result of chapter 7, the existence of lyotropic liquid crystalline phase of rr-P3HT.

While we associate the formation of undulating pattern with a layered LC phase of rr-P3HT, we also need to open the possibility that the undulating pattern observed in this chapter is a thermal gradient driven instability [43-46]. Although it must be complicated and difficult to carry out experiments in a controlled fashion to prove the temperature gradient instability formation in an evaporating solution, an meticulous and systematic approach to test the temperature gradient instability is strongly demanded and it will be very helpful to elucidate the mechanism of the formation of undulating pattern.

8.5 References

[1] Pisula, W.; Zorn, M.; Chang, J. Y.; Mullen, K.; Zentel, R. “Liquid Crystalline Ordering and Charge Transport in Semiconducting Materials” *Macromolecular Rapid Communications,* **30**, 1179-1202 (2009).

[2] O'Neill, M.; Kelly, S. M. “Ordered Materials for Organic Electronics and Photonics” *Advanced Materials,* **23**, 566-584 (2011).

[3] Iino, H.; Hanna, J. “Availability of Liquid Crystallinity in Solution Processing for Polycrystalline Thin Films” *Advanced Materials,* **23**, 1748-1751 (2011).

[4] Ong, B. S.; Wu, Y. L.; Liu, P.; Gardner, S. “High-performance semiconducting polythiophenes for organic thin-film transistors” *Journal of the American Chemical Society,* **126**, 3378-3379 (2004).

[5] McCulloch, I.; Heeney, M.; Bailey, C.; Genevicius, K.; Macdonald, I.; Shkunov, M.; Sparrowe, D.; Tierney, S.; Wagner, R.; Zhang, W. M.; Chabinyc, M. L.; Kline, R. J.; McGehee, M. D.; Toney, M. F. “Liquid-crystalline semiconducting polymers with high charge-carrier mobility” *Nature Materials,* **5**, 328-333 (2006).

[6] Winokur, M. J.; Wamsley, P.; Moulton, J.; Smith, P.; Heeger, A. J. “Structural evolution in iodine-doped poly(3-alkylthiophenes)” *Macromolecules,* **24**, 3812-3815 (1991).

[7] Tashiro, K.; Ono, K.; Minagawa, Y.; Kobayashi, K.; Kawai, T.; Yoshino, K. “Structural changes in the thermochromic solid-state phase transition of poly(3-alkylthiophene” *Synthetic Metals,* **41**, 571-574 (1991).

[8] Prosa, T. J.; Winokur, M. J.; Moulton, J.; Smith, P.; Heeger, A. J. “X-ray structural studies of poly(3-alkylthiophenes) - An example of an inverse comb” *Macromolecules,* **25**, 4364-4372 (1992).

[9] Bao, Z.; Dodabalapur, A.; Lovinger, A. J. “Soluble and processable regioregular poly(3-hexylthiophene) for thin film field-effect transistor applications with high mobility” *Applied Physics Letters,* **69**, 4108-4110 (1996).

[10] Chang, J. F.; Sun, B. Q.; Breiby, D. W.; Nielsen, M. M.; Solling, T. I.; Giles, M.; McCulloch, I.; Sirringhaus, H. “Enhanced mobility of poly(3-hexylthiophene)

transistors by spin-coating from high-boiling-point solvents" *Chemistry of Materials,* **16**, 4772-4776 (2004).

[11] Kim, Y.; Cook, S.; Tuladhar, S. M.; Choulis, S. A.; Nelson, J.; Durrant, J. R.; Bradley, D. D. C.; Giles, M.; McCulloch, I.; Ha, C. S.; Ree, M. "A strong regioregularity effect in self-organizing conjugated polymer films and high-efficiency polythiophene: fullerene solar cells" *Nature Materials,* **5**, 197-203 (2006).

[12] Sirringhaus, H.; Brown, P. J.; Friend, R. H.; Nielsen, M. M.; Bechgaard, K.; Langeveld-Voss, B. M. W.; Spiering, A. J. H.; Janssen, R. A. J.; Meijer, E. W.; Herwig, P.; de Leeuw, D. M. "Two-dimensional charge transport in self-organized, high-mobility conjugated polymers" *Nature,* **401**, 685-688 (1999).

[13] Ho, V.; Boudouris, B. W.; Segalman, R. A. "Tuning Polythiophene Crystallization through Systematic Side Chain Functionalization" *Macromolecules,* **43**, 7895-7899 (2010).

[14] Boudouris, B. W.; Ho, V.; Jimison, L. H.; Toney, M. F.; Salleo, A.; Segalman, R. A. "Real-Time Observation of Poly(3-alkylthiophene) Crystallization and Correlation with Transient Optoelectronic Properties" *Macromolecules,* 44, 6653-6658 (2011).

[15] Moroni, M.; Lemoigne, J.; Luzzati, S. "Rigid-rod conjugated polymers for nonlinear optics .1. Characterization and linear optical-properties of poly(aryleneethynylene) derivatives" *Macromolecules*, **27**, 562-571 (1994).

[16] Knaapila, M.; Stepanyan, R.; Lyons, B. P.; Torkkeli, M.; Monkman, A. P. "Towards general guidelines for aligned, nanoscale assemblies of hairy-rod polyfluorene" *Advanced Functional Materials,* **16**, 599-609 (2006).

[17] Flory, P. J. "Phase equilibria in solutions of rod-like particles" *Proceedings of the Royal Society of London Series a-Mathematical and Physical Sciences,* **234**, 73-89 (1956).

[18] Papkov, S. P. "Liquid-crystalline order in solutions of rigid-chain polymers" *Advances in Polymer Science,* **59**, 75-102 (1984).

[19] Vroege, G. J.; Lekkerkerker, H. N. W. “Phase-transitions in lyotropic colloidal and polymer liquid-crystals” *Reports on Progress in Physics,* **55**, 1241-1309 (1992).

[20] Odijk, T. “Theory of lyotropic polymer liquid crystals” *Macromolecules,* **19**, 2313-2329 (1986).

[21] Sato, T.; Teramoto, A. “Concentrated solutions of liquid-crystalline polymers” *Biopolymers Liquid Crystalline Polymers Phase Emulsion,* **126**, 85-161 (1996).

[22] Flory, P. J. “Molecular theory of liquid crystals” *Advances in Polymer Science,* **59**, 1-36 (1984).

[23] Miller, W. G. “Stiff chain polymer lyotropic liquid crystals” *Annual Review of Physical Chemistry,* **29**, 519-535 (1978).

[24] Livolant, F.; Bouligand, Y. “Liquid-crystalline phases given by helical biological polymers (DNA, PBLG AND Xanthan) - Columnar textures” *Journal De Physique,* **47**, 1813-1827 (1986).

[25] Livolant, F.; Leforestier, A. “Condensed phases of DNA: Structures and phase transitions” *Progress in Polymer Science,* **21**, 1115-1164 (1996).

[26] Smalyukh, II; Zribi, O. V.; Butler, J. C.; Lavrentovich, O. D.; Wong, G. C. L. “Structure and dynamics of liquid crystalline pattern formation in drying droplets of DNA” *Physical Review Letters,* **96** (2006).

[27] Deegan, R. D.; Bakajin, O.; Dupont, T. F.; Huber, G.; Nagel, S. R.; Witten, T. A. “Capillary flow as the cause of ring stains from dried liquid drops” *Nature,* **389**, 827-829 (1997)

[28] Rey, A. D. “Liquid crystal models of biological materials and processes” *Soft Matter,* **6**, 3402-3429 (2010).

[29] Hagerman, P. J. “Flexiblity of DNA” *Annual Review of Biophysics and Biophysical Chemistry,* **17**, 265-286 (1988).

[30] Strzelecka, T. E.; Davidson, M. W.; Rill, R. L. “Mulitiple liquid crystal phases of DNA at high concentrations” *Nature,* **331**, 457-460 (1988).

[31] Delaye, M.; Ribotta, R.; Durand, G. “Buckling instability of layers in a smectic-A liquid-crsytal” *Physics Letters A,* **A 44**, 139-140 (1973).

[32] Clark, N. A.; Meyer, R. B. “Strain-induced instability of monodomain smectic A and cholesteric liquid-crystals” *Applied Physics Letters,* **22**, 493-494 (1973).

[33] Wang, Z. G. “Response and instabilities of the lameallar phase of diblock copolymers under uniaxial-stress” *Journal of Chemical Physics,* **100**, 2298-2309 (1994).

[34] Onuki, A.; Fukuda, J. “Electric field effects and form birefringence in diblock copolymers” *Macromolecules,* **28**, 8788-8795 (1995).

[35] Sharma, V.; Park, K.; Srinivasarao, M. “Colloidal dispersion of gold nanorods: Historical background, optical properties, seed-mediated synthesis, shape separation and self-assembly” *Materials Science & Engineering R-Reports,* **65**, 1-38 (2009).

[36] Heffner, G. W.; Pearson, D. S. “Molecular characterization of poly(3-hexylthiophene)” *Macromolecules,* **24**, 6295-6299 (1991).

[37] J. C. Loudet, *et al.*, “Undulation Instabilities in the Meniscus of Smectic Membranes,” *Physical Review Letters,* **106**, 117802 (2011).

[38] de Gennes, P. G.; Prost, J. *The Physics of Liquid Crystals*, 2nd ed. Oxford: Clarendon Press, pp. 364-369. 1993.

[39] Hu, H.; Larson, R. G. “Evaporation of a sessile droplet on a substrate” *Journal of Physical Chemistry B,* **106**, 1334-1344 (2002).

[40] Chopra, M.; Li, L.; Hu, H.; Burns, M. A.; Larson, R. G. “DNA molecular configurations in an evaporating droplet near a glass surface” *Journal of Rheology,* **47**, 1111-1132 (2003).

[41] Marko, J. F.; Siggia, E. D. *Science* **1994**, *265,* 506. “Fluctuations and supercoiling of DNA” *Science,* **265**, 506-508 (1994).

[42] Perkins, T. T.; Smith, D. E.; Chu, S. “Single polymer dynamics in an elongational flow” *Science,* **276**, 2016-2021 (1997).

[43] Palmer, H. J. “Hydrodynamic stability of rapidly evaporating liquids at reduced pressure” *Journal of Fluid Mechanics*, **75**, 487-512 (1976).

[44] Prosperetti, A.; Plesset, M. S. “The stability of an evaporating liquid surface” *Physics of Fluids,* **27**, 1590-1602 (1984).

[45] Oron, A.; Davis, S. H.; Bankoff, S. G. “Long-scale evolution of thin liquid films” *Reviews of Modern Physics,* **69**, 931-980 (1997).

[46] Dubois, E. “Determination of thermal instabilities thresholds for homeotropic and planar nematic liquid crystal samples” *Solid State Communications,* **14**, 767-771 (1974).

CHAPTER 9

IN-SITU ANALYSIS AND CORRELATION OF STRUCUTRAL CHANGES AND DRAIN CURRENT OF POLY(3-HEXYLTHIOPHENE) DURING FILM FORMATION VIA SOLUTION PROCESS

9.1 Introduction

The design and development of viable plastic devices requires understanding of how molecular structure affects critical device parameters such as charge carrier mobility. A great dear of effort has been devoted to characterizing the morphology (or microstructure) of semiconducting polymer layers by varying a number of experimental parameters such as regio-regularity [1-3], molecular weight [4-7], solvents [8-11], deposition techniques [7, 12-14], and nature of substrate [15-18]. Despite the vast literature, the correlation of the morphology (or microstructure) of polymer layers has been limited to how the post-processing of the deposited film affects device performance.

In general, except for completely glassy polymers, conjugated polymer layers via solution processing form semi-crystalline phases [19], in which some fraction of the polymer remains un-crystallized (or amorphous) trapped between the crystalline domains. Given the fact that the semi-crystalline state of quenched thin polymer films is a non-equilibrium structure [20, 21], the history of film formation via solvent evaporation, through which the "memory" of chain conformation in solution state may be retained, may be a primary factor in determining the final morphology of the polymer layers [5, 10, 22]. In addition, a coherent description of the electrical properties associated with the evolving structure of conducting channel upon solution process is also not complete, in contrast to that from vacuum-deposited organic semiconductors where the onset of current between source and drain electrodes is believed to occur by geometric percolation between organic semiconductor islands grown on gate dielectric substrates [23]. Therefore, interrogating the structural changes of conjugated polymer in the solidification process through which the conducting channel is formed in concert with the evolution of charge transport is essential not only to establish a comprehensive structure-electrical property relationship, but also to manipulate the morphology of the active polymer layer for different device applications.

To address this issue, we devoted our efforts to address the history of conjugated polymer solidifying to final morphology and the effect of this sequence on observable device parameter using the standard *p*-type material in polymer-based field-effect transistors [24, 25] and the standard electron-donating material in bulk hetero-junction organic photovoltaic devices [3, 26]. We conducted the real-time observations of Raman spectral changes while simultaneously measuring drain current during drop-cast film formation. The drain current reflects the results of structural changes occurring during the formation of the conducting channel, while the Raman spectra provide information on the structural changes. Precise comparisons of the Raman spectra with measured drain currents with elapsed time should enable us to elucidate the solidification mechanism of P3HT chains in solution process, and allow us to correlate the structural changes on the electrical properties. The consequence will help open new ways for tailoring final morphology of conjugated polymer films for various electro-optic devices, which demand distinct morphologies for their high performances.

9.2 Experiments

9.2.1 In-situ Drain Current and Raman Measurements

We fabricated two-contact devices for the *in-situ* current measurements. A highly doped silicon wafer served as a gate electrode, and source and drain electrodes (Au (50 *nm*)/Cr (2*nm*)) were patterned using photolithography with the channel length of 50 μm and the width of 2 *mm*. Two-contact measurements were performed using a semiconductor parameter analyzer (*Agilent* 4155C). The same solution studied in chapter 7 (P3HT with 94% regio-regularity, M_w of 47.7kD dissolved in 1,2,4-trichlorobenzene (TCB), 3*mg/mL*) was prepared and a 2 μL droplet of the P3HT solution was deposited onto the channel of device for *in-situ* current measurements during solvent evaporation. The volume of a droplet of solution was controlled using a micropipette. Upon deposition of the solution, measurements of the drain were made in 15 sec time intervals until the solidification of the film.

In order to correlate Raman spectral changes and *in-situ* measured currents, we focused the excitation laser (15 μm diameter) on the conducting channel at which drain current is measured. (see Figure 9.1). Excitations at 785 *nm* of a diode laser were used and the irradiation power was kept below 0.1 $mW/\mu m^2$. No sample degradation induced by the irradiation was observed during the acquisition of Raman spectra. In order to monitor spectral changes as a function of solvent evaporation time, series of Raman spectra were recorded for 15 seconds (5 seconds for exposure time × 3 accumulation times) consecutively after the solution deposition during the same period of *in-situ* current measurements. All the electrical and Raman measurements were carried out in air.

Band components analysis was done using the "*Peak Fitting*" function in the spectracalc, *Grams*. On fitting peaks, we used the mixed Gaussian-Lorentzian function as a peak shape and reproducible results were obtained with square regression coefficient of R^2 greater than 0.995.

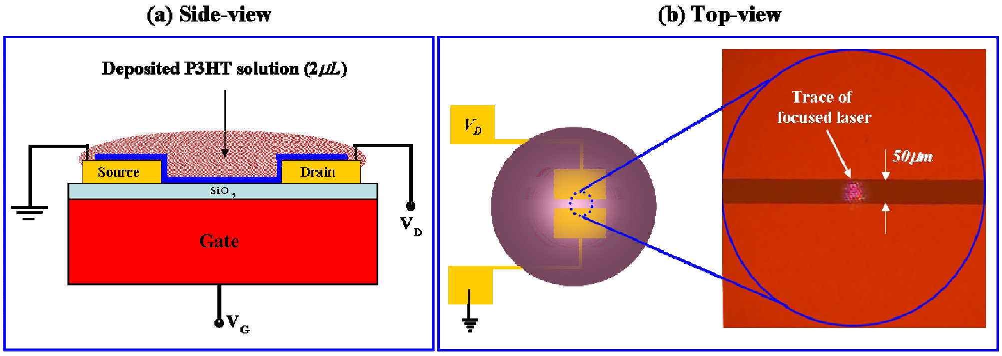

Figure 9.1 Experimental setup for *in-situ* current and Raman measurements: (a) A schematic side view of the two-contact device with solution deposition. Solution was deposited between two conducting channel. (b) Left is a schematic top view of the two-contact device. Right is an optical microscopic image after depositing solution. Trace between the channels with 50 μm length is a reflected image of focused laser for the Raman measurement. Red color in right image comes from the deposited P3HT solution.

9.3 Results

9.3.1 Comparisons of Drain Current and Raman Spectral Changes

Time evolution of the measured drain current is plotted in Figure 9.2 (a), which illustrates some interesting features; the drain current increases sharply at a specific time after the solution deposition on a device and reaches a maximum value followed by a gradual decrease before leveling off. Simultaneous measurements of the Raman spectral changes and the drain current changes were made during the entire time of the film formation (0-1200 minutes after deposition), and the results of the time duration of particular interest, from the onset of abrupt increase up to its maximum, are plotted in Figure 9.2 (b) and 9.2 (c). In Figure 9.2 (b), we have labeled four different periods of measurements, A-D. Region A represents the time when the drain current begins to increase rapidly and D is labeled as the time when the drain current reaches a maximum. Raman spectra obtained at the times denoted by A and D are shown in Figure 9.2 (c), in which Raman spectra at moment A and D resembles that of neat solute of P3HT with low regio-regularity (<50% head-tail regularity, amorphous phase) and that of neat powder of highly regio-regular P3HT (94% head-tail regularity, semi-crystalline phase) (see Figure 9.2 (d)), respectively.

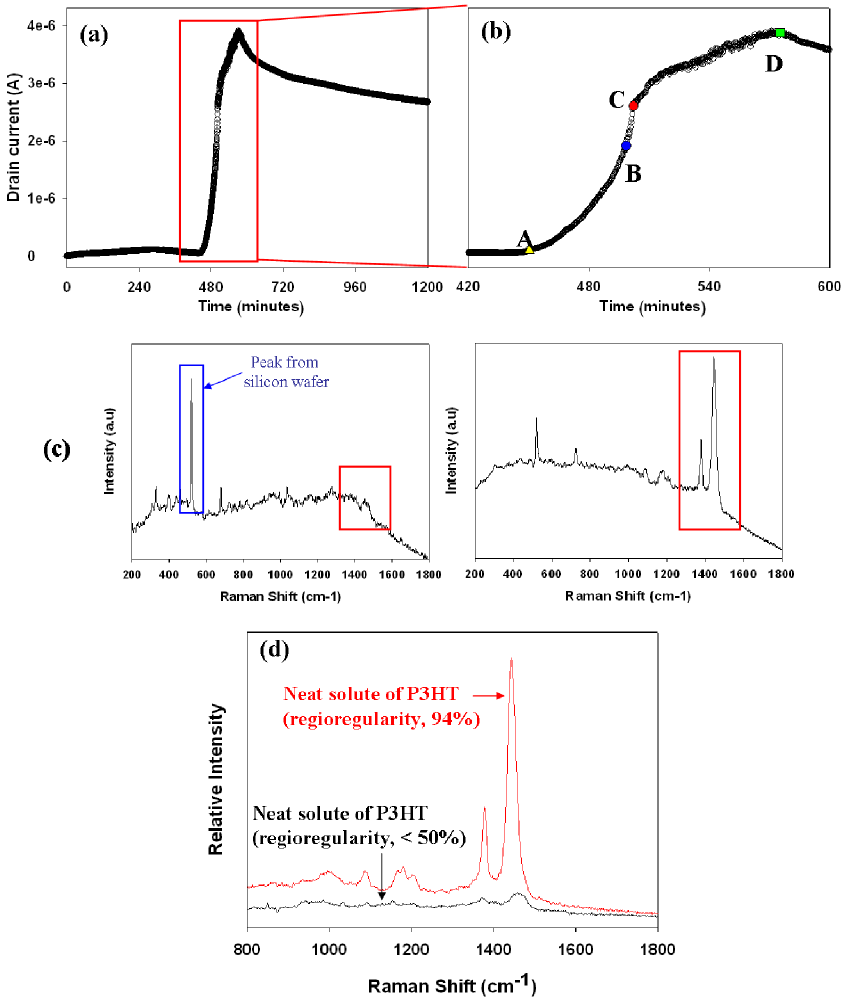

Figure 9.2 Time evolution of the drain current (a) over the entire elapsed time during the measurements and (b) during the period when significant changes of drain current occur. **A** is the moment at which the drain current begins to increase sharply. **D** is the moment of maximum current. The moments **B** and **C** were arbitrarily partitioned based on significant changes of Raman spectra obtained between these moments (see Figure 9.3). Raman spectrum at the moment **B** consists of weak and blurry peaks whereas Raman spectrum recorded at the moment **C** shows very strong peaks, of which shapes are similar to those obtained at the moment **D**. (c) Raman spectra obtained at the moment **A** (left) and at the moment **D** (right). Peaks with the red squares are characteristic Raman bands of P3HT and the strong peak at 520 cm^{-1}arises from a silicon wafer. (d) Raman spectra for high (94%, red spectrum) and low (<50%, black spectrum) regio-regular neat powder of P3HT.

We have partitioned the times of B and C based on significant changes in Raman spectra obtained between these time intervals. (From now on, we designate the regions A-D by just **A, B, C, D**). Figure 9.3 presents Raman spectra obtained between **B** and **C**, in which spectral changes are abrupt (within ca. 2 minutes). Raman spectrum obtained at **B** consists of weak, blurry peaks, whereas that recorded at **C** shows very strong and sharp peaks, which looks similar to the spectral shape obtained at **D** and afterwards. We repeated the same experiments 15 times, and obtained the results with the same trend that time intervals when Raman spectra change abruptly (duration of 2~3 minutes), i.e., regions between B and C in Figure 9.2(b), was placed somewhere halfway of rapid increase in drain current.

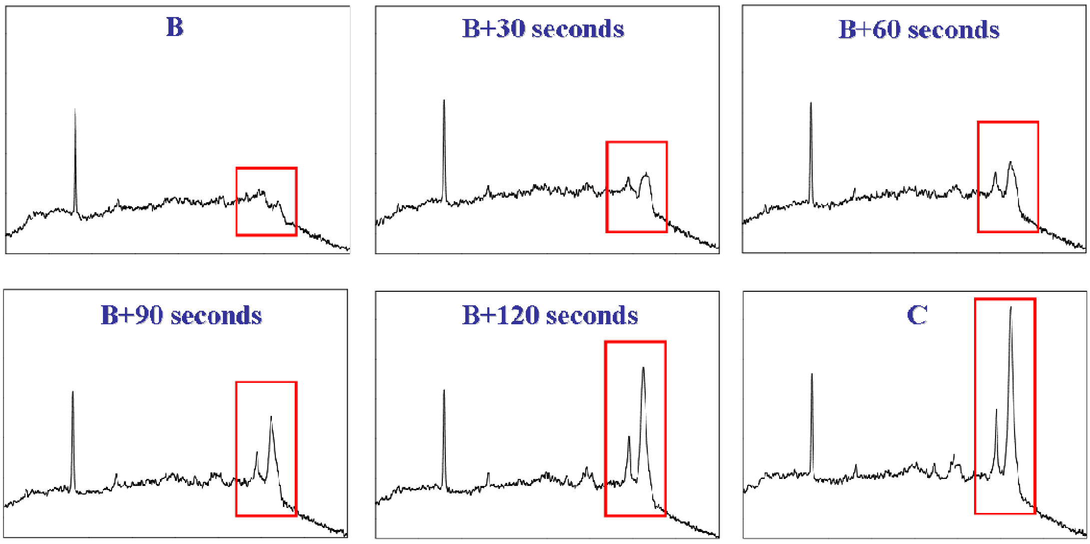

Figure 9.3 The variation of Raman spectra obtained between **B** and **C**. Peaks within red squares are characteristic Raman bands of P3HT.

We also monitored the intensity change of Raman peak at 667 cm^{-1} assigned to *C-Cl* stretching of 1,2,4-TCB [27], so that the evolution of drain current can be related to the residual solvent in the measured area. The intensity variation of the 677 cm^{-1} peak is plotted along with the time evolution of the drain current in Figure 9.4, in which the peak intensity is normalized to the peak intensity at $t=0$ minute. We were able to detect the signal of Raman band at 677 cm^{-1} for a while even after the onset of sharp increase in drain current. (*i.e.* point **A**). The implication of the solvent peak detection after **A** will be discussed in the following section. Again, the result of detecting Raman signal at 677 cm^{-1} with non-negligible intensity at the moment drain current starts to increase sharply was reproducible for all cases of 15 trials.

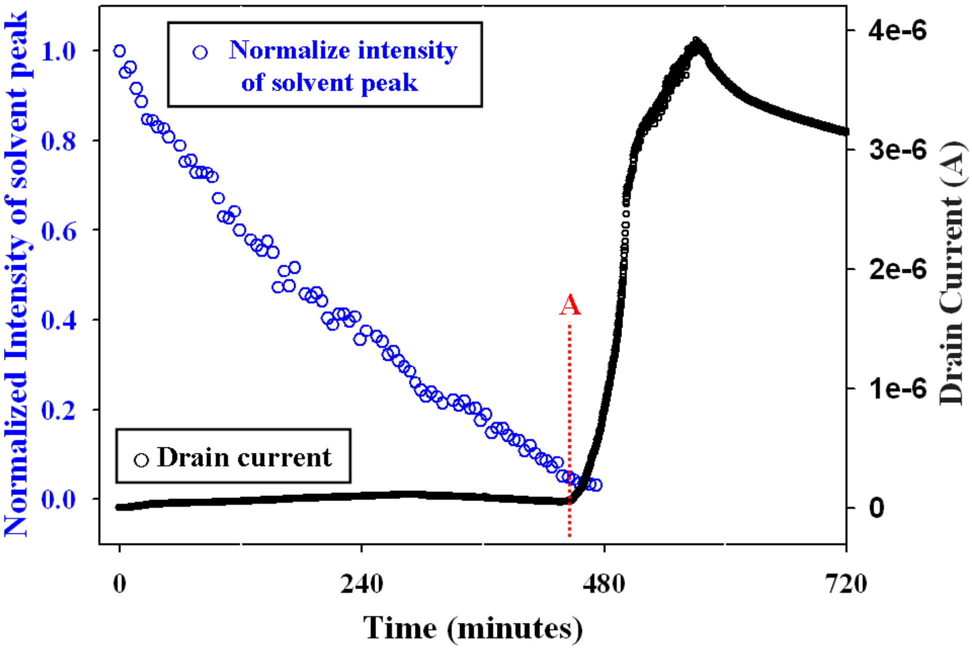

Figure 9.4 Time evolution of the drain current and the intensity of Raman peak at 667 cm^{-1}, which is normalized to the intensity at $t = 0$.

9.3.2 Peak Shape Analysis

We performed the peak shape analysis including intensity, position, and bandwidth for the Raman spectra measured after **B**. Most intense peak attributed to $C=C$ stretching (ca. at 1445 cm^{-1}) was analyzed as this vibration band is sensitive not only to the conformational changes of P3HT chains, but also to interactions between neighboring chains [28-31]. Figure 9.5 presents the intensity variation of Raman peak for $C=C$ stretching mode ($I_{C=C}$) measured after **B** (the peak intensities are normalized with respect to the intensity of peak measured at **D**). The intensity increases very rapidly until **C** and then slowly increases up to **D**, beyond which it eventually saturates.

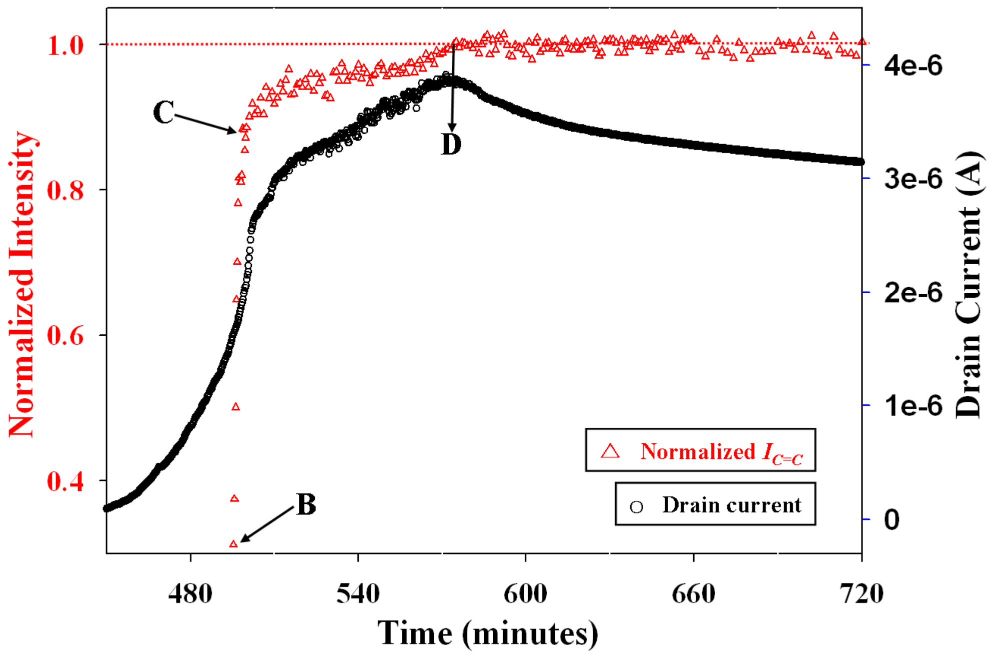

Figure 9.5 Correlation between the intensity variation of Raman peak assigned to $C{=}C$ stretching and drain current with time after point B. Intensity was normalized by the intensity at **D**.

Careful observations of the spectra measured between **B** and **C** show different symmetries in spectral shape. For the spectrum measured at **B**+30 seconds, the spectral shape for $C{=}C$ stretching (see the spectral shape highlighted with orange colored rectangular in Figure 9.6) is apparently asymmetric whereas the spectral shape measured at **C** exhibits mostly symmetric form. We decomposed this peak into two Raman bands, one at ca. 1460 cm^{-1} and the other at ca. 1446 cm^{-1}, both of which are attributed to $C{=}C$ stretching, but result from the vibration of molecules in the phase with different order. According to prior results [30, 32, 33], the C=C mode has been considered to be a superposition of the modes characteristic of the two different phases, where Raman peak from $C{=}C$ stretching of amorphous P3HT chains (ca. 1460 cm^{-1}) is distinguished from that of crystalline P3HT chains (ca. 1446 cm^{-1}) by selectively enhancing peaks using resonance effects

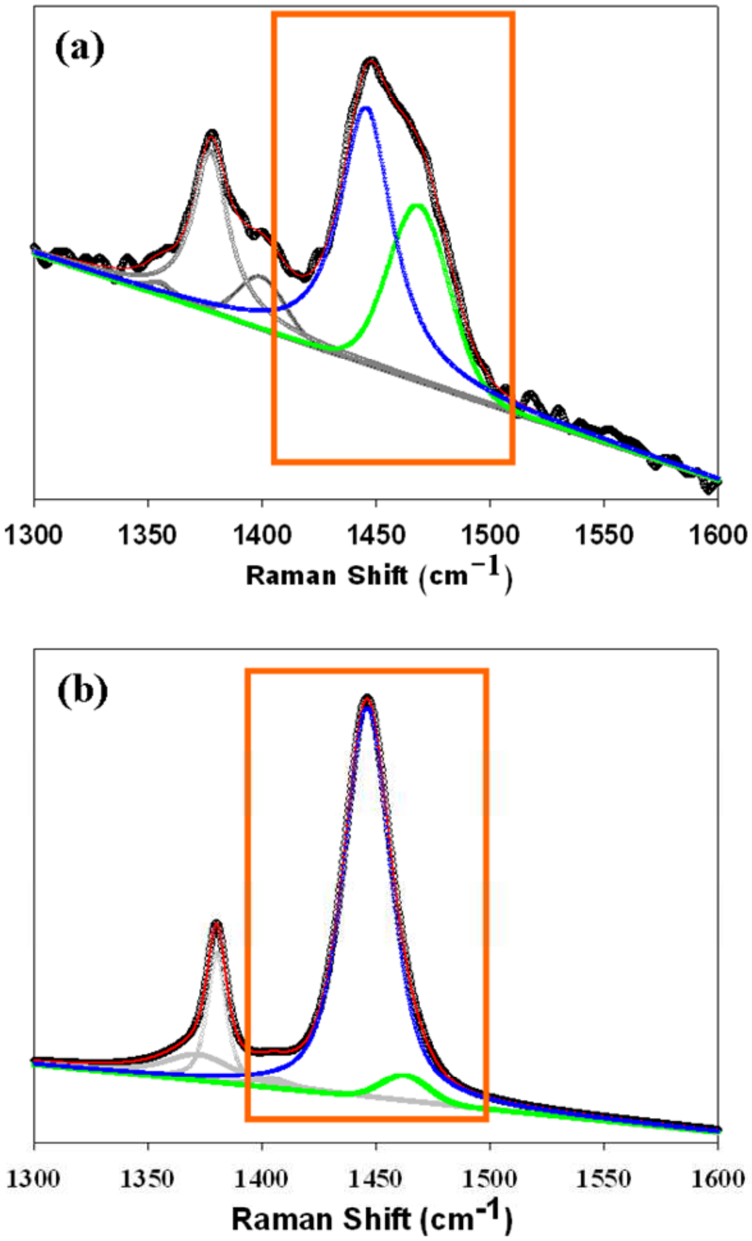

Figure 9.6 Fitting results for peaks around 1300 ~ 1550 cm^{-1} in Raman spectra measured (see the inside of the orange rectangles) (a) at the moment of **B**+30 seconds and (b) at the moment of **C**. Raw peaks are plotted with symbol (●) and red solid line (–) is the fitting result. Plots with red (□) and blue (△) dots are attributed to *C=C* stretching mode of P3HT in less ordered and highly ordered state, respectively.

Herein, we focused on the variation of the position and the bandwidth of the Raman peak at ca. 1446 cm^{-1} in order to explore how P3HT chains form a highly ordered microstructure during the solidification of P3HT. The time evolutions of the peak position (Raman shift) and the bandwidth (FWHM) are plotted for Raman spectra obtained after **C**. While the magnitude of change is relatively small, the position and FWHM of the peak obviously evolves with time even after **C** as shown in Figure 9.7. Peak position continuously shifts to lower wave number from ca. 1446.5 cm^{-1} with time and settles around about 1445.0 cm^{-1} after 1050 minutes from the deposition time. FWHM also continuously changes with time, but in a different manner: the peak width at **C** is almost consistent till **D**, then continuously increase with time up to the saturation (ca. 27cm^{-1}) around 900 minutes.

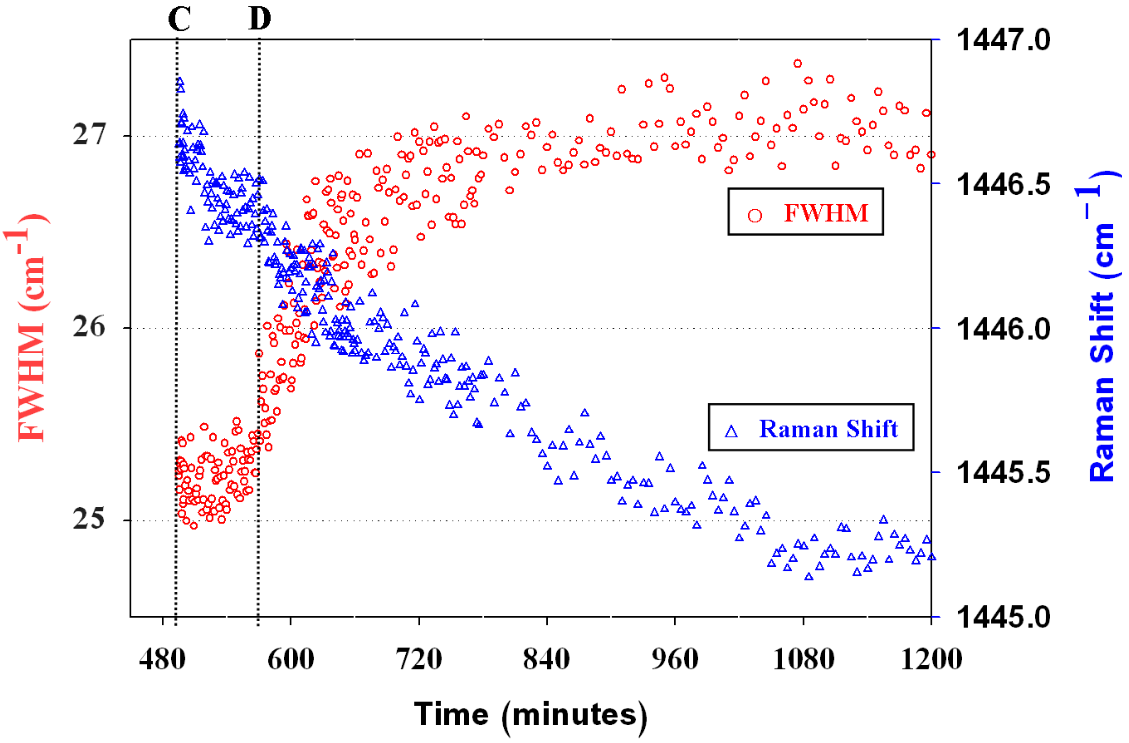

Figure 9.7 Time evolution of the position and FWHM of the Raman peak attributed to $C{=}C$ stretching of P3HT after the moment **C**.

9.4. Discussion

In the Raman spectra, we observe two very distinctively different sets of peaks; one consisting of weak and blurry peaks (as shown in left spectrum in Figure 9.2(c)) and the other showing strong and sharp peaks (see right spectrum in Figure 9.2 (c)). Several studies have shown that increasing the regio-regularity of poly(alkyl thiophenes) (PATs) enhances the conformational order of chains as well as denser packing of chains, resulting in π-π stacking leading to crystallization [1, 34]. Thus, the obvious difference of the spectral shape between high regio-regular P3HT (94%) and low regio-regular (<50%) P3HT in Figure 9.2 (d) is thought to arise from two distinct structures, *i.e.*, disordered (amorphous) and ordered (crystalline) states. We speculate that the difference of vibrational motion in different ordered phases results in significantly different spectral shape. In principle, vibration motion in a crystal lattice (so called "phonon") is superimposed by collective vibrations of atoms [35], which leads to distinguish Raman peak of P3HT in a crystalline state from that in an amorphous state. The excitation resonance effect, i.e., adjustment of the incoming energy source with the electronic transition of P3HT, is not likely to be responsible for this difference in spectral shape. It is because the energy of the excitation (~1.58 *eV*, 785 *nm*) is far smaller than the energy of electronic transitions of P3HT (>1.91 *eV*, <650 *nm*), determined by the UV-visible absorption, in both solution and dried regio-regular P3HT films (see Figure 9.8). Accordingly, we tentatively conclude the substantial change of Raman spectra obtained between **B** and **C**, which looks similar to the spectral difference between amorphous (less regio-regular P3HT) and ordered (high regio-regular P3HT) state, is associated with the existence of crystalline regions.

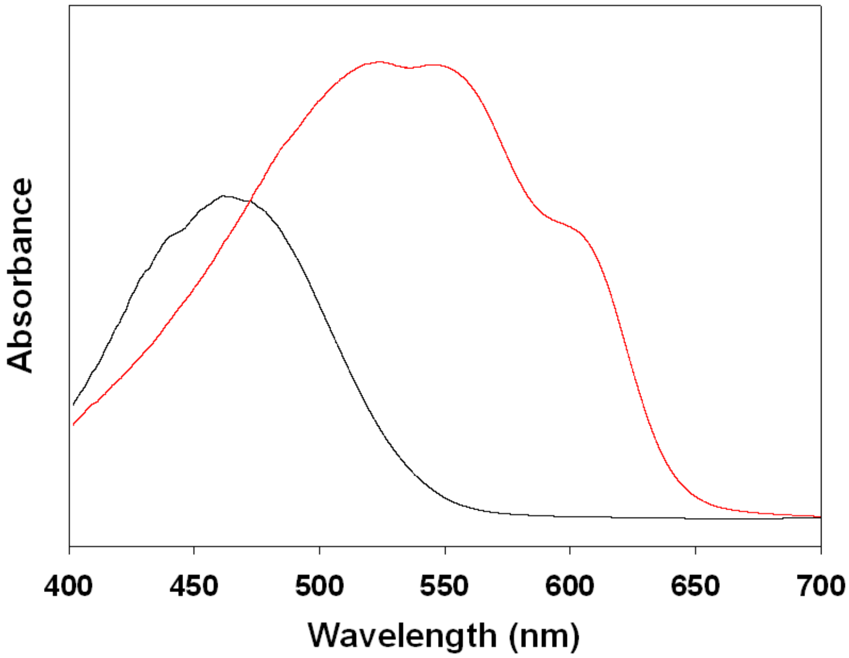

Figure 9.8 Optical absorption spectrum of dilute solution (black solid line) and dried regio-regular P3HT film (red solid line), respectively.

9.4.1 Correlation of Initial Increase of Drain Current with P3HT Structure

As obviously seen in Figure 9.2 (c), it is clear that that the Raman spectrum measured at **A** resembles spectral feature of disordered state of P3HT chains. From the observation that there remains solvent to be detected by Raman even after **A** (Figure 9.4), the residual solvent is assumed to act as a plasticizer of P3HT chains and restrain P3HT chains from crystallizing. Although solvent peak was not clearly distinguishable from the noise and background in the Raman spectrum measured at **B**, there may remain some solvent [36, 37], which prevent the P3HT chains from organizing to crystalline order yet.

It is interesting that the considerable increase in drain current (up to **B**) is associated with the P3HT chains that do not form obvious crystalline order. Given the fact that charge transport requires the charges be able to move from molecule to molecule via molecular conjugation without being trapped or scattered [38, 39], it is likely that intimate contacts among neighboring polymer chains, strong enough to conduct charges, take place at **A** and the extent of conjugation keeps increasing thereafter in the disordered region. One plausible model for above interpretation is planarization of P3HT backbone chains induced by solvent loss in a evaporating solution and corresponding increase of π-π interaction. It is generally thought that the packing of poly(alkylthiophenes) (PATs) chains induced by solvent loss in a solution process is a planarization process, in which the torsion and bending of adjacent thiophene rings are restricted, so that the conjugation of P3HT chains are extended [40, 41]. Therefore, we interpret that the continuous increase of drain current until B is attributed to the extension of planarity of P3HT backbone along with high proximity of thienyls with solvent loss induced thinning of P3HT layer. The interconnections of P3HTs with conjugation is likely adequate to form a conductive pathway, but at the same time, the interchain distances and π-π interactions may not have reached the threshold for P3HT chains to self-organize into crystalline structure up to **B**.

In summary, even in the absence of crystalline order of P3HT chains, significant electrical conductivity was observed, which is ascribed to the increased conformational order and interconnectivity of P3HT chains forced by high density P3HT layer, but the degree of structural order is not high enough for the molecules to crystallize.

9.4.2 Crystallization of P3HT Chains

As seen in Figure 9.3, Raman spectrum measured at **C** looks similar to the spectrum obtained from the dried regio-regular P3HT film possessing crystalline regions. Significant changes in spectral shapes (Figure 9.3) and rapid increase in Raman intensities (Figure 9.5) from **B** to **C** are probably due to that P3HT chains began to crystallize. Peak shape analysis for the spectra obtained between **B** and **C** provide qualitative information about the growth of crystallization. In Figure 9.6, we observed the transformation of spectral shape (attributed to $C{=}C$ stretching) from asymmetric to mostly symmetric form. We interpret this observation as a result of the growth of crystallization. As P3HT chains initially crystallize at around **B**, the intensity of the peak coming from the crystallites (at ca. 1446 cm^{-1}) is comparable to that from P3HT in the disordered state (at ca. 1460 cm^{-1}), such that none of two peaks dominates, resulting in apparently asymmetric spectral shape overlapped with these two peaks. As the crystallization proceeds rapidly, however, the more intense peak coming from crystalline P3HT chains (at ca. 1446 cm^{-1}) dominates the spectral shape and the asymmetry becomes attenuated. Finally, after **C**, spectral shape is ruled by the peak coming from P3HT chains with a crystalline order and appears to be almost symmetric. Judging from the evolution of asymmetric shape of Raman band for $C=C$ stretching mode combined with the rapid increase in the peak intensity from **B** to **C**, we propose that initiation of crystallization and its rapid growth take place between **B** and **C**. (We tentatively define the moment initiating the crystallization as the moment B, but accurate time for P3HT chains to initiate crystallization may be a little different.)

Another observation that may support the existence of the transition between different ordered states in the period between **B** and **C** is the manner of the drain current evolution. Should the drain current be strongly related to the morphology of P3HT layer, the drain current in different structural states might show different manner of evolution. This is the case of our result. In Figure 9.2 (b), we can see that the drain current continuously increases from **A**, but its time dependences among three regions, *i.e.*, **A**~**B**, **B**~**C**, and **C**~**D**, look qualitatively different. Especially, the rate of increase in drain current is most drastic from B to C.

9.4.3 Correlation of Drain Current with Subtle Structural Changes after Crystallization

In Figure 9.5, we noticed that both drain currents and Raman peak intensities change for a considerable amount of time after **C**, which indicates that the morphology of P3HT layer may still change. The variations in the position and width of Raman peak characteristic to P3HT in crystalline phase (Figure 9.7) provide us with the evidence of subtle structural changes that is critical to drain current. In Figure 9.7, the continuous red shift implies that the conjugation become extended with time until ca. 1050 minutes after the deposition. Based on theoretical calculation of the shift of Raman band associated with the extent of conjugation [42-44], it is thought that further increase of conformational order (backbone planarity) and the enhancement of π-π interaction forced by the increase in the P3HT concentration.

Broadness of Raman band reflects a distribution of molecular transition frequencies. Thus, one can anticipate the existence of imperfect molecular ordering/packing in a system based on the change of bandwidth. From this point of view, more or less constant FWHM between **C** and **D** indicates that the distribution of chain ordering does not noticeably change. Thus, continuous increase of drain current until **D** is attributed to continuous increase in conjugation. Broadening of bandwidth after **D,** however**,** is important in understanding of the origin of decreasing drain current after its maximum at **D**. Semi-crystalline P3HT films consist of many small crystal grains that may aggregate with time. As Kline *et al*. [45] reported the aggregations of crystal grains in film may lead adjacent crystal grains to be distorted with each other, which produces grain boundaries and other defects. In polymer layers, grain boundaries composed of polymer chains may bridge adjacent crystalline grains [46, 47], thereby imparting electrical connectivity. However, if the grain boundaries become spatially sharp or abrupt they may restrict the charge transport among adjacent grains in the macroscopic scale [48].

We can estimate the effects associated with the existence of the inhomogeneities and defects in the conducting layer from the increase of FWHM after **D** in Figure 9.7. Knapp et al. [49] and Knoester et al. [50] proposed the model of line broadening coming from a distribution of molecular transition frequencies due to static disorder such as lattice defects, impurities and so on. It was also reported that the soft mode phonon band exhibits the broadening of peak shape due to phonon damping and inhomogeneities in crystalline structure [51, 52]. Thus, we associate the broadening of FWHM with the aggregations induced structural disorder at macroscopic scale. Since the drain current is a macroscopic quantity, these aggregations may be responsible for the decrease in the drain current. While the extent of conjugation keeps increasing, judged from a continuous red shift of peak position, the advent of such aggregations may deplete the drain current.

9.5. Conclusion

We have conducted real time investigation of solidification of the P3HT chains and correlated the structural changes of P3HT with the evolution of the drain current using Raman spectroscopy. From simultaneous comparisons of Raman spectra with the evolution of the drain current, it is thought that P3HT layer conducts drain current significantly before P3HT chains form a crystalline state. In addition, subtle morphological changes in P3HT layer take place after P3HT chains crystallized, which significantly influence conducting drain current. From the above results, we can expect to select specific moments and quench the polymer layer so that we can manipulate the final morphology of conducting layer for various applications requiring different electronic process. We believe the clarification of the mechanism of conducting channel formation and correlation between the morphology and the drain current will help open new ways for tailoring final morphology of conjugated polymer films for various applications.

9.6 References

[1] Chen, T. A.; Wu, X. M.; Rieke, R. D. "Regiocontrolled synthesis of poly(3-alkylthiophenes) mediated by rieke zinc-Their characterization and solid-state properties" *Journal of the American Chemical Society,* **117**, 233-244 (1995).

[2] McCullough, R. D. "The chemistry of conducting polythiophenes" *Advanced Materials,* **10**, 93-116 (1998).

[3] Kim, Y.; Cook, S.; Tuladhar, S. M.; Choulis, S. A.; Nelson, J.; Durrant, J. R.; Bradley, D. D. C.; Giles, M.; McCulloch, I.; Ha, C. S.; Ree, M. "A strong regioregularity effect in self-organizing conjugated polymer films and high-efficiency polythiophene: fullerene solar cells" *Nature Materials,* **5**, 197-203 (2006).

[4] Kline, R. J.; McGehee, M. D.; Kadnikova, E. N.; Liu, J. S.; Frechet, J. M. J. "Controlling the field-effect mobility of regioregular polythiophene by changing the molecular weight" *Advanced Materials,* **15**, 1519-1522 (2003).

[5] Zen, A.; Pflaum, J.; Hirschmann, S.; Zhuang, W.; Jaiser, F.; Asawapirom, U.; Rabe, J. P.; Scherf, U.; Neher, D. "Effect of molecular weight and annealing of poly (3-hexylthiophene)s on the performance of organic field-effect transistors" *Advanced Functional Materials,* **14**, 757-764 (2004).

[6] Kline, R. J.; McGehee, M. D.; Kadnikova, E. N.; Liu, J. S.; Frechet, J. M. J.; Toney, M. F. "Dependence of regioregular poly(3-hexylthiophene) film morphology and field-effect mobility on molecular weight" *Macromolecules,* **38**, 3312-3319 (2005).

[7] Verilhac, J. M.; LeBlevennec, G.; Djurado, D.; Rieutord, F.; Chouiki, M.; Travers, J. P.; Pron, A. "Effect of macromolecular parameters and processing conditions on supramolecular organisation, morphology and electrical transport properties in thin layers of regioregular poly(3-hexylthiophene)" *Synthetic Metals,* **156**, 815-823 (2006).

[8] Chang, J. F.; Sun, B. Q.; Breiby, D. W.; Nielsen, M. M.; Solling, T. I.; Giles, M.; McCulloch, I.; Sirringhaus, H. "Enhanced mobility of poly(3-hexylthiophene) transistors by spin-coating from high-boiling-point solvents" *Chemistry of Materials,* **16**, 4772-4776 (2004).

[9] Yang, H. C.; Shin, T. J.; Yang, L.; Cho, K.; Ryu, C. Y.; Bao, Z. N. "Effect of mesoscale crystalline structure on the field-effect mobility of regioregular poly(3-

hexyl thiophene) in thin-film transistors" *Advanced Functional Materials,* **15**, 671-676 (2005).

[10] Surin, M.; Leclere, P.; Lazzaroni, R.; Yuen, J. D.; Wang, G.; Moses, D.; Heeger, A. J.; Cho, S.; Lee, K. "Relationship between the microscopic morphology and the charge transport properties in poly(3-hexylthiophene) field-effect transistors" *Journal of Applied Physics,* **100**, 033712 (2006).

[11] Ho, P. K. H.; Chua, L. L.; Dipankar, M.; Gao, X. Y.; Qi, D. C.; Wee, A. T. S.; Chang, J. F.; Friend, R. H. "Solvent effects on chain orientation and interchain pi-interaction in conjugated polymer thin films: Direct measurements of the air and substrate interfaces by near-edge X-ray absorption spectroscopy" *Advanced Materials*, **19**, 215-221 (2007).

[12] Kobashi, M.; Takeuchi, H. "Inhomogeneity of spin-coated and cast non-regioregular poly(3-hexylthiophene) films. Structures and electrical and photophysical properties" *Macromolecules,* **31**, 7273-7278 (1998).

[13] Reitzel, N.; Greve, D. R.; Kjaer, K.; Hows, P. B.; Jayaraman, M.; Savoy, S.; McCullough, R. D.; McDevitt, J. T.; Bjornholm, T. "Self-assembly of conjugated polymers at the air/water interface. Structure and properties of Langmuir and Langmuir-Blodgett films of amphiphilic regioregular polythiophenes" *Journal of the American Chemical Society,* **122**, 5788-5800 (2000).

[14] Zhai, L.; McCullough, R. D. "Layer-by-layer assembly of polythiophene" *Advanced Materials,* **14**, 901-905 (2002).

[15] Chen, X. L.; Lovinger, A. J.; Bao, Z. N.; Sapjeta, J. "Morphological and transistor studies of organic molecular semiconductors with anisotropic electrical characteristics" *Chemistry of Materials,* **13**, 1341-1348 (2001).

[16] Wang, G. M.; Moses, D.; Heeger, A. J.; Zhang, H. M.; Narasimhan, M.; Demaray, R. E. "Poly(3-hexylthiophene) field-effect transistors with high dielectric constant gate insulator" *Journal of Applied Physics,* **95**, 316-322 (2004).

[17] Kim, D. H.; Park, Y. D.; Jang, Y. S.; Yang, H. C.; Kim, Y. H.; Han, J. I.; Moon, D. G.; Park, S. J.; Chang, T. Y.; Chang, C. W.; Joo, M. K.; Ryu, C. Y.; Cho, K. W. "Enhancement of field-effect mobility due to surface-mediated molecular ordering in regioregular polythiophene thin film transistors" *Advanced Functional Materials,* **15**, 77-82 (2005).

[18] Park, Y. D.; Lim, J. A.; Lee, H. S.; Cho, K. "Interface engineering in organic transistors" *Materials Today,* **10**, 46-54 (2007).

[19] Hugger, S.; Thomann, R.; Heinzel, T.; Thurn-Albrecht, T. "Semicrystalline morphology in thin films of poly(3-hexylthiophene)" *Colloid and Polymer Science,* **282**, 932-938 (2004).

[20] Tant, M. R.; Wilkes, G. L. "An overview of the non-equilibrium behavior of polymer glasses" *Polymer Engineering and Science,* **21**, 874-895 (1981).

[21] Wunderlich, B. "Reversible crystallization and the rigid-amorphous phase in semicrystalline macromolecules" *Progress in Polymer Science,* **28**, 383-450 (2003).

[22] Nguyen, T. Q.; Doan, V.; Schwartz, B. J. "Conjugated polymer aggregates in solution: Control of interchain interactions" *Journal of Chemical Physics,* **110**, 4068-4078 (1999).

[23] Park, B. N.; Seo, S.; Evans, P. G. "Channel formation in single-monolayer pentacene thin film transistors" *Journal of Physics D-Applied Physics,* **40**, 3506-3511 (2007).

[24] Sirringhaus, H.; Tessler, N.; Friend, R. H. "Integrated optoelectronic devices based on conjugated polymers" *Science,* **280**, 1741-1744 (1998).

[25] Sirringhaus, H.; Brown, P. J.; Friend, R. H.; Nielsen, M. M.; Bechgaard, K.; Langeveld-Voss, B. M. W.; Spiering, A. J. H.; Janssen, R. A. J.; Meijer, E. W.; Herwig, P.; de Leeuw, D. M. "Two-dimensional charge transport in self-organized, high-mobility conjugated polymers" *Nature,* **401**, 685-688 (1999).

[26] Campoy-Quiles, M.; Ferenczi, T.; Agostinelli, T.; Etchegoin, P. G.; Kim, Y.; Anthopoulos, T. D.; Stavrinou, P. N.; Bradley, D. D. C.; Nelson, J. "Morphology evolution via self-organization and lateral and vertical diffusion in polymer: fullerene solar cell blends" *Nature Materials,* **7**, 158-164 (2008).

[27] Scherer, J. R.; Evans, J. C. "Vibrational spectra and assignments for 16 chlorobenzenes" *Spectrochimica Acta,* **19**, 1739-1775 (1963).

[28] Furukawa, Y.; Akimoto, M.; Harada, I. "Vibrational key bands and electrical-conductivity of polythiophene" *Synthetic Metals,* **18**, 151-156 (1987).

[29] Navarrete, J. T. L.; Zerbi, G. "Lattice-dynamics and vibrational-spectra of polythiophene .1. Oligomers and polymer" *Journal of Chemical Physics,* **94**, 957-964 (1991).

[30] Louarn, G.; Trznadel, M.; Buisson, J. P.; Laska, J.; Pron, A.; Lapkowski, M.; Lefrant, S. “Raman spectroscopic studies of regioregular poly(3-alkylthiophenes)” *Journal of Physical Chemistry,* **100**, 12532-12539 (1996).

[31] Park, M. S.; Aiyar, A.; Park, J. O.; Reichmanis, E.; Srinivasarao, M. “Solvent Evaporation Induced Liquid Crystalline Phase in Poly(3-hexylthiophene)” *Journal of the American Chemical Society,* **133**, 7244-7247 (2011).

[32] Gao, Y. Q.; Grey, J. K. “Resonance Chemical Imaging of Polythiophene/Fullerene Photovoltaic Thin Films: Mapping Morphology-Dependent Aggregated and Unaggregated C=C Species” *Journal of the American Chemical Society,* **131**, 9654-9662 (2009).

[33] Tsoi, W. C.; James, D. T.; Kim, J. S.; Nicholson, P. G.; E., N. C.; Bradley, D. D. C.; Nelson, J.; Kim, J.-S. “The Nature of In-Plane Skeleton Raman Modes of P3HT and Their Correlation to the Degree of Molecular Order in P3HT:PCBM Blend Thin Films” *Journal of the American Chemical Society,* **133**, 9834-9843 (2011).

[34] Katz, H. E.; Bao, Z. N.; Gilat, S. L. “Synthetic chemistry for ultrapure, processable, and high-mobility organic transistor semiconductors” *Accounts of Chemical Research,* **34**, 359-369 (2001).

[35] Quinn, J. J.; K-S., Y. *Solid State Physics: Principles and Modern Applications*. New York: Springer, pp. 37-79. 2009.

[36] Frank, C. W.; Rao, V.; Despotopoulou, M. M.; Pease, R. F. W.; Hinsberg, W. D.; Miller, R. D.; Rabolt, J. F. “Structure in thin and ultrathin spin-cast polymer films” *Science,* **273**, 912-915 (1996).

[37] Bistac, S.; Schultz, J. “Solvent retention in solution-cast films of PMMA: study by dielectric spectroscopy” *Progress in Organic Coatings,* **31**, 347-350 (1997).

[38] Rughooputh, S.; Hotta, S.; Heeger, A. J.; Wudl, F. “Chromism of soluble polythiophenes” *Journal of Polymer Science Part B-Polymer Physics,* **25**, 1071-1078 (1987).

[39] Coropceanu, V.; Cornil, J.; da Silva, D. A.; Olivier, Y.; Silbey, R.; Bredas, J. L. “Charge transport in organic semiconductors” *Chemical Reviews,* **107**, 926-952 (2007).

[40] Winokur, M. J.; Spiegel, D.; Kim, Y.; Hotta, S.; Heeger, A. J. “Structural and absorption studies of the thermochromic transition in poly(3-hexylthiophene)” *Synthetic Metals,* **28**, 419-426 (1989).

[41] Tashiro, K.; Ono, K.; Minagawa, Y.; Kobayashi, K.; Kawai, T.; Yoshino, K. “Structural changes in the thermochromic solid-state phase transition of poly(3-alkylthiophene” *Synthetic Metals,* **41**, 571-574 (1991).

[42] Navarrete, J. T. L.; Zerbi, G. “Lattice-dynamics and vibrational-spectra of polythiophene .2. Effective coordinate theory, doping induced, and photoexcited spectra” *Journal of Chemical Physics,* **94**, 965-970 (1991).

[43] Castiglioni, C.; Delzoppo, M.; Zerbi, G. “Vibrational Raman spectroscopy of polyconjugated organic oligomers and polymers” *Journal of Raman Spectroscopy,* **24**, 485-494 (1993).

[44] Milani, A.; Brambilla, L.; Del Zoppo, M.; Zerbi, G. “Raman dispersion and intermolecular interactions in unsubstituted thiophene oligomers” *Journal of Physical Chemistry B,* **111**, 1271-1276 (2007).

[45] Kline, R. J.; McGehee, M. D.; Toney, M. F. “Highly oriented crystals at the buried interface in polythiophene thin-film transistors” *Nature Materials,* **5**, 222-228 (2006).

[46] Street, R. A.; Northrup, J. E.; Salleo, A. “Transport in polycrystalline polymer thin-film transistors” *Physical Review B,* **71**, 165202 (2005).

[47] Jimison, L. H.; Toney, M. F.; McCulloch, I.; Heeney, M.; Salleo, A. “Charge-Transport Anisotropy Due to Grain Boundaries in Directionally Crystallized Thin Films of Regioregular Poly(3-hexylthiophene)” *Advanced Materials,* **21**, 1568-1572 (2009).

[48] Salleo, A.; Kline, R. J.; DeLongchamp, D. M.; Chabinyc, M. L. “Microstructural Characterization and Charge Transport in Thin Films of Conjugated Polymers” *Advanced Materials,* **22**, 3812-3838 (2010).

[49] Knapp, E. W. “Lineshapes of molecular aggregates - Exchange narrowing and intersite correlation” *Chemical Physics,* **85**, 73-82 (1984).

[50] Knoester, J. “Nonlinear optical line shapes of disordered molecular aggregates - Motional narrowing and the effect of intersite correlations” *Journal of Chemical Physics,* **99**, 8466-8479 (1993).

[51] Vogt, H. “Refined treatment of the model of linearly coupled anharmonic-oscillators and its application to the temperature-dependence of the zone-center soft-mode frequencies of $KTaO_3$ and $SrTiO_3$” *Physical Review B*, **51**, 8046-8059 (1995).

[52] Sirenko, A. A.; Akimov, I. A.; Fox, J. R.; Clark, A. M.; Li, H. C.; Si, W. D.; Xi, X. X. “Observation of the first-order Raman scattering in $SrTiO_3$ thin films” *Physical Review Letters*, **82**, 4500-4503 (1999).

APPENDIX A

EXPANSION OF THE EQUATION OF POLARIZED RAMAN INTENSITY CONSIDERING ORIENTATION DISTRIBUTION FUNCTION

✓ ELECTRIC FIELD EQUATIONS FOR SAMPLE GEOMETRY [1]

$$\begin{aligned} E_{ZZ} &= a'_{zz}\left[\cos(\beta)\cos(\theta)-\sin(\beta)\sin(\theta)\cos(\alpha)\right]^2 \\ &\quad + a'_{xx}\left[\sin(\beta)\cos(\theta)+\cos(\beta)\sin(\theta)\cos(\alpha)\right]^2 \\ &\quad + a'_{yy}\left[\sin(\alpha)\sin(\theta)\right]^2 \end{aligned}$$

$$\begin{aligned} E_{YZ} &= a'_{zz}\left[\cos(\beta)\cos(\theta)-\sin(\beta)\sin(\theta)\cos(\alpha)\right]\cdot\left[\cos(\beta)\sin(\theta)+\sin(\beta)\cos(\theta)\cos(\alpha)\right] \\ &\quad + a'_{xx}\left[\sin(\beta)\cos(\theta)+\cos(\beta)\sin(\theta)\cos(\alpha)\right]\cdot\left[\sin(\beta)\sin(\theta)-\cos(\beta)\cos(\theta)\cos(\alpha)\right] \\ &\quad - a'_{yy}\left[\sin(\alpha)\sin(\theta)\right]\cdot\left[\sin(\alpha)\cos(\theta)\right] \end{aligned}$$

✓ ORIENTATION DISTRIBUTION FUNCTION (ODF) [2, 3]

$$\begin{aligned} f(\alpha,\beta) &= \sum_{L=0}^{4}\sum_{m=0}^{4}\frac{2L+1}{4\pi^2}\left\langle P_{Lm0}\right\rangle P_{Lm0}(\alpha,\beta,\gamma) \\ &= \frac{1}{8\pi^2}\left\{\begin{aligned} &1 \;+\; \frac{5}{2}\;\left\langle P_{200}\right\rangle\left(3\cos^2\beta-1\right) \;+\; 15\;\left\langle P_{220}\right\rangle\left(1-\cos^2\beta\right)\cos(2\alpha) \\ &+\frac{9}{8}\left\langle P_{400}\right\rangle\left(3-30\cos^2\beta+30\cos^4\beta\right) \\ &+\frac{135}{2}\left\langle P_{420}\right\rangle\left(-1+8\cos^2\beta-7\cos^4\beta\right)\cos(2\alpha) \\ &+\frac{315}{4}\left\langle P_{440}\right\rangle\left(1-2\cos^2\beta+\cos^4\beta+\right)\cos(4\alpha) \end{aligned}\right\} \end{aligned}$$

✓ RAMAN INTENSITY [4, 5]

$$\begin{aligned} I_{ll}(\theta) &= I_{ZZ}(\theta) = k\int_\alpha\int_\beta f(\alpha,\beta)\sin(\beta)\left[E_{ZZ}(\alpha,\beta)\right]^2 d\alpha d\beta \\ I_{\perp}(\theta) &= I_{YZ}(\theta) = k\int_\alpha\int_\beta f(\alpha,\beta)\sin(\beta)\left[E_{YZ}(\alpha,\beta)\right]^2 d\alpha d\beta \end{aligned}$$

$$
\begin{aligned}
&I_{ll}(\boldsymbol{\theta}) \\
&= \frac{1}{3360\pi}\left\{
\begin{aligned}
&-210\sin^4\theta\cdot\left(\alpha_{yy}^{'}\right)^2\left[-3+20\langle P_{220}\rangle+36\langle P_{420}\rangle-21\langle P_{440}\rangle\right] \\
&+140\sin^2\theta\cdot\alpha_{yy}^{'}\alpha_{zz}^{'}\cdot\left[3+\cos 2\theta+(3+5\cos 2\theta)\langle P_{200}\rangle-12\cos^2\theta\langle P_{220}\rangle-54(1+\cos 2\theta)\langle P_{420}\rangle-27(1-\cos 2\theta)\langle P_{440}\rangle\right] \\
&+6\alpha_{zz}^2\left[\begin{aligned}&56+40(1+3\cos 2\theta)\langle P_{200}\rangle+480\sin^2\theta\langle P_{220}\rangle+(9+20\cos 2\theta+350\cos 4\theta)\langle P_{400}\rangle \\ &+(180+240\cos 2\theta-420\cos 4\theta)\langle P_{420}\rangle+(210-280\cos 2\theta+70\cos 4\theta)\langle P_{440}\rangle\end{aligned}\right] \\
&+\alpha_{xx}\left[\begin{aligned}&-70\sin^2\theta\cdot\alpha_{yy}^{'}\left\langle-9-7\cos 2\theta+2(3+5\cos 2\theta)\langle P_{200}\rangle+96\cos^2\theta\langle P_{220}\rangle+9(1-\cos 2\theta)\langle P_{440}\rangle\right\rangle \\ &+\alpha_{zz}\left\langle\begin{aligned}&273+140\cos 2\theta+35\cos 4\theta+5(9+20\cos 2\theta+35\cos 4\theta)\langle P_{200}\rangle \\ &+120(15+7\cos 2\theta)\sin^2\theta\langle P_{220}\rangle-(108+240\cos 2\theta+420\cos 4\theta)\langle P_{400}\rangle \\ &+(-270-2880\cos 2\theta+3150\cos 4\theta)\langle P_{420}\rangle+(315-420\cos 2\theta+105\cos 4\theta)\langle P_{440}\rangle\end{aligned}\right\rangle\end{aligned}\right] \\
&+\alpha_{xx}^2\left[\begin{aligned}&2\left(448\cos^4\theta+336\cos^2\theta\sin^2\theta+63\sin^4\theta\right)-5(57+164\cos 2\theta+35\cos 4\theta)\langle P_{200}\rangle \\ &+180(9+7\cos 2\theta)\sin^2\theta\langle P_{220}\rangle+6(9+20\cos 2\theta+35\cos 4\theta)\langle P_{400}\rangle \\ &+2\left(8640\cos^2\theta\sin^2\theta+2340\sin^4\theta\right)\langle P_{420}\rangle+210\sin^4\theta\langle P_{440}\rangle\end{aligned}\right]
\end{aligned}\right\} \\
&+
\end{aligned}
$$

$$I_{\perp}(\theta)$$

$$= \frac{1}{13440\pi}\left\{\begin{array}{l}
-210\ \sin 2\theta\cdot\left(\alpha'_{yy}\right)^{2}\cdot\left[-3+20\left\langle P_{220}\right\rangle+36\left\langle P_{420}\right\rangle-21\left\langle P_{440}\right\rangle\right]\\
-280\sin^{2}2\theta\cdot\alpha'_{yy}\cdot\alpha'_{zz}\cdot\left[1+5\left\langle P_{200}\right\rangle-6\left\langle P_{220}\right\rangle-54\left\langle P_{420}\right\rangle+27\left\langle P_{440}\right\rangle\right]\\
+8\left(\alpha'_{zz}\right)^{2}\left[\begin{array}{l}56+40\left\langle P_{200}\right\rangle+240\left\langle P_{220}\right\rangle+\left(9-105\cos 4\theta\right)\left\langle P_{400}\right\rangle\\ +\left(180+1260\cos 4\theta\right)\left\langle P_{420}\right\rangle+\left(210-210\cos 4\theta\right)\left\langle P_{440}\right\rangle\end{array}\right]\\
+\left(\alpha'_{xx}\right)^{2}\left[\begin{array}{l}623-175\cos 4\theta+20\left(-19+35\cos 4\theta\right)\left\langle P_{200}\right\rangle+60\left(11+21\cos 4\theta\right)\left\langle P_{220}\right\rangle\\ +\left(72-840\cos 4\theta\right)\left\langle P_{400}\right\rangle+\left(5220+6300\cos 4\theta\right)\left\langle P_{420}\right\rangle+105\left(1-\cos 4\theta\right)\left\langle P_{440}\right\rangle\end{array}\right]\\
+\alpha'_{xx}\left[\begin{array}{l}-70\sin^{2}2\theta\cdot\alpha'_{yy}\cdot\left(-7+10\left\langle P_{200}\right\rangle+48\left\langle P_{220}\right\rangle-9\left\langle P_{440}\right\rangle\right)\\ +2\cdot\alpha'_{yy}\cdot\left\langle\begin{array}{l}189+35\cos 4\theta+35\cos 4\theta+5\left(-3+35\cos 4\theta\right)\left\langle P_{200}\right\rangle\\ -30\left(-39+7\cos 4\theta\right)\left\langle P_{220}\right\rangle+\left(36-420\cos 4\theta\right)\left\langle P_{400}\right\rangle\\ +\left(2610+3150\cos 4\theta\right)\left\langle P_{420}\right\rangle-105\left(1-\cos 4\theta\right)\left\langle P_{440}\right\rangle\end{array}\right\rangle\end{array}\right]
\end{array}\right\}$$

$$+$$

Since Raman tensor is thought to be uniaxial symmetry along primary axis (z), $a'_{xx} = a'_{yy}$ and $r = {a'_{yy}}/{a'_{zz}}$

Then

$$R(\theta) = \frac{I_\perp(\theta)}{I_{ll}(\theta)} = \frac{I_{YZ}(\theta)}{I_{ZZ}(\theta)}$$

$$= \frac{(-1+r)^2 \left\{ \begin{array}{l} -40\langle P_{200}\rangle - 240\langle P_{220}\rangle + (105\cos 4\theta - 9)\langle P_{400}\rangle \\ -2\left[28 + 90(1+7\cos 4\theta)\langle P_{420}\rangle + 210\sin^2\theta\langle P_{440}\rangle\right] \end{array} \right\}}{\left\{ \begin{array}{l} 40(4r^2 - r - 3)\left[(1+3\cos 2\theta)\langle P_{200}\rangle + 12\sin^2\theta\langle P_{220}\rangle\right] \\ -3(r-1)^2(9 + 20\cos 2\theta + 35\cos 4\theta)\langle P_{400}\rangle \\ -8\left[7(3+4r+8r^2) + 30(r-1)^2\sin^2\theta\left(3(5+7\cos 2\theta)\langle P_{420}\rangle + 7\sin^2\theta\langle P_{440}\rangle\right)\right] \end{array} \right\}}$$

✓ REFERENCES

[1] D. A. Long, *The Raman Effect : A Unified Treatement of the Theory and Raman Scatterign by Molecules*. Chichester: Wiley, pp. 85-94, 2002.

[2] Luckhurst, G. R.: Veracini, C. A., Eds., *The Molecular Dynamics of Liquid Crystals* (On the Description of Ordering in Liquid Crsytals. Dordrecht: Kluwer Academic Publishers, pp.11-36, 1994.

[3] Southern, C. D.: Gleeson, H. F. “Using the full Raman depolarisation in the determination of the order parameters in liquid crystal systems” *European Physical Journal E*, **24**, 119-127 (2007).

[4] Jones, W. J.; Thomas, D. K.; Thomas, D. W.; Williams, G. “Raman scattering studies of homogeneous and twisted-nematic liquid crystal cells and the determination of < P2 > and < P4 > order parameters” *Journal of Molecular Structure*, **614**, 75-85 (2002).

[5] Jones, W. J.; Thomas, D. K.; Thomas, D. W.; Williams, G. “On the determination of order parameters for homogeneous and twisted nematic liquid crystals from Raman spectroscopy” *Journal of Molecular Structure*, **708**, 145-163 (2004).